

Ph.D. Thesis  
Department Chemistry  
Ludwig Maximilian University Munich

**The combined AFM manipulation and  
fluorescence imaging of single DNA molecules**

Andrew Hards  
from London

2004

## Declaration

This thesis was supervised by Prof. Dr. Ch. Bräuchle, as specified in §13 clauses 3 and 4 of the university PhD thesis protocol from January 29th 1998.

## Statutory declaration

This thesis was completed independently, without illegitimate help.

Munich, 27.02.2004

Thesis submitted	27.02.2004
1. Referee:	Dr. A. Zumbusch
2. Referee:	Prof. Dr. Ch. Bräuchle
Oral exam	19.04.2004

## Table of Contents

Foreword	1
<b>1. INTRODUCTION</b>	<b>2</b>
<b>2. AFM FORCE SPECTROSCOPY OF SINGLE MOLECULES</b>	<b>6</b>
2.1 General principles of AFM force spectroscopy	6
2.2 Force spectroscopy of sugars	19
2.3 Force spectroscopy of DNA on transparent surfaces	33
<b>3. SINGLE MOLECULE FLUORESCENCE MICROSCOPY</b>	<b>49</b>
3.1 General principles	50
3.2 Methods of single molecule microscopy	53
3.3 The general optical setup	57
3.4 Confocal microscopy and single molecule fluorescence spectra	62
3.5 Hemicyanine dyes for combined SM and AFM experiments	67
3.6 Total internal reflection (TIR) imaging	72
<b>4. DNA OPTICAL EXPERIMENTS</b>	<b>83</b>
4.1 The photophysical parameters of TO-PRO-3 <sup>®</sup> with DNA	83
4.1.1 TO-PRO-3 bulk fluorescence spectra	85
4.1.2 Dye photobleaching	87
4.1.3 Anti-bleaching agents	92
4.1.4 The TO-PRO-3/DNA rate kinetics	96
4.1.5 The binding constant of TO-PRO-3 to DNA	102
4.1.6 Salt dependence	103
4.1.7 Conclusion of the imaging experiments	104
4.2 Imaging of single molecule DNA strands	105
4.2.1 DNA on polylysine surfaces	106
4.2.2 DNA condensation on polylysine surfaces	109
4.2.3 Silanised surfaces and super-long $\lambda$ -phage DNA	118

<b>5. COMBINED OPTICAL IMAGING AND AFM</b>	<b>126</b>
5.1 The combined optics/AFM setup	126
5.2 Cantilever luminescence	132
5.3 The manipulation of DNA on polylysine: writing with DNA	137
5.4 DNA manipulation on silane surfaces	142
5.5 Combined force spectroscopy/optical imaging	145
5.5.1 Combined experiments on polylysine	145
5.5.2 Combined experiments on silanised surfaces	148
5.5.3 Conclusion of the combined experiments	150
5.6 Single molecule lateral force spectroscopy of DNA	152
5.7 Discussion of the combined AFM/optical experiments on DNA	167
<b>6. CONCLUSION AND OUTLOOK</b>	<b>172</b>
6.1 Summary and conclusion	172
6.2 Outlook	174
Appendix 1: Coverslip surface preparation procedures	178
Appendix 2: Sample preparation: polysaccharides	180
Appendix 3: DNA force spectroscopy	181
Appendix 4: LabView® programs	182
Appendix 5: DNA imaging protocols	183
Appendix 6: DNA straightening procedures	185

## Foreword

One of the great scientific breakthroughs at the end of the 20th century was the development of methods to directly access single molecules on the nanometer scale. Among these have been the scanning probe microscopes such as the atomic force microscope (AFM), with which it was possible to detect and interact with individual molecules or even atoms on surfaces. At the same time, highly sensitive optical techniques such as confocal or wide-field imaging microscopy have enabled new insights into the fluorescence properties of single fluorophores at the ultimate analytical limit of chemistry.

In the drive towards ever greater miniaturisation, this step down to the atomic scale may have appeared inevitable, but science has come a long way considering the ancient history of the atomic theory. It was proposed in antiquity by the Greek atomistic schools of philosophy, as a solution to reconcile the fleeting world of appearances with the desire for a more permanent underlying order. Atomism was reborn in chemical terms with Lavoisier and Dalton, to be confirmed by the physical experiments of Thomson and Rutherford, and finally elaborated by Bohr and quantum mechanics. Actually “seeing” an atom in the conventional sense by reflection of photons may not be possible, because the wavelength of visible light is beyond the atomic dimensions. None of the aforementioned pioneers could have dreamed of ever visualising a single atom or even the Platonic “shadows” thereof, generated by indirect imaging techniques. New methods such as AFM force spectroscopy with which single polymer chains can be stretched and their elastic properties determined add an extra dimension to the manipulation of particles on the nanometer scale, bringing polymeric molecules such as DNA – the blueprint of biological life - closer to the human experiences of the macroscopic world.

# 1. Introduction

With the development of the scanning tunnelling microscope (STM) by Binnig and Rohrer in 1981 it became possible to image surfaces with atomic resolution [1]. The images were generated by raster scanning a fine metallic tip over a conductive surface and measuring the tunnelling current to the tip apex. In 1986, Binnig et al. presented the atomic force microscope (AFM), with which also insulating surfaces could be scanned and imaged [2]. The force microscope detects the sample topography by monitoring the mechanical cantilever deflection as the tip is directed over the surface. Atomic resolution was achieved on hard crystalline terraces [3, 4]. Importantly, the AFM has also enabled significant progress to be made in the imaging of soft non-conducting biological material such as single DNA strands [5-8].

The direct investigation of single molecule mechanical properties - *single molecule force spectroscopy* - has been achieved by various methods. Among these were the stretching of individual DNA strands in a fluid shear flow [9-11], with the aid of magnetic beads [12-15] or with optical tweezers [16-20]. Using these kinds of apparatus it was possible to measure the applied forces on single polymers with pN accuracy. The breakthrough for the AFM in this field was achieved in 1994 with the construction of a one-dimensional vertical pulling AFM. This apparatus enabled the observation of a single streptavidin-biotin complex bond rupture [21, 22]. The new method called *AFM Force Spectroscopy* used the cantilever tip to pick up and pull at single molecules - most notably polymers. By exploiting the high vertical force resolution of the AFM, force-distance curves could be generated which describe the mechanical tension on a single polymer in relation to the pulling distance [23]. The applications for single molecule AFM force spectroscopy have become very diverse, ranging from material science [24] to biology [25]. Generally five classes of molecular systems have been examined [24]: Ligand-receptor interactions [26, 27], metal complexes [28], polysaccharides [29, 30], proteins and conformational analysis [31-35], synthetic organic polymers [36, 37] and, finally, polynucleotides such as DNA [38-41]. The extremely broad force range from a few pN to several nN has permitted the

measurement of the strength of a single covalent Si-C or S-Au bond to be about 1-2nN [42].

*Single molecule fluorescence spectroscopy* has established itself in the last 12 years as an optical technique to image individual fluorophores [43]. This method is based on the laser excitation and fluorescence detection of highly diluted dyes in condensed matter. Although early experiments were conducted at cryogenic temperatures [44-48], the room temperature examination of, especially, biological systems [49-52] has become increasingly significant. The main methods for room temperature spectroscopy of single molecules are: confocal scanning microscopy [53-55], wide-field imaging [56], scanning near-field microscopy (SNOM) [57] and total internal reflection (TIR) imaging [58-62].

However, both single molecule force spectroscopy and fluorescence imaging have shortcomings. Conventional AFM force spectroscopy, while powerful in the analysis of single molecule mechanics, relies on the unspecific attachment of polymers to the tip. Fluorescence microscopy, on the other hand, can visualise single molecules, but provides no means for mechanical interaction. The motivation of this work was therefore to overcome these restrictions by combining both established methods and constructing a setup with which single molecules could be imaged and specifically manipulated at the same time.

Various approaches to intermarrying optics with an AFM have previously been made. Among these are SNOM microscopes that channel light through a tip aperture to the sample surface, thus enabling near-field optical microscopy [57, 63-65]. Hybrid confocal/AFM scanning microscopes [66-68] have also been implemented and the combination of the AFM with a wide-field optical microscope was realised as early as 1992 by Putman, who examined the topography and optical features of chromosomes [69]. More recently, the FRET signal of a single tip-attached acceptor dye has been examined, while exciting the sample donor dye by wide-field illumination [70]. Finally, the group of H. Gaub used light pulses to switch the conformation of AFM-stretched azobenzene polymers and measured the resulting changes in molecular extension with force spectroscopy [71].

However, these approaches do not allow for an independent simultaneous mechanical interaction with the sample during the imaging process. The goal was therefore, to construct an integrated setup, including a wide-field optical microscope and an AFM, by which the manipulation process itself could be viewed in real-time. Finally, with this new apparatus we hope to conduct force spectroscopy on single fluorescent polymers with concomitant imaging. After a long heuristic process, the main technical challenge was overcome by constructing a microscope stage for the AFM head, so that both the AFM cantilever and the microscope objective have access to the sample coverslip from the top and from below, respectively.

First experiments focussed on synthesising organic polymer molecules with incorporated single fluorophores. By pulling at these polymers, it was hoped that the optical properties of a single dye, e.g. the fluorescence spectrum, could be examined under mechanical strain. Although theoretical calculations indicated a shift in the spectra for certain dyes [72, 73], the experiments proved to be unproductive, due to the low dye photostability and difficulties in the surface chemistry at the single molecule level.

A more promising system for this new apparatus was found in DNA, intercalated with the fluorophore TO-PRO<sup>®</sup>-3. The dye molecules bind to the DNA electrostatically and stack between the nucleotides. This intercalation greatly enhances the fluorescence of the bound dyes. Although DNA was long regarded as being too thin (ca. 2nm) for optical detection, in 1981 Yanagida et al. presented fluorescent images of single DNA molecules with similar dyes using an optical microscope [74]. Since then, new cyanine dyes have been developed that provide better images of individual DNA chains [75, 76]. Among these was the dye TO-PRO<sup>®</sup>-3, which possesses a low photo-bleaching rate, a high binding affinity to DNA and a high fluorescence quantum yield enhancement on binding to the DNA [77]. Furthermore, DNA - already ubiquitous in biology - has been of special interest as a substrate for examining the mechanical properties of single polymers [40]. The unique elasticity and the availability of fluorescing intercalators make DNA the ideal candidate for optical detection and simultaneous manipulation with a combined AFM/fluorescence setup.

## Synopsis

Chapter II begins with a description of the *AFM force spectroscopy* setup and methodology. The force spectra for a series of polysaccharides are presented. Furthermore, a second class of force curves, displaying horizontal plateau events, is explained with a new model based on the hydration energy of single polymer chains in poor solvents. This is followed by the force spectroscopic work on DNA, including statistics on the rupture force and rupture length on transparent surfaces, such as polylysine-coated and silanised glass, as well as the characteristic effect of TO-PRO-3 on DNA force curves.

Chapter III gives an overview of the optical *single molecule imaging* techniques. These include confocal scanning microscopy, single molecule spectroscopy, wide-field imaging and total internal reflection (TIR) imaging methods. Experiments on the terrylenediimide (TDI) and cyanine5 systems are described, as well as a series of new hemicyanine dyes, which are examined for their suitability as single molecule dyes in combined AFM/optics experiments. A new setup is used to monitor the evanescent TIR field by employing the cantilever as a luminescent probe.

Chapter IV presents the optical imaging experiments on single DNA strands. A detailed analysis of the photophysics of the TO-PRO-3/DNA system is provided, followed by the DNA imaging results on various surfaces. DNA aggregation on polylysine is explained with the condensating effect of charged polycationic chains. The discovery of super-long DNA strands on silanised surfaces is discussed with respect to DNA junction formation.

Chapter V deals with simultaneous optical detection and manipulation experiments on the DNA system. This includes a description of the combined setup, a study of cantilever luminescence and real-time DNA manipulation experiments on polylysine and silane surfaces. A method is presented for writing  $\mu\text{m}$ -sized letters with DNA ink. The results of the combined optical imaging/force spectroscopy experiments are discussed, explaining the difficulties encountered. A new method, *single molecule lateral force spectroscopy*, is presented, which enables the analysis of dye fluorescence under DNA chain tension – the original goal of this work.

A conclusion in chapter VI provides an outlook on future experiments.

## 2. AFM force spectroscopy of single molecules

### 2.1 General principles of AFM force spectroscopy

The AFM enables a high force resolution. Typical forces range from 10pN - 10nN (magnetic tweezers: 0.01 - 10pN; optical tweezers: 0.1 - 100pN [13]). This sensitivity is achieved by measuring the bending curvature of the AFM cantilever through the displacement of a laser beam, which is focussed onto the cantilever shank (*deflection signal*). In this way small changes in the curvature can be detected and correlated with the forces acting on the cantilever tip. Under low noise conditions, forces of ~3pN can be resolved.

By comparison, the repulsion experienced through the photonic pressure of a 1mW laser pointer is similarly ca. 3.3pN. Furthermore, the smallest measurable forces are those responsible for the Brownian motion of bacteria in water at room temperature. These forces, which buffet the tiny particles about, are comparable to the weight of the bacteria of ca. 10fN (assuming mass of bacterium  $\sim 1 \cdot 10^{-15}$  kg). Molecular motors typically convert chemical energy to mechanical work by hydrolysis of ATP. One ATP yields about  $5.6 \cdot 10^{-20}$  J. Over 10nm this corresponds to a force of ca. 6pN. Hydrogen bonding forces and those due to hydrophobic interactions occur in the order of ca. 100pN [78], whereas the strongest bonds on the molecular level, the covalent bonds, can withstand forces of up to a 1-2nN [42].

To enable the analysis of these microscopic forces, the conventional scanning AFM is converted into a one-dimensional pulling device, with which it is possible to pick up single molecules [79]. By lifting the cantilever away from the sample surface, molecules, which are attached to the cantilever tip, can be pulled taut and stretched. The resultant tension directly reflects the elastic properties of the pulled polymer chain. The exact mechanism or chemical background for the attachment, which frequently works unspecifically for a whole range of polymers, is to date unclear, although electrostatic and hydrophobic interactions are probably involved.

## Force-distance curves

The results of the force spectroscopic measurements are expressed in the form of force curves (cf. Figure 2), in which the force is plotted against the distance moved by the piezo. However, to determine the molecular elasticity of a stretched polymer, these force curves must first be converted into force-distance curves. The difference between the two is a consequence of the cantilever curvature. The actual distance between the sample and the tip (cf.  $Z$  in Figure 1) is not the same as that travelled by the piezo (cf.  $L$  in Figure 1), because the tip bends downwards under a load. The correction is easily made by determining the tip curvature under a certain force - the cantilever sensitivity  $S$ .  $A$  is the deflection signal in Volts. The sensitivity is usually calculated from a surface indentation curve, taken prior to the actual experiments (cf. stage 2 in Figure 2). Thus, the true tip-sample distance is given by:

eq. 1 
$$Z = L - \frac{A}{S}$$

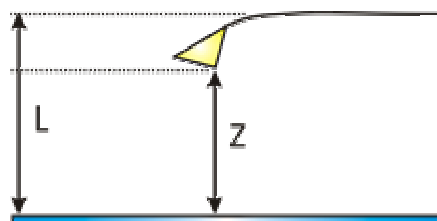


**Figure 1: Length correction due to cantilever bending. The measured piezo movement  $L$  is related to the actual tip-sample distance  $Z$  through the cantilever sensitivity.**

Plotting  $F(z)$  against  $z$  gives a force-distance curve, from which quantitative data concerning polymer mechanics can be gained. However, frequently the force curves themselves are sufficient to establish rupture forces or plateau heights etc.

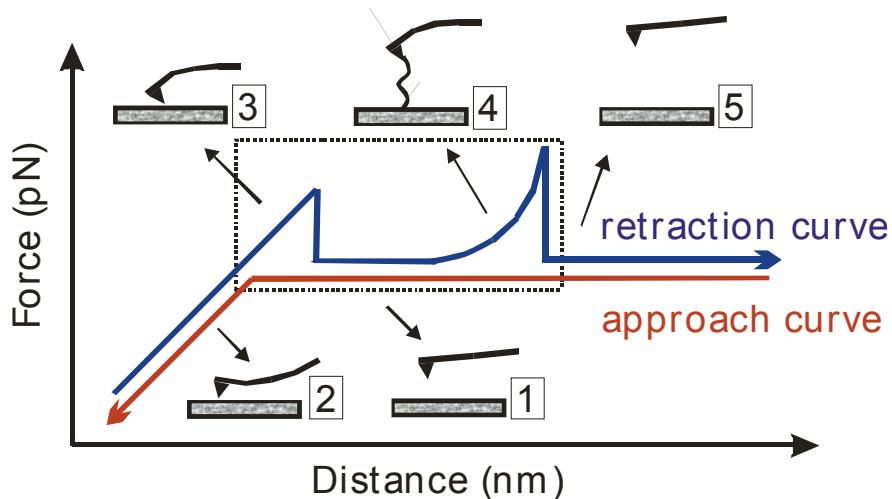


**Figure 2:** A typical force-distance curve is characterised by an approach curve (red), (1) during which the cantilever descends towards the sample surface. (2) At the point of contact the cantilever is bent upwards. (3) During retraction (blue) the tip often adheres unspecifically to the surface, thus bending downwards, before snapping off and straightening out. (4) If a molecule is attached, the tension in the strand can be correlated with the curvature of the tip. (5) Finally the strands rupture. The region describing the tip-molecule interaction is given by the dotted area.

A generalised force curve is presented in Figure 2, together with a schematic description of the corresponding cantilever position. The region of interest in Figure 2 is the dotted area, which provides information on the molecular mechanical parameters. A single molecule force curve can be divided roughly into three force regions.

At zero force, the natural conformation of a polymer is a random coil. Straightening the chain, results in an entropically driven restoration force. In principle, the force to align a polymer of identical rigid units is in the order of  $k_B T/b \sim 0.1 \text{ pN}$ , where  $b$  is the length of one unit [8]. However, the entropic elasticity required to disentangle a real polymer is usually described by models to ca. 5-10 pN.

At medium forces of up to a few hundred pN, enthalpic conformational changes become significant, which are the result of bond angle changes between the chain segments. The deformation energies of complex conformational transitions are difficult to describe by simple models, especially for large molecules such as DNA [13].

Finally, in the high force regime of up to 2nN, the intramolecular bonds themselves are extended, which eventually leads to strand rupture. Due to the long timescale of the pulling experiment as compared to the average lifetime of a stretched bond under tension, this bond fracture usually occurs at a lower force than theoretically predicted by comparatively fast molecular dynamics simulations.

### **Polymer elasticity models**

Single molecule force experiments provide unique access to the mechanical parameters of individual polymers, which would otherwise be hidden by ensemble averaging. To extract these factors analytical models have been proposed that fit the measured force curves, thus affording parameters for the chain elasticity or stiffness.

### **The freely-jointed chain model**

The FJC model describes the polymer chain as a series of  $N$  rigid segments of length  $l_k$  (Kuhn length) that have complete freedom of rotation around the segment joints [80] (cf. Figure 3). Thus, the conformations of the chain can be described by a random walk in which each step  $l_k$  is placed randomly with respect to its predecessor [81]. In this case the total contour length  $L_c$  of the polymer is given by:

eq. 2 
$$L_c = Nl_k$$

According to this model, the probability of a certain end-to-end distance  $R$  of a polymer follows a Gaussian distribution around the mean value of  $\langle R \rangle = 0$ . The quadratic end-to-end distance is proportional to the quadratic Kuhn length and the number of segments  $N$ :

eq. 3 
$$\langle R^2 \rangle = Nl_k^2$$

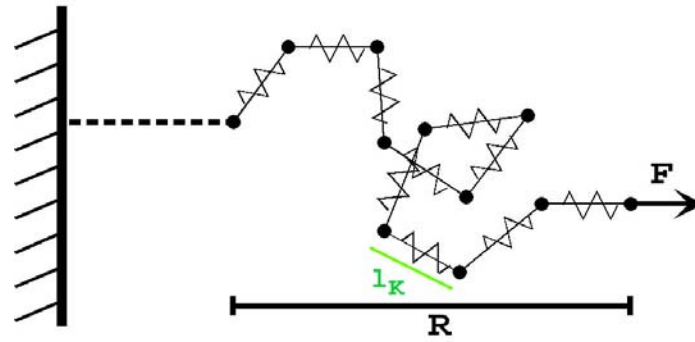


**Figure 3:** The FJC chain model assumes a chain of length  $L_c$ , with rigid and freely rotating, so called Kuhn segments of length  $l_K$ , each with a specific orientation. Based on this model an expression is derived that describes the end-to-end distance  $R$  in relation to the force  $F$ .

With increasing force and pulling distance the probability distribution of  $R$  is shifted to more extended configurations and thus the entropy of the polymer system drops. An entropically driven restoration force  $F$  is the result. The exact configuration is not known for each time, but an equation for the polymer extension  $R$  with force  $F$  can be derived by expressing the system in the form of a configuration state partition function  $Z(F)$  [80]. Here, the terms  $l_1 \dots l_N$  describe the orientational vectors of the  $N$  segments composing the chain. The end-to-end distance  $R$  is thus the sum of all the segment vectors and the energy of an overall polymer configuration state is given by  $E(l_1 \dots l_N)$ . The applied force attenuates the energy of a given state with an extra term  $F \cdot R$  such that [82]:

$$\text{eq. 4} \quad Z(F) = \int \dots \int e^{-\frac{E(l_1 \dots l_N) - FR}{k_B T}} dl_1 \dots dl_N$$

The energies  $E(l_1 \dots l_N)$  are constant for independent segments with no intrachain interaction and the integral of the partition function can be solved by using spherical coordinates:

$$\text{eq. 5} \quad Z(F) = \left[ 4\pi \frac{k_B T}{Fl} \sinh\left(\frac{Fl}{k_B T}\right) \right]^N$$

Furthermore, the average observable end-to-end distance  $\langle R \rangle$  is related to the partition function according to eq. 6 [82]:

$$\text{eq. 6} \quad \langle R \rangle = k_B T \frac{\partial \ln Z(F)}{\partial F}$$

Inserting eq. 5 into eq. 6, the following expression can be derived for the end-to-end pulling length  $x(F)$ :

$$\text{eq. 7} \quad x(F) = N l_k \left[ \coth \left( \frac{F l_k}{k_B T} \right) - \frac{k_B T}{F l_k} \right]$$

This is usually expressed with the function  $L^{-1}$  - the inverse of the Langevin function ( $\coth(x) - 1/x$ ) - to comply with the force-distance curves:

$$\text{eq. 8} \quad \boxed{F(x) = \frac{k_B T}{l_k} L^{-1} \left( \frac{x}{N l_k} \right)}$$

However, this model assumes rigid segments and purely entropic restoring forces. To account for deformations in bond length or other enthalpic components a further parameter is introduced: the segment elasticity  $K_s$ .

$$\text{eq. 9} \quad x(F) = L_c L \left( \frac{F l_k}{k_B T} \right) + \frac{N}{K_s} F$$

The assumption made in the FJC model of wholly independent segments works better for long flexible chains such as simple polysaccharides, RNA or organic polymers.

To describe the effect of the FJC model parameters on the force curve a series of hypothetical force curves have been plotted in Figure 4 [83]. The black curve shows a polymer with a contour length  $L_c = 100\text{nm}$ , a Kuhn length  $l_k = 1\text{nm}$  and a very high segment elasticity value of  $K_s = 10^9\text{pN/nm}$ . An increase in the contour length shifts the curve to the right (red curve:  $L_c = 110\text{nm}$ ), whereas making the polymer more elastic by reducing the segment elasticity value (blue curve:  $K_s = 10^4\text{pN/nm}$ ) results in the polymer extending beyond its contour length. Finally, decreasing the Kuhn length,

which is equivalent to an increased number of segments, leads to greater entropic restoration forces at low extensions (green curve:  $l_k = 0.1\text{nm}$ ).

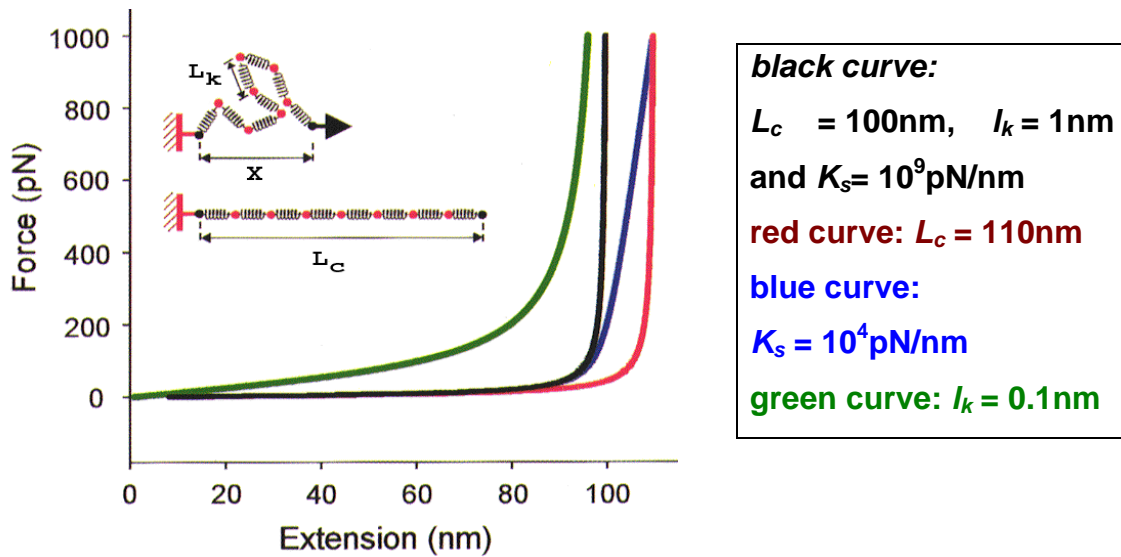


Figure 4: Force extension relationships for a series of hypothetical polymers constructed using the FJC equation [from Fisher et al. [83]].

### Worm-like-chain model

For continuous semi-flexible (stiff) polymers such as DNA a different model has been developed [84]. The worm-like-chain model treats the polymer as a series of hypothetical segments along a continuously curving, homogeneous rod-like chain. The segments have the length  $L_p$ , the persistence length, which is the distance along which the molecule can be considered as rigid i.e. the distance after which the orientation of a chain segment is no longer correlated to that of a previous segment. Enthalpic angle bending costs are taken into consideration in this model.

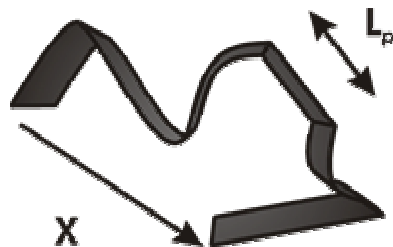


Figure 5: The WLC model describes a polymer as a uniform flexible rod with a characteristic length  $L_p$ , which is proportional to the chain stiffness.

In 1994 Marko and Siggia [85] established an expression for the semi-flexible chain, by determining the partition function and forming the derivative with respect to the force. Although the exact solution can only be calculated numerically, an analytical function can be given that applies asymptotically to the limiting low and high force region and only falls short by <10% in the middle force range.

$$\text{eq. 10} \quad F(x) = \frac{k_B T}{L_p} \left[ \frac{x}{L_c} + \frac{1}{4} \left( 1 - \frac{x}{L_c} \right)^{-2} - \frac{1}{4} \right]$$

In a real polymer, the chain contour length  $L_c$  is variable and bond lengths can be stretched [86]. To incorporate for chain elasticity, the term  $(x/L_c)$  is substituted for  $(x/L_c - F/K_0)$ , for which  $K_0$  is the specific stiffness of the chain.

$$\text{eq. 11} \quad F(x) = \frac{k_B T}{L_p} \left[ \frac{x}{L_c} - \frac{F}{K_0} + \frac{1}{4} \left( 1 - \frac{x}{L_c} + \frac{F}{K_0} \right)^{-2} - \frac{1}{4} \right]$$

For flexible chains with infinitely small chain units the important relationship between the Kuhn length and the persistence length can be established:

$$\text{eq. 12} \quad l_k = 2L_p$$

Attempts have been made to reduce the discrepancy between the Marko/Siggia approximation and the exact numerical solution by extending the function with a seventh order polynomial [87].

## The MFP force microscope

AFM force pulling experiments were carried out using an Asylum Research<sup>®</sup> *Molecular Force Probe*<sup>™</sup> (MFP). Igor Pro<sup>®</sup> software controlled the data acquisition and analysis. Typically, a 2kHz sampling rate for the deflection signal and a pulling velocity of 2 $\mu\text{m/s}$  was used. To reduce vibrational noise, the MFP stage was placed on an air cushioned laser table and surrounded by a wooden, egg-box foam covered acoustic box.

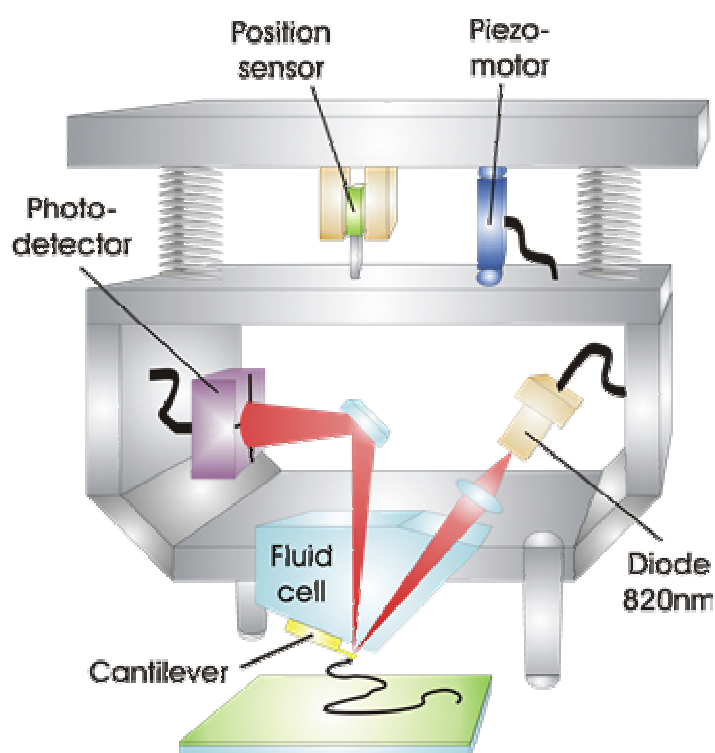


**Figure 6: Schematic description of the MFP setup. The force on the cantilever was determined by the deflection of a diode laser source on the tip, as measured by the signal A-B of a photodetector with segments A and B. Movement in the z-axis was driven by a piezo-driven motor in the MFP head and regulated by an inductive position sensitive device to  $<2\text{\AA}$  RMS.**

$\text{Si}_3\text{N}_4$  Microlevers<sup>™</sup> (ATOS<sup>®</sup> GmbH) with a spring constant  $k$  of 15mN/m were commonly used and mounted on the MFP fluid cell. The cantilevers appear as frail “teeth of a key” on the end of the  $\text{Si}_3\text{N}_4$  chip (cf. Figure 7).

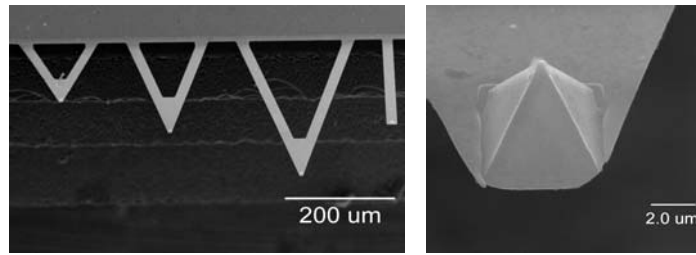


**Figure 7: Scanning electron microscope images of the cantilevers [88].**

The laser diode was positioned on the back of the tip with the help of a simple home-built microscope, which was composed of a 20x objective and a small CCD camera. An optical image taken with this adjustment microscope is shown in Figure 8. The arrow indicates the laser focus on the tip shank, as seen from below the cantilever chip. The back of the cantilever is gold-coated to increase laser reflectivity.



**Figure 8: Alignment of the AFM laser onto the gold-coated back surface of the cantilever. The red arrow indicates the position of the laser focus on the shank.**

### **Cantilever calibration**

To convert the measured voltage signal from the photodetector into a force in newtons, the cantilever must first be calibrated. Depending on the position of the laser spot, the deflection signal will be more or less sensitive towards forces applied to the tip. This sensitivity (i.e. the change in deflection signal for a given cantilever curvature) is measured by pressing the cantilever into a hard sample surface and determining the slope of the force curve at the indentation region (cf. Figure 2, no.2). The sensitivity  $S$  has the units [mV/μm].

The next step is to determine the cantilever spring constant  $k$ , which is calculated according to the thermal noise method [89]. By approximation, the cantilever can be described as a Hookean spring.

eq. 13 
$$F = -kx$$

According to the equipartition theorem, each degree of freedom in a thermodynamic system is assigned the same thermal energy. Therefore a freely swinging cantilever eigenmode will be excited with the energy  $1/2k_B T$ .

eq. 14 
$$\frac{1}{2}k_B T = \frac{1}{2}k\langle x^2 \rangle$$

The value  $\langle x^2 \rangle$  is the time-average square amplitude of the cantilever thermal fluctuation. This value is conveniently determined by integration of the harmonic oscillation peak in the frequency domain of a power spectrum. According to Parseval's theorem, integrating the power spectral density of a thermally excited, resonant oscillation in the frequency domain  $x(\omega)^2$  is equal to  $x(t)^2$  in the time domain and thus describes the total energy of that degree of freedom. Therefore  $\langle x^2 \rangle$  can be determined from the resonance peak in the power spectrum of a thermally excited cantilever. Inserting  $\langle x^2 \rangle$  in eq. 14 affords the spring constant  $k$ . A more detailed analysis of the detector geometry, which actually measures the curvature of the cantilever and not the extension amplitude  $x$ , leads to the following corrected relationship [90]:

eq. 15 
$$k \sim 0.8 \frac{k_B T}{\langle x^2 \rangle}$$

Finally, by bringing the two calibration constants together, the photodetector deflection signal  $A$  in volts can be converted into a force value:

eq. 16 
$$F = k * \frac{A}{S}$$

Generally, the force resolution is limited by the thermal noise of the cantilever to about 3pN. There are various ways to reduce cantilever noise and increase the sensitivity of the experiment below 1pN resolution. One method is to use short cantilevers with lower viscous dampening, lower spring constants (softer cantilevers), but also persistently high resonance frequencies [91].

In practice these improvements are only significant if external noise sources, such as low frequency vibrations of the building or acoustic noise in the room, e.g. from other electronic equipment or the air conditioning, can be excluded. To this end the AFM head was placed on an air cushioned laser table and surrounded by an acoustic hood. Furthermore, it was found that glass coverslips (thickness 170 $\mu$ m) were the source of a strong perturbation frequency when spanned over the large opening of the sample holder (cf. Figure 99). Microscope slides, which are thicker (1.2mm), showed no such resonant vibration. Fortunately, the microscope oil objective dampened this noise source, when brought into contact with the coverslips from below.

### **Sources of error in AFM force spectroscopy**

Cantilever *thermal drift* is one of the main difficulties in force experiments that last longer than about a second. Due to the different thermal expansion coefficients of gold and Si<sub>3</sub>N<sub>4</sub>, local temperature changes result in an unequal expansion of the two cantilever layers – the bimetal effect. This results in the cantilever gradually bending towards one side or the other. By careful temperature equilibration of the sample solution prior to the measurement, this effect can be reduced significantly, but it remains a source of error for very long experiments.

On the other hand, fast pulling experiments give rise to *hydrodynamic drag* of the tip, as it is forced through the fluid medium. This is especially significant for pulling speeds greater than 5 $\mu$ m/s and can be seen as an offset between the approach and retraction curves of the cantilever moving towards or away from the sample surface (cf. Figure 2). The various hydrodynamic effects become complex in the vicinity of the surface and the offset is no longer a constant value.

Piezoelectric crystalline materials, such as those used for positioning the AFM z-axis, exhibit a hysteresis in their expansion behaviour when reversibly subjected to a voltage signal. However, the AFM can correct for these errors by using an inductive coil as a feedback-loop position sensor (cf. Figure 6), which determines the piezo position to sub-Ångstrom accuracy.

Finally, high forces  $>10\text{nN}$  can bend the cantilever beyond its elastic regime so that viscoelastic properties come into play and the cantilever requires a certain time lag to regain its original curvature. However, most measurements do not reach such high forces.

## 2.2 Force spectroscopy of sugars

Polysaccharides, such as cellulose and amylose, are one of the main polymer classes that can be examined with AFM force spectroscopy [83]. In preparation for the experiments on DNA, these well characterised systems were chosen for first experiments with the AFM setup. In addition, new systems including palladium-complexed cellulose were examined to study the effect of the bound metal on the chain elasticity and derive the structure of the complex. Pd-cellulose cannot be examined with X-ray crystallography, because the long cellulose chains do not form a defined crystal structure.

Cellulose ( $\beta$ -[1,4]-polyglucose) is the most common polysaccharide. It is found naturally in wood and other plants, but also has considerable industrial significance in e.g. paper and cotton. Unlike its sugar counterparts such as amylose, however, canonical cellulose forms crystalline fibres and is thus water insoluble.

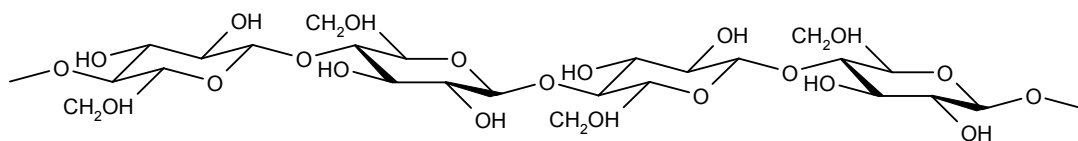


**Figure 9: Cellulose is composed of 1,4- $\beta$  linked D-Glucose subunits**

The chain solubility in water can be increased by introducing carboxymethyl groups into the polymer. These have the tendency to break up the intermolecular bonds, thus rendering the polymer soluble and also enabling single molecule force experiments. Carboxymethylcellulose (CM-cellulose) is itself an important industrial product, which is found in foodstuffs as a gelling agent or emulsifier.

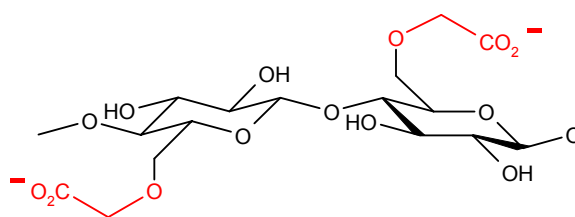


**Figure 10: Carboxymethylcellulose**

Another traditional method to bring cellulose into solution is by complexation with “Schweizer’s reagent” [Cu-NH<sub>3</sub> complex]. Ahlrichs et al. have recently developed a new method to provide molecularly disperse cellulose by complexation with palladium-ethylenediamine [92]. However, these complexes tend to form gels and so X-ray crystallography of the structures is impossible. In the light of this problem, force spectroscopy may help to elucidate the generated structures by providing information on the mechanical properties of the chain.

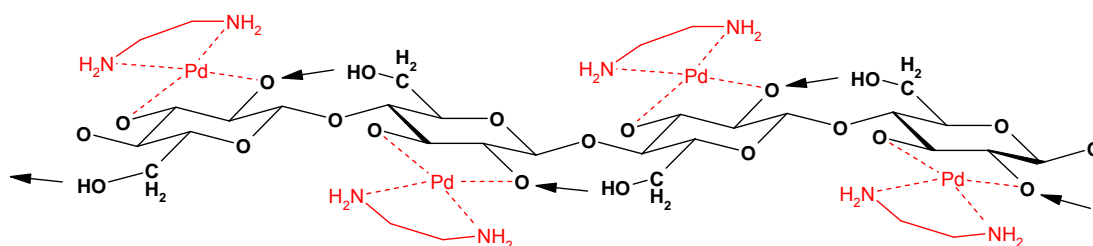


**Figure 11: Proposed structure of Pd-en cellulose. Additional intramolecular bonding due to the complexation with palladium-ethylenediamine could reduce chain flexibility.**

### Force spectroscopy of the cellulose derivatives

The force spectrum of CM-cellulose has been measured on numerous occasions [30, 93]. Generally cellulose behaves much like an entropic polymer, as anticipated by the FJC model. Relatively low entropic forces are followed by a sharp increase in force as the extension approaches the contour length. CM-cellulose is comparatively stiff with a Kuhn length of  $L_k = 4\text{nm}$  and a segment elasticity of  $K_s \sim 50\,000\text{pN/nm}$  [94].

For our experiments, CM-cellulose samples are prepared by overnight incubation on a glass coverslip and measuring in PBS buffer the following day (cf. Appendix 2: Sample preparation: polysaccharides). The force-distance curve in Figure 12 is typical for a single CM-cellulose polymer. Fitting the curve with the FJC model affords the mechanical parameters of the chain. Generally, the Kuhn lengths measured for about 15 curves varied between 1.7 - 3.3nm, whereas the segment elasticity of CM-cellulose was between 30 000 - 40 000pN/nm.

In Figure 12 the rupture force is 1.8nN, which is exceptionally high and in the force range of a covalent bond [42]. Furthermore, the contour length of the molecule is ca. 800nm, which is consistent with the average polymer length of 1.4 $\mu$ m (3200 monomer units) for this CM-cellulose sample.

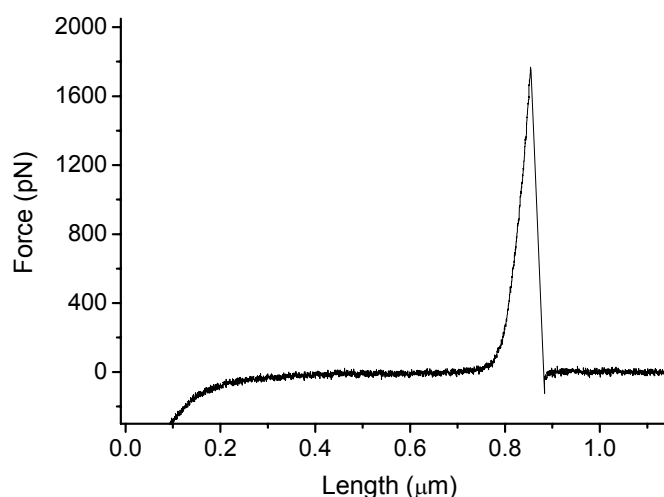


**Figure 12: CM-cellulose force-distance curve measured in PBS buffer.**

The Pd-en CM-cellulose samples are prepared according to the procedures developed in the Klüfers group [92] and measured in PBS buffer under the same conditions as the CM-cellulose samples. The resulting force spectra are similar in shape to the cellulose curves. The FJC fits give Kuhn lengths of  $L_k = 0.5 - 1\text{nm}$  and a segment elasticity of  $K_s \sim 50\,000\text{pN/nm}$ . There is a certain variance in the determined parameters, which may be due to experimental conditions such as the pulling geometries of the molecules. However, a general trend is apparent. With introduction of the complexing Pd metal the Kuhn length drops from  $\sim 1.7 - 3.3\text{nm}$  to  $\sim 0.5 - 1.0\text{nm}$ .

For comparison the normalised fitting functions for a CM-cellulose and a Pd-cellulose force curve are plotted in Figure 13. The Pd-complexed cellulose curves display a higher flexibility as compared to the pulls of CM-cellulose, which is reflected in a larger entropic restoration force at extensions below the contour length.

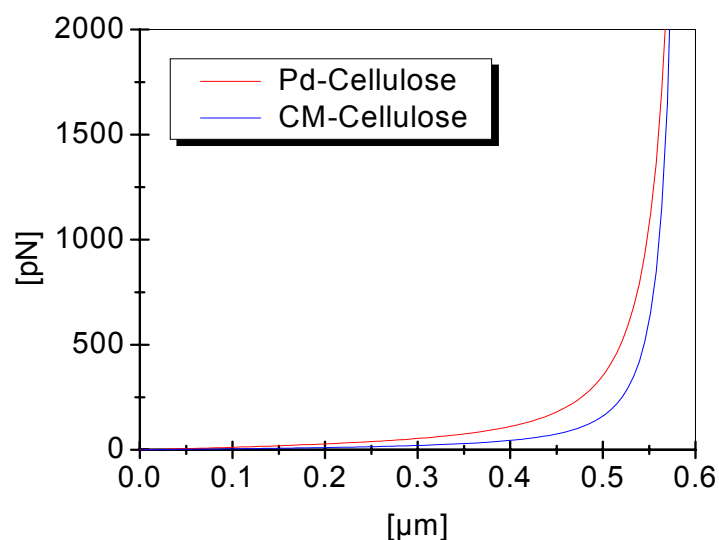


**Figure 13: Comparison of the normalised fit functions for CM-cellulose and Pd-en cellulose**

Contrary to the expected effect of an increased rigidity, due to additional intrachain bonding, this reduction in stiffness suggests that hydrogen-bond bridges between the chain segments may have been blocked by the metal complex, thus increasing chain flexibility. In fact, the resulting Kuhn length of 0.5nm is approximately the length of a single polysaccharide monomer [95]. Furthermore, this result is consistent with gyration radii measurements in light scattering experiments performed in the group of Prof. Klüfers, which show a decrease in persistence length for complexed Pd-en cellulose [92].

Polysaccharide	Kuhn length $L_k$	Segment elasticity $K_s$
CM-cellulose	1.7 – 3.3nm	30 000 – 40 000 pN/nm
Pd(en)-cellulose	0.5 – 1.0nm	~ 50 000 pN/nm
CM-cellulose literature [94]	~4nm	~ 50 000 pN/nm

**table 1: Comparison of the mechanical parameters for the cellulose derivatives.**

## Amylose and CM-amylase

Amylose ( $\alpha$ -[1,4]-polyglucose) is commonly found as starch in plants and foodstuffs and is thus an important nutritious sugar. In contrast to cellulose, which has a  $\beta$ -C<sub>1-4</sub> conformation, the attachment in amylose is  $\alpha$ -C<sub>1-4</sub>. As a consequence, cellulose forms flat sheet-like structures, whereas amylose tends towards helical configurations. The amylose chains consist of 1000 - 5000 glucose units.

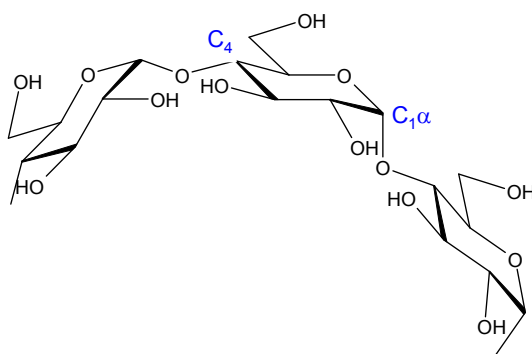
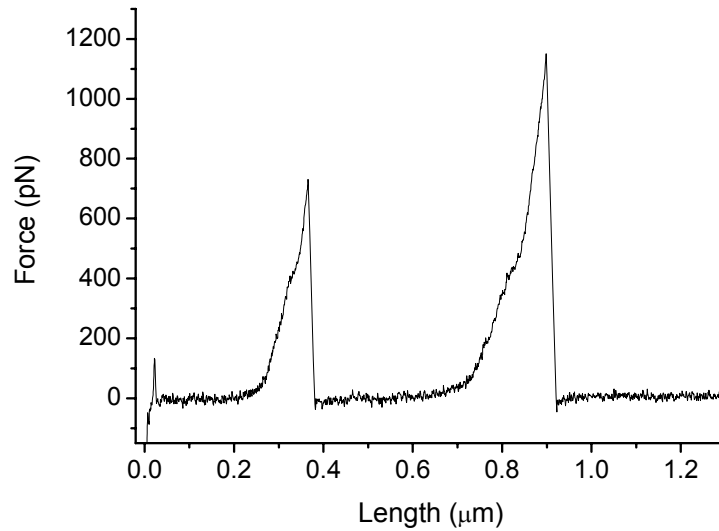


Figure 14: Amylose has an  $\alpha$ -C<sub>1-4</sub> conformation, which leads to helical structures

## Force spectroscopy of CM-amylase

The force curves of CM-amylase show an important difference as compared to purely entropic CM-cellulose chains. They display a clear enthalpic shoulder at ca. 300pN. The Kuhn lengths have previously been determined to 0.45nm before, and 0.54nm after the shoulder [96] with an increase in segment elasticity from 11000pN/nm to 28000pN/nm, i.e. a stiffening of the chain [94].

Our experiments are conducted on glass coverslips, after overnight incubation of the CM-amylase sample, followed by measuring the next day in aqueous PBS buffer solution or HPLC-grade water. A typical force curve with two single molecule pulling events is shown in Figure 15. The polymers are ca. 800nm and ca. 300nm long and both display a clear shoulder at  $\sim$ 300pN.



**Figure 15: CM-amylose force-distance curve**

When fitting CM-amylose with the FJC function, the determined Kuhn lengths for the curve before the shoulder are between  $L_k = 0.35\text{nm} - 1.5\text{nm}$  ( $L_k = 0.68 \pm 0.55\text{nm}$ ). After the shoulder the chain stiffens and the slope of the force curves is steeper, corresponding to an increased Kuhn length ( $L_k = 0.90 \pm 0.54\text{nm}$ ). Furthermore, some form of enthalpic conformational transition occurs in the chain at ca. 300pN. The explanation for this is found in the structure of amylose, as compared to cellulose. The  $\beta\text{-C}_{1-4}$  conformation in cellulose leads to straight chains that can only expand by stretching bonds and bending rigid bond angles. Cellulose is therefore relatively rigid and has a high Kuhn length.

On the other hand, the corresponding  $\alpha\text{-C}_{1-4}$  CM-amylose polymer forms a coiled structure, which is not fully extended. When stretched, CM-amylose can straighten out by undergoing a reversible transition from the natural chair form into the boat conformation. Theoretical models predict an extension per monomer unit from 0.45nm to 0.54nm, which corresponds well with the measured Kuhn lengths [95]. The chair-boat phase transition costs energy, which is supplied by the stretching force and corresponds to the area under the shoulder in the force-distance curve.

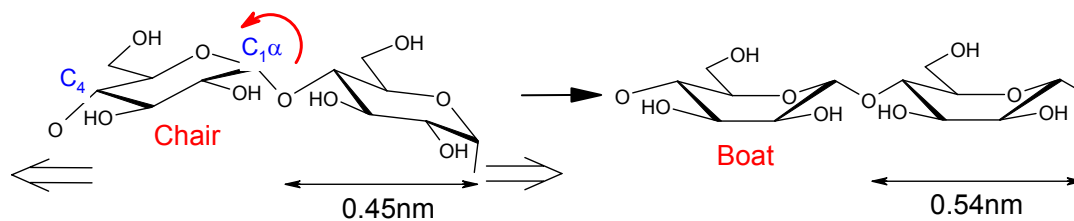


Figure 16: Schematic description of the chair-boat transition in CM-amylose under force.

Polysaccharide	Kuhn length $l_k$ and segm. elasticity $K_s < 300\text{pN}$	Kuhn length $l_k$ and segm. elasticity $K_s > 300\text{pN}$
CM-amylose	$L_k = 0.68\text{nm} \pm 0.55\text{nm}$	$L_k = 0.90 \pm 0.54\text{nm}$
CM-amylose lit1 [96]	$L_k = 0.45\text{nm}$ $K_s = 5600 \text{ pN/nm}$	$L_k = 0.54\text{nm}$
CM-amylose lit2 [94]	$L_k = 0.54\text{nm}$ $K_s = 11000 \text{ pN/nm}$	$K_s = 28000 \text{ pN/nm}$

table 2: The mechanical parameters of CM-amylose

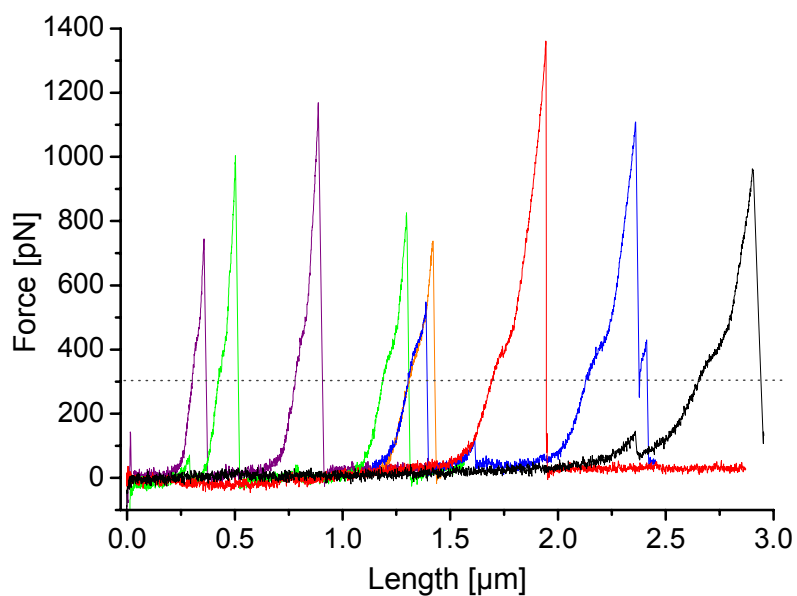
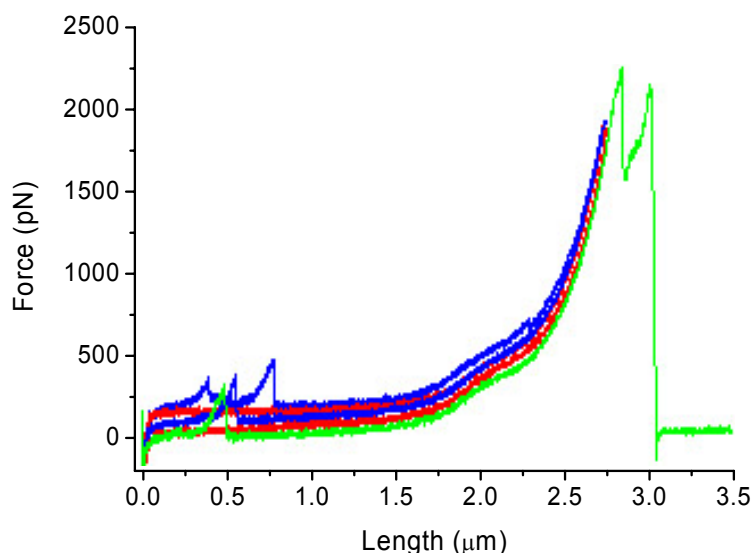


Figure 17: CM-amylose force curves

A single polysaccharide will display a characteristic force curve, which is typical of the substance examined and is essentially a force spectroscopic fingerprint of the molecule [30]. The graph in Figure 17 shows many CM-amylose curves taken from different samples, which all present the characteristic shoulder starting at ca. 300pN and can, in principle, be distinguished from other polymers in a mixed sample. However, to compare polymer force curves of molecules with different lengths these must first be normalised to a common extension i.e. by dividing the length axis of each curve by the polymer contour length.

Future chain manipulation experiments require attached molecules that can be pulled through successive stretching cycles without falling off the tip. For example, to accurately determine the change in fluorescence of a single dye molecule under tension, it is important that the stretching process is reversible and that any observed effects are reproducible for the same molecule. A force curve series of CM-amylose is displayed in Figure 18. By gradually increasing the pulling distance the molecule could be stretched reversibly up to a length of 3 $\mu$ m, before finally rupturing.



**Figure 18: Reversible pulling series showing the retraction (blue) and approach (red) curves of a CM-amylose molecule. In the last curve (green) the attachment finally ruptures. The cumulative force offset between each curve is 50pN.**

## Plateau force curves and the hydration energy of a single polymer

An interesting discovery during the work on polysaccharides was the observation and study of a different type of force curve. The classical peak events, termed *Langevin force curves* [97], are characterised by a constant increase in force followed by an abrupt drop as the molecule ruptures. The new class of *plateau force curves* display a constant force height, followed by a “digital” drop. In nearly all cases this second type of curve is preceded by a large unspecific adhesion peak - the result of multiple overlapping short-range rupture events, which are typical for highly concentrated samples. This indicates that the plateau events may be long chains being pulled out of a large polymer aggregate on the surface.

A typical CM-cellulose pulling experiment with plateau type rupture events is shown in Figure 19. The unspecific adhesion peak is frequently in the range of 1-10nN. The two plateau events are 135nm and 190nm long. Both end abruptly in a step down to a lower force level. The plateau height of the first level is 74pN, whereas the second plateau has a force of 132pN. Apparently, these force increments are cumulative, with each additional chain adding a certain force level to the total plateau height.

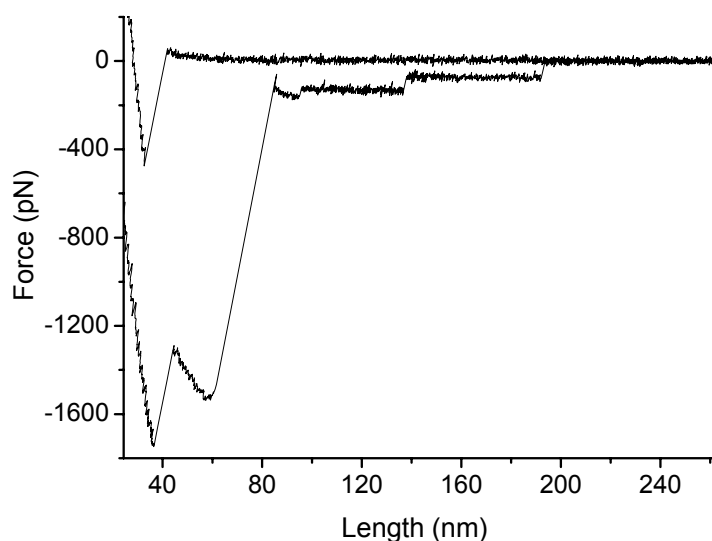


**Figure 19: CM-cellulose force curve with plateau type pulling event. Following a large unspecific adhesion peak are two plateaus with constant force values of 132pN and 74pN.**

This type of pulling event has been described recently in the literature [98-100] and various explanations have been suggested to explain the effect. The desorption theory [37] proposes that the polymer chain is gradually pulled off the surface, thereby rupturing many weak bonds, which sum up to a constant force. The *rupture length* reflects the section of the molecule, which is gradually zipped off the surface. The plateau force is therefore the result of chain desorption from the adhesive surface. For two molecules the plateaus add up and form the observed cascading steps [101]. Under these circumstances the plateau height should be proportional to the pulling speed. However, our results show that this is not the case.

In 2002 a new explanation was put forward based on the solvation of the polymers in a poor solvent [97]. In poor solvents the polymers form collapsed globules on the surface and the process of pulling-out single or multiple strands, monomer-by-monomer, into the solvent requires a constant force. On the other hand, in good solvents the classical “*Langevin-type*” peak force events are still observed. Therefore the rupture length corresponds to the chain length extracted, when it is debouched from the globule. However, insufficient plateau data was available to verify that the plateau heights were quantised. In another experiment, force plateaus with up to three steps were observed on fused lipid bilayers when they were pulled apart by an AFM tip [102].

For our experiments, the system CM-cellulose in water proved to be very fruitful for measuring plateau events. Evidently, the solvent is good enough to prevent complete aggregation of the molecules, but poor enough for frequent plateau curves. After accumulating tens of thousands of CM-cellulose plateau force curves, a thorough statistical analysis reveals that the plateau steps are in fact quantised. The graph in Figure 20 shows a collage of force curves with multiple plateaus. Curves with up to 8 plateaus were registered.

The plateau heights occur at specific quantised levels. Statistical analysis of these levels provides a distribution histogram, which can be fitted with a multi-peak Gaussian function. The resulting peaks of this fit are summarised in table 3.

Evidently the first two steps are higher, after which the successive steps converge to approximately the same force increment. This result is not compatible with the desorption-model, for which the difference in step levels should be the same.

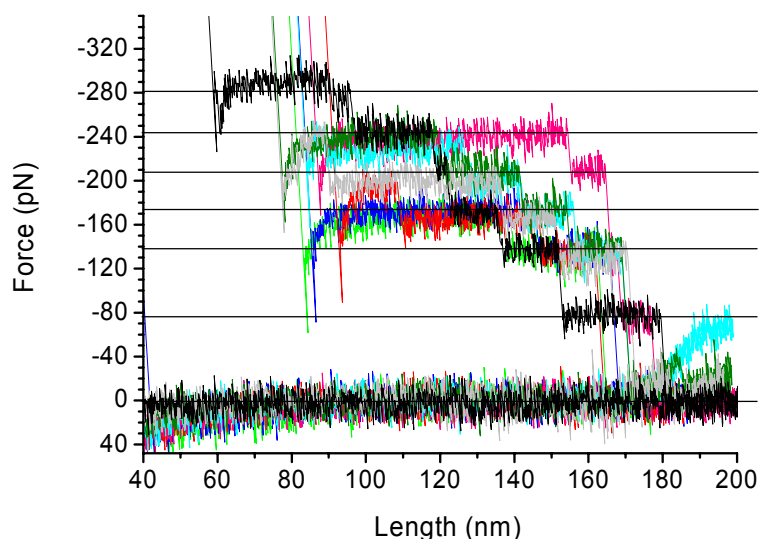


**Figure 20: CM-cellulose force curves with multiple plateau events. The step heights are clearly quantised as indicated by the horizontal lines.**

Plateau n	Force(n) (pN)	$\Delta$ Force [n-(n <sub>1</sub> )] (pN)	$\Delta$ Force(n)/Force(n <sub>1</sub> ) %
1	76.6 ± 0.2	76.6	-
2	138.8 ± 0.2	62.2	81.1
3	174.3 ± 0.3	35.4	46.2
4	207.9 ± 0.4	33.7	43.8
5	242.4 ± 1.2	34.5	45.1
6	~277	~ 35	~45

**table 3: The plateau heights for each step were determined with a multiple-peak Gaussian fit of the step height distribution histogram.**

Based on the alternative *chain-pull-out* theory a new model was proposed by the author's colleague C. Zhou, which can account for the differences in step height. This *solvation energy model* describes the plateau force in terms of the hydration energy required to extract the polymer chain from an aggregated

globule into a poor solvent [97]. Considering the cellulose chain as a tube of length  $L$  with a surface tension in water of  $\sigma$  [mN/m], the energy of hydration is given by:

$$\text{eq. 17} \quad E = -2\pi r L \sigma$$

The corresponding force is therefore:

$$\text{eq. 18} \quad F = -2\pi r \sigma$$

The surface tension of cellulose in water has been determined independently to be 70mN/m [103]. By inserting the plateau forces, a tube radius of  $r = 0.175\text{nm}$  ( $\varnothing \sim 0.35\text{nm}$ ) can be calculated. This is in fact approximately the diameter of a single cellulose chain of  $\varnothing \sim 0.4\text{nm}$ .

Furthermore, the differences in step height can be explained by the reduction in surface area, when bundles of cellulose containing two or more strands are extracted. A single chain experiences the full solvation energy, whereas two strands shield each other by intersection of the hydration layers. The perimeter of two overlapping bundles  $2 \cdot 2\pi$  is therefore reduced by  $2 \cdot \beta$ :

$$\text{eq. 19} \quad F_2 = -(2 \cdot 2\pi - 2\beta)r \sigma$$

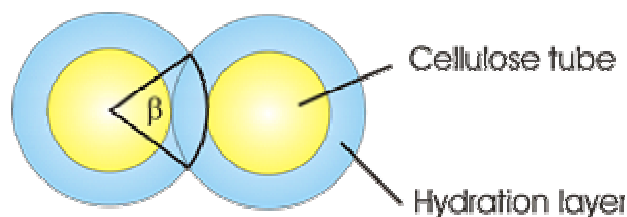


**Figure 21: Intersection of hydration layers (blue) in a cellulose bundle with two chains.**

Inserting for  $\sigma$ ,  $r$  and  $F_2 = 62.2\text{pN}$  affords the intersection angle  $\beta = 35^\circ = 0.63\text{rad}$ .

For higher order bundles the difference in surface area for each added strand can be calculated in a similar manner. To obtain the bundle perimeter

for three or more tubes, the enclosed area between the tubes  $(n-2)*\pi$  must be subtracted, which is essentially the area enclosed by a polygon formed between the centre points of the chains with  $n$  angles (cf. Figure 22). In addition, the strand overlap is slightly lower for the higher order bundles than for the double strand. The intersection angle for the higher order plateau heights  $F_{>2}$  can must therefore be reduced to ca.  $\frac{3}{4}\beta$  to correspond to the measured values.

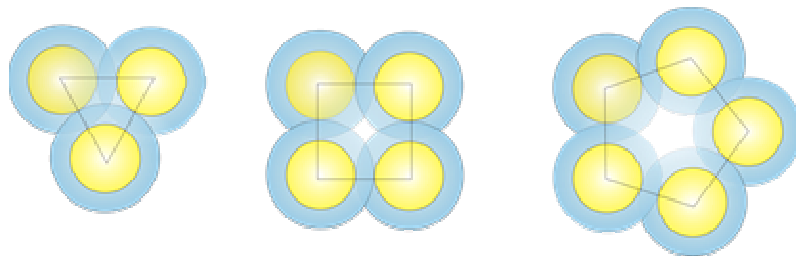


**Figure 22: Higher order CM-cellulose bundles with multiple chains.**

For bundles with 7 tubes the last tube is completely enclosed by the others and no additional surface area is gained. The plateau force is therefore indistinguishable from a bundle with 6 tubes. By calculating the perimeter of a bundle with  $n$  tubes, the following equation can be given for the plateau force:

$$\text{eq. 20} \quad F_{n=2-6} = - \left[ n \left( 2\pi - \frac{3}{4}\beta \right) - (n-2)\pi \right] r\sigma = - \left[ (n+2)\pi - n\frac{3}{4}\beta \right] r\sigma$$

A comparison of the theoretically calculated step heights with the experimental values in table 4 shows that the model accurately predicts the plateau heights.

Step n	Force experiment (pN)	Force calculated (pN)
1	76.6	76.9
2	138.8	138.5
3	174.3	175.0
4	207.9	207.7
5	242.4	240.4

**table 4: Comparison of the experimental plateau height forces with the calculated theoretical values as determined by the solvation energy model.**

Furthermore, the solvation energy of a single CM-cellulose chain of e.g. 1 $\mu$ m length (~2200units [96]) in water is the area under the plateau curve:  $E_1 = F_1 * 1\mu\text{m} = 7.66 * 10^{-17} \text{J}$ . This corresponds to a solvation energy per cellulose chain of 46 000kJ/mol and per glucose unit of 23kJ/mol, which is approximately the energy required to break 2-3 hydrogen bonds with 9.8kJ/mol [104].

### **Conclusion plateau force curves**

In summary, the plateau force statistics on CM-cellulose confirm the chain-pull-out theory. Furthermore, a new *solvation energy model* based on the extraction of CM-cellulose bundles with intersecting hydration layers is proposed that accurately predicts the quantised plateau forces measured. This model is based on the solvation energy of a single polymer chain, as it is pulled out of a polymer globule into a poor solvent. For the first time the hydration energy of a single molecule can be measured directly.

## 2.3 Force spectroscopy of DNA on transparent surfaces

The DNA system was chosen as the main substrate for the combined optical and AFM experiments for various reasons. First of all, the characteristic mechanical properties of the double-helix can be measured with single molecule force spectroscopic methods [8, 13, 40, 41]. Secondly, imaging techniques to visualise [75, 105] single DNA strands have been established during the last 10 years. Although both methods are experimentally challenging, in principle, it should be possible to simultaneously visualise the DNA, while the strands are manipulated with an AFM tip. However, a prerequisite for this combined experiment is a transparent surface that enables the recording of AFM force curves of DNA. Conventional gold substrates readily provide good force spectroscopic results, but the low transparency and fluorescence quenching effects prohibit the use of these surfaces for imaging. In the quest for the optimum surface, polylysine coated and silanised substrates were compared to gold and bare glass. It was possible to achieve characteristic and reversible AFM force spectra of single DNA strands on silanised glass and a statistical analysis of the rupture forces, plateau heights and rupture lengths was compiled.

### The system DNA with TO-PRO-3

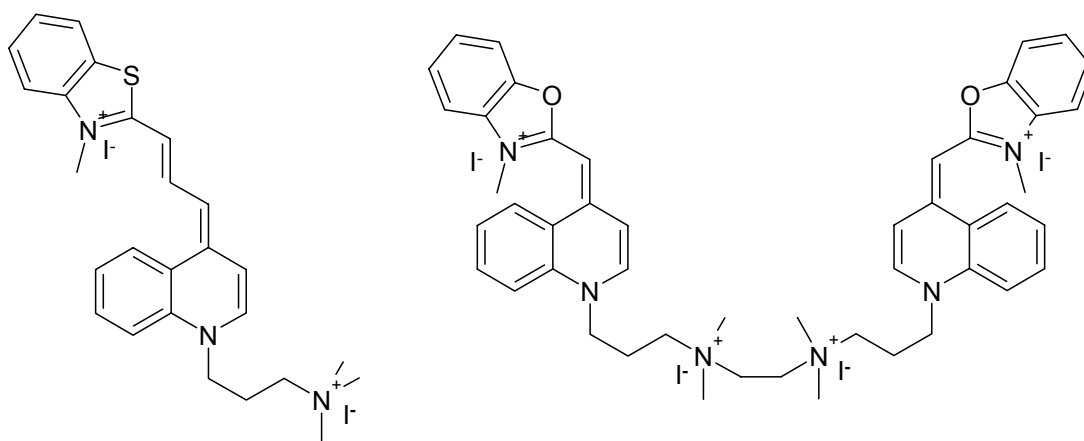


Figure 23: The monomeric TO-PRO-3 (left) and dimeric YOYO-1 (right) cyanine dyes.

TO-PRO<sup>®</sup>-3 is a DNA binding fluorescence cyanine dye ( $\lambda_{\text{abs}}=642\text{nm}$ ,  $\lambda_{\text{em}}=661\text{nm}$ ) [77]. When bound to DNA the fluorescence

quantum yield of the dye increases 200-fold, thereby enabling high contrast imaging of the DNA strand against an essentially non-fluorescing background of dye in solution. TO-PRO-3 is a member of a series of cyanine dyes including prominent DNA intercalators such as the monomeric dyes YO-PRO-1 (oxazole ring), TO-PRO-1 (thiazole ring), PO-PRO-1 and the dimeric dyes YOYO-1, TOTO-1 or POPO-1 [106]. By convention the -1 or -3 in the cyanine dye names indicates the number of carbon atoms in the conjugated bridge between the aromatic groups (cf. Figure 23).

There is some evidence that TO-PRO-3 intercalates by insertion of the planar  $\pi$ -conjugated segments into the DNA together with an additional electrostatic stabilisation [107]. Furthermore, although TO-PRO-3 does also bind to single stranded ssDNA [8], Chen et. al. have demonstrated that the fluorescence from TO-PRO-3 is about two orders of magnitude higher when mixed with double stranded DNA than single stranded ssDNA, suggesting a far stronger fluorescence enhancement when binding to the latter [108]. Nonetheless, unspecific electrostatic interactions between the positively charged dyes and the negatively charged DNA background, or groove binding modes may also be involved at higher dye/base pair ratios, as has been deduced from hole burning experiments [109].

### **The transparent surfaces**

DNA immobilisation is an important factor for single molecule imaging and thus many methods have been devised to fix DNA on transparent surfaces [110]. The two basic approaches to DNA immobilisation exploit either the hydrophobic nature of the unhybridised free base pairs at the DNA termini - the so called *sticky ends* - [111] or the electrostatic nature of the DNA phosphate backbone, due to the overall negative charge [112].

Similar to single stranded ssDNA, which is known to be very sticky, attaching non-specifically to most surfaces [112], the *sticky ends* are attracted to hydrophobic surfaces (cf. Figure 96). Hydrophobic surfaces include coatings of gold [113] or vinyl terminated silanes [10, 114-117], whereas electrostatically positive surfaces can be generated with ammonium functionalised silanes (APTES) [118], cationic fluid support membranes [76,

119], polylysine coated glass [112, 120] or by adding divalent cations to generate positive charges on mica [121-124]. DNA adsorbs very poorly to cleaned silicon surfaces even in the presence of divalent cations [125]. Based on these experiences, silanised and polylysine coated surfaces were chosen and examined as to their suitability for single molecule force spectroscopy of DNA.

Gas phase adsorption of (7-octen-1-yl)trimethoxysilane has been used to prepare silane monolayers with vinyl functionalities [110]. Usually the coated substrates are then baked in an oven at 100°C, which leads to extensive cross-linking between the silane termini. This curing process creates a stable silane network covering the substrate surface.

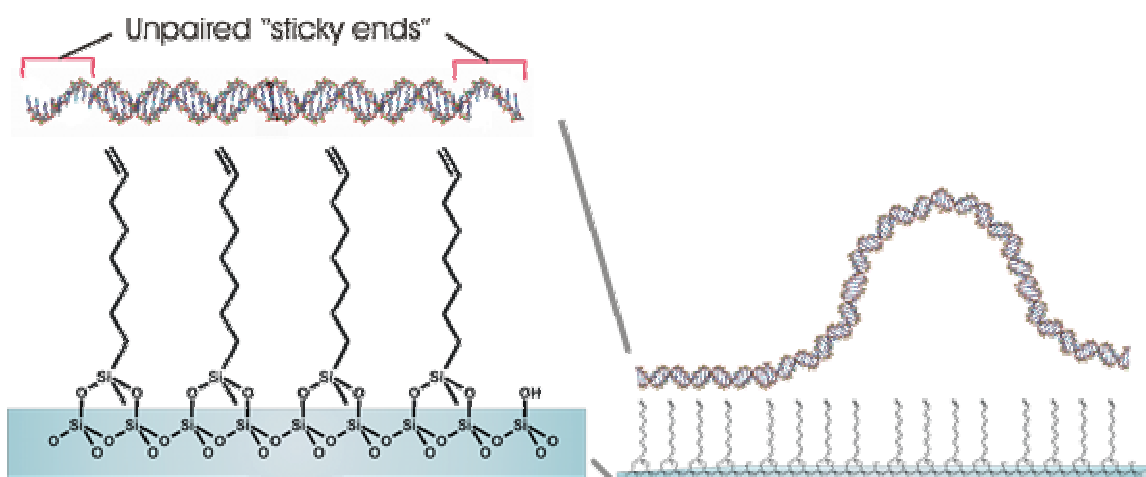


**Figure 24: The hydrophobic DNA sticky ends attach to a (7-octen-1-yl)trimethoxysilane surface.**

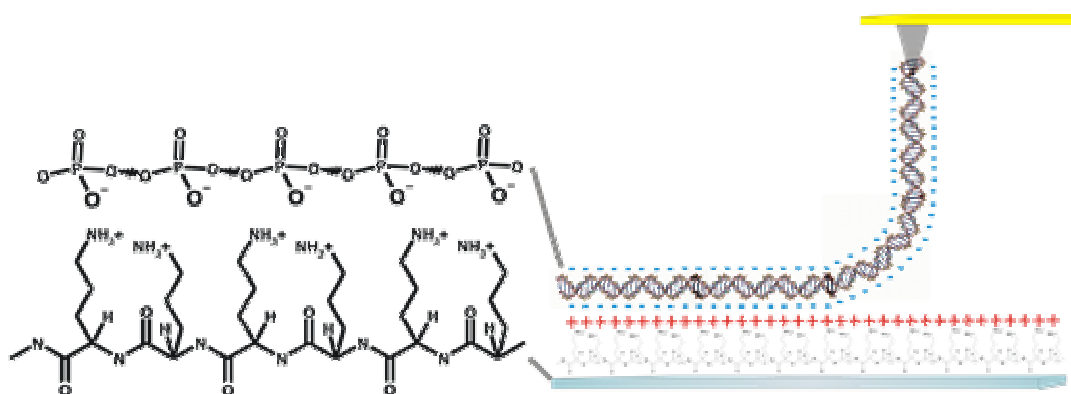


**Figure 25: Electrostatic attraction of the DNA phosphate backbone to a positively charged polylysine surface.**

In addition, polylysine coated coverslips have been generated that exhibit an electrostatically attractive surface [112, 120, 126]. At pH = 8 the ammonium function on polylysine is positively charged (iso-electric point pH = 10.0), so that it readily binds the oppositely charged DNA filaments. By exploiting laminar flow techniques, single DNA molecules could be immobilised and also elongated on polylysine coated glass coverslips [127, 128].

### **Single molecule DNA manipulation and force spectroscopy**

To date, the mechanical manipulation of single DNA molecules has focussed on stretching the strands with the help of a fluid shear flow, optical tweezers, magnetic beads or AFM cantilevers [8, 41]. Each of these methods provides a different means to interact with single molecules, although a universal tool has yet to be found.

Early experiments by Chu et al. demonstrated that it was possible to stretch out single, dye labelled  $\lambda$ -Phage DNA strands in a fluid shear flow [11]. Likewise, most of the other aligning procedures for DNA rely on laminar flow stream straightening of a terminally attached strand to unwind DNA from its natural random coil conformation [127, 128]. An effective method to generate the necessary flow is the *molecular combing* process developed by Bensimon and Croquette, which stretches DNA on silanised surfaces, using a receding water meniscus [10, 114].

A different set of experiments pioneered in 1992 by C. Bustamante and S. Smith showed that it was possible to stretch single DNA molecules with magnetic beads [12] and thereby measure the elasticity and force-extension curves of the molecule in the force range of 0.1–10pN [13]. The method was extended by applying a rotating magnetic field, which enabled twisting and stretching of the DNA coil [15].

Slightly higher forces of up to 100pN can be achieved with optical tweezers, providing considerable insights into the mechanical properties of individual DNA molecules, such as the force-extension profiles [129] and persistence length [87]. Cluzel [16] and Smith [17] showed that, at a stress of 65pN, dsDNA underwent a reversible transition to a stretched “S-form”, which was 1.7 times longer than the canonical B-form DNA. The transition is highly

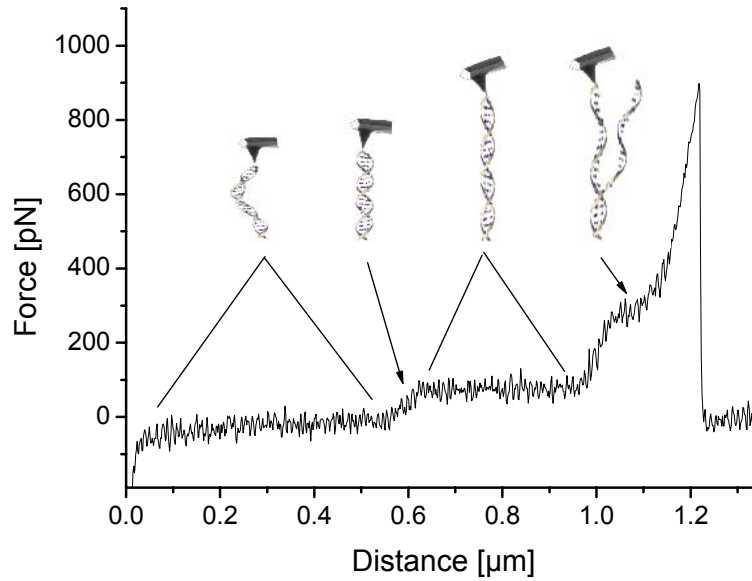
co-operative, occurring within a narrow force regime of 2pN and increasing the rise per base pair from 3.4 to 5.8Å. Finally, Kinoshita et al. managed to tie knots into DNA using two terminally attached polystyrene beads [20].

To access stretching forces >100pN atomic force microscopy (AFM) has proved to be an invaluable tool [15]. By picking up and applying a vertical force to single DNA chains, the molecular elasticity of DNA can be measured and described in the form of a force-distance spectrum [23, 130]. A second “melting” transition was observed in these force curves at ca. 150pN, which was attributed to the dissociation of the double helix under high tension [38]. In addition, the effect of intercalating dyes on the force spectra was tested [131, 132]. However, a drawback of AFM force spectroscopy has to date been the unspecific random attachment of a molecule to the cantilever tip [31]. To increase the chance of picking up a single polymer, the force pulling experiments are routinely performed from coated surfaces with high levels of coverage. Possibly, the direct optical visualisation of the DNA can improve attachment specificity. Finally, scanning AFM setups have also been employed to manipulate single DNA chains, albeit without measuring the acting forces [133, 134].

### **DNA force spectroscopy**

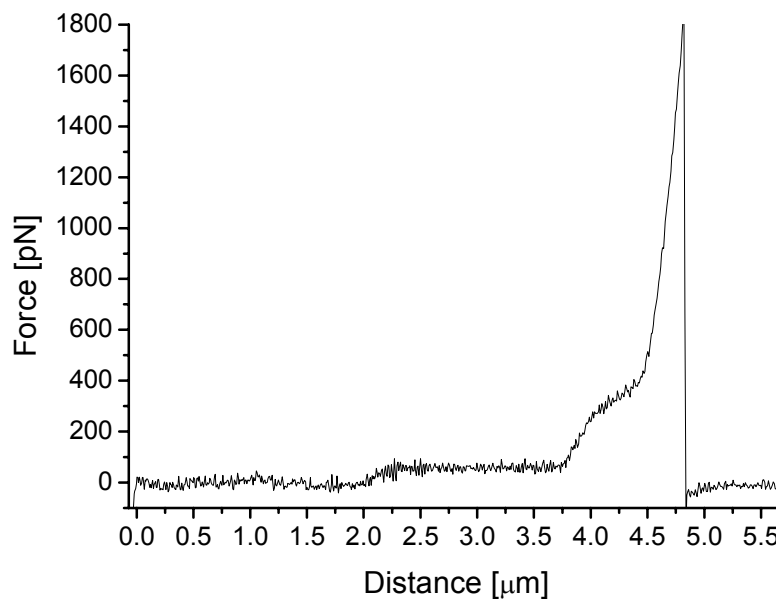
The control experiments show that DNA cannot be picked up readily on cleaned bare glass and no force pulls are observed. However, to first confirm the results achieved by other groups [39], DNA samples were prepared and examined on gold coated coverslips. A typical DNA force curve pulled on gold is shown in

Figure 26. The schematic DNA images describe the stretching mechanics at various characteristic stages in the force curve, as suggested according to the standard model [135]. After initial straightening to the full contour length, an additional force of 65pN results in a conformational change, the B-S overstretching transition, during which the DNA can be extended to ca. 1.7 times the original length. This plateau is followed by a shorter shoulder at 200-400pN (the melting transition), which is attributed to the gradual dehybridisation of one of the single strands in DNA [39].



**Figure 26: Force spectrum of  $\lambda$ -phage BSTE II digest DNA on gold and schematic description of the stages in the stretching process.**

After having reproduced DNA force curves on gold, new transparent surfaces were examined. On positively charged polylysine coated glass a strong electrostatic DNA adhesion was expected. Nevertheless, characteristic single molecule force curves are rare. An example with an exceptionally high rupture force of 1.9nN is shown in Figure 27.



**Figure 27: Force spectrum of  $\lambda$ -phage BSTE II digest DNA on polylysine coated glass.**

However, on hydrophobic silanised surfaces reversible pulls are readily available. The following waterfall graph (cf. Figure 28) shows a series of 0.5 Hz pulling cycles of the same DNA molecule. By increasing the pulling distance for each cycle the DNA could be stretched through the first and second transitions, before finally rupturing.

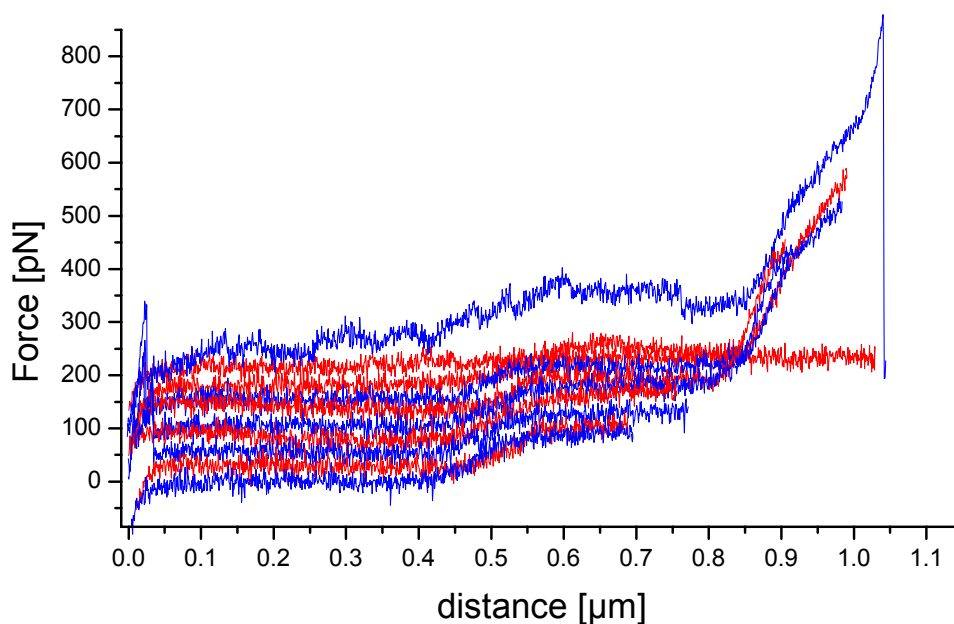


**Figure 28: Waterfall graph of a reversible 0.5 Hz pulling series of  $\lambda$ -phage BSTE II digest DNA on a silanised surface. The surface retraction curve (blue) is followed by a subsequent approach curve (red). The final cycle shows the strand rupture event. The force offset between each of the curves is 25pN.**

These qualitative force curves demonstrated that it is possible to reversibly stretch DNA on transparent surfaces; especially silanised glass afforded frequent characteristic DNA curves.

### **Statistics on DNA force curves**

To quantify the results, statistics on the B-S plateau force, the rupture force and rupture length were compiled for each surface. The plateau heights were determined by averaging the points along the B-S transition section of the force curve and calculating the difference in force to the baseline (B-DNA). A

histogram of the plateau heights for 131 DNA force curves, displaying a clear plateau on silanised glass, is shown in Figure 29. Fitting the points of the histogram with a Gauss function reveals a peak value of 63.8pN (mean value = 67.7pN,  $\sigma = \pm 14.3$ pN). The distribution of values is probably a consequence of cantilever sensitivity and spring constant calibration, which both relate directly to the forces measured or of the specific DNA pulling geometries.

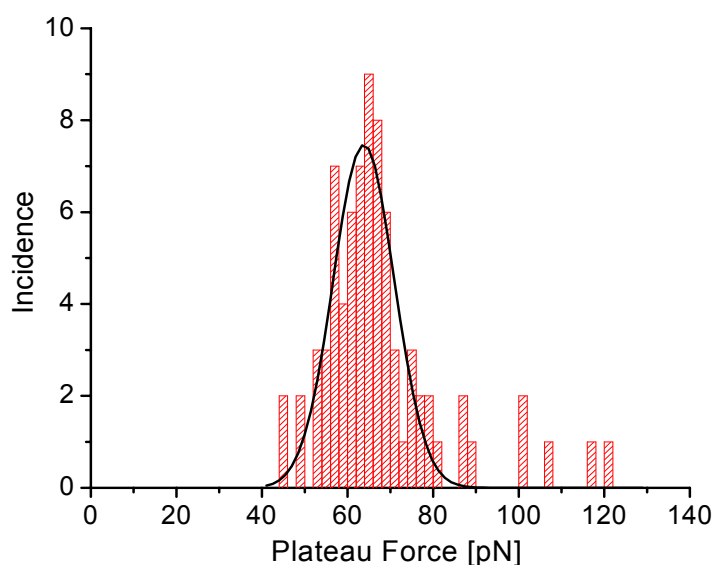


**Figure 29: Distribution and Gauss fit ( $F_{\max} = 63.8$ pN) of the DNA plateau heights on a silanised surface.**

Likewise, the rupture forces were determined and summarised in a histogram (cf. Figure 30). To avoid vitiation of the results due to unspecific adhesion or multiple overlapping rupture events, the events under 50pN were discarded. The mean value of 375pN for the rupture force varies considerably with a standard deviation of  $\sigma = 327$ pN. This suggests multiple rupture mechanisms, which may not necessarily have to do with DNA bond breakage, but could be due to desorption of the DNA either from the tip or the surface.

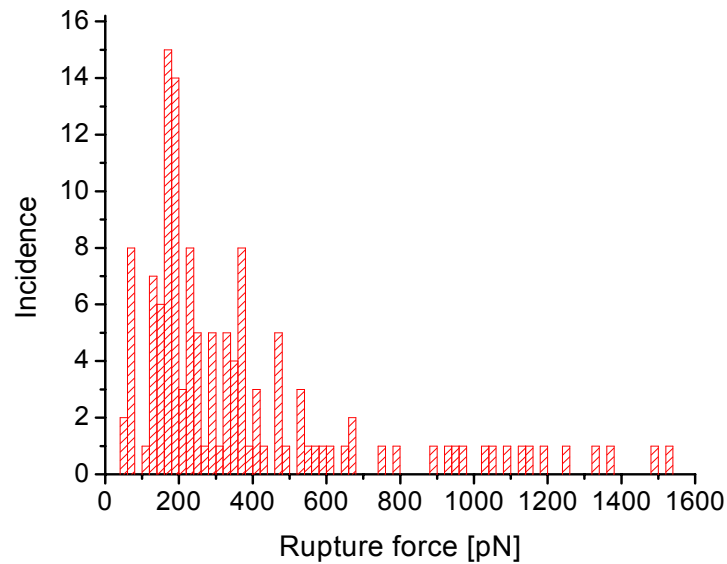


**Figure 30: Histogram of the DNA rupture forces for the events in Figure 29 on silanised glass.**

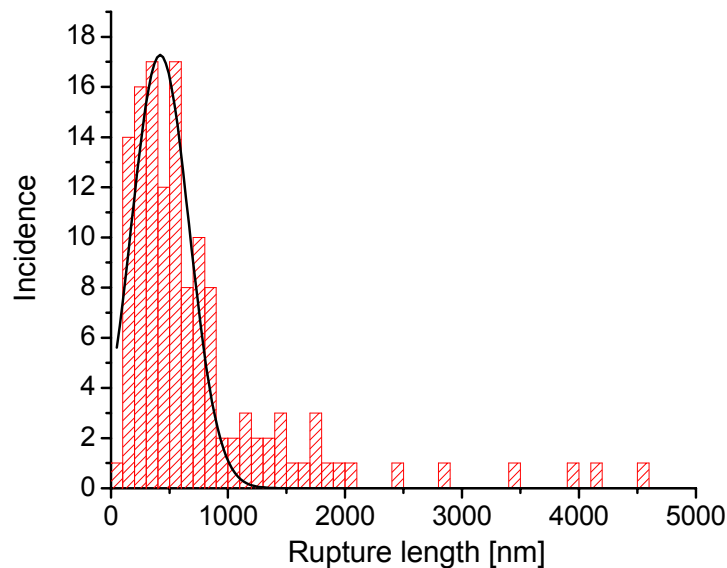


**Figure 31: Histogram and Gauss fit ( $L_{\max} = 420\text{nm}$ ) of the rupture lengths for  $\lambda$ -phage BSTE II digest DNA on silanised glass.**

The histogram in Figure 31 shows a distribution of the rupture lengths as measured for the 131 pulling events with a clear B-S plateau. The  $\lambda$ -phage BSTE II digest sample contained a mixture of 14 fragments of the original  $\lambda$ -phage DNA (length distribution of 117-8454bp  $\approx$  40nm-2900nm). Therefore, it was no surprise to measure a distribution of contour lengths with an average value of 754nm, and a large standard deviation of  $\sigma = 775\text{nm}$ . Pulls shorter

than 100nm were disregarded because individual events could not be distinguished from overlapping multiple events.

The statistical distributions of the rupture forces and lengths for 90 pulling events of  $\lambda$ -phage digest DNA on polylysine are shown in Figure 32 and Figure 33, respectively.

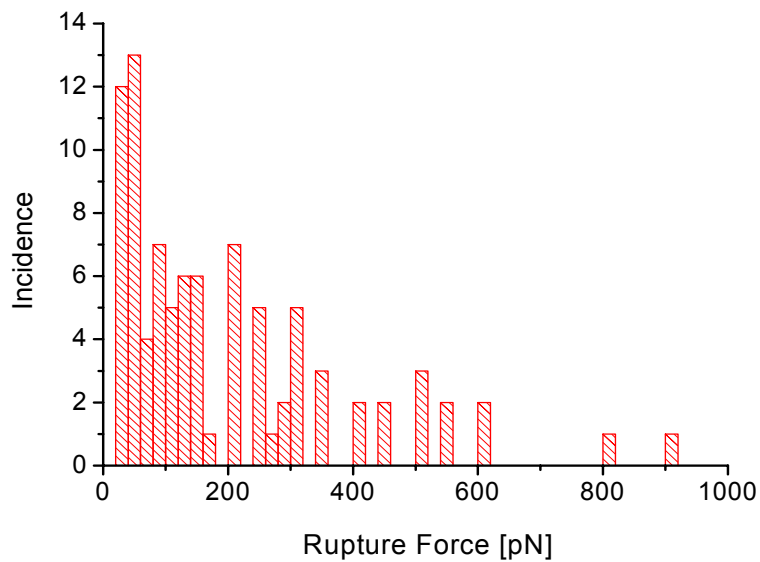


**Figure 32: Histogram of the DNA rupture forces on polylysine**

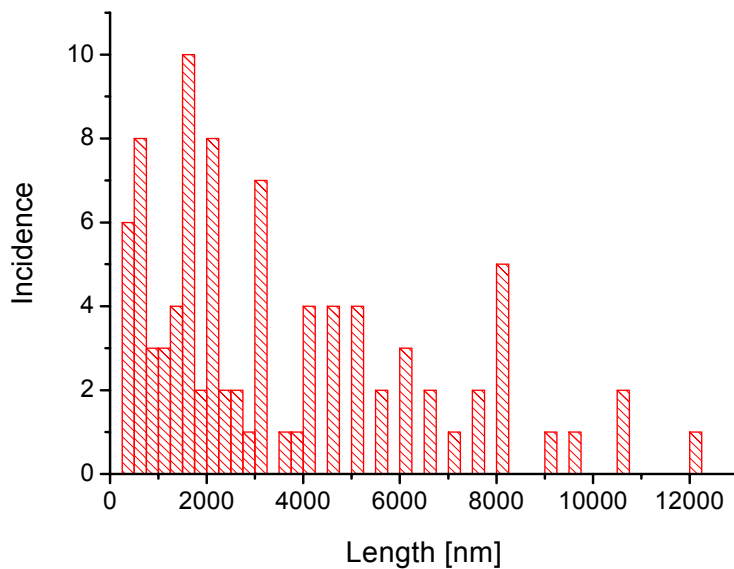


**Figure 33: Histogram of the DNA rupture lengths on polylysine**

Similar statistics were put together for gold coated glass surfaces. The results are summarised in table 5.

Mean value	Rupture force [pN]	Rupture length [nm]	Plateau force [pN]
Gold	320pN	-	65pN ±15pN
Polylysine	193pN ±183pN	3370nm ±2800nm	54pN ±21pN
Silane	375pN ±327pN	754nm ±775nm	68pN ±14pN

**table 5: Summary of the mean values for rupture force, rupture length and plateau height of  $\lambda$ -phage BSTE II digest DNA on various surfaces.**

The average plateau forces are generally around 65pN for all of the three surfaces, which corresponds to the previously proposed plateau height value of ca. 65pN for DNA on gold [38]. Apparently, the plateau force of DNA is independent of the surface. The mean rupture forces of single DNA strands on gold or silanised glass are between 300-400pN, albeit with a large standard deviation. The notable exception is polylysine with a value of ca. 200pN.

Furthermore, the average rupture lengths on polylysine (3370nm) are far longer than on silane (754nm). In many cases these pulling events even exceed the maximum contour length of the longest DNA fragment (2.9 $\mu$ m) in the  $\lambda$ -phage BSTE II digest mixture. This cannot be due to erroneous stretching of single polylysine strands from the surface. Control experiments without DNA on polylysine show no pulls at all and the length of an average polylysine strand of ca. 100nm is hardly long enough to explain the pulling lengths measured. Furthermore, plateau events are relatively seldom on polylysine, occurring in only ca. 5% of the prepared samples, whereas gold and silane surfaces readily afford characteristic DNA pulls. Evidently there is a marked difference between the force curves achieved on polylysine on the one hand and on gold/silane on the other. This effect has been attributed to

the condensating effect of the cationic polylysine chain on DNA and will be discussed in detail in the conclusion of the force pulling experiments on DNA.

### **The effect of TO-PRO-3 on DNA force curves**

Various attempts have been made to establish the mechanical effect exerted on a DNA strand by intercalating and groove binding dyes [136]. AFM force spectroscopic data show that intercalating agents such as cis-platinum [137], proflavine [132] or ethidium bromide [131] expand the contour length and shorten the B-S transition region of the DNA, due to a partial unwinding of the chain. In addition, a marked reduction in cooperativity of the transition is observed, meaning that the plateau no longer occurs at a specific force, but increases gradually with the pulling length.

On the other hand, groove binders such as SYBR green<sup>®</sup> [138] or berenil have less influence on DNA force curves [131, 132]. Cooperativity is reduced as with the intercalators, but to a lesser extent. The plateau remains prominent and its relative length does not change significantly.

For the cyanine dye YOYO-1 a 1.2 fold elongation of the DNA on intercalation and a clear hysteresis in the force curves were measured in optical tweezers experiments [139]. The fluorescence polarisation for aligned strands indicates that two distinct binding modes coexist: intercalation and groove binding. Although some optical experiments suggest predominant intercalation for the similar cyanine dye TO-PRO-3 [107], groove binding modes may play a role at higher dye/base pair ratios [109].

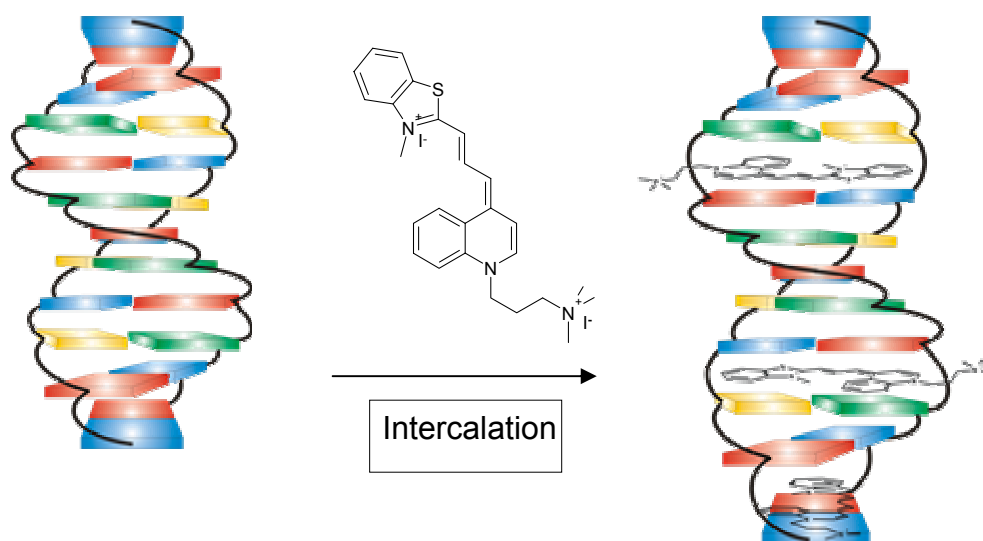


**Figure 34: Schematic description of TO-PRO-3 intercalation between the base pairs.**

To determine the effect of TO-PRO-3 on the mechanics of single DNA strands, the AFM force measurements on silanised glass were repeated with a dye concentration of  $5 \cdot 10^{-6} \text{M}$ . A superposition of the normalised force curves (cf. Figure 35) clearly shows the loss in cooperativity. The clear structure of the flat transition at 65pN and the step to the melting transition at 200pN are lost to a gradual increase in force with pulling length. This behaviour is typical of intercalators and indicates that this binding mode is significant at high TO-PRO-3 concentrations, although some simultaneous groove binding cannot be excluded.

Furthermore, due to dye intercalation the DNA is partially unwound, thereby increasing the contour length so that the onset of the B-S plateau is postponed. However, the dye has no effect on the slope of the force curve during and after the melting transition. According to the standard model the DNA has denatured into two single strands at this stage [39], possibly having extruded the intercalators. Combined optical-AFM experiments may shed light on the exact mechanisms of dye binding during DNA stretching.

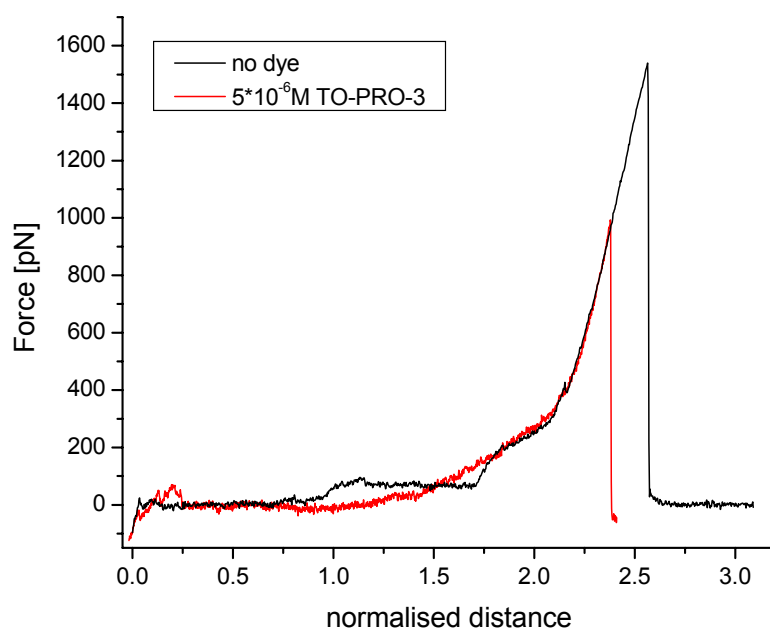


**Figure 35: DNA force curves without (black curve) and with TO-PRO-3 (red curve) normalised to the contour length.**

A summary of the statistics of 141 pulling experiments for DNA with TO-PRO-3 is presented in table 6. Although there is a strong qualitative change in the shape of the force curves, there is no significant difference in the average rupture force or rupture length compared to the curves measured without dye.

Mean value	Rupture force [pN]	Rupture length [nm]	Plateau force [pN]
Silane	375pN $\pm$ 327pN	754nm $\pm$ 775nm	68pN $\pm$ 14pN
Silane + dye	394pN $\pm$ 301pN	811nm $\pm$ 629nm	-

**table 6: Statistics of the force curves for DNA on silanised glass with TO-PRO-3.**

## Conclusion and discussion DNA force spectroscopy

With careful handling it is possible to attach and reversibly stretch a single DNA molecule through a few hundred characteristic pulling cycles on silanised glass surfaces. The plateau forces ( $68\text{pN} \pm 14\text{pN}$ ) are comparable to the results previously achieved on gold [38]. Likewise, the rupture forces on silane and gold are similar. Applying the intercalating dye TO-PRO-3 has little influence on either the rupture force or the rupture length, although a marked qualitative loss of cooperativity is observed in the B-S plateau.

To explain the similarities between gold and silane it is useful to note that both surfaces are expected to be hydrophobic [113, 140]. Furthermore, DNA is ten times more likely to bind to a hydrophobic surface by an extremity than by a mid-section [10]. This effect may have its origin in the 12 bases unpaired region at the ends of  $\lambda$ -phage DNA, often referred to as “sticky ends” (cf. Figure 24). These termini are of hydrophobic nature, whereas in the paired mid-region the negatively charged hydrophilic phosphate-backbone prevails (cf. Figure 36). In fact, hydrophobic interactions may be the predominant binding mechanism in most force spectroscopic pulling experiments on biological or organic polymers.

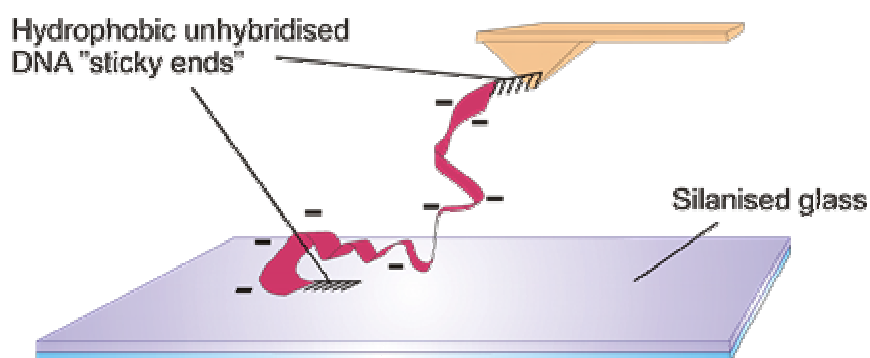


**Figure 36: Hydrophobic attachment of DNA  $\lambda$ -phage “sticky ends” to the cantilever tip and the silanised surface.**

In the experiments on polylysine few samples afforded characteristic DNA force curves with clear B-S and melting transitions. Furthermore, the force curves are generally far longer than on gold or silane surfaces. The results obtained in the imaging experiments show that the condensating and

aggregating effect of polycations on DNA could be responsible for this effect. Probably multiple-strand DNA fibres are being pulled, which are held together by positively charged polylysine chains. This explains the rare and unusually long DNA lengths measured. The electrostatic attraction is so large that it leads to DNA agglomeration on the surface, thus reducing the availability of the strands for force pulling experiments and resulting in the frequently uncharacteristic force curves without a clear plateau. The DNA condensation and aggregation process is described in chapter 4.2.

### 3. Single molecule fluorescence microscopy

The primary goal was to employ the combined optical/AFM setup to study the influence of an applied force on the fluorescence properties of single molecule dyes. Especially spectral shifts or changes in the overall brightness of the dye fluorescence were envisaged as potential properties for investigation. The main focus was thereby on the system DNA/TO-PRO-3, but early experiments were also conducted on single organic dyes, which could be attached to a glass surface and pulled by the AFM via a connected polymer tether. Systems such as cyanine5 (Cy5) with polyethyleneglycol (PEG) and also a series of hemicyanine dyes were examined.

To gain a thorough understanding of the required techniques, single molecule experiments were conducted on these dyes to determine their optical suitability. Although the properties of such common good dyes as terrylenediimide (TDI) or cyanine5 (Cy5) could be verified, the new stilbene derivatives were inferior in fluorescence quantum yield and could therefore not be used for single molecule experiments. Furthermore, the chemical synthesis and single molecule attachment of these tethered, highly diluted single molecules turned out to be challenging. The experiences gained were therefore adapted to study the DNA/intercalator system, for which combined experiments were more feasible.

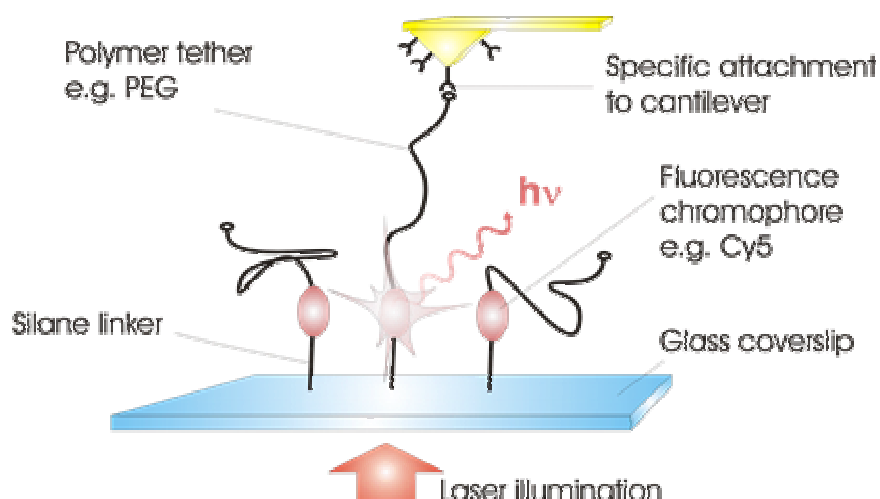
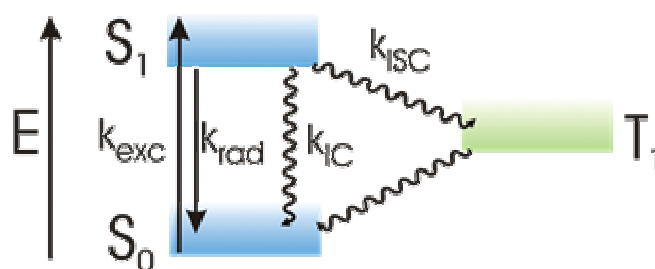


Figure 37: By applying a force with the AFM tip via a polymer tether, single dye molecules can be stretched, while their fluorescence is monitored.

### 3.1 General principles

In this chapter the basic photophysical concepts and the prerequisites for good single molecule dyes shall be discussed. It can be shown that the new cyanine dyes do not meet the necessary standards, which explains why good fluorescence images were not easily attained of these molecules. In comparison, the dyes Cy5 and especially TDI fully comply with the requirements for good single molecule imaging.

The convenient optical detection of single fluorescing dye molecules is a fairly recent technique [43, 46]. The basic photophysical processes involved are described in Figure 38. After exciting a dye with laser-light from the electronic ground state  $S_0$  to an excited state  $S_1$ , the absorbed energy is typically given off within 1 to 10ns - the *fluorescence lifetime* of the dye. This can occur as fluorescence radiation with the rate  $k_{\text{rad}}$  [ $\text{s}^{-1}$ ]. The fluorescence is usually red-shifted compared to the excitation light. This *Stokes-shift* is the result of the radiative transition into higher order vibrational states of the  $S_0$  ground state. Accordingly, the arrow  $k_{\text{rad}}$  is shorter in Figure 38, corresponding to a lower energy and a longer emission wavelength. If the molecule relaxes to the  $S_0$  via a non-radiative transition through internal conversion  $k_{\text{IC}}$ , no fluorescence is emitted. In principle, the intersystem crossing (ISC) transition to a triplet state  $T_1$  via spin flip is forbidden, but a (usually weak) spin-orbit coupling can enable a low transition probability. Likewise, the relaxation from  $T_1$  to  $S_0$  is slow, resulting in a relatively long lifetime of the triplet state ( $\mu\text{s}$ - $\text{ms}$ ).



**Figure 38: Jablonski energy scheme of the relevant electronic states and transitions in single molecule fluorescence; wavy arrows are non-radiative.**

## Suitable single molecule dyes

Various consequences for the spectroscopy of single molecule fluorescence dyes can be derived from the description in Figure 38. In the ideal case, assuming saturated excitation and that all excitation cycles result in radiative emission, the dye will emit  $k_{\text{rad}} = k_{\text{Fl}} = 10^9$  photons/sec, corresponding to a fluorescence lifetime of  $\tau_{\text{Fl}} = 1/k_{\text{Fl}} = 1\text{ns}$ . Even assuming a detection efficiency of ca. 2%, this is still well in excess of the number of photons/second required for single molecule fluorescence detection or spectroscopic analysis. Usually however, the radiative emission rate is reduced by the non-radiative processes  $k_{\text{IC}}$  and  $k_{\text{ISC}}$ :

$$\text{eq. 21} \quad k_{\text{rad}} = k_{\text{Fl}} - k_{\text{IC}} - k_{\text{ISC}}$$

The proportion of radiative emission to total excitation relaxation is given by the fluorescence quantum yield  $\Phi_{\text{Fl}}$  [%]:

$$\text{eq. 22} \quad \Phi_{\text{Fl}} = \frac{k_{\text{rad}}}{k_{\text{rad}} + k_{\text{IC}} + k_{\text{ISC}}}$$

Obviously a high fluorescence quantum yield is desirable for a good single molecule dye. As a rule of thumb the practical limit is ca.  $\Phi_{\text{Fl}} > 10\%$ .

Although the triplet rates  $k_{\text{ISC}}$  are usually relatively low, they are important for determining of the suitability of a single molecule dye. Since the triplet state has a comparatively long lifetime, a molecule that enters a triplet state is essentially caught there for  $\mu\text{s}$ - $\text{ms}$  and cannot continue to produce photons through the radiative photocycle. A low triplet quantum yield  $\Phi_{\text{trip}} < 0.1\%$  is therefore an essential prerequisite for a good single molecule dye.

Another important factor is the photostability of a dye. This is expressed in the photobleaching quantum yield  $\Phi_{\text{d}}$ :

$$\text{eq. 23} \quad \Phi_{\text{d}} = \frac{1}{\text{no. photocycles before bleaching}}$$

It is essentially the factor of the total number photocycles that lead to irreversible dye bleaching [141]. Typical values for  $\Phi_d$  in single molecule dyes are in the range of  $10^{-6}$  to  $10^{-8}$  [142, 143]. The photostability is related to the triplet quantum yield, because the reaction with singlet oxygen is assumed to be one of the main pathways leading to dye bleaching. By quenching the dye triplet state, the normal triplet oxygen  $^3\text{O}_2$  is converted into the highly reactive singlet  $^1\text{O}_2$  form, which is a potent photooxidant [141]. In effect, the photodestruction quantum yield expresses the total number of photons that can be gleaned from a single dye before it bleaches, whether they are interrupted by dark states such as  $T_1$  or not. Obviously, an uninterrupted stream of photons will provide better images with higher signal to background ratios but, given breaks, a good single molecule dye should emit at least  $10^5$  photocycles over a time period of 1 sec.

Finally, good single molecule dyes have high molar extinction coefficients of  $\epsilon(\nu) > 50\,000$  [ $\text{l mol}^{-1}\text{cm}^{-1}$ ] and correspondingly high absorption cross-sections. They absorb the excitation light sufficiently well to afford enough fluorescence photocycles for imaging with typical laser excitation powers of ca.  $1\text{-}10\text{ kW/cm}^2$ . Dyes with weaker extinction coefficients would require higher laser excitation powers, which bring with them a host of adverse effects, such as a higher background signal and faster dye photobleaching rates. Examples of good dyes are tetramethylrhodamine (TMR) [142], cyanine 5 (Cy5) [144, 145] and especially terrylenediimide (TDI) [146].

### **Properties of single molecules**

The advent of single molecule fluorescence microscopy has sparked the desire to measure the unique photophysics of individual molecules. Conventional bulk samples with many molecules can provide only an average ensemble picture. For example it was found that single molecules do not fluoresce at a constant rate, but instead turn on and off [44, 147] - a phenomenon that has been termed blinking [55]. A dye may emit "bunches" of photons before jumping into a non-fluorescent "dark state", such as a triplet state [48, 148]. The detectable intervals can range from a few  $\mu\text{s}$  in the case

of a triplet to several seconds for longer lasting dark-states that may have their origin in photochemical reactions or conformational changes in the dye [145].

On an even shorter time-scale another single molecule phenomenon can be observed, termed “antibunching” [149]. Based on the fluorescence lifetime (usually a few nanoseconds), a finite time span is required for a dye to complete a full photocycle. A single molecule cannot be re-excited until it has relaxed back into the starting ground state and the number of photocycles per second is limited.

Furthermore, in contrast to the isotropic polarisation of a bulk sample, single dyes absorb the excitation light according to their individual absorption transition dipole moments  $\vec{\mu}$ , which depend on the orientation of the molecule [150]. The observed fluorescence is higher when the excitation light is polarised with the same orientation as  $\vec{\mu}$ . The fluorescence is thus proportional to the angle  $\varphi$  between the electric field vector  $\vec{E}$  of the excitation light and the dipole moment:

eq. 24 
$$I_{\text{fl.}} \propto \cos^2 \varphi$$

Finally, single molecules exhibit abrupt spectral shifts in their absorption and emission spectrum – *spectral diffusion*, which are probably related to conformational reorientations or changes in the immediate dye environment [48, 151-153].

These inherent single molecule attributes are relevant to the planned pulling experiments. By applying a mechanical force to a single dye molecule, the influence of molecular tension on the photophysical properties could be investigated. Especially spectral shifts, due to molecular reorientations under strain are expected.

### 3.2 Methods of single molecule microscopy

This chapter gives a brief comprehensive summary of the common fluorescence microscopy techniques, which have been employed previously to generate images or spectra of single molecules. This is followed by the

conducted experiments on the dye systems Cy5 and TDI using confocal, wide-field and TIR imaging, which are presented in detail in the following sections.

### **Spectral isolation of single molecules at low temperatures**

In order to resolve single molecules in a sample they must be separated either spatially or spectrally [154]. The latter approach has been achieved in a solid matrix at low temperatures of a few K, for which molecules can be identified according to their slightly different, i.e. inhomogeneous, narrow-band absorption frequencies [43]. A prominent example is pentacene in a para-terphenyl solid [44, 47]. Due to its low phonon coupling to the matrix and its high absorption cross section of the zero-phonon line, the homogenous absorption lines of individual pentacene guest molecules can be identified in the host matrix with a narrow line laser beam.

### **Near-field scanning microscopy**

The alternative approach to resolve individual molecules by spatial separation is achieved by preparing highly diluted samples with  $\sim 10^{-10}$ M of dye. The first method to use this approach was the *scanning near-field optical microscope* (SNOM) [57]. The resolution of an optical fluorescence experiment is generally restricted by the wavelength of the excitation light to ca.  $\lambda/2$  – the *diffraction limit*. To circumvent this limitation the SNOM microscope was developed, which uses a 50-100nm diameter fibre aperture surrounded by a thin aluminium coating to illuminate the sample [63]. In effect, the light is “squeezed” out of this opening at 5-10nm above the surface. The optical resolution is limited to the aperture dimensions of ca. 50nm to 100nm, which is 3-5 times better than the optical diffraction limit. A sample image can be generated by scanning the tip at a constant height over the sample.

### **Far-field confocal microscopy**

Confocal microscopy is a far-field illumination technique that generates a sample image by scanning a diffraction limited illumination spot over the sample and detecting the fluorescence e.g. with an APD (avalanche

photodiode) [53-55]. An optical microscope in epi-configuration and a high  $N_A$  (numerical aperture) objective is used to focus a laser beam onto the sample. By placing a pinhole in the image plane of the microscope, the fluorescence light from out-of-focus illuminated regions is rejected, while most of the fluorescence from the focal volume can pass through to the detector. Through convolution of the illumination and pinhole-generated detection volumes, a relatively high lateral resolution can be achieved [155]:

eq. 25 
$$\Delta x_{FWHM} \approx \frac{0.4\lambda}{N_A}$$

Confocal microscopy enables a non-invasive detection and a three dimensional sectioning capability. By focussing on a single dye, time-traces can be captured with a high time resolution, which show the on-off dynamics such as blinking [156].

### **Wide-field microscopy**

Using wide-field illumination techniques, sample images can be achieved without scanning [56, 157]. By defocussing the illuminating laser beam in an epi-fluorescence microscope setup, a wide illumination field can be projected onto the sample surface and then detected with a highly sensitive CCD camera. This generates immediate images of the whole illumination area with time intervals of up to 10ms. Such high frame rates enable studies on single molecule movement and diffusion rates [56], such as the monitoring of single viruses labelled with ca. 100 fluorescent dye molecules [158] or recently the study of single dye labelled viruses [52]. The lateral resolution is approximately [155]:

eq. 26 
$$\Delta x_{FWHM} \approx \frac{0.51\lambda}{N_A}$$

However, the positioning accuracy of dilute fluorescent molecules is significantly higher than the spatial resolution. It is limited by the signal to noise ratio. Unfortunately the background fluorescence noise from out-of-focus regions is not suppressed in conventional wide-field imaging.

## **Total internal reflection (TIR) microscopy**

One way around the problem of high background noise in imaging is to employ evanescent wave excitation by total internal reflection (TIR) of the laser light at the glass/liquid or glass/air interface [58-60]. If the illumination light hits the glass/sample interface at a glancing angle that is greater than the critical angle for the two media, then the beam is totally reflected. However, the electromagnetic field does not abruptly drop to zero above the glass, but rather penetrates the sample with an exponentially decaying intensity and a characteristic decay length of ~100nm. This is sufficient to excite dye molecules immediately on the glass surface, but greatly reduces the out-of-focus background signal. The two main methods for achieving TIR excitation are the prism based geometry and the objective-type TIR geometry, which both provide large illumination fields with an extremely thin sample excitation thickness [61, 62, 159].

## **Single molecule spectra at room temperature**

In addition to the imaging techniques, it is also possible to study the spectral emission characteristics of a single dye molecule. The fluorescence spectrum of a single molecule can be measured by using either a prism or a grating as the dispersive element. Although the grating has higher losses, because a significant portion of the light is directed into higher diffraction orders, it provides a higher spectral resolution and a linear dispersion of the light. Gratings have therefore displaced the prism as the primary dispersive elements in modern spectroscopy, although the latter are still applied for single molecule detection, due to the lower signal losses. The spectra of single molecules are unique and can shift as a result of environmental influences on the molecular states responsible for the fluorescence [151]. Conformational changes or photochemical reaction can also induce single molecule *spectral diffusion*. Single molecule spectra have been investigated for various different dyes [145, 146, 152, 153, 160].

### 3.3 The general optical setup

The laser setup for the imaging experiments is composed of three sections: the excitation laser pathway, the inverted optical microscope and the fluorescence detection pathway.

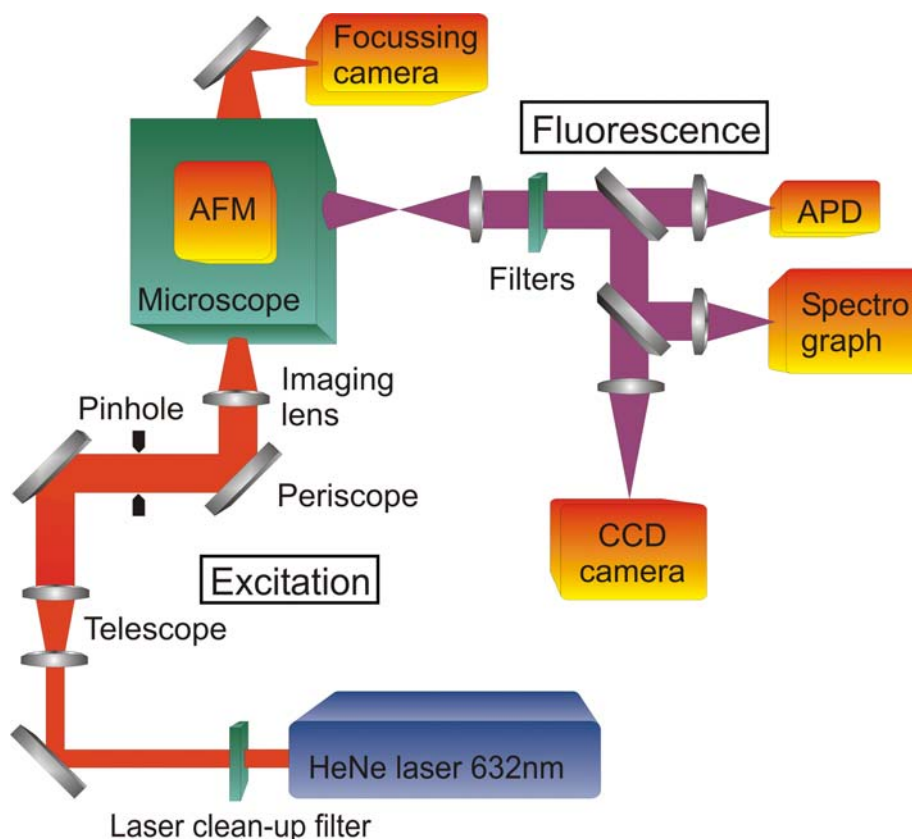


Figure 39: The optical setup showing the excitation and detection pathway

#### The excitation pathway and the inverted microscope

A He-Ne laser (Laser2000<sup>®</sup>) provides a 4mW 632.8nm laser light source, which is expanded with a telescope and trimmed by pinholes to a diameter of ca. 8mm – the full objective aperture. The periscope is then used to align the excitation beam according to the optical axis of the microscope. For normal epi-illumination confocal microscopy, parallel laser light is used, which results in a diffraction-limited spot at the objective focus.

The imaging experiments are achieved by pre-focussing the excitation beam with the help of an imaging lens, such that the focus coincides with the

microscope objective back-focal-plane. The generated light then reaches the mounted glass coverslip as a parallel beam, thus enabling the illumination of a wide sample area.

For objective-type TIR imaging, the periscope and lens are shifted laterally, thereby moving the laser beam from the optical axis to the peripheral edge of the objective aperture. The resultant parallel light rays exit the objective at a sufficiently large angle, so that total internal reflection occurs on the sample coverslip surface. A 100x oil immersion objective (Zeiss®,  $N_A=1.45$ ) is employed, which enables large exit angles of up to  $73.2^\circ$  (cf. section 3.6) for a detailed description of objective numerical aperture and beam exit angles).

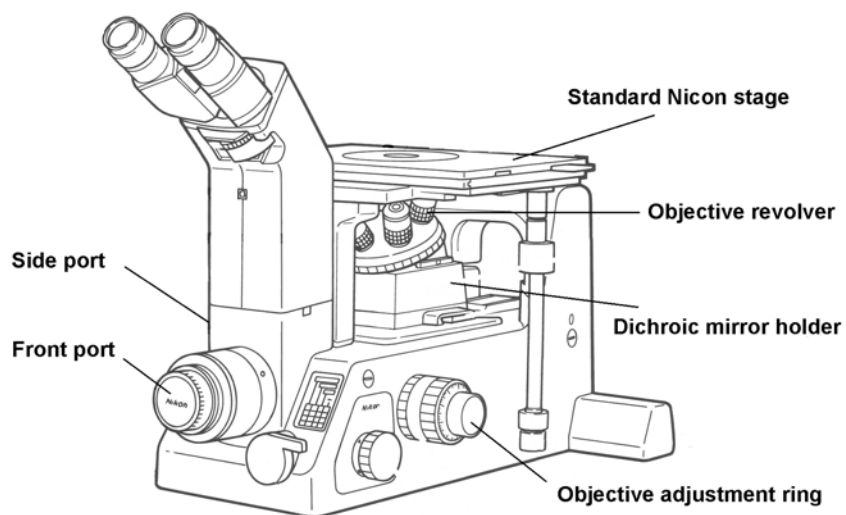


**Figure 40: Nikon TE300 microscope [adapted from Nikon microscope handbook]**

### **The detection pathway**

The sample fluorescence signal is collected by the objective and directed back down into the microscope. After passing a dichroic mirror (AHFanalysentechnik®, cut-off 645nm), which separates the reflected laser light from the transmitted fluorescence, the fluorescence light is guided to the side port of the microscope. In the case of confocal microscopy, a pinhole is placed in the image plane of the microscope to block out-of-plane background from the fluorescence signal. The beam is then sent through a 700/75 or

720/150 band-pass filter (AHFAnalysestechnik®). These filters let the appropriate fluorescence light pass (662-738nm or 650-790nm), but block all other wavelengths. The transmission spectra of the bandpass filters are shown in Figure 41. They display a high blocking optical density of ca. OD6 and a transmission of ca. 95%. The remaining fluorescence is then projected either onto the chip of a water cooled back-illuminated charged coupled device (CCD) camera (SpectraVideo™ Camera, Pixelvision®) for imaging or an avalanche photodiode (APD, EG&G® Canada) for confocal microscopy. The CCD chip (1100\*330 pixels) has a pixel size of 24µm<sup>2</sup>. For single molecule spectra the fluorescence light is first dispersed by a spectrometer (Kaiser optical systems®, Holospec™, linear dispersion 16.0nm/mm) and then directed onto the chip of another air cooled CCD camera (Roper Scientific®).

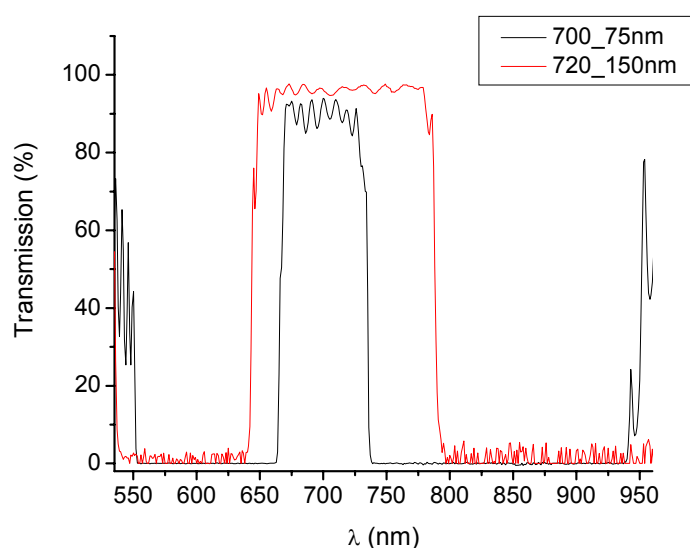


**Figure 41: Transmission spectra of the fluorescence bandpass filters**

## Experiments using confocal illumination

Confocal microscopy provides a convenient method to image single molecules in a matrix or on a surface. Images are generated by scanning a single molecule sample through a focussed laser spot (cf. Figure 42).

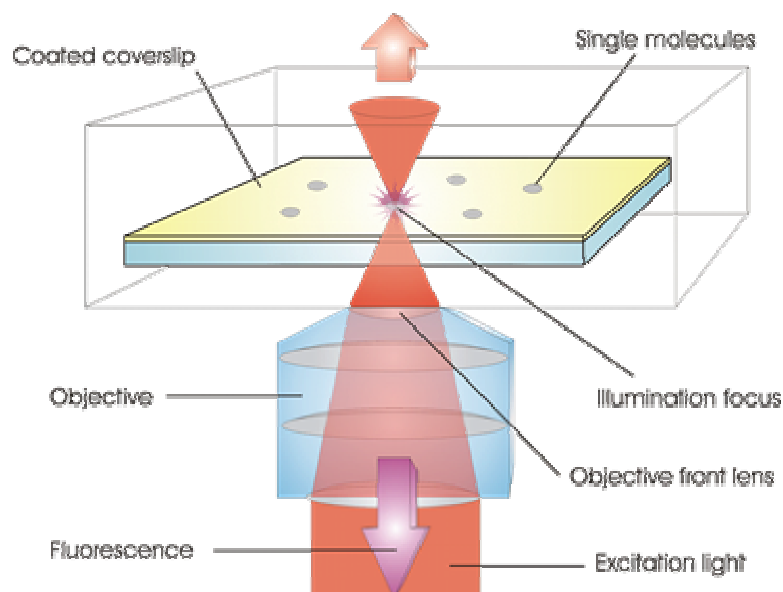


**Figure 42: Confocal illumination of a single molecule sample.**

A piezo system is used to move the sample. The exact position is controlled via a LabView<sup>®</sup> program (cf. Appendix 4: LabView<sup>®</sup> programs), which simultaneously monitors the APD fluorescence signal for each scanned pixel through a counter card (National Instruments<sup>®</sup>, AT-MIO-16XE). Furthermore, by directing the illumination spot to a dye position, time-traces with up to 20 $\mu$ s time resolution can be taken, which show the temporal development of the single molecule fluorescence emission. It is also possible to re-direct the fluorescence signal onto a spectrograph to measure the spectral dynamics of a single illuminated dye.

## Experiments using wide-field illumination

For wide-field imaging the excitation beam is focussed onto the back-focal-plane of the objective, so that a cone of light illuminates the sample with a diameter of ca. 20-100 $\mu$ m (cf. Figure 43). Fluorescence from this area is captured by the objective and projected onto a CCD camera.

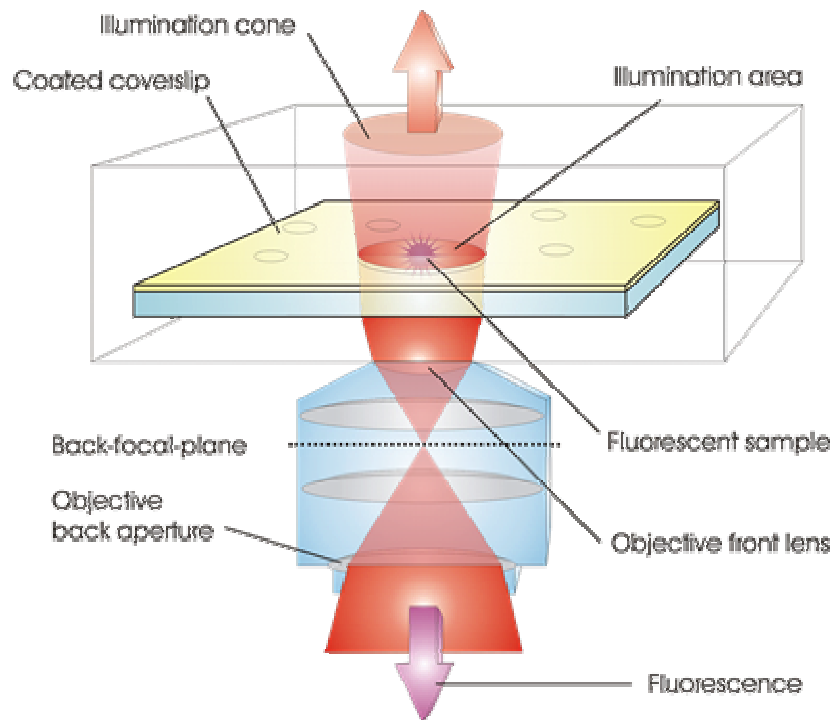


**Figure 43: Wide-field imaging by focussing on the back-focal plane.**

An additional commercial colour camera is mounted on the front exit of the microscope and employed to focus the sample prior to the experiment (cf. Figure 39). When the sample is in focus, the edges of the illumination pinhole are depicted sharply, as can be seen in the laser light reflection image in Figure 44. The regular striped pattern is due to interference between the light reflected from the coverslip surfaces. These images show condensed DNA rods on a polylysine coated glass surface.

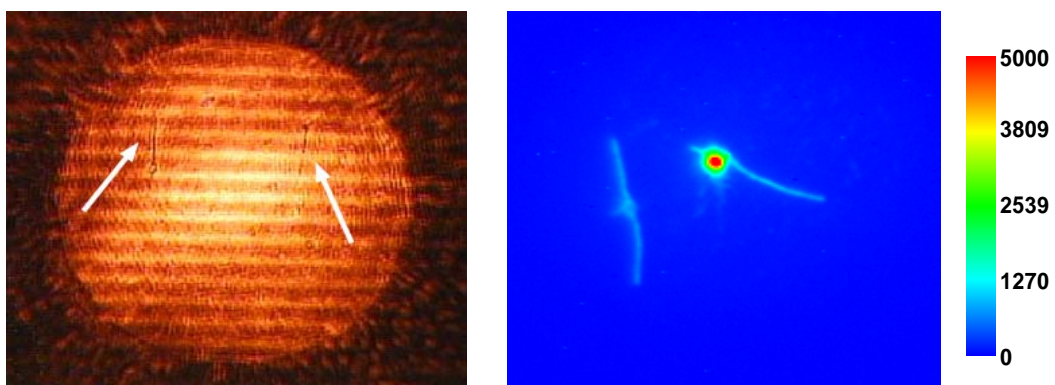


**Figure 44: Reflection image of DNA rods.**

**Figure 45: Fluorescence image of DNA rods. The arrows indicate stretched DNA rods; illumination spot  $\varnothing \sim 35\mu\text{m}$ ; laser power  $20 \text{ W/cm}^2$ .**

The imaging camera data is analysed with the image-processing software Davis™ (Lavisision®, Göttingen, Germany), saved in the IMX format and displayed on screen as a pixel image. To speed up data processing, a program was written in DAVIS™ script that enables an automated transfer of the fluorescence intensity results to a data text file. Davis also offers the possibility of displaying consecutive individual image frames as animated movies.

### 3.4 Confocal microscopy and single molecule fluorescence spectra

Ultimately, the aim is to investigate the spectral dynamics of a fluorescent dye under mechanical tension. To this end, the common single molecule dyes TDI and Cy5 were investigated using confocal microscopy and fluorescence spectroscopy. The technique of single molecule confocal microscopy was introduced in section 3.2. The following chapter describes the experiments and results achieved with this imaging method.

#### The results of the confocal images and spectra of TDI

Terrylene diimide (TDI) is the best single molecule dye known to date, with an exceptionally high photostability and a fluorescence quantum yield near unity [161]. The absorption and fluorescence spectrum of TDI is shown in Figure 46.

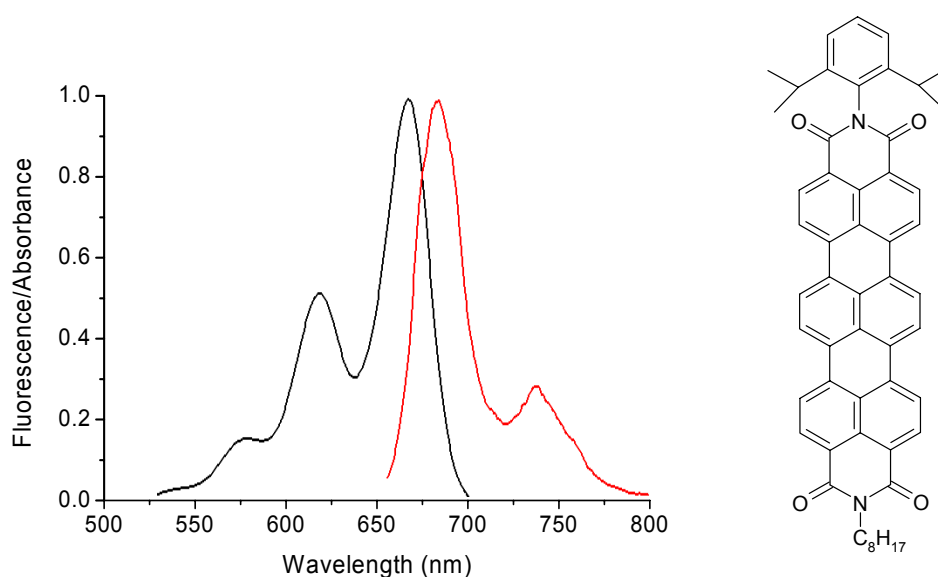
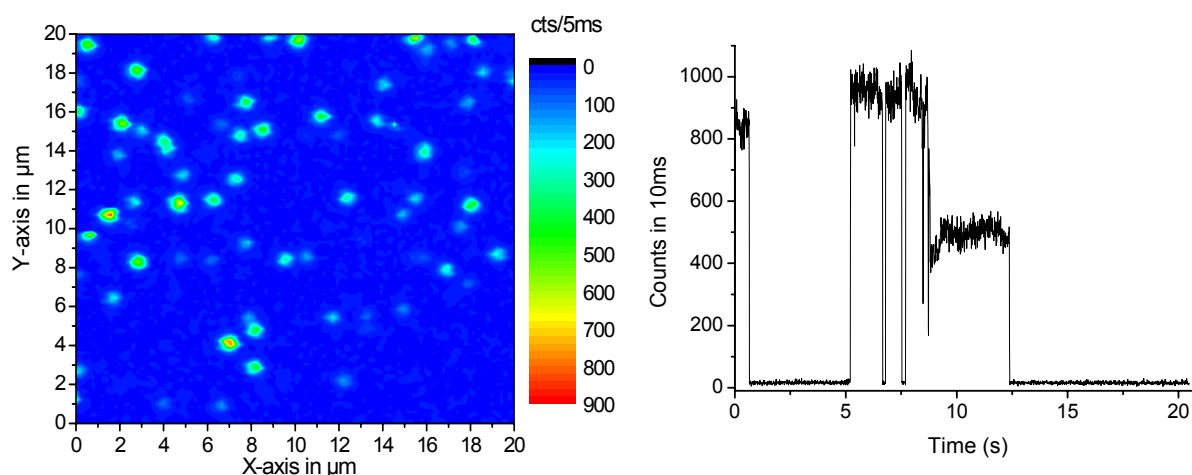


Figure 46: Absorption (black) and fluorescence (red) spectrum of TDI

The single molecule samples are prepared by spin-coating a highly dilute ( $10^{-9}$ M) dye solution in PMMA (polymethylmethacrylate)/chloroform (10% wt.) onto a cleaned glass coverslip. At 3000rpm the chloroform evaporates leaving a thin polymer film of  $\sim 20$ nm thickness (determined with a DecTac<sup>®</sup> thickness profiler) in which the dyes are immobilised. The resultant confocal scanning images are generated by illumination with 633nm laser light and integrating for 5ms/pixel. A 60x objective (Nicon<sup>®</sup>) and a 100 $\mu$ m pinhole is used to capture the fluorescence light. For the single molecule spectra, a 633nm notch filter blocks the excitation light. The spectrograph is calibrated with the help of three laser lines. All spectral series were taken with 50 $\mu$ W illumination intensity, which corresponds to ca. 60kW/cm<sup>2</sup> (enough for saturated excitation). Lower excitation powers could improve dye photostability, although a balance with overall dye brightness must be found.

As can be seen in Figure 47, the TDI molecules outshine the background signal. A time-trace of a single TDI molecule reveals on-off blinking and a second fluorescent state with about half the fluorescence count rate. Finally the dye bleaches irreversibly.



**Figure 47: left: confocal scanning image of TDI immobilized in PMMA polymer; illumination intensity: 30 $\mu$ W. right: time trace of a single TDI molecule showing blinking and digital bleaching; illumination intensity: 50 $\mu$ W.**

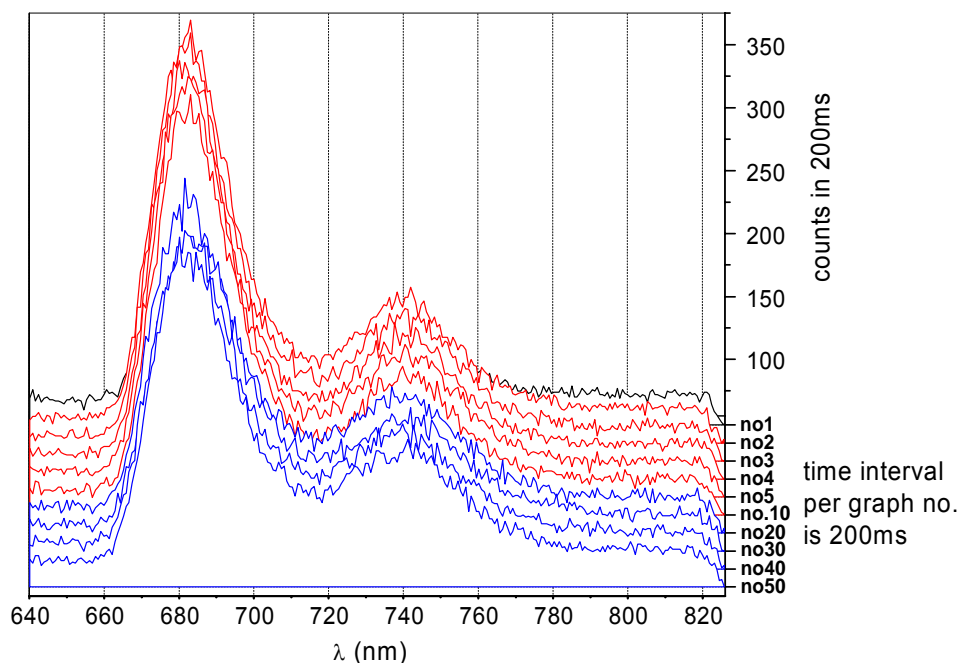


**Figure 48: Single molecule fluorescence spectrum series of TDI with two states (displayed in red and blue). The z-axis shows the spectrum number of the series, for which a graph was taken every 200ms (N.B. the change in scale on the time axis between graph no.5 and no.10). The jump between the two states occurs between graph no.10 and no.11 i.e. between 2.0 and 2.2 seconds. The illumination intensity was 50 $\mu$ W.**

A series of fluorescence spectra from a single TDI molecule is shown in Figure 48. Although no spectral shift is observed in this case, two distinct fluorescence states with differing brightness can be identified. The switch to the darker state occurs after 2 seconds. Such single fluorophore *intensity jumps* have been described previously by Blum et al. [153]. They need not be accompanied by a spectral shift, although most emission *spectral jumps* of a molecule lead to some form of intensity change. The jumps have been attributed to conformational changes within the molecule, such as the rotation of single bond. A similar conformational change may be possible in TDI, in which the phenyl group can rotate around the bond to the imide nitrogen. These conformational changes distort or shift the ground and excited state potentials, thus leading to different fluorescence bands.

Jumps into a completely nonemitting state are a special case of an *intensity jump*, which is usually called “blinking” or “reversible photobleaching”. An example of this is shown in the second spectrum series in Figure 49. After 400ms the molecule turns on for ca. 200ms, it then goes out for 4s, only to return again for another 500ms. After a total of 5s the dye eventually bleaches irreversibly. Although the examples shown here do not display clear spectral shifts, in some cases the fluorescence peaks were observed to jump to a different wavelength. The second peak at 730nm - the vibronic side band - may also be susceptible to spectral dynamics. For example, a narrowing of the ground state potential may lead to a larger energetic distance between the primary emission maximum and the vibronic side band [153]. These phenomena are not observed in bulk samples, for which the averaged fluorescence peaks are always at the same wavelength in a given solvent (e.g. 670nm and 730nm in CHCl<sub>3</sub>).

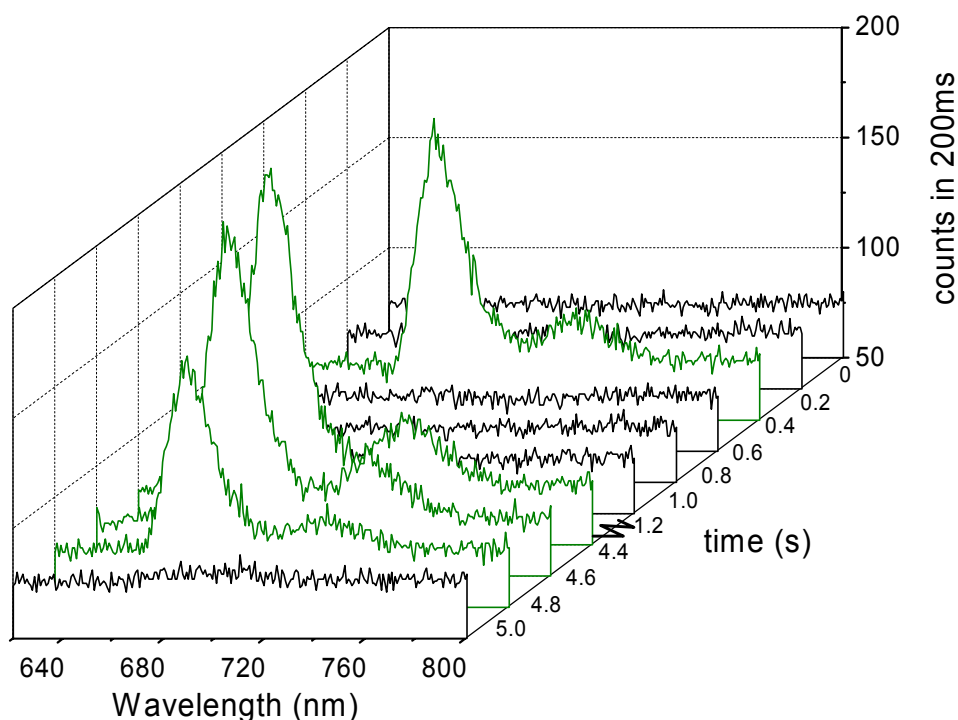


**Figure 49: Graph of the TDI spectrum showing dye blinking; illumination intensity: 50 $\mu$ W. (N.B. the change in scale on the time axis between 1.2 and 4.4 sec)**

## The results of the confocal images and spectra of Cy5

Unlike TDI, the cyanine dye Cy5 is water soluble and therefore frequently used in biochemical labelling assays. However cis-isomerisation in the double bond bridge leads to a reduction in fluorescence yield and the photostability of Cy5 is clearly lower than for TDI [142].

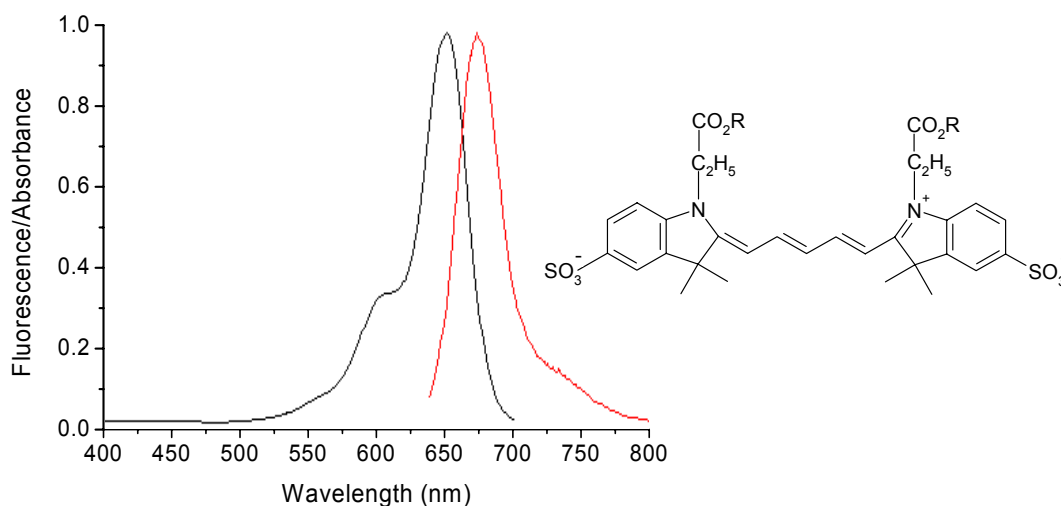


Figure 50: Absorption (black) and fluorescence (red) spectrum of Cy5

An example of a single molecule confocal image of Cy5 and a typical time-trace with on-off blinking is shown in Figure 51.

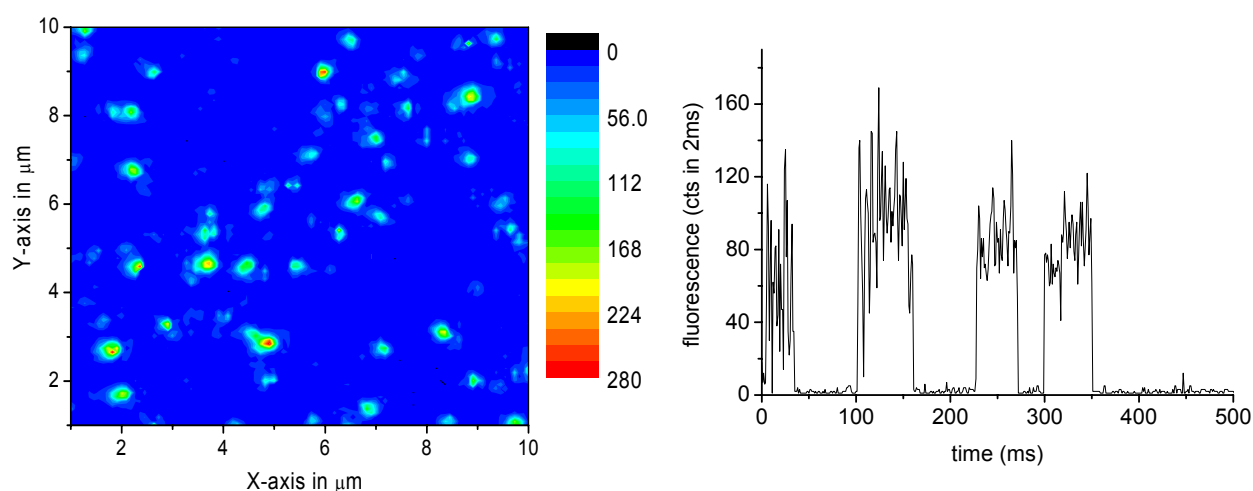
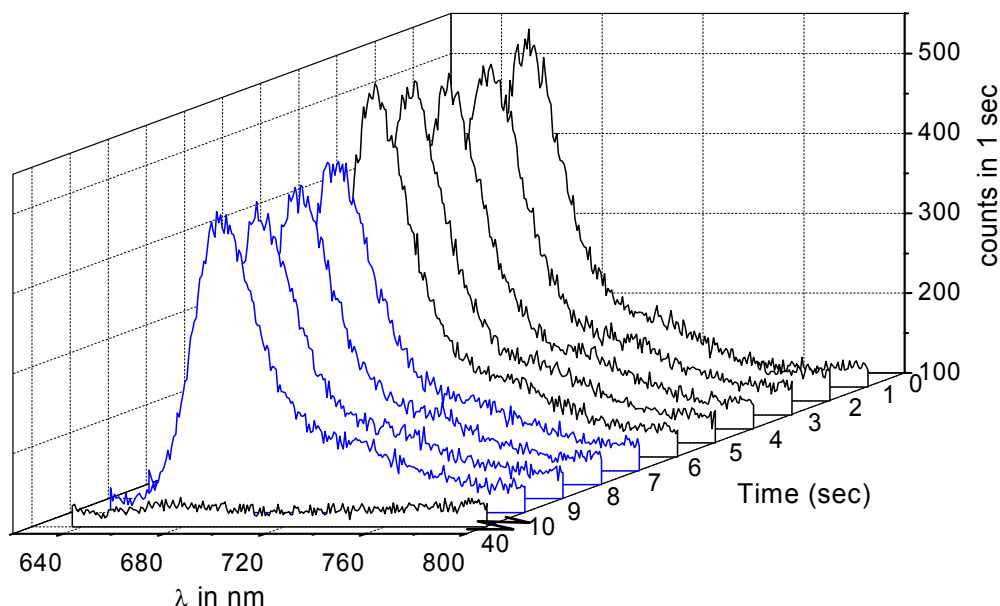


Figure 51: left: confocal image of Cy5 prepared on a glass coverslip; illumination intensity 7.5 $\mu$ W.

right: Cy5 time-trace with blinking; illumination intensity 7.5 $\mu$ W.

The single molecule spectrum series of Cy5 in PMMA (cf. Figure 52) shows an *intensity jump* of the dye after 6 seconds. Finally after 40 seconds the dye bleaches.



**Figure 52: Spectrum series of Cy5 in PMMA; illumination intensity: 50 $\mu$ W.**

In principle, it is possible to image single molecules by confocal scanning microscopy. TDI molecules, and occasionally Cy5, afford sufficient photons/second to generate a spectrum series. Blinking and spectral shifts of the dyes can be observed.

However, attempts to fix Cy5 to the glass surface by covalent bonding to an epoxysilane layer and subsequent attachment to the cantilever tip, via a polyethyleneglycol (PEG) spacer, proved to be unsuccessful. Therefore different systems were sought after.

### **3.5 Hemicyanine dyes for combined SM and AFM experiments**

In order to determine the suitability for single molecule experiments, a series of hemicyanine dyes was investigated. Based on the known styrene derivative (4,4-dimethylaminostyryl)-N-methyl-pyridinium iodide, two new dyes were synthesised by Dr. Markus Seitz as part of a collaboration with the group of

Prof. H. Gaub to investigate the spectral shifts of dyes under mechanical tension. The measured absorption and fluorescence emission spectra of these dyes are shown in Figure 53.

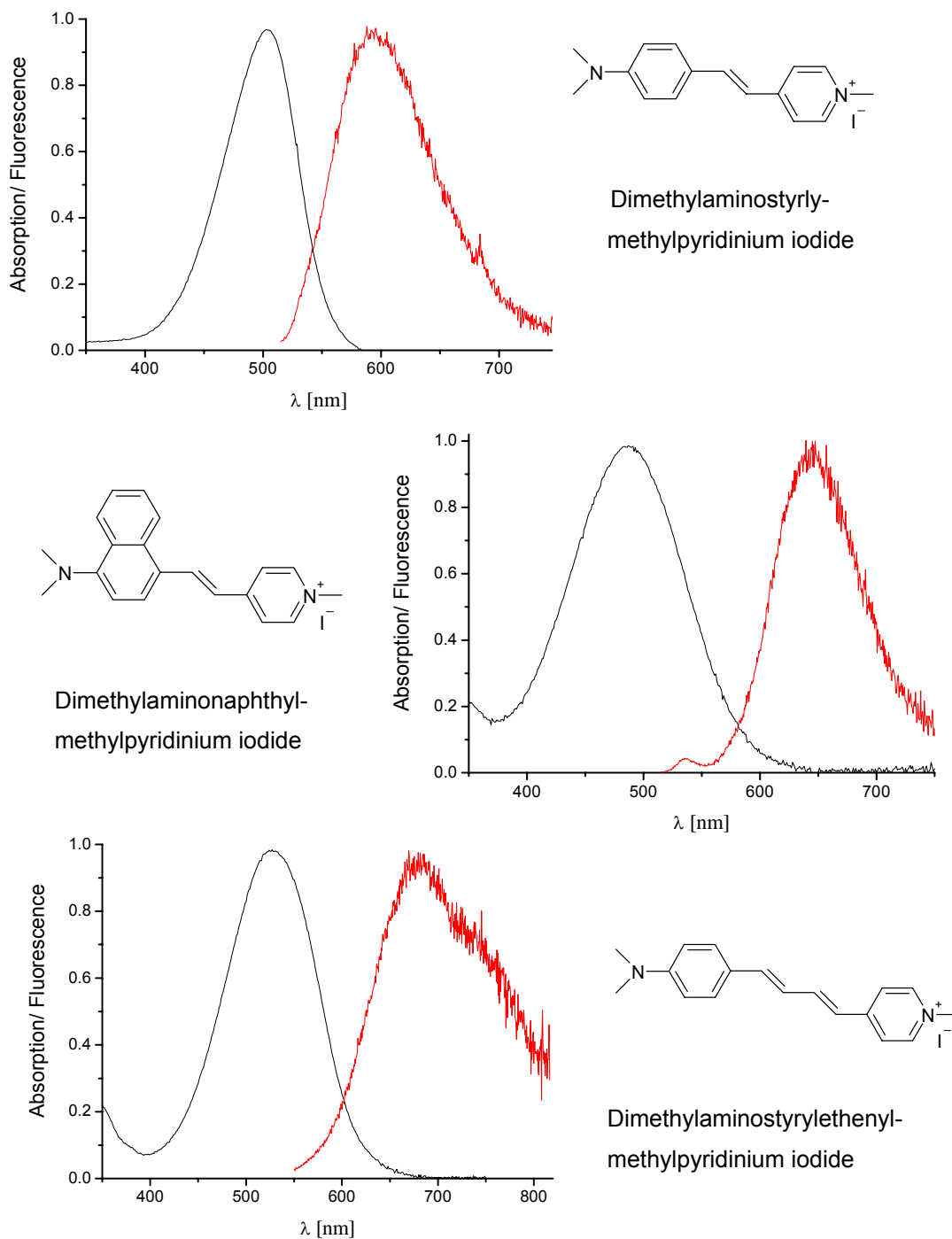


**Figure 53: Normalised absorption and fluorescence emission spectra of the hemicyanine dyes in  $\text{CHCl}_3$ .**

	Extinction coefficient Lit.	$\lambda_{\max}$ Abs. (CHCl <sub>3</sub> )	Lit. Absorption	$\lambda_{\max}$ Emi. (CHCl <sub>3</sub> )	Lit. Emission
Styryl dye [162]	37 000 (CHCl <sub>3</sub> )	504nm	500nm (CHCl <sub>3</sub> )	592nm	590nm (CHCl <sub>3</sub> )
Naphthyl dye		486nm		643nm	
Ethenylstyryl dye		528nm		676nm	
Rhodamine 6G [142, 163, 164]	97 000 (Ethanol)	534nm	530nm (Ethanol)	557nm	556 (Ethanol)

table 7: Summary of the absorption and fluorescence emission peaks of the hemicyanine dyes.

Both new styryl dyes derivatives display a bathochromic shift in the fluorescence. Particularly the ethenylstyryl dye is of interest as it can be excited at 532nm. Unfortunately, the rather broad emission spectrum of the ethenylstyryl dye may be the result of other fluorescent impurities generated during the dye synthesis, which were not completely removed during purification. Generally dyes that absorb and emit further in the red are desirable for single molecule detection, because the background fluorescence is lower.

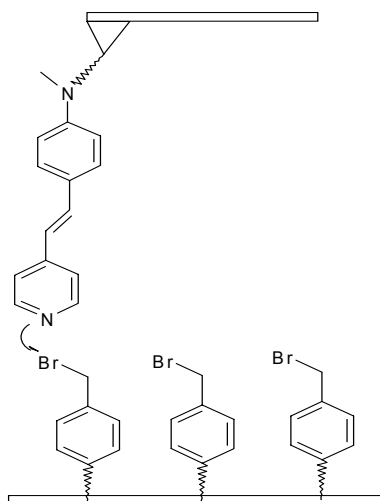


Figure 54: In situ generation of the fluorescent dye by reaction of the pyridine derivative with a bromine functionality.

The final goal was to generate the dye in situ by nucleophilic reaction of the pyridine functionality with a bromine group on the surface (cf. Figure 54). Any fluorescing molecules are then automatically attached to the cantilever and the surface. The absorption maximum of the pyridine derivative is at 368nm, which would therefore not be excited by the laser. However, the first single molecule confocal scanning experiments failed to afford good images of the samples. The reason for this turned out to be the low fluorescence quantum yield of the dyes.

### Fluorescence quantum yield measurements on the hemicyanines

A convenient method to measure the quantum yield is by comparison of the fluorescence emission of the dye solution with that of another standard dye solution of known quantum yield [163].

eq. 27

$$\phi_U = \frac{A_S F_U n_U^2}{A_U F_S n_S^2} \phi_S$$

The formula in eq. 27 gives the  $\Phi_{FI}$  for an unknown fluorescence dye  $U$  in terms of the standard dye  $S$ . The parameter  $A$  stands for the absorbance,  $n$  is the solvent index of refraction and  $F$  is the number of emitted photons. A value for  $F$  can be calculated by integration of the area under the fluorescence emission curve. For quantitative experiments it is important to use a calibrated fluorescence spectrometer. Errors can be reduced by exciting all dye solutions at the same wavelength and comparing dyes with similar emission spectra.

Furthermore, to solve for the  $\Phi_{FI}$  in eq. 27 the number of absorbed photons  $A$  must be the same for each dye solution. This is achieved by adjusting the concentrations so that the extinction coefficients are identical at the appropriate excitation wavelength. This has been done for the dyes in Figure 55, which have the same absorption at 510nm.

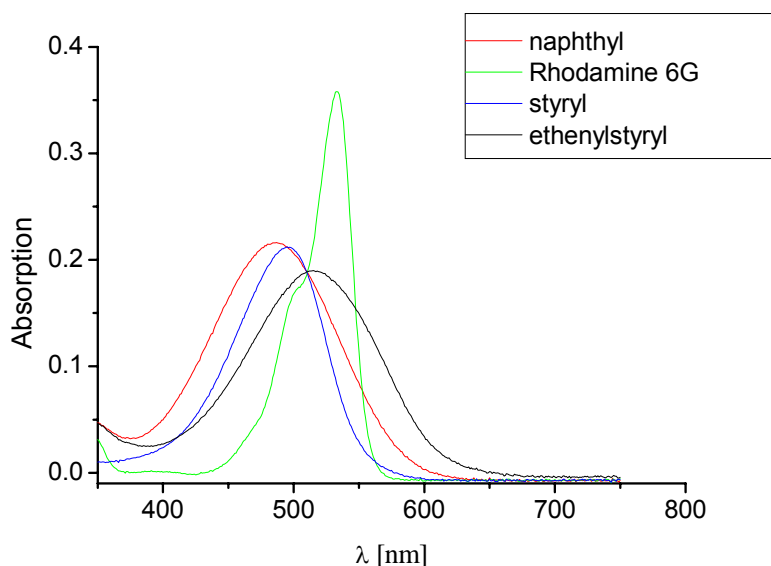


**Figure 55: Adjustment of the solution optical density to OD = 0.185 at the excitation wavelength of 510nm.**

Rhodamine 6G was chosen as the standard dye. It has a quantum yield of 95% in ethanol [161]. The index of refraction for ethanol is  $n = 1.359$  and for chloroform  $n = 1.444$ .

	Quantum Yield Lit.	Calculated Q.Y.
<b>Rhodamine 6G</b>	95% (Ethanol) [58, 59, 165]	-
<b>Styryl dye</b>	7.1% (CHCl <sub>3</sub> ) [62]	11%
<b>Naphthyl dye</b>		8%
<b>Ethenylstyryl dye</b>		28%

**table 8: Summary of the quantum yield calculations for the styryl dyes.**

The results of the quantum yield measurements are summarised in table 8. Except for the ethenylstyryl derivative the respective quantum yields are relatively low. Therefore, the styryl dyes are unsuited for single molecule experiments.

### 3.6 Total internal reflection (TIR) imaging

Total internal reflection microscopy (TIR) is a specific form of wide-field imaging that provides a means to image fluorescence samples with an extremely shallow excitation depth, thereby reducing the out-of-plane background signal [61, 166]. Our results show that cantilever auto-luminescence is a serious problem for combined AFM/optical experiments. However, by employing TIR, the evanescent excitation field is restricted to the immediate coverslip surface and the cantilever is not illuminated. In this way the relatively strong cantilever luminescence can be avoided. TIR can be achieved through various methods [167], such as the prism arrangement [159], but since the space above the microscope is reserved for the AFM, the TIR excitation must occur through the microscope objective, by the objective-type TIR arrangement [167].

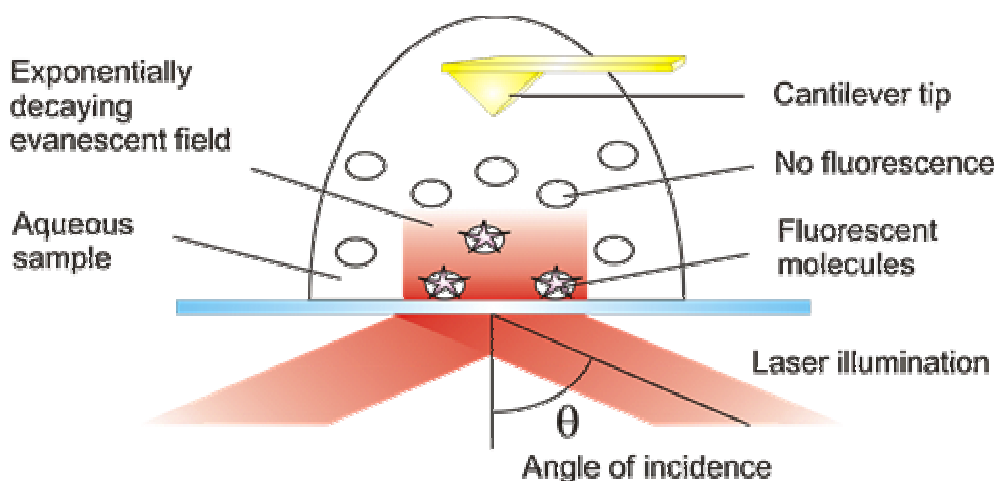


**Figure 56: Objective-type TIR illumination of an aqueous single molecule sample. Dyes in the immediate surface vicinity are excited, whereas dyes outside the evanescent TIR field are not illuminated.**

## The principle of TIR

Total internal reflection can occur when light crosses the interface from a medium with a high refractive index  $n_3$  to a medium, of lower index  $n_1$ . If the difference is sufficient, then the light is reflected back into the high index medium provided it reaches the interface at a minimum obtuse angle of incidence. According to Snell's law, the relationship between the critical minimum angle of incidence  $\theta_c$  required for total internal reflection and the difference in refractive index is described by the following equation:

eq. 28 
$$\theta_c = \sin^{-1}(n_1/n_3)$$

Typical materials for TIR are glass ( $n = 1.515$ ), water ( $n = 1.330$ ) or air ( $n = 1.000$ ). The critical angle for glass-air is  $\theta_c = 41.30^\circ$ , whereas for glass-water it is  $\theta_c = 61.39^\circ$ .

However, classical electrodynamics does not allow for the electromagnetic wave to vanish discontinuously at an interface. Instead an evanescent field is generated above the reflection area that decreases exponentially with distance  $r$  from the interface. The decline is characterised by the penetration depth  $d$ , within which the intensity of the field drops to 37% ( $1/e$ ) [159].

eq. 29 
$$I(r, \theta) = I(0)e^{-r/d}$$

$$d = \frac{\lambda_0}{4\pi} \frac{1}{\sqrt{n_3^2 \sin^2 \theta - n_1^2}}$$

At the interface glass-water the characteristic penetration depth is 147nm, assuming a typical incident angle of  $\theta = 65^\circ$  and a laser wavelength of 633nm. For the interface glass-air  $d = 53.5$ nm. The exponential decay curves for the water and air samples are shown in Figure 57. Due to the higher difference in refractive index, the field decreases faster for the glass/air interface.

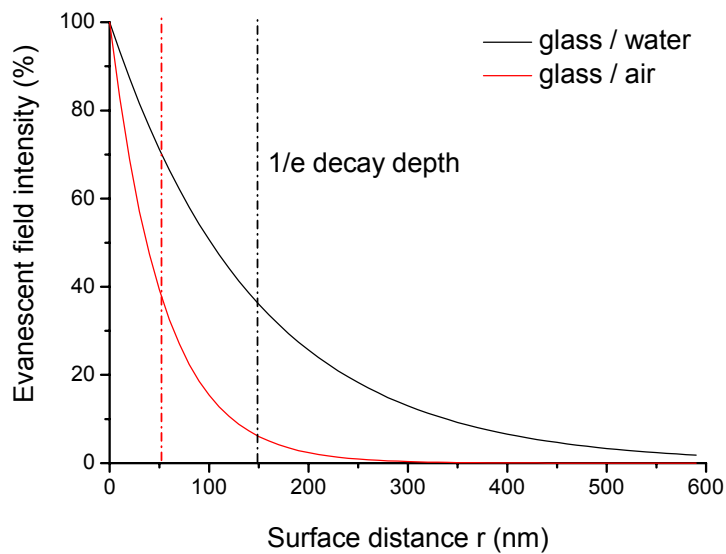


**Figure 57: The decay curve of the evanescent field at the interface between glass/water (black curve) and glass/air (red curve) for an incident angle of 65°.**

### Objective-type TIR

Parallel beams are generated by focussing the excitation laser light onto the back-focal-plane of the objective. As in conventional wide-field imaging, an area spot is illuminated on the sample, rather than a diffraction limited focal spot in confocal microscopy. Furthermore, by shifting the beam off-axis, it no longer exits the objective centrally, but instead at an angle. After reflection at the coverslip/sample interface, the excitation beam re-enters the objective (cf. Figure 58).

The beam width at the back focal plane can be calculated according to eq. 30 [168]. Given an objective back aperture of ca. 8mm, there is sufficient space to place the beam on the outer perimeter of the objective aperture lens, thereby achieving a maximum emission angle.

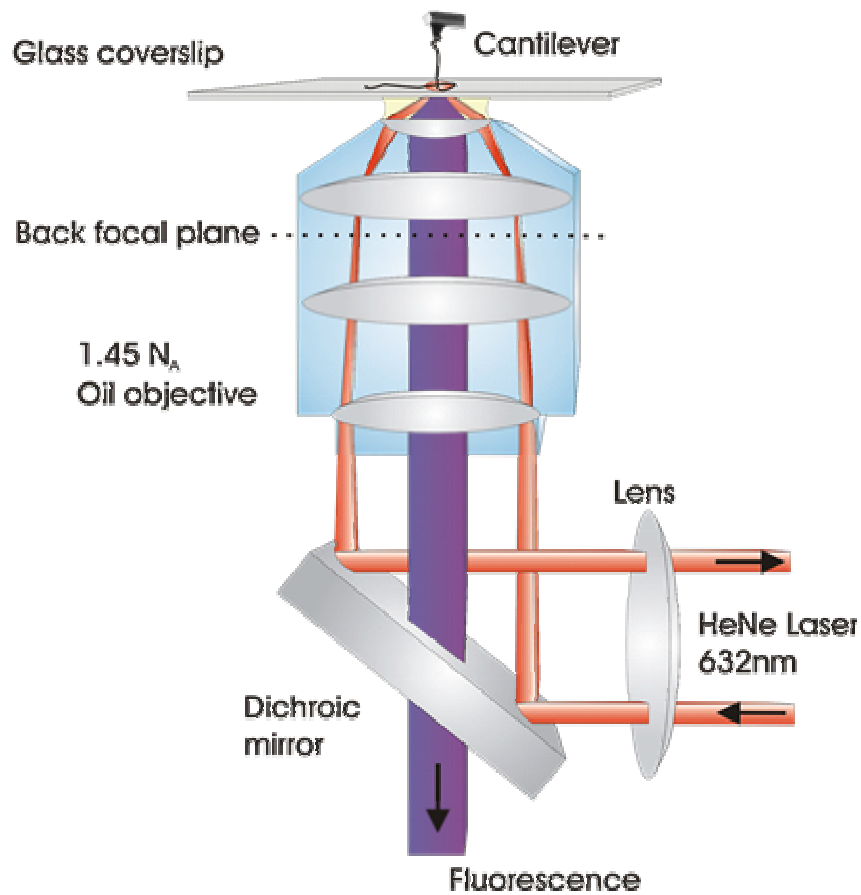


Figure 58: Objective-type TIR arrangement.

eq. 30 
$$\omega = \frac{\lambda \cdot f}{\pi \cdot n \cdot \omega_0} = \frac{0.633 \mu\text{m} \cdot 400 \cdot 10^3 \mu\text{m}}{\pi \cdot 1 \cdot 10 \cdot 10^3 \mu\text{m}} = 8.06 \mu\text{m}$$

- $\lambda$  = laser wavelength
- $f$  = lens focal length
- $n$  = index of refraction
- $\omega_0$  = beam radius in front of the lens (10mm)

The maximum angle of incidence  $\alpha$  at which the objective can emit (and collect) is restricted by the numerical aperture  $N_A$ :

eq. 31 
$$N_A = n_0 \sin \alpha$$

To achieve TIR conditions the incident angle must be between  $\alpha > \theta > \theta_c$ , e.g. a critical angle of  $\theta_c = 61.39^\circ$  in water. The maximum emission angles for

various oil immersion objectives are presented in table 9. For an oil immersion objective the index of refraction is  $n_o = 1.515$  ( $n_{(oil)} = n_{(glass)} = n_{(Obj)}$ ).

NA	1.30	1.35	1.40	1.45
$\alpha$	59.1°	63.0°	67.5°	73.2°

**table 9: The relationship between numerical aperture and maximum emission angle of a high  $N_A$  oil immersion objective.**

Total internal reflection requires that the objective  $N_A$  be higher than the refractive index of the specimen. Until recently the highest available  $N_A$  was 1.40, which is just enough to achieve TIR in an aqueous sample ( $n = 1.33$ ). However, new objectives with numerical apertures of up to 1.65 are now available, which facilitate TIR measurements in water, but require a special volatile high refractive index immersion oil ( $n_o = 1.78$ ) and coverslip glass ( $n_o = 1.79$ ) [167]. For our measurements objectives with either  $N_A = 1.40$  or  $N_A = 1.45$  are employed, which can be used with conventional glass coverslips and immersion oils.

A TIR image of single TDI molecules is shown in Figure 59. Compared to the spot in conventional imaging, the illuminated area in TIR is slightly oval.

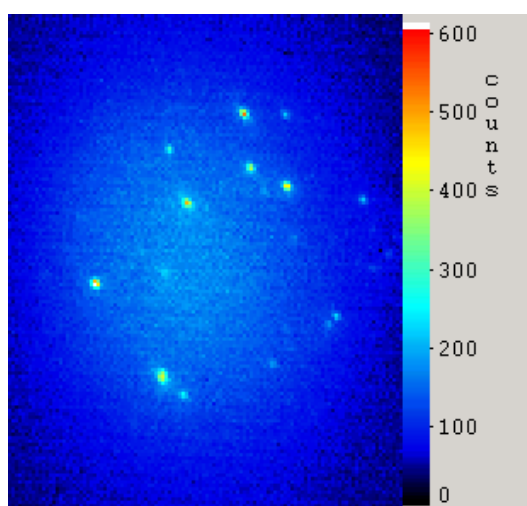


**Figure 59: TIR image of single TDI molecules immobilised in a PMMA polymer matrix. The illumination intensity is  $0.33\text{kW}/\text{cm}^2$ , with a camera exposure time of 1sec.**

## Measuring the TIR field with the AFM cantilever

In order to characterise the evanescent field, a method is presented to determine the field intensity by using an AFM cantilever as a local probe. The luminescence of a  $\text{Si}_3\text{N}_4$  tip is proportional to the laser excitation intensity and can therefore be used as a measure of the evanescent field strength. A series of images is taken of the cantilever during an approach cycle towards the glass interface. Then the average signal intensity for the cantilever image is plotted against the distance from the surface. The high axial position accuracy of the AFM enables an exact plot of the field intensity with distance. By fitting the decay graphs with an exponential function the characteristic field penetration depth  $d$  can be calculated. The graph in Figure 60 shows the decay curve of the luminescence signal for a water sample with an oil immersion objective  $N_A = 1.45$ . The mono-exponential fit of the data affords a characteristic decay depth of  $d = 230\text{nm}$ . This is slightly higher than the theoretical value of  $147\text{nm}$  for  $\theta \sim 65^\circ$ . The reason for this is probably that the  $65^\circ$  angle of incidence was not achieved in this experiment, because the beam was not exactly on the perimeter of the objective back aperture. A penetration depth of  $230\text{nm}$  would be expected for an incident angle of  $\theta \sim 62^\circ$  at the glass/water interface.

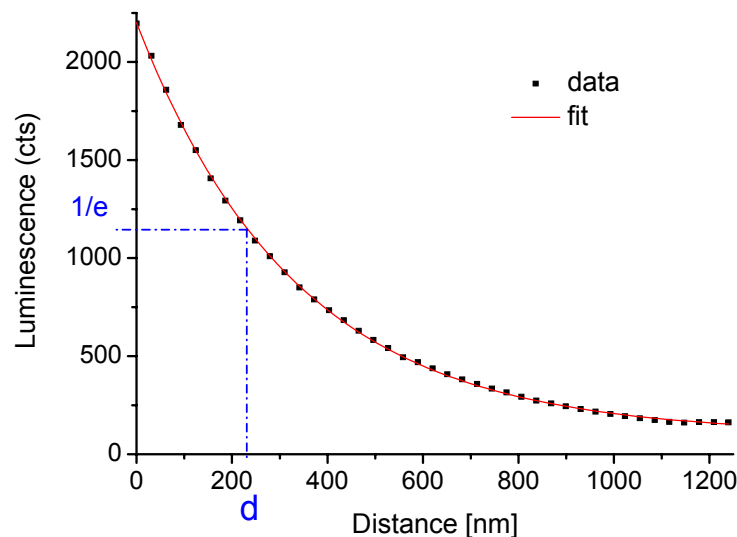


**Figure 60:** Plot and exponential fit of the luminescence decay curve for TIR illumination at the interface glass/water; objective  $N_A = 1.45$ .

By comparison, the graph in Figure 61 shows the decay curve for TIR at the glass/air interface using a 1.40  $N_A$  objective. The decay length in this example is 232nm. Although a shorter penetration depth is always observed at the glass/air interface as compared to glass/water and a value of  $d = 53.5\text{nm}$  could theoretically be achieved for  $\theta \sim 65^\circ$ , the 1.40NA objective is generally restricted to lower angles of incidence than the 1.45  $N_A$  objective and the full  $65^\circ$  is not always accessible. Measuring the TIR field with the 1.40  $N_A$  objective at the glass/water interface afforded a decay length of 330nm.

A typical phenomenon observed for AFM measurements in air is the “jump to contact”. Electrostatic and capillary water forces pull the cantilever onto the coverslip surface. This is one reason why AFM force spectroscopy is generally conducted in fluid.

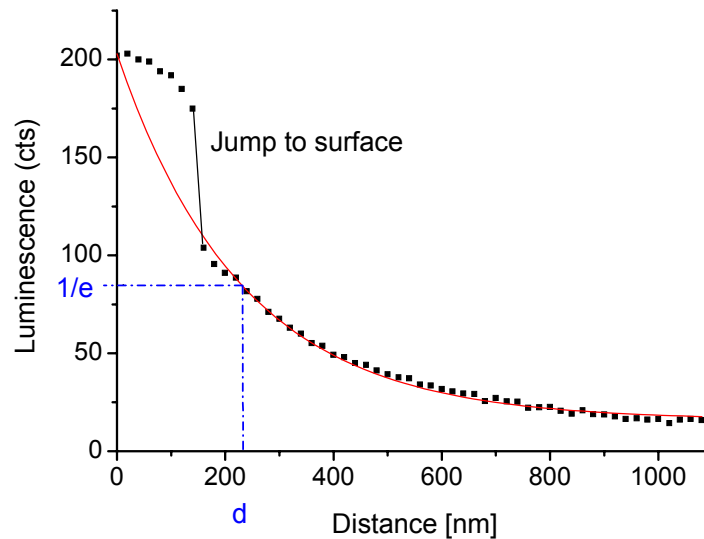


**Figure 61: Plot and exponential fit of the luminescence decay curve for TIR illumination at the interface glass/air; objective  $N_A = 1.45$ . At  $\sim 160\text{nm}$  the cantilever jumps onto the surface.**

### TIR penetration depth and angle of incidence

According to eq. 32 the characteristic decay depth of the evanescent field depends on the angle of incidence of the TIR beam.

eq. 32 
$$d(\theta) = \frac{633}{4\pi} [n_3^2 \cdot \sin^2 \theta - n_1^2]^{-\frac{1}{2}}$$

A graph of this function is given in Figure 62 for the glass/air and glass/water interface. The maximum angle achievable with the high  $N_A$  objectives is plotted as a blue dotted line.

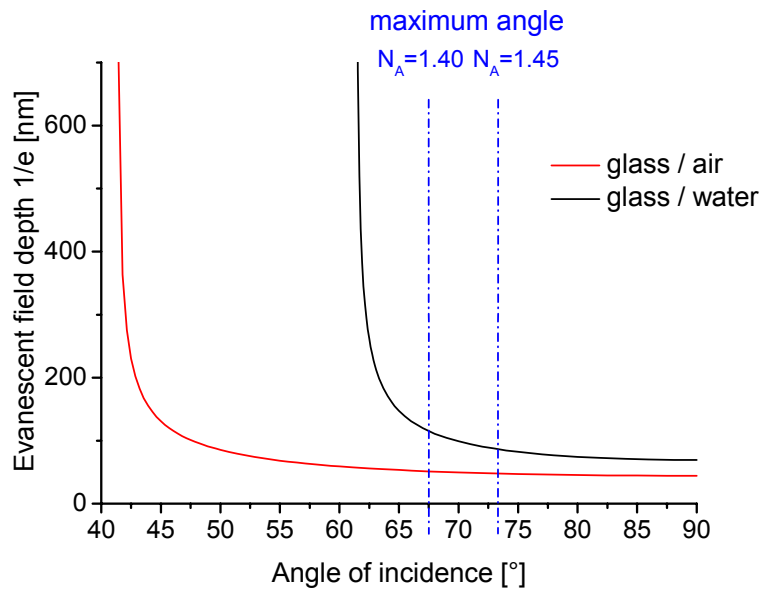


**Figure 62: Theoretical relationship between the evanescent field penetration depth and the angle of incidence for the glass/air and glass/water interface.**

By shifting the beam off-axis with respect to the objective back aperture, the TIR angle can be increased. The image series in Figure 63 shows the qualitative effect on the cantilever luminescence, when the angle of incidence is varied. The tip was positioned on the coverslip surface.

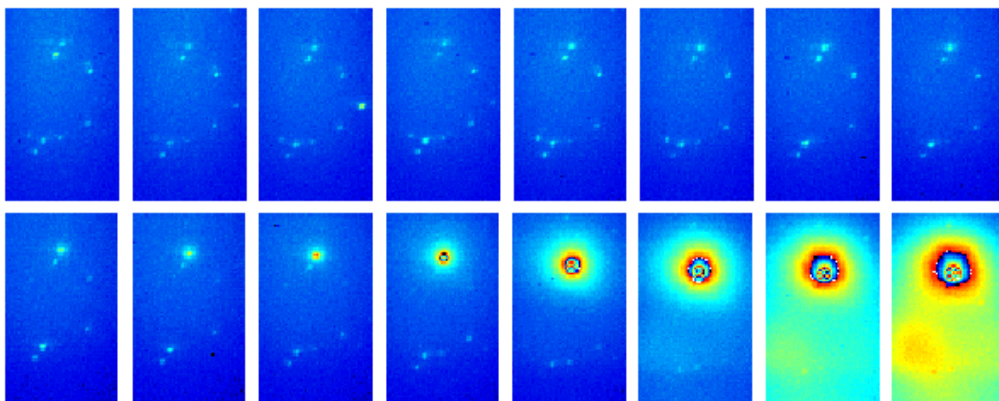


**Figure 63: The cantilever luminescence as a function of TIR incident angle. By decreasing the angle of incidence the TIR mode is converted into conventional imaging.**

The top left image was taken in full TIR mode. Only the cantilever tip apex can be seen together with a few single dye molecules. By gradually decreasing the angle of incidence the penetration depth of the evanescent field is increased and more of the cantilever is illuminated. Finally the TIR condition breaks down and the evanescent field is replaced by conventional imaging illumination. In this case the whole cantilever shank is illuminated (tip length  $\sim 4\mu\text{m}$ ).

The decay curves and the field penetration depths can be measured for various angles of incidence and plotted against the incident TIR angle. The angle of incidence is thereby calculated from the measured entrance position of the beam on the objective back aperture. The results for a  $N_A = 1.45$  objective with water are shown in

Figure 64. Although the data points conform to the theoretical curve, more measurements are required around the critical angle  $\theta_c = 61.4^\circ$ .

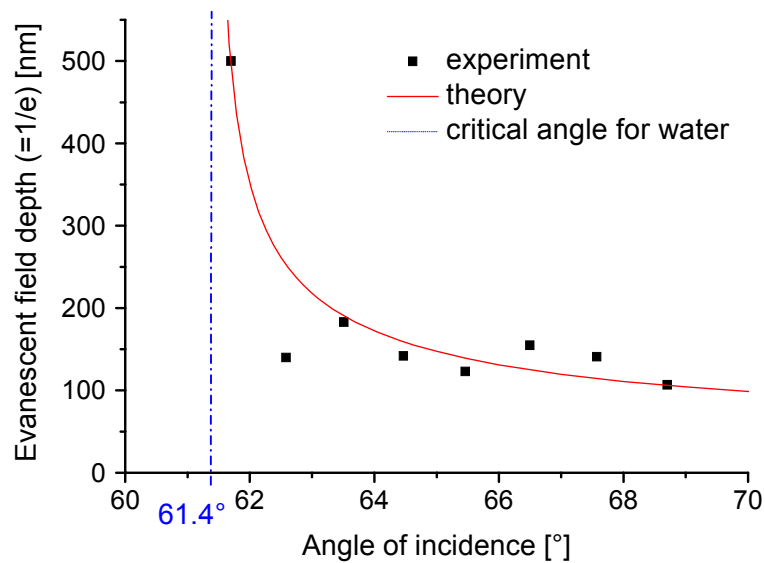


**Figure 64: Plot of the evanescent decay lengths for various angles of incidence. Each point represents the characteristic decay length of a curve measured at a different beam angle of incidence.**

Beyond the critical angle the evanescent field breaks down and turns into conventional imaging. Moreover, in some cases light scattering structures or inhomogeneities on the interface surface can increase the apparent penetration depth of the evanescent TIR field.

## Comparison of TIR and conventional imaging

The images in Figure 65 show the same cantilever positioned on the glass surface in a water sample using either TIR imaging (left) and conventional imaging (right). Only the tip apex is visible in TIR mode, whereas the whole cantilever shank is illuminated with wide-field excitation.

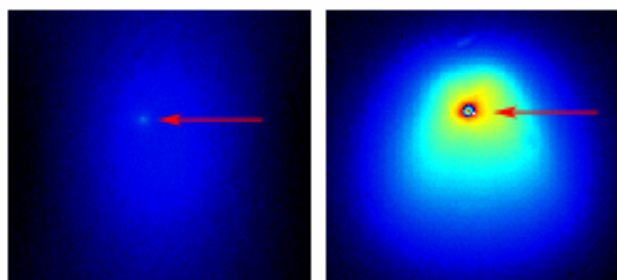


**Figure 65: Comparison of a cantilever image taken in TIR mode (left) and conventional imaging mode (right); the red arrow indicates the cantilever position.**

The luminescence intensity of a cantilever during an approach curve in conventional imaging mode is plotted in Figure 66.

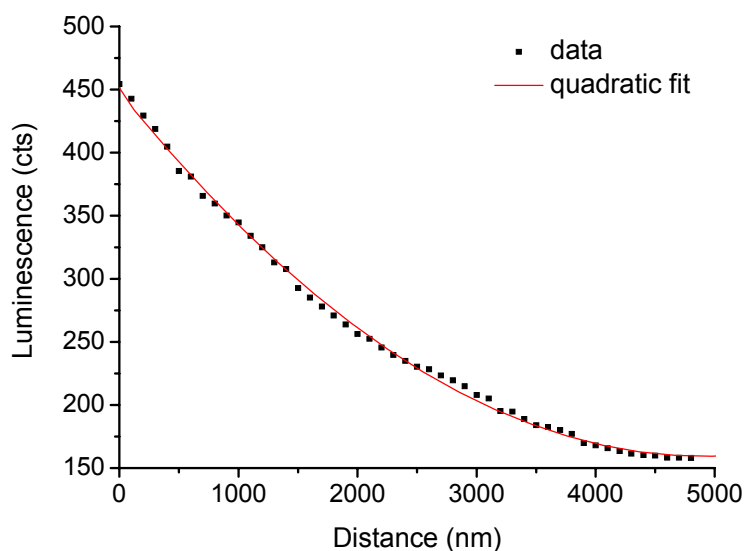


**Figure 66: The cantilever luminescence decrease with distance in conventional imaging mode can be fitted with a quadratic function.**

In contrast to the TIR exponential decay curves the data points can be fitted with a quadratic function. In conventional imaging the illumination light propagates in the form of a cone. The cone area will increase with distance from the objective in a quadratic manner. If the field intensity is proportional to the cone area, then the quadratic relationship found for wide-field imaging can be explained.

### **Conclusion TIR imaging**

Previous experiments by other groups have successfully employed the photon pressure on a dielectric sphere [169] or the tip scattering of a  $\text{Si}_3\text{N}_4$  cantilever [170] to probe the evanescent field generated at an interface. However, due to poor signal resolution, the results could not provide a clear exponential decay curve or accurate values for the characteristic penetration depth.

Our experiments show that the decay profile of the evanescent field in objective-type TIR illumination can be probed quantitatively with high axial resolution by imaging the cantilever luminescence. The characteristic exponential penetration depths can be determined for different interfaces and compared with the predicted theoretical calculations. Wide-field imaging decay curves are fitted with quadratic functions. In addition, the dependency of the evanescent field depth on the TIR angle of incidence was measured and compared to theory.

Finally, the objective-type TIR imaging of single molecule samples is possible and the background luminescence from a cantilever in the imaging spot can be greatly reduced by TIR mode imaging.

## 4. DNA optical experiments

The results of AFM force spectroscopy on DNA show that it is possible to stretch single DNA strands on transparent polylysine coated or silanised surfaces. Therefore, a combined optics/AFM experiment with DNA should be realisable. However, the next step is to elucidate the optimum imaging conditions for single DNA molecules. To this end, the experimental factors pertaining to the DNA/TO-PRO-3 system were investigated. These include the general photophysical parameters of the DNA-intercalator complex, such as the fluorescence quantum yield enhancement of TO-PRO-3 on binding to DNA or the effect of salt concentration, laser power and anti-bleaching agents. Furthermore, bleaching and dye kinetics studies afforded a description of the dye association/dissociation rates and binding constant to DNA.

Implementing these findings, images of DNA on either polylysine coated or silanised surfaces are presented and discussed. There is a marked difference in DNA morphology between DNA on polylysine and on silane surfaces, which is explained in terms of DNA condensation through the effect of positively charged lysine groups in the polylysine chain. In addition, a particular preparation protocol for  $\lambda$ -phage DNA, including a change in pH, led to the discovery of extremely long DNA strands with up to 300 $\mu$ m length.

### 4.1 The photophysical parameters of TO-PRO-3<sup>®</sup> with DNA

The binding modes of TO-PRO-3 to DNA have been discussed previously (cf. 2.3 Force spectroscopy of DNA on transparent surfaces). The dye is a member of the class of cyanine dyes that fluoresce brightly on intercalation or binding to DNA, but are dark in solution. Due to this enhancement in fluorescence these dyes can be used to image DNA.

#### **DNA intercalating dyes: ethidium bromide and cyanine dyes**

Among the first DNA intercalator dyes was ethidium bromide, which has traditionally been used for DNA staining in gel electrophoresis [171]. Ethidium bromide inserts between the DNA base pairs, resulting in a strikingly increased fluorescence quantum yield and an extension of the overall DNA chain length [172]. The fluorescence enhancement could be due to restricted

rotation of the central methane bridge in the dye on intercalation or because ethidium bromide is protected from quenching by the aqueous solvent when it is immersed in the hydrophobic region of the nucleic acid.

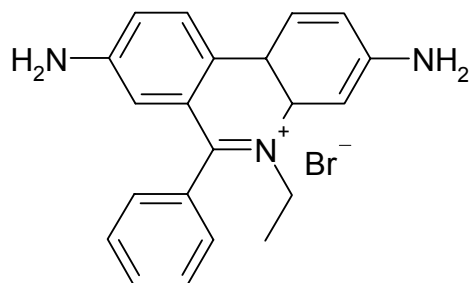


**Figure 67: Ethidium bromide**

At high and low pH ( $3 > \text{pH} > 12$ ) there is an abrupt drop in fluorescence [173] (cf. Figure 68). Since this occurs at the same pH values as for the acid and alkaline denaturation of DNA there is evidence that double stranded DNA is required for binding ethidium bromide.

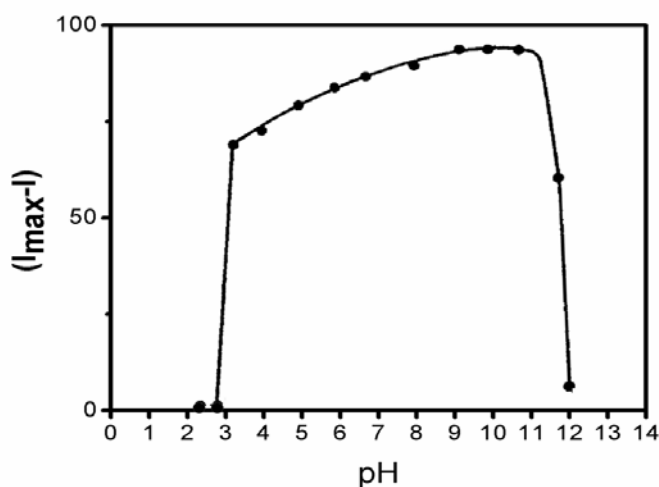


**Figure 68: The effect of pH on DNA/ethidium bromide fluorescence [173].**

This attribute of intercalated dyes may be used to prove whether the B-S transition, observed in DNA force curves, is in fact due to double strand melting (denaturation), as has been asserted [174], or merely a co-operative conformational change. If melting is involved in the B-S plateau, then, by analogy with the high and low pH experiments, a similar drop in TO-PRO-3

fluorescence would be observable during mechanical stretching of DNA. The results showing that double strand melting is not involved in the B-S plateau are presented in chapter V.

Ethidium bromide stained dyes have been used to image single DNA molecules, but contrast and image brightness are poor [175]. However, new enhanced cyanine dyes (Molecular Probes<sup>®</sup>) have been developed, which show high molar absorptivity, with extinction coefficients typically greater than  $50\,000\text{ cm}^{-1}\text{M}^{-1}$  [106]. They also have large fluorescence quantum yield enhancements on binding to DNA and thus enable high contrast imaging of individual DNA molecules [176, 177]. Among these is the dimeric cyanine dye YOYO-1 (cf. Figure 23) with a fluorescence enhancement factor of 460 upon binding and a binding affinity of  $K_a = 6 \cdot 10^8\text{ M}^{-1}$  [75].

The cyanine dye family, including YOYO-1, have been used extensively to image single DNA molecules for screening [178], DNA restriction analysis [118, 179], exonuclease activity [180], DNA conformation analysis on lipid bilayers [76, 119] or DNA double strand damage [181]. Interestingly, YOYO-1 can also prevent polycation induced condensation of large DNA strands [182]. Apparently, the intercalator can elongate the chain, increasing the overall stiffness and persistence length. By contrast, the minor groove binding DAPI, which is also used for DNA staining, shows no such effect [182].

#### 4.1.1 TO-PRO-3 bulk fluorescence spectra

On binding to DNA the spectra of the cyanine dyes shift to longer wavelengths [183] (cf. Figure 69 and Figure 70). This bathochromic shift reflects changes in the microenvironment of the dye such as a more hydrophobic surrounding.

For a TO-PRO-3<sup>®</sup> solution the absorption and excitation spectra indicate a maximum absorption peak at  $\lambda_{\text{exc}} = 632\text{nm}$ , whereas the maximum fluorescence in the emission spectrum is at  $\lambda_{\text{emi}} = 652\text{nm}$  (cf. Figure 69). If a low DNA concentration of  $1 \cdot 10^{-10}\text{ mol/l}$  is added, the Stokes shift of 20nm is maintained, but both maxima are shifted bathochromically by ca.10nm to afford:  $\lambda_{\text{exc}} = 643\text{nm}$  and  $\lambda_{\text{emi}} = 662\text{nm}$ . This is consistent with the literature values of  $\lambda_{\text{max}} = 642/661\text{nm}$  [106]. A solution of  $1 \cdot 10^{-10}\text{ mol/l}$  DNA

corresponds to a base pair concentration of  $4.85 \cdot 10^{-6}$  mol/l ( $\lambda$ -phage DNA contains 48502 bp). This means that in a dye solution of  $1.6 \cdot 10^{-6}$  mol/l there is approximately one dye molecule for every three DNA base pairs, a value which is close to the ratio assumed for complete intercalator saturation of the DNA [184].

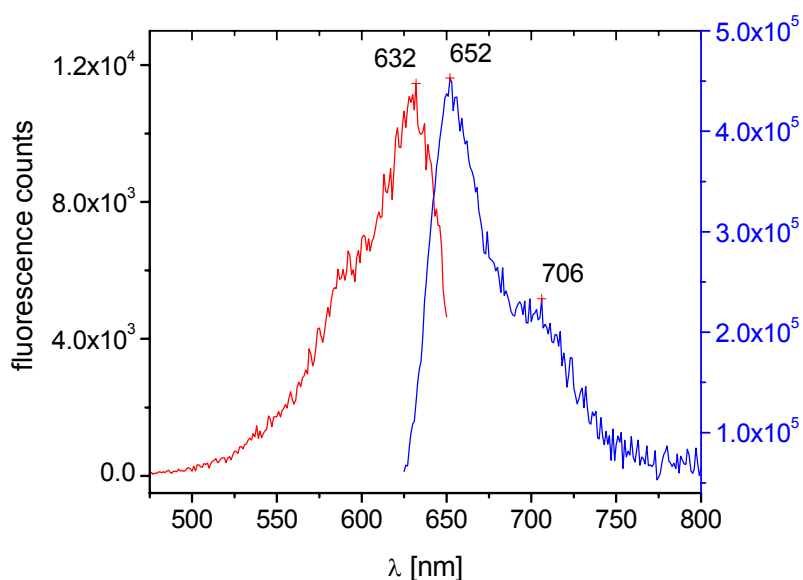


**Figure 69:** Excitation and emission spectra of TO-PRO-3 in water ( $4 \cdot 10^{-5}$  M).

**Excitation spectrum:  $\lambda_{\text{det}} = 655\text{nm}$ ; emission spectrum:  $\lambda_{\text{abs}} = 620\text{nm}$ .**

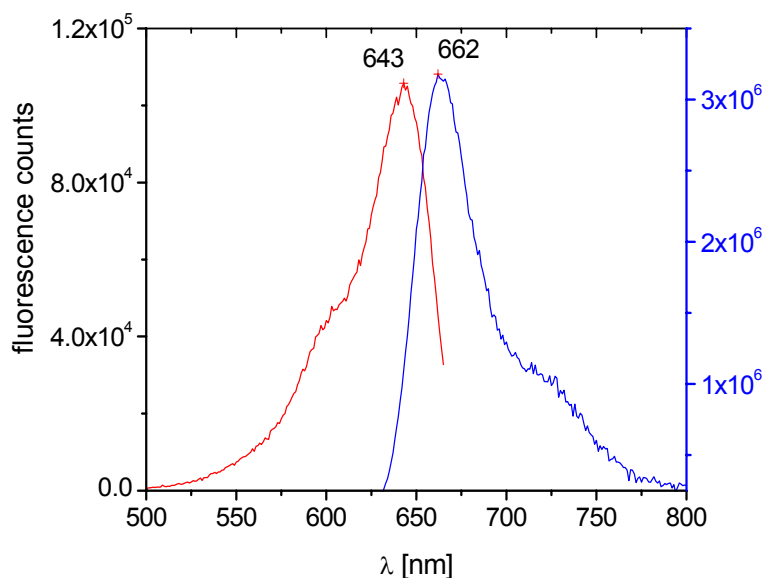


**Figure 70:** Excitation and emission spectra of TO-PRO-3 ( $1.6 \cdot 10^{-6}$  M) in aqueous DNA ( $1 \cdot 10^{-10}$  M).

**Excitation spectrum:  $\lambda_{\text{det}} = 670\text{nm}$ ; emission spectrum:  $\lambda_{\text{abs}} = 620\text{nm}$ .**

## **TO-PRO-3 quantum yield enhancement**

Generally, the fluorescence quantum yields ( $\Phi_{\text{Fl}}$ ) of cyanine dyes are enhanced by a factor of ~200-1800 on binding to DNA [183]. Accordingly, free TO-PRO-3<sup>®</sup> shows practically no fluorescence. The literature value for the quantum yield of TO-PRO-3<sup>®</sup> with DNA is 11% [185]. From this, the  $\Phi_{\text{Fl}}$  for free dye and the enhancement factor on intercalation can be calculated. According to eq. 27 and by comparison of the fluorescence emission of the bound dye (cf. Figure 70), with the free TO-PRO-3<sup>®</sup> fluorescence (cf. Figure 69),  $\Phi_{\text{Fl}}$  is 0.06%, which corresponds to a 200fold enhancement on intercalation.

### **4.1.2 Dye photobleaching**

An important problem of these dyes is photo-bleaching and photo-cleavage of the bound DNA. Measurements of bleaching rates of YOYO-1 and DNA have shown that there are two distinct types of binding of YOYO-1 to DNA [186]. At low dye/nucleotide ratios, intercalation is preferred, but above a critical value of ca. 0.2 dyes/nucleotide external binding (i.e. groove binding/ electrostatic binding) of excess dyes occurs. The externally bound dyes bleach faster than the intercalated ones, leading to a bi-exponential decay rate at high dye concentrations [186]. At low dye concentrations the decay rate is lower and mono-exponential. The mechanisms for bleaching are unclear, but probably involve either singlet oxygen ( $^1\text{O}_2$ ) or hydroxyl radicals ( $\cdot\text{OH}$ ) formed via a Fenton reaction.

Photo-cleavage has been examined and occurs especially at high illumination intensities [186]. Free dyes cause negligible cleavage, but both externally bound and intercalated dyes generate single strand breaks [187].

### **Single molecule bleaching rates of TO-PRO-3**

To study the bleaching rates for TO-PRO-3, a new method was developed involving single DNA strands and bundles prepared on a polylysine coated glass surface and imaged using the wide-field setup with various dye concentrations and illumination powers.

Photobleaching will result in a drop in concentration of the fluorescing dye and thus also a decrease in fluorescence intensity  $I(t)$ . Under constant illumination conditions the photobleaching reaction can be characterised by a first-order rate constant  $k_{bl}$  [141, 188].

eq. 33

$$\frac{dI(t)}{dt} = -k_{bl}I(t) \quad , \quad \tau_{bl} = \frac{1}{k_{bl}}$$

$$I(t) = I(0)\exp^{-k_{bl}t}$$

An experimental prerequisite to measuring the bleaching rates of intercalated TO-PRO-3 with sufficient fluorescent signal is that the dye concentration adsorbed to the DNA should be maximal:  $[dye_{DNA}] = \max$ . Furthermore, to reduce the background signal and dye association/dissociation processes, the free dye concentration must be kept minimal:  $[dye_{sol}] = \min$ .

The fluorescence intensity of the emitting DNA strands can then be monitored by a sequence of images, followed by integration of the counts for a selected image area containing the DNA strand. In this way the bleaching rates for varying laser powers and dye concentrations can be measured. The graph in Figure 71 describes the fluorescence bleaching of a DNA sample with  $5 \cdot 10^{-6}M$  TO-PRO-3. Fitting the data shows that a bi-exponential curve is required to adequately describe the bleaching process.

eq. 34

$$I(t) = I_1 \exp^{-\frac{t}{\tau_1}} + I_2 \exp^{-\frac{t}{\tau_2}}$$

Two fluorescence decay times  $\tau_1$  and  $\tau_2$  are obtained. This is consistent with the literature, which describes two processes responsible for DNA-bound dye bleaching [186]: a fast process, which originates from  $^1O_2$  mediated bleaching of externally bound dyes (e.g. groove binding) and a slower process involving the intercalated dyes and  $OH\cdot$  radicals. Especially for high dye concentrations externally bound dyes may become an increasing factor, but the bleaching processes of these dyes are likely to be complex and less significant for force spectroscopic investigations, so the fast rate is not investigated further.

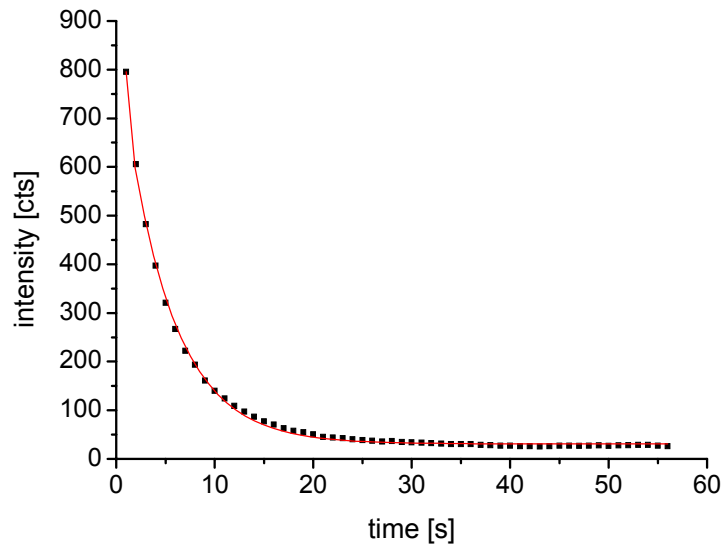


Figure 71: Bleaching curve with bi-exponential decay fit (red);  $[TO-PRO-3] = 5 \cdot 10^{-6} M$ .

### Laser power dependence of the bleaching constants

Assuming an excess of dye and no multi-photon processes, it is expected that the bleaching rate should show a linear dependence on laser power [143].

$$\text{eq. 35} \quad \frac{1}{\tau_{bl}} \propto I_{Laser} \Rightarrow \tau_{bl} = C \frac{1}{I_{Laser}}$$

To determine the proportionality factor  $C$ ,  $\tau_{bl}$  is plotted against  $1/I_{laser}$  for a series of medium laser powers. The graph in Figure 72 shows the plot for dye the concentration  $[dye] = 10^{-5} M$ .

$$\text{eq. 36} \quad \tau_{bl} = C \frac{1}{I_{Laser}} + A$$

For higher illumination intensities the bleaching rates are faster and the bleaching time  $\tau$  is proportional to the reciprocal of the laser power. For a dye concentration of  $[dye] = 10^{-5} \text{ mol/l}$  the slope is  $135 \mu J$ . All dye concentrations display a non-zero intercept  $A$  (e.g.  $\tau_0 = 0.41 \text{ sec}$  for  $10^{-5} \text{ mol/l}$ ). This value corresponds to a remaining non-zero bleaching rate, even for zero laser power. In previous bleaching experiments on single dyes no such underlying bleaching has been reported [143], therefore it probably originates from dye

dissociation into the solution or non-radiative bleaching processes e.g. through radicals in the solution.

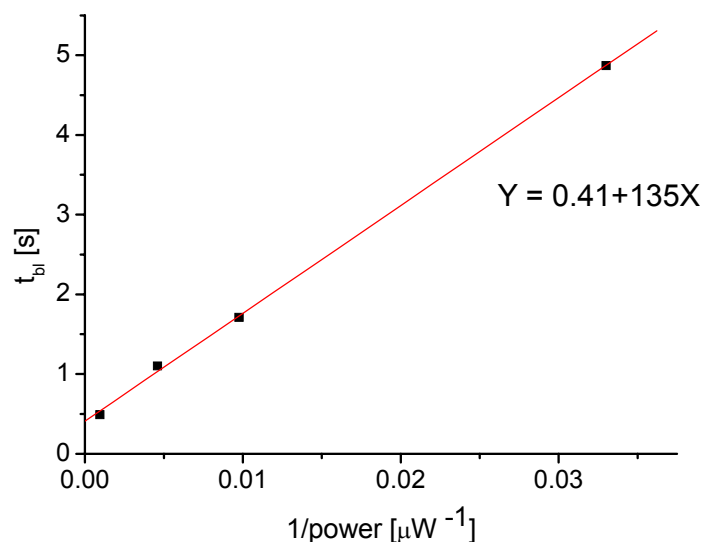
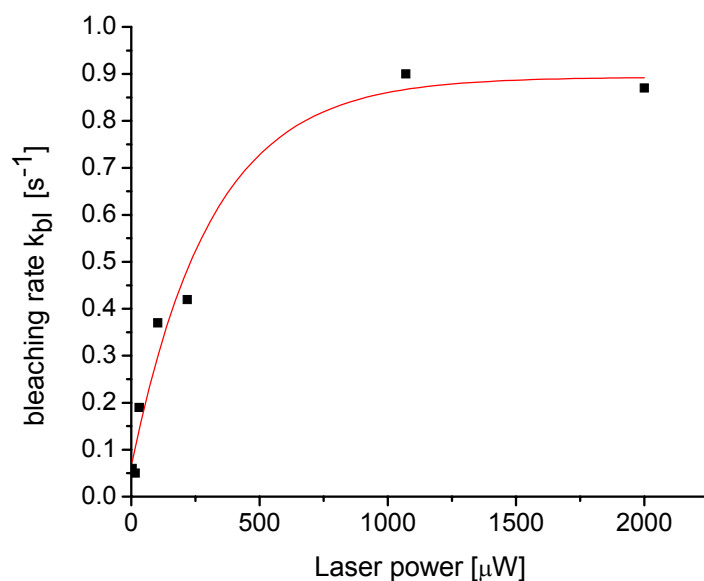


Figure 72: Typical plot of decay times  $\tau_{bl}$  against  $1/I_{laser}$  for  $[\text{dye}] = 10^{-5}\text{M}$ .

The values of  $C$  and  $A$  vary slightly for each series, but are generally independent of the dye concentrations. Therefore, taking also very high and low laser powers into account, a summary of the average bleaching rates is presented in table 10 and plotted in Figure 73.

Laser power $I_{Laser}$ [ $\mu\text{W}$ ]	Laser intensity [ $\text{W cm}^{-2}$ ]	Average bleaching rate $k_{bl}$ [ $\text{s}^{-1}$ ]
2000	636.6	0.87
1070	340.6	0.90
218	69.4	0.42
102.5	32.6	0.37
30	9.6	0.19
15	4.8	0.05
3	1.0	0.06

table 10: Summary of the average bleaching rates for different laser powers



**Figure 73: Average bleaching rates with laser power.**

The data can be fitted to an exponential curve as described in eq. 37.

eq. 37 
$$y = k_0 + A(1 - e^{-x})$$

For high laser powers the bleaching rate eventually saturates at an asymptotic value of  $A = 0.82 \text{sec}^{-1}$ . Contrary to this result, the photobleaching rate was originally assumed to increase linearly with laser power or even non-linearly, as multi-photon processes become more important [141]. However, the observed asymptotic effect is probably due to the replacement of fresh dyes from solution for bleached TO-PRO-3 in the DNA. This eventually levels out the bleaching rate, albeit at a relatively high rate.

### **Conclusions of the bleaching experiments**

Importantly, bleaching is dramatically reduced for low laser powers. Especially for long exposure times, fluorescence recovery processes and dye exchange with the solution become significant factors. Experience shows that low laser intensities of ca.  $1\text{-}10 \text{ W/cm}^2$  give the best results, especially in combination with relatively high dye concentrations.

For these high dye concentrations, dye replacement balances bleaching and a significant reduction in fluorescence signal can be avoided altogether, thus enabling prolonged high contrast imaging of single DNA strands. A suitable dye concentration with the best signal to background ratios is  $1 \cdot 10^{-6} \text{M}$  to  $5 \cdot 10^{-6} \text{M}$  TO-PRO-3. For an estimated DNA concentration on the surface of ca.  $8 \cdot 10^{-12} \text{mol/l}$  [ $c(\text{bp}) = 3.9 \cdot 10^{-7} \text{mol/l}$ ], this corresponds to  $\sim 2.5\text{-}12$  dye molecules per base pair, which is in 10-50 fold excess of the 0.2-0.3 dyes per base pair theoretically needed for complete intercalation [171, 184]. The downturn of using high dye concentrations is an increased fluorescence background of free dyes in solution, reducing image contrast, but possibly also an increase in the number of unspecifically adsorbed dyes on the DNA perimeter.

### 4.1.3 Anti-bleaching agents

#### Oxygen

Various approaches have been taken to reduce photobleaching and thus increase signal to background ratios in fluorescence images. The role of oxygen has been investigated extensively [141]. Although triplet oxygen  $^3\text{O}_2$  initially quenches the excited triplet states of organic dye molecules, thus increasing the number of photocycles available, the by-product of this reaction is singlet oxygen  $^1\text{O}_2$ . The latter readily reacts with organic dye double bonds, thus destroying dye photo-activity. Therefore it is prudent to choose dyes with low triplet quantum yields, which rarely convert to a triplet state [141]. One approach is to deoxygenate solutions by the use of catalase or extensive bubbling with nitrogen or argon gas. Although these procedures have been successful in some cases, the accumulation of dyes in their triplet states often balances the reduced photo-destructive effect experienced in the absence of oxygen.

To investigate the effect of oxygen, solutions were bubbled with argon or nitrogen gas prior to use. In addition, a hood for the apparatus was constructed, which kept the sample under a constant argon stream. However, only a slight improvement in fluorescence contrast could be observed in the images and so this approach was not pursued further.

## Stabilisers

Considerable effort has been made to find effective anti-bleaching agents [141]. These stabilisers are often either singlet oxygen quenchers or radical scavengers, such as  $\beta$ -mercaptoethanol. However, these additives work best in high concentrations, for which they often quench dye fluorescence. In addition, high levels of anti-oxidising agents or radical scavengers could have a distorting influence on the native properties of DNA. A case by case choice of stabiliser concentration must be made.

Another important factor is DNA photocleavage. The same processes by which dyes are bleached are also responsible for nicking of the DNA strand. When two single strand (ss) nicks occur in close proximity (ca. 15bp apart), an irreversible double strands (ds) break can result [181, 186]. By the same logic that prevents dye bleaching, photodamage to the DNA can be avoided with stabilising agents. The influence of anti-bleaching agents on DNA damage has been reported on other occasions [186].

For the final optimum conditions used in single DNA strand imaging i.e. low laser power and a high dye concentration, no significant deterioration of the DNA was observed. However, low salt concentrations led to a very rapid fragmentation of the double helix.

## Antifade<sup>®</sup>

Antifade<sup>®</sup> and Slowfade<sup>®</sup> are Molecular Probes<sup>®</sup> products that inhibit bleaching by free radical scavenging [185]. In principle, Antifade works by reducing the accumulation of reactive oxygen species. A comparison of the bleaching curves for TO-PRO-3 with and without antifade is shown in Figure 74. For a TO-PRO-3 concentration of  $5 \cdot 10^{-6}$  M and a laser power of  $I_{laser} = 69 \text{ W/cm}^2$ , the bleaching time increased from  $\tau_1 = 2.46$  to  $\tau_1 = 7.02$ . Especially for high dye concentrations, a decrease in the bleaching rate was observed. Possibly antifade also induces a slight fluorescence quenching effect.

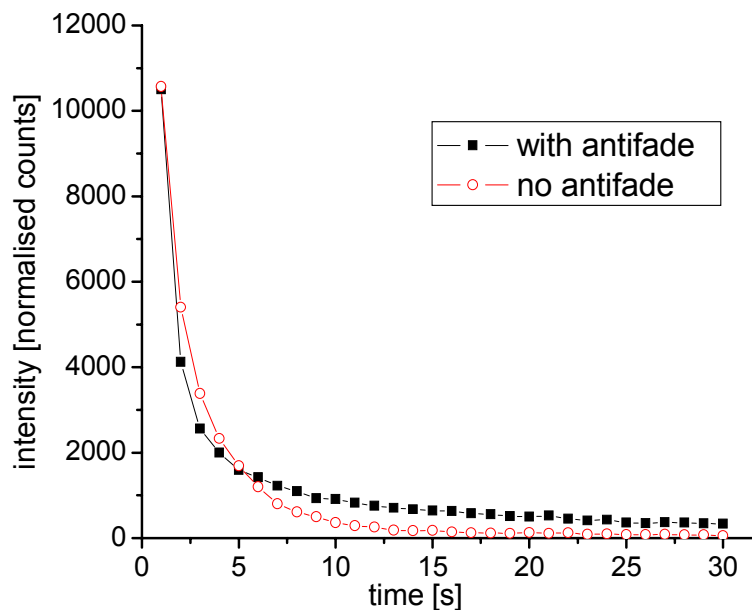


**Figure 74: Comparison of the bleaching rates for [TO-PRO-3] =  $5 \cdot 10^{-6}$  mol/l with antifade. For clarity the data points have been connected.**

Although the bleaching rate could be decreased by the use of antifade, overall bleaching remained. In addition, the application of Antifade was cumbersome and its high viscosity probably had a significant influence on the native DNA-dye environment. Therefore antifade was deemed inadequate for the TO-PRO-3/DNA system.

### **Slowfade<sup>®</sup>**

In contrast to Antifade<sup>®</sup>, the Slowfade<sup>®</sup> kit can be applied as a solution without prior mixing. To compare the effect of Slowfade on dye fluorescence, the bleaching rate was first measured at high laser intensity  $I_{laser} = 637 \text{ W/cm}^2$  and then left to recover for 30 min. After the recovery time, 20  $\mu\text{l}$  of the Slowfade solution was added to the sample and the bleaching rate was re-measured. The results are presented in Figure 75.

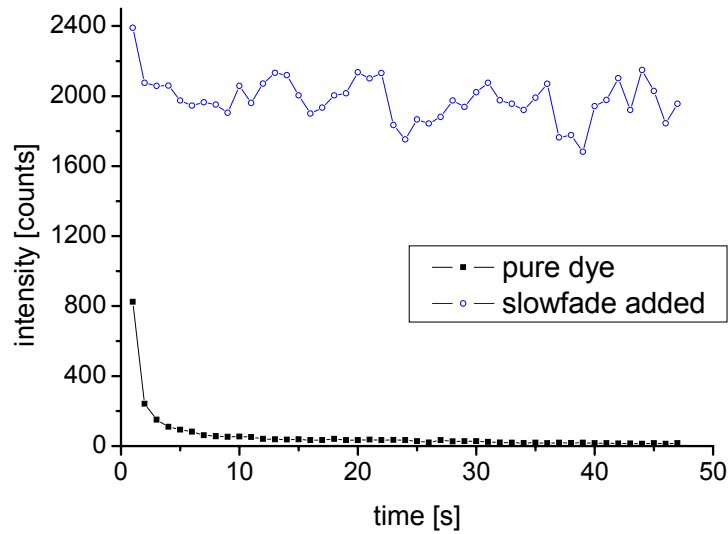


**Figure 75: Bleaching rates with slowfade<sup>®</sup> at 637 W/cm<sup>2</sup> and 5\*10<sup>-6</sup> mol/l TO-PRO-3. For clarity the data points have been connected.**

In comparison to the normal bleaching curve shown in black, the samples with Slowfade<sup>®</sup> (blue) rapidly reach an equilibrium fluorescence rate for which bleaching is negligible. However, these experiments were conducted with very high Slowfade mixtures of ~20%. A lower concentration of Slowfade seems prudent. Empirical experience led to the use of a 5\*10<sup>-6</sup>M TO-PRO-3<sup>®</sup> solution in TRIS/EDTA with only 1% slowfade<sup>®</sup>. It constitutes a compromise between a slightly improved fluorescence performance and a low disruption of the native DNA environment.

#### 4.1.4 The TO-PRO-3/DNA rate kinetics

To describe the association and dissociation rates, a model of the DNA is proposed, for which there are a fixed number of vacant positions between the rungs of the double helix, into which free TO-PRO-3 can intercalate. The number of base pairs per site, i.e. the base pair occlusion, is ca. 2-3 bp for each dye molecule slot [184]. The value is generally reduced for low salt concentrations, but increases to about 5bp/dye for 300mM salt, probably due to charge shielding effects.

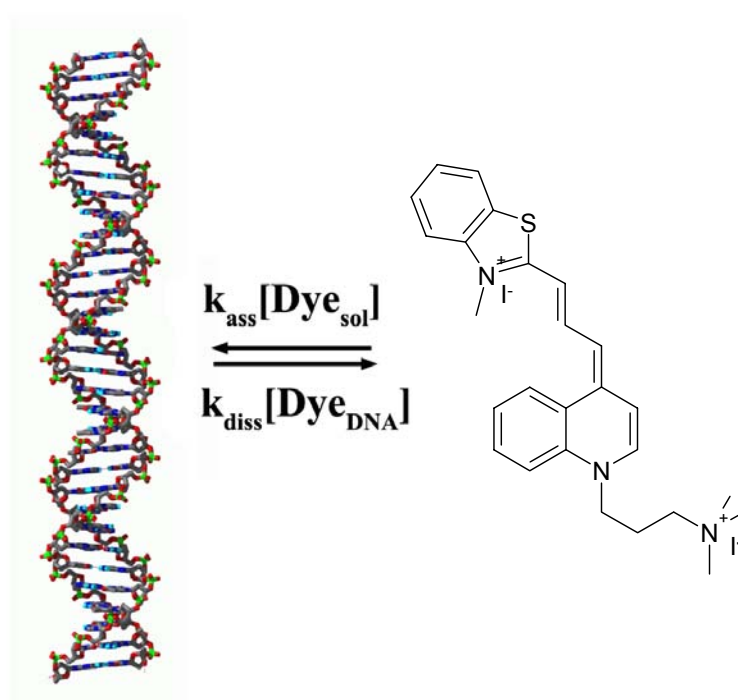


Figure 76: The DNA/TO-PRO-3 system rate model

After dye addition, the system will equilibrate according to the rate constants and starting concentrations. If the rates of association  $k_{\text{Ass}}$  and dissociation  $k_{\text{diss}}$  can be measured, it would be possible to calculate the binding constant  $K_{\text{bind}}$  of TO-PRO-3 to DNA.

eq. 38

$$K_{\text{bind}} = \frac{k_{\text{Ass}}}{k_{\text{diss}}}$$

By measuring the dye fluorescence from single DNA strands in a series of images, the association, and dissociation rates can be determined.

### The association rate $k_{Ass}$

The speed of dye association to the DNA can be described by the following rate equation:

$$\text{eq. 39} \quad \frac{d[I_{Fl}]}{dt} \approx \frac{d[\text{Dye}_{DNA}]}{dt} = k_{Ass} [\text{Dye}_{sol}] \left( [\text{DNA}_{bp}] - [\text{Dye}_{DNA}] \right)$$

Since the TO-PRO-3 fluorescence is greatly enhanced on intercalation, the fluorescence intensity  $I_{fl}$  is directly proportional to the intercalated dye concentration  $[\text{Dye}_{DNA}]$ . Therefore, the association process can be described by a second order rate equation. The change in  $[\text{Dye}_{DNA}]$  is related to the association rate  $k_{Ass}$ , the dye concentration in solution  $[\text{Dye}_{sol}]$  and the number of free intercalation sites on the DNA. The latter is given by the total number of sites minus the number of occupied sites  $[\text{DNA}_{bp}] - [\text{Dye}_{DNA}]$ .

Further, taking into account that the concentration of dye in solution is not reduced significantly by adsorption to the DNA:

$$\text{eq. 40} \quad \frac{d[\text{Dye}_{sol}]}{dt} \cong 0$$

Thus  $[\text{Dye}_{sol}] = \text{constant}$  and the rate equation can be simplified to a pseudo first order reaction rate, with the new association rate constant  $k'_{Ass}$ .

$$\text{eq. 41} \quad k'_{Ass} = k_{Ass} [\text{Dye}_{sol}]$$

$$\text{eq. 42} \quad \frac{d[\text{Dye}_{DNA}]}{dt} = k'_{Ass} \left( [\text{DNA}_{bp}] - [\text{Dye}_{DNA}] \right)$$

To determine the association rate  $k'_{Ass}$ , any dye-DNA dissociation should be avoided. The best way to do this is to begin the experiment with no dye  $[\text{Dye}_{DNA}] = 0$  and start the measurement immediately after dye addition. Under these premises any change in fluorescence due to dissociation is negligible, as long as the concentration of  $[\text{Dye}_{DNA}]$  is low. Eventually sufficient dye will

have intercalated and equilibrium between the association and the increased dissociation of TO-PRO-3 will be reached. In addition, to circumvent bleaching of the sample, relatively low irradiation intensities are used for which  $k_{bl}$  is marginal.

Based on the proposed model the following fluorescence intensity function can be derived. Reformulating eq. 42 and integrating gives:

$$\text{eq. 43} \quad [\text{Dye}_{\text{DNA}}] = [\text{Dye}_{\text{bp}}] - C' e^{-k'_{\text{Ass}} t}$$

At time ( $t=0$ ) the bound dye concentration is negligible. Inserting for  $[\text{Dye}_{\text{DNA}}] = 0$ , provides the constant  $C'$ , which corresponds to the  $[\text{DNA}_{\text{bp}}]$  - the total number of sites.

$$[\text{Dye}_{\text{DNA}}(t=0)] = 0 \Rightarrow C' = [\text{DNA}_{\text{bp}}] = \text{const.}$$

$$\text{eq. 44} \quad \Rightarrow [\text{Dye}_{\text{DNA}}] = [\text{DNA}_{\text{bp}}](1 - e^{-k'_{\text{Ass}} t})$$

Therefore, the fluorescence eventually reaches an asymptotic value  $[\text{DNA}_{\text{bp}}]$ , which is proportional to the total number of DNA slots available for intercalation.

The results of the fluorescence measurements for the highest dye concentration used  $[\text{Dye}] = 10^{-5}$  M (strong fluorescence signal) and the lowest laser intensity of  $1.0 \text{ W/cm}^2$  (low bleaching) are shown in Figure 77. As with the bleaching experiments, the DNA samples were prepared on polylysine coated glass coverslips and focussed according to the laser reflection image Figure 44. A camera image series was then started just prior to addition of the dyes droplet, so that the increase in fluorescence could be monitored as the dye intercalated into the DNA.

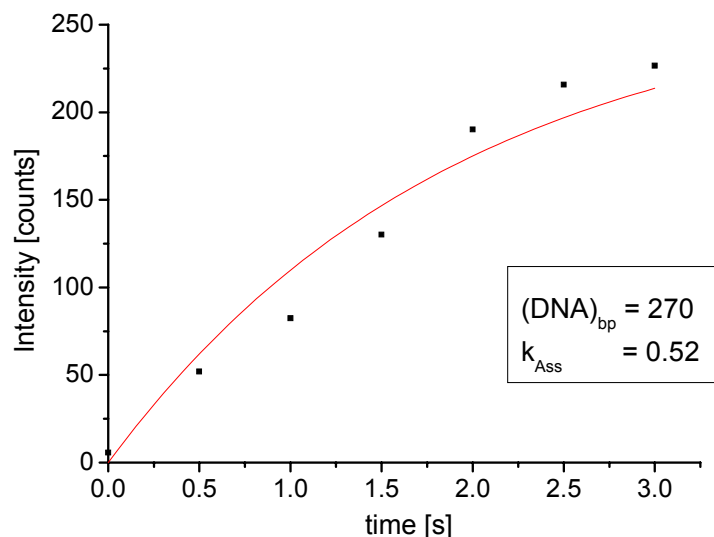


**Figure 77: Association experiment for [TO-PRO-3] =  $10^{-5}$ M and  $1.0 \text{ W/cm}^2$ ; camera exposure time 500ms;**

According to Figure 77 the association rate is  $k'_{Ass} = 0.5 \text{ s}^{-1}$ . Evidently the adsorption of TO-PRO-3 is a relatively rapid process. For a dye concentration of [Dye] =  $10^{-5}$  M (cf. eq. 41) the final value for the association rate is:

$$k_{Ass} = 5 \cdot 10^4 \text{ s}^{-1} \text{ mol}^{-1} \text{ L}$$

These results correspond to previous literature work, which infers similarly large association rates for TO-PRO-1 from bulk absorption spectra [184]. TO-PRO-1 is the homologue of TO-PRO-3 with only one instead of three carbon atoms in the conjugated cyanine chain bridge (cf. Figure 76).

### **The dissociation rate $k_{diss}$**

To determine  $k_{diss}$ , a method is needed to measure the dissociation speed of TO-PRO-3 from the DNA. Luckily the previous association experiments show that  $k_{Ass}$  is very fast and free binding sites are instantaneously filled with fresh dye from solution. The rate determining step for dye exchange is therefore given by the dissociation rate  $k_{diss}$ .

By intense irradiation ( $637 \text{ W/cm}^2$ ) of an equilibrated, dye saturated system the intercalated dyes can be bleached so that any fluorescence signal

measured thereafter must originate from fresh dye that has just entered from solution. The rate of fluorescence recovery after bleaching will therefore correspond to the dissociation rate of the dye. Again bleaching during the recovery experiment will falsify the results, so low laser powers are used to exclude bleaching in the time frame of the experiment. The rate equation for the dye dissociation process is given by:

eq. 45 
$$\frac{d[\text{Dye}_{\text{DNA}}]}{dt} = -k_{\text{diss}}[\text{Dye}_{\text{DNA}}]$$

In analogy to the association experiment, a limiting maximum fluorescence signal is expected, which will be reached when all of the bleached dye molecules are exchanged for fresh TO-PRO-3. Consequently the same model as described in the previous chapter can be applied for the fluorescence recovery experiment.

Various dye concentrations were examined and fitted to provide the parameters for  $[\text{Dye}_{\text{DNA}}]$  and  $k_{\text{diss}}$ .

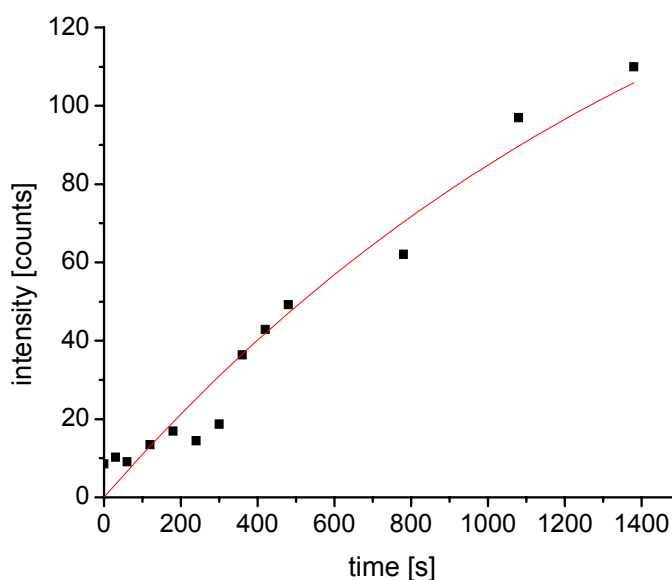


**Figure 78: Fluorescence recovery experiment with  $[\text{dye}] = 10^{-7}\text{M}$  and;  $(1.0 \text{ W/cm}^2)$**

The measured values for  $k_{\text{diss}}$  varied by about a factor of ten depending on the dye concentration in solution, but with no clear trend (e.g.  $6 \cdot 10^{-4}\text{s}^{-1}$  for  $[\text{dye}] = 10^{-7}\text{M}$ ). The individual DNA environment is probably responsible for

the distribution of dissociation rates. Loosely bound groove binders and electrostatically attached dyes could increase the dissociation rate, especially at high dye concentrations, for which these binding modes are favoured. However, the dye concentration in solution should not influence the dissociation rate. The mean value of the measured rates is:

$$k_{diss} = 3.2 \cdot 10^{-3} (\pm 4.3 \cdot 10^{-3}) \text{ s}^{-1}$$

### Summary of the TO-PRO-3 rate kinetics

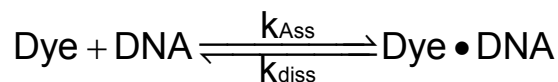
The results of the dye kinetics experiments are summarised in table 11.

$k_{bl}$	0,05 to 0,9 $\text{s}^{-1}$ ( $I_{Laser} = 1$ to 637 $\text{W}/\text{cm}^2$ )
$k_{Ass}$	$5 \cdot 10^4 \text{ s}^{-1} \text{ mol}^{-1}$ ( $[\text{Dye}_{sol}] = 10^{-5} \text{ M}$ )
$k_{diss}$	$3.2 \cdot 10^{-3} \text{ s}^{-1}$

table 11: Summary of the rate constants

The association rate  $k_{Ass}$  is the fastest process, followed by the bleaching rate  $k_{bl}$  and finally  $k_{diss}$ . On a time scale of seconds, the characteristic dye association time is therefore  $\tau_{Ass} \sim 2 \text{ sec}$  ( $k'_{Ass} \sim 0.5 \text{ sec}$  for  $[\text{Dye}_{sol}] = 10^{-5} \text{ M}$ ), bleaching occurs at  $\tau_{bl} \sim 15 \text{ sec}$  (depending on the laser power), and finally the dissociation time from the DNA is  $\tau_{diss} \sim 300 \text{ sec}$  (5 min).

Eventually the fluorescence for the whole system will equilibrate, as summarised in eq. 46. For a certain DNA and dye concentration and a given laser power the system will be in balance. The aim is to reach this equilibrium with high fluorescence intensity and image contrast, but low photobleaching.



$$\frac{d[I]}{dt} \approx k'_{Ass} ([\text{DNA}_{bp}] - [\text{Dye}_{DNA}]) - k_{diss} [\text{Dye}_{DNA}] - [k_{bl} [\text{Dye}_{DNA}]]_{hv} = 0$$

eq. 46: The complete fluorescence rate equation

#### 4.1.5 The binding constant of TO-PRO-3 to DNA

Insertion of the established values for  $k_{Ass}$  and  $k_{diss}$  into eq. 38 affords the binding constant of TO-PRO-3 to DNA:

$$K_b = \frac{k_{Ass}}{k_{diss}} = \frac{5 \cdot 10^4 \text{ s}^{-1} \text{ mol}^{-1}}{3.2 \cdot 10^{-3} \text{ s}^{-1}}$$

$$K_b = 1.5 \cdot 10^7 \text{ mol}^{-1}$$

##### Equation 1: Binding constant of TO-PRO-3 to DNA

The binding constants of the structurally similar (cf. Figure 23) monomeric dyes TO-PRO-1 ( $3.2 \cdot 10^6 \text{ M}^{-1}$ ) and YO-PRO-1 ( $7.9 \cdot 10^5 \text{ M}^{-1}$ ) have been estimated by relative absorption spectra of the free and bound dye [184]. They are dependent on the salt concentration in solution [189]. Probably the sodium ions compete with the dye for free DNA binding sites on the negatively charged DNA. At low salt concentrations (20mM NaCl) the value for TO-PRO-1 increases to  $K_b = 5 \cdot 10^7 \text{ M}^{-1}$ .

The bichromophoric intercalators such as YOYO-1 or TOTO-1 are essentially composed of two linked cyanine dye fragments. They have higher binding constants such as  $K_b$  (YOYO-1) =  $6.0 \cdot 10^8 \text{ M}^{-1}$  and  $K_b$  (TOTO-1) =  $1.0 \cdot 10^9 \text{ M}^{-1}$  [75, 183], which probably reflects their ability for co-operative double intercalation into DNA [190]. By comparison the binding constant of the strong biotin/streptavidin complex is:  $K_b = 10^{15} \text{ M}^{-1}$ .

Thus, the binding affinity of the monomeric dye TO-PRO-3 to DNA can be measured by a new single molecule method. With  $K_b = 1.5 \cdot 10^7 \text{ M}^{-1}$  the binding strength for TO-PRO-3 is somewhat weaker than that of the bichromophoric dye TOTO, but still stronger than for the shorter homologue TO-PRO-1.

#### 4.1.6 Salt dependence

The effect of ionic strength on fluorescence imaging of DNA has been investigated previously [173, 184]. A reduction in binding affinity at higher ionic strengths leads to a lower overall fluorescence brightness of the DNA. Generally the binding constants of cyanine dyes decrease with increasing ionic strength, reflecting the electrostatic interactions between the negatively charged DNA backbone and the positively charged dyes. This argument holds true for all kinds of binding modes, but is particularly significant for groove binders and unspecifically adsorbing dyes, which both rely heavily on electrostatic attraction rather than intercalation. In fact, high salt concentrations favour intercalation over electrostatic binding [184].

Furthermore, low salt concentrations reduce DNA stability and lead to denaturation. At the same time the DNA persistence length is increased, with the negative surface charges no longer balanced by counter ions from solution [191]. Consequently, the DNA stretches out to avoid electrostatic repulsion in the chain. On the other hand, high salt concentrations can induce DNA collapse and agglomeration [192]. A high salt concentration may also reduce electrostatic binding of DNA to surfaces, such as polylysine, by attenuating the negatively charged DNA phosphate groups. Therefore, there are strong arguments for maintaining the physiological salt concentration of 150mM Na<sup>+</sup> for the DNA experiments, although this entails a slightly reduced fluorescence signal.

To confirm this assumption, DNA imaging experiments were conducted with low salt concentrations (0.025mM NaCl). In these cases a rapid fragmentation of the DNA was observed (c.f. arrows Figure 79), similar to the results presented by Bustamante et al. for high illumination powers [75].

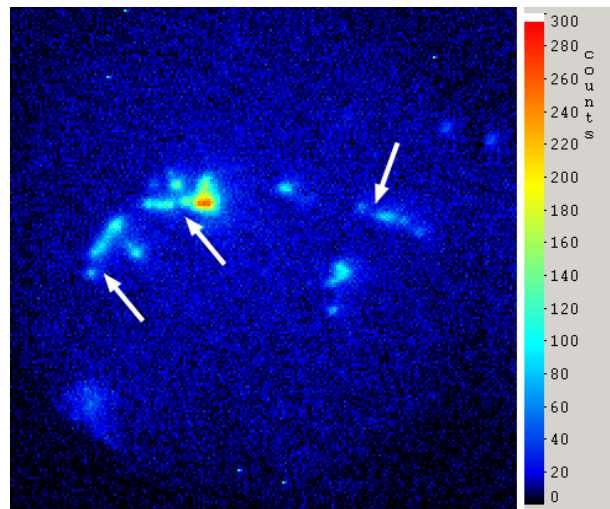


**Figure 79: Rapid DNA strand fragmentation in 0.025mM NaCl; image size 41 $\mu$ m<sup>2</sup> on polylysine coated glass; illumination intensity 2.4W/cm<sup>2</sup>.**

#### **4.1.7 Conclusion of the imaging experiments**

Through a new method the bleaching, association and dissociation kinetics of the fluorescent dye TO-PRO-3 were measured on single DNA molecules. Essential to the combined AFM experiments are long observation times with low bleaching and also minimum photodamage, which could deteriorate the mechanical properties of the DNA. In the light of these requirements, the consequences for the single molecule imaging experiments are the following:

- A 200 fold quantum yield enhancement on intercalation is sufficient for imaging DNA against the background of free dye in solution.
- Low laser intensities of ca. 1-10 W/cm<sup>2</sup> significantly reduce the bleaching rate.
- This, in combination with relatively high dye concentrations of 1\*10<sup>-6</sup>M to 5\*10<sup>-6</sup>M, provides sufficient fluorescence brightness for imaging single DNA strands with negligible bleaching.
- Addition of 1% Slowfade<sup>®</sup> reduces photobleaching. Single DNA strands can be imaged for minutes to hours without significant bleaching.
- The original TRIS/EDTA solution (salt: 150mM NaCl, 10mM Tris, 1mM EDTA, pH8) provides the best DNA stability and adhesion to polylysine, with acceptable losses in dye binding and fluorescence.

## **4.2 Imaging of single molecule DNA strands**

Before it is possible to manipulate single DNA molecules using an AFM tip with real-time optical detection, good fluorescence images are required. Incorporating the knowledge gained from the single molecule photophysical experiments, various surfaces and preparation protocols were tested for imaging elongated single DNA strands.

### **Previous work on imaging DNA**

Scanning AFM microscopy is a useful tool for obtaining high resolution DNA images - a field which was pioneered by Hansma [6] and Lyubchenko in 1993 [5, 193]. Further results describe DNA triplex formation [194], ethidium bromide intercalation induced changes in DNA structure [195], increased DNA length on binding on drugs [172], and proteins [196], contour length analysis of DNA [7], and also AFM images of DNA on gold surfaces [197, 198].

However, some biological reactions, such as DNA transcription by RNA polymerase, are too quick even for fast scanning AFMs with small cantilevers and 2s/image frame [199]. In addition, binding biomolecules tightly to flat surfaces, as required for good AFM imaging, may interfere with their biological activity. These difficulties may be circumvented by real-time optical imaging of DNA. Furthermore, force spectroscopy pulls molecules vertically away from the bound surface, thus providing a more natural biological environment for studying e.g. enzyme kinetics on a single DNA strand.

Early optical imaging experiments used dyes such as DAPI [74, 200] to image DNA filaments. However, new cyanine dyes provide better images of individual DNA chains [75, 76]. Particularly YOYO-1 has been used extensively. From the photophysical experiments, TO-PRO-3 is expected to afford similarly good results. In addition, the dye can be excited in the red region of the visible spectrum at 632nm, for which background fluorescence from impurities is lower.

### **DNA immobilisation**

Although DNA adheres to mica surfaces in the presence of divalent cations, it will not readily stick to bare glass or silicon [125]. Preparing DNA on bare

clean glass leads to DNA globules, which are only weakly absorbed to the surface and are difficult to straighten out – an important prerequisite to identifying and imaging single DNA strands. Therefore, surface treatment is required to increase the adhesiveness of the substrate for DNA. In principle, two approaches can be taken. One is to exploit the hydrophobic nature of DNA, especially of the terminal sticky-ends. This was achieved on silanised surfaces. The other is to bind the DNA by electrostatic interaction of a positively charged surface with the negatively charged DNA phosphate backbone. To this end, coverslips were coated with polylysine. At pH = 8 the ammonium function on polylysine is positively charged. Therefore, a surface covered with this polypeptide (in our case with a charge density of ca. 23 000 moieties/ $\mu\text{m}^2$ ) will be highly attractive for the whole DNA chain.

#### 4.2.1 DNA on polylysine surfaces

Three experimental parameters determine the outcome of DNA immobilisation on polylysine: the polylysine surface density, the DNA concentration and the sample preparation method (DNA straightening technique).

Firstly, the polylysine (PL) concentration is the most critical factor for good immobilisation and DNA straightening results. The PL concentrations were varied between 1  $\mu\text{g}/\text{ml}$  and 2000  $\mu\text{g}/\text{ml}$  to determine the optimum density. In a 5  $\mu\text{l}$  drop of polylysine (MW 50 000  $\approx$  100nm length) spread out over two coverslips (2\*24\*60mm) (cf. Appendix 6: DNA straightening procedures) the corresponding surface coverage is between 21 and 42 000 strands/ $\mu\text{m}^2$ .

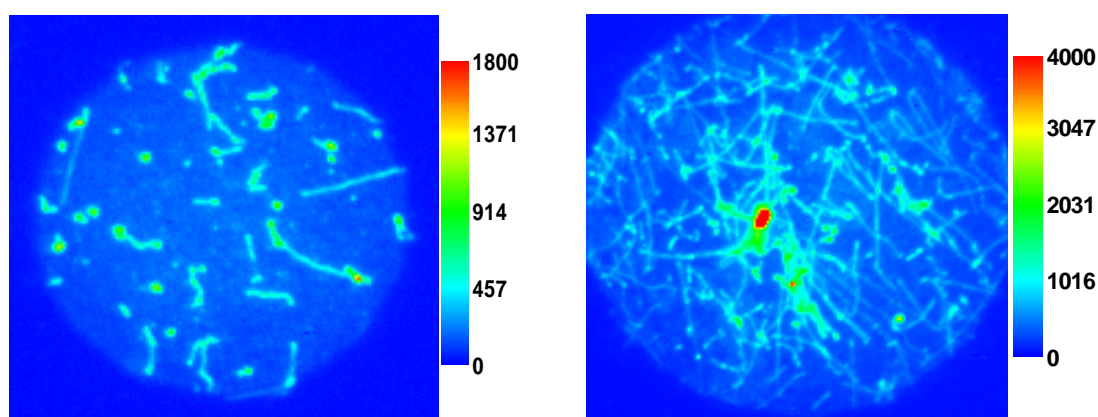
Polylysine conc. [ $\mu\text{g}/\text{ml}$ ]	Polylysine surface density [PL strands/ $\mu\text{m}^2$ ]	No. of lysine groups/ $\mu\text{m}^2$ (M=227g/mol)
1	21	4600
5	105	23 000
12.5	262	57 500
2000	42 000	$9.2 \cdot 10^6$

table 12: Polylysine strand density

According to the literature, the optimum polylysine (MW = 350 000) surface density for stretching DNA is between  $\sim 50$  strands/ $\mu\text{m}^2$  [127] to  $\sim 200$  strands/ $\mu\text{m}^2$  [128]. This corresponds to 350 strands/ $\mu\text{m}^2$  and 1400 strands/ $\mu\text{m}^2$  in our experiments (MW = 50 000).

We found that the best results are achieved for the 5 - 12.5  $\mu\text{g}/\text{ml}$  PL solutions, corresponding to a strand density of ca. 100 - 300 strands/ $\mu\text{m}^2$ . For lower concentrations the DNA attachment is poor. Higher values lead to dense DNA coverage, but also an increased agglomeration of the DNA.

Secondly, the effect of a tenfold increased DNA concentration can be seen in Figure 80. Preparing either a  $3 \cdot 10^{-11}\text{M}$  or a  $3 \cdot 10^{-10}\text{M}$  DNA mixture with antifade on polylysine and applying the pressure stretching method afforded the following images:



**Figure 80: Fluorescence images of a dilute  $3 \cdot 10^{-11}\text{M}$  (left) concentrated  $3 \cdot 10^{-10}\text{M}$  (right)  $\lambda$ -phage DNA solution prepared on a polylysine coated coverslip (image size  $38\mu\text{m}^2$ ).**

### **DNA straightening methods**

The pressure straightening method is based on the hydrodynamic flow procedures, developed by Chu [11] and Bensimon [117]. After terminal attachment, the DNA could be stretched by the hydrodynamic frictional forces experienced in the fluid shear flow between two pressed coverslips (cf. Figure 81). This method has been adapted for polylysine coated glass by Lyon [127] and Taylor [128].

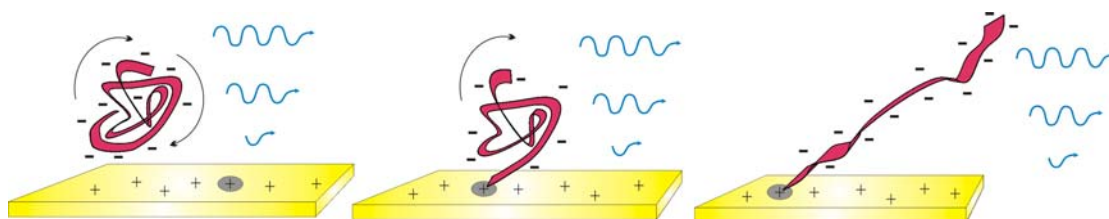


**Figure 81: DNA stretching in a shear flow on a PL coated glass**

Compared to the samples on bare glass, about half of the DNA balls are at least partially stretched out on PL after pressure stretching (cf. Figure 80). A few of the strands can be extended to nearly the full contour length of  $16\mu\text{m}$ . However, the DNA alignment is random, which suggests that the fluid flow experienced by the DNA is possibly turbulent rather than laminar. Nevertheless, a preferred alignment direction was usually observed.

A second method to elongate the DNA is spin coating. The technique was first proposed by Yokota et al. [121], who dispensed a small droplet of DNA solution on a  $\text{MgCl}_2$  soaked mica surface, while spinning the sample at 4000-7000 rpm. By applying a high centrifugal force to the sample, the DNA was thrust outwards and aligned according to the acting forces. The shear force experienced by the DNA was estimated to be  $\sim 10\text{pN}$ , while DNA fragmentation occurred at 8000 rpm.

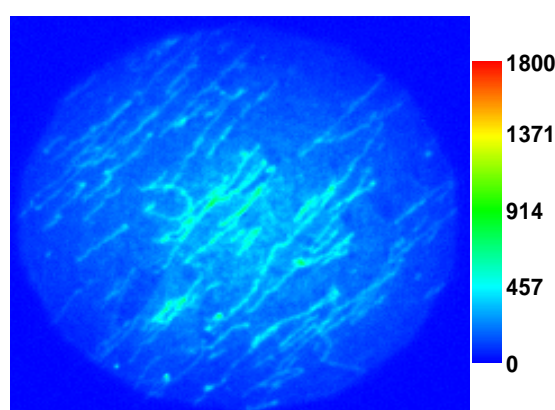


**Figure 82: Dilute  $\lambda$ -phage DNA ( $3 \times 10^{-11}$ ) dispensed on a PL coated glass coverslip and spun at 5000rpm; image size  $41\mu\text{m}^2$ .**

Our experiments show that a spinning rate of ~3000rpm is sufficient for partial elongation of the DNA strands, which attach spontaneously to a polylysine covered surface. For full extension, speeds of at least 5000rpm are necessary (cf. Figure 82). In contrast to the pressure stretching method, the molecules are aligned in the same direction by the centrifugal forces acting on the spinning fluid.

#### **4.2.2 DNA condensation on polylysine surfaces**

Lyon [127] and Taylor [128] describe single elongated DNA strands stretched out on PL coated glass surfaces. Although these results could be confirmed for some cases, DNA imaging on polylysine has turned out to be a complex process involving a number of experimental parameters. These include the dye and DNA concentration, the PL coverage, the pH and salt concentration, the sample preparation method and finally the addition of either antifade or slowfade. Depending on the combination of parameters chosen, different qualitative imaging results are attained. In particular, an unexpected phenomenon is observed: DNA condensation. Instead of forming discrete individual chains, the DNA tends to aggregate on polylysine coated surfaces to generate higher order structures, such as DNA rods or globules. This problem is inherent in all PL coating experiments, but appears to be more severe when Slowfade is used instead of Antifade. Possibly the increased viscosity in the Antifade sample has a favourable influence on the DNA condensation process.

#### **DNA condensation**

DNA is known to collapse and condensate in the presence of polycations or high salt concentrations. Due to negative charges along the chain, DNA is soluble in water and the energy to bend a DNA strand into a circle is ca.  $1k_B T/\mu\text{m}$  [201]. Electrostatic screening of  $\text{Na}^+$  counterions in solution plays an important role in determining DNA flexibility and solubility in water. For a 100mM salt solution the screening length is ca. 1nm [201]. According to Mannig's theory, the cations gradually balance the negatively charged DNA, thus reducing strand repulsion [202, 203]. Finally, at a sufficiently high ion or

salt concentration, the forces holding the DNA apart break down and the coil condenses on itself. If more than one strand is involved many DNA coils may further aggregate to form larger conglomerates.

Polycations can mediate attractive interactions between adjacent helices [204]. It has been suggested that  $Mg^{2+}$  ions enhance the binding of DNA to a mica surface via salt bridges, because both DNA and mica having excess negative charges. This attractive force can be revealed by single molecule force spectroscopy of DNA and leads to a plateau in the force-distance graphs [123]. Furthermore, highly positively charged polyamines ( $>2^+$ ) such as spermidine ( $3^+$ ) [205] or also cobalt hexamine have the capacity to precipitate DNA from solution [192]. The condensating effect of spermidine and  $Co(NH_3)_6$  on single DNA molecules has been examined with optical tweezers force spectroscopy [204]. These reagents provoked DNA condensation at low stretching extensions and markedly increase bending flexibility i.e. decrease chain persistence length. However, keeping DNA in an extended straightened state with optical tweezers appears to prohibit looping and nucleation, which are prerequisites for the condensation process [204]. In nature, DNA condensation occurs during packaging in the cell nucleus. By wrapping the double-helix around positively charged histones, a highly compacted chromatin strand is formed [201, 206].

In principle, DNA condensation can also be achieved with sufficiently high polylysine concentrations of ca. 5:1 lysine to nucleotide ratios [206]. At these mixing ratios circular DNA will coil or fold to form toroids or rod-like structures with a six to eightfold reduced contour length, as has been found in AFM images. However, compared to other polycations, condensation due to polylysine is extremely weak [206, 207]. By mixing  $\lambda$ -Phage DNA with polycations such as polylysine or histones, compact globular or rod-like DNA complexes can be formed and observed by fluorescence imaging. These networks demonstrate the condensating effect of polylysine in solution [208].

However, a thin layer of polylysine should be sufficiently fixed to the coverslip, so as not to condense surface bound DNA. No condensation was mentioned by Lyon et al. when single DNA strands were immobilised on polylysine coated surfaces [127, 128].

Nevertheless, in our experience the DNA frequently aggregated to form higher order multi-strand structures on the polylysine surfaces. This condensation process, from discrete individual chains to globular DNA balls, can be characterised by distinct stages, which differ in their morphology. Although the actual condensation process was not monitored in real-time, images were taken on different samples, which show the DNA with various degrees of condensation. After classifying these stages, a model is proposed to describe the aggregation process.

### The stages of DNA condensation

Single DNA strands are shown in Figure 83. The samples are generally prepared by pressing a ( $3 \times 10^{-10}$  mol/l) DNA solution on a  $5 \mu\text{g/ml}$  PL surface and imaging with  $5 \times 10^{-6}$  M TO-PRO-3 at  $\sim 1.2 \text{ W/cm}^2$  632.8 nm laser light (cf. Appendix 5: DNA imaging protocols).

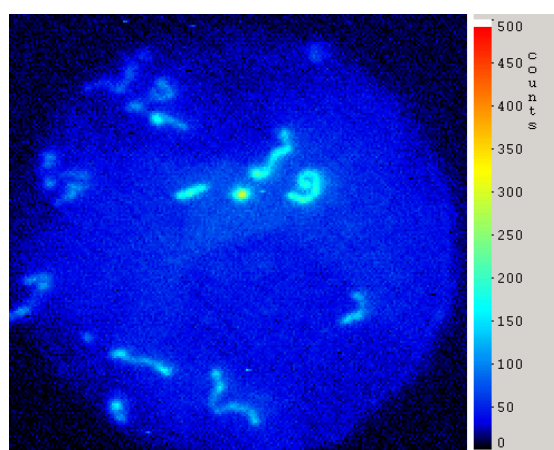


**Figure 83: Single DNA strands on polylysine (image size  $25 \mu\text{m}^2$ ).**

These single chains can group together to form thick DNA fibres, which display strong fluorescence. The resulting DNA bundles are generally broader and longer than the single strands. A good example of a DNA bundle can be seen in Figure 84, with single strands on the right interweaving to form a large DNA bundle on the left.

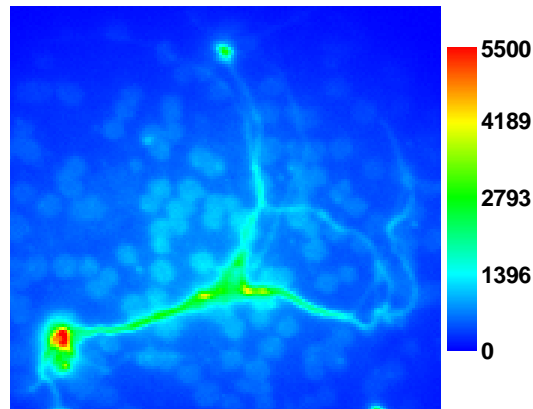


**Figure 84: Fluorescence image of a DNA bundle branching out into many single DNA strands (image size  $29\mu\text{m}^2$ ).**

An even higher degree of condensation is seen in the compacted rigid DNA rods. These structures are well aligned, indicating a high persistence length and rigidity. The rods are brighter than single DNA strands and can be detected in the laser scattering reflection image (cf. Figure 44), which indicates that their width is larger than that of a single DNA helix. The exact nature of the long rod-like structures is not clear, but they are frequently observed in conjunction with DNA globules at the ends. This could be an indication that the rods are generated by partial unwinding of the DNA globules. A thin strand can be observed detaching from a condensed DNA rod on the left. Clearly the thick bright DNA rod has a more condensed constitution than the thin DNA strand adjacent to it. From the fluorescence intensity, the thin strand is probably composed of only one or two single DNA chains.

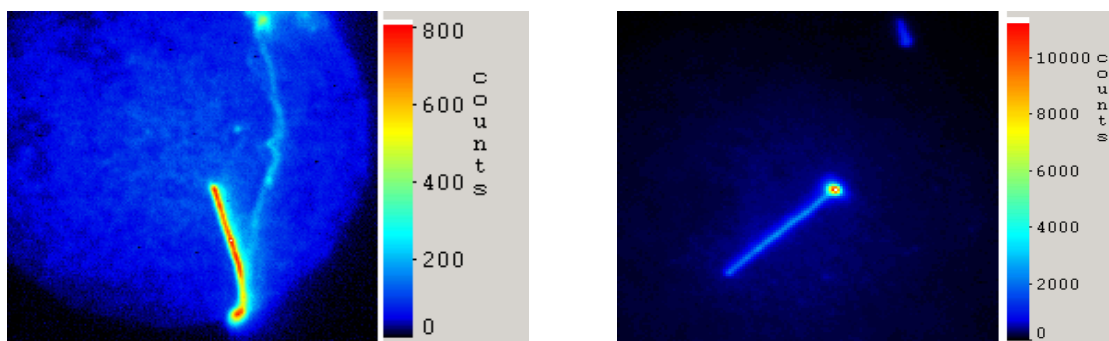


**Figure 85: DNA rods (image size  $26\mu\text{m}^2$  and  $41\mu\text{m}^2$ ).**

Both bundles and rods regularly appeared in conjunction with large DNA globules to form typical “dumbbell-like” structures.

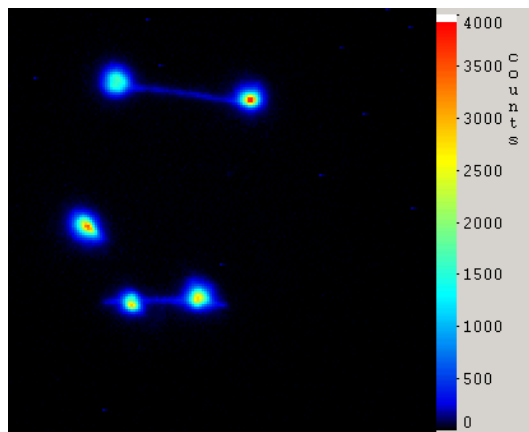


**Figure 86: DNA “dumbbells” (image size  $40\mu\text{m}^2$ ).**

A profile cross section of the rod as indicated in Figure 87 (red line) shows that the DNA has a FWHM diameter of 738nm, which is much wider than the expected diffraction limited length for a single strand of ca. 300nm.

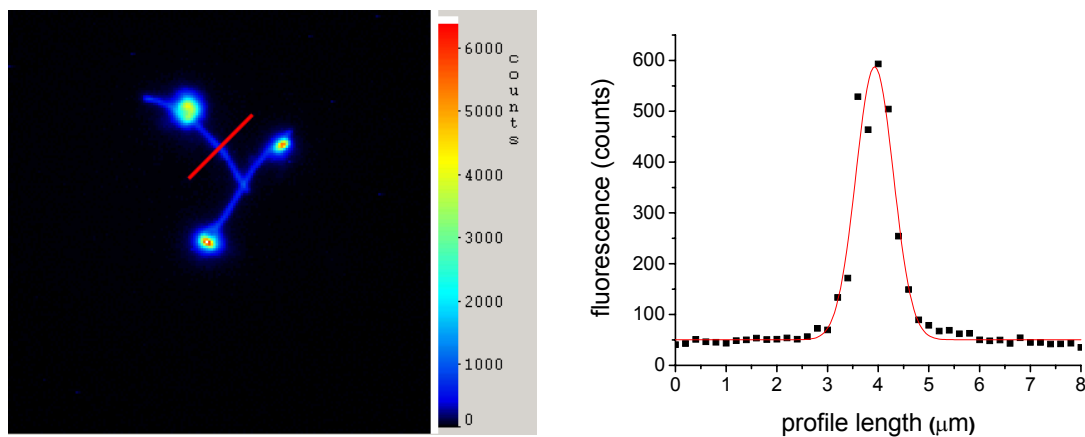


**Figure 87: DNA dumbbells with image cross-section profile ( $34\mu\text{m}^2$ )**

In the final stage of condensation, DNA forms large, globular agglomerates, which display high fluorescence intensities. An image cross section profile (red line) through a series of globules is shown in Figure 88.

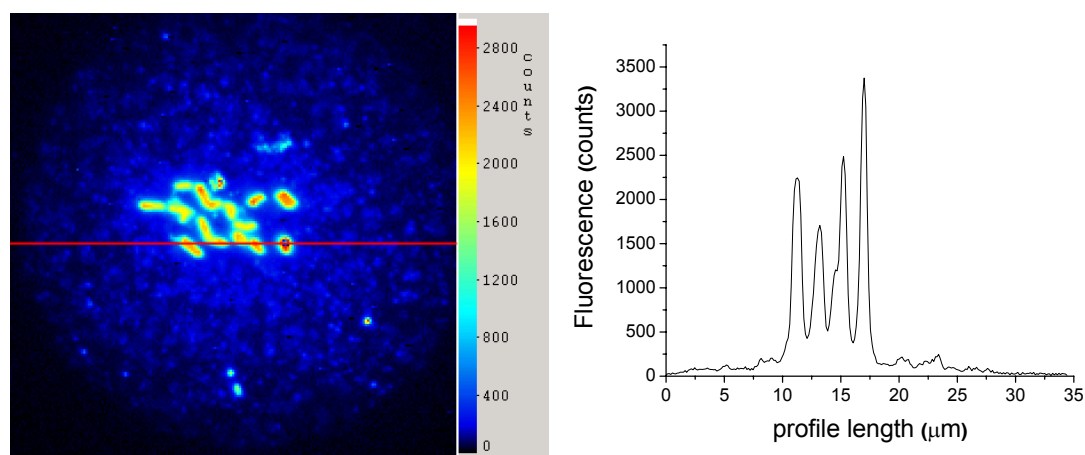


**Figure 88: DNA dumbbells with fluorescence profile (image size  $34\mu\text{m}^2$ ).**

### **The DNA condensation process**

A hierarchical flow chart has been devised that lists the stages of condensation from the most condensed DNA globules down to the isolated individual DNA strand. There is a distinct difference between the dense rod-like structures and the more loosely associated bundles. The AFM pulling experiments with very long pulling lengths suggest that some form of polylysine aggregate involving multiple DNA chains is responsible for these effects, although the exact nature of this interaction is unknown.

The highest order of condensation is achieved in an aggregated DNA globule. Here many condensed DNA fibres are coiled up on each other to form a randomly tangled ball. Given sufficient shear flow, these DNA balls can be unravelled to afford dumbbell-like structures. However, the DNA fibres that have been extracted from the globules are themselves composed of highly condensed strands - termed DNA rods. Similar rod-like DNA structures have been observed by scanning AFM microscopy [133]. Occasionally, a few relatively uncondensed DNA strands aggregate to form bundles. In this case

the chains wrap around each other in a fairly loose manner, quite unlike the dense association achieved in DNA rods. Finally, when low polylysine concentrations are used and combined with DNA straightening procedures, individual DNA strands can be observed.

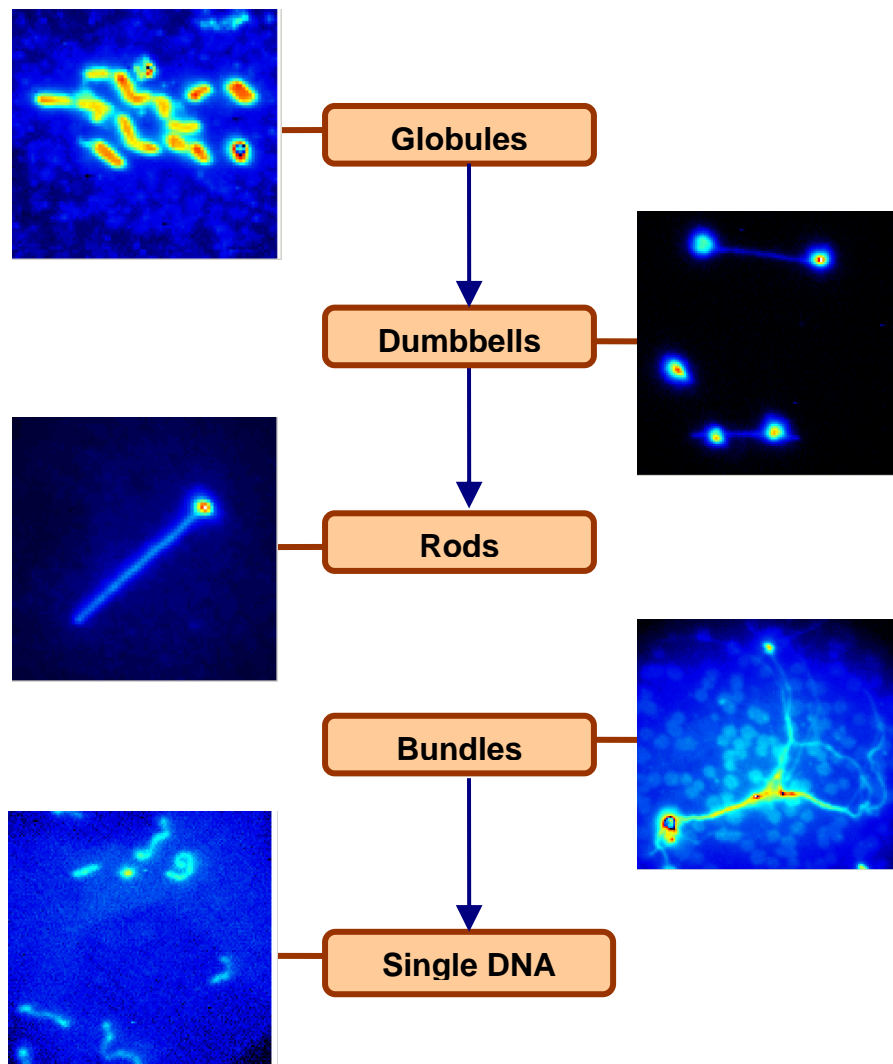
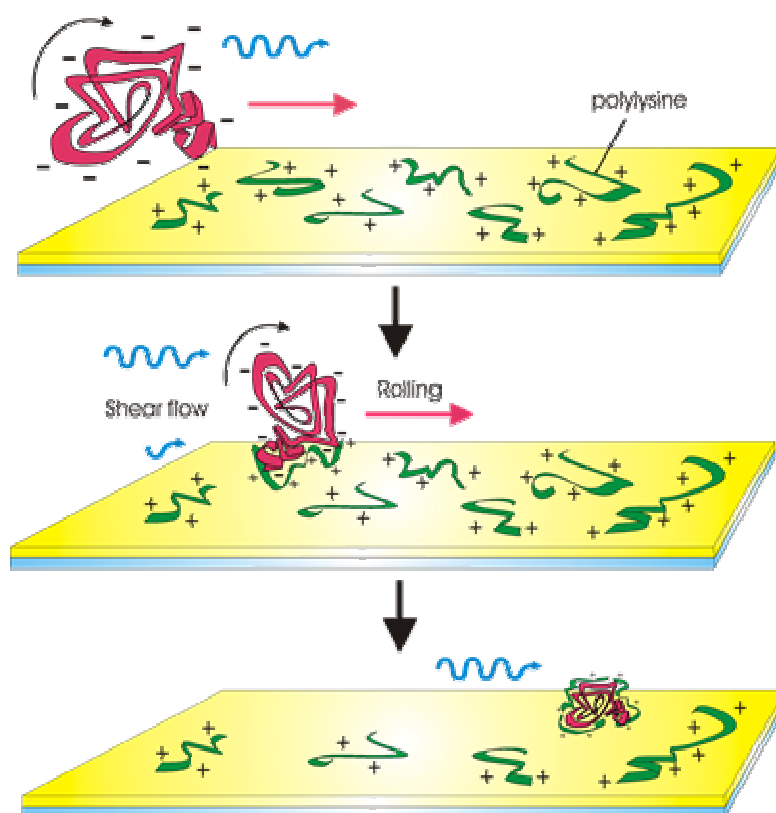


Figure 89: Flow chart of the stages in DNA condensation

## The roll-stick model

Although the positively charged polylysine coating does not necessitate the mixing and complexation of the negatively charged DNA strands, considerable condensation is observed. Possibly some physisorbed PL strands are re-dissolved upon addition of the DNA solution. These soluble polylysine strands would then bind to the DNA and induce condensation. In order to explain the formation of the typical DNA structures, such as the DNA dumbbells, a model was devised - the *roll-stick model*.



**Figure 90:** The roll-stick model to describe DNA (red strand) condensation on polylysine (green strands) coated coverslips. By rolling over the surface, the DNA ball gradually accumulates sufficient polylysine to condensate into a dense globular structure.

The conventional DNA straightening methods generate a fluid shear flow to align DNA. In a shear flow, the fluid velocity is zero directly on the coverslip, but increases with distance from the surface. The DNA, which coils into a statistical ball in solution, will initially be loosely attracted to the oppositely

charged polylysine coverslip. It is likely to move along the substrate in a rolling fashion, because the parts further from the surface will experience an increased fluid velocity. By rolling over the coated surface, the DNA ball will gradually recruit sufficient polylysine for condensation before finally attaching and straightening out.

The sticky-ends of the DNA have a higher probability of attachment. In the case of a terminal fixation, the DNA will gradually unravel, as parts of the fixed end stick to the surface, while the remaining DNA ball is propelled further by the fluid flow. The observation of partially extended DNA balls, with protruding straightened rods, supports this model. If the initial fixing point is not at a terminal sticky-end, then the unwinding process will lead to a globule on both sides, as seen in the dumbbell DNA structures.

Evidence that this kind of process may be involved comes from an AFM imaging report of DNA bound to multivalent cationic silane surfaces [125]. A positively charged silane covered silicon surface was used to immobilise DNA. However, at low salt concentrations, the circular DNA plasmids were condensed into toroids or rod-like structures. The authors explained this observation with the condensing effect of freely diffusing silanes that had not formed covalent bonds during the film generating process and were not rinsed off during washing. In fact, curing the substrates at high temperature, a common step in silanising surfaces, which drives the formation of covalent bonds between the silanes in the film, eliminated the DNA condensation effect.

## **Conclusion**

DNA condensation turned out to be a complex process, which depended on a number of sample parameters, such as the DNA stretching procedure, pH and salt concentration etc. However, the key parameter is the polylysine concentration. At high PL concentrations the DNA readily adheres to the surface, but tends to condense into globules. On the other hand, below 1 $\mu$ g/ml, DNA adhesion is too rare to be useful for imaging experiments. In addition, soluble polylysine chains are probably responsible for the wide variety of different DNA condensation products. These higher order DNA aggregates are difficult to assess in the optical images. In addition, it is not

clear to which extent the free positively charged polylysine moieties compete with dye molecules for DNA association, thus reducing the overall fluorescence intensity. DNA condensation may also lead to considerable dye self-quenching, as the distance between the dyes is reduced in a condensed environment [209].

Moreover, DNA-polylysine aggregates are responsible for the non-plateau pulling events with very long stretching lengths, observed in the AFM experiments on polylysine covered surfaces (cf. 2.3 Force spectroscopy of DNA on transparent surfaces).

Finally, the DNA is strongly attracted to the polylysine coated surfaces by the whole length of the DNA chain, which leads to tightly fixed DNA molecules. With respect to retaining the biological activity or the free mechanical movement of the DNA chain, strongly clamped down DNA strands are undesirable. Therefore, a new immobilisation surface is necessary, which should preferably rely on hydrophobic rather than electrostatic DNA attraction.

#### **4.2.3 Silanised surfaces and super-long $\lambda$ -phage DNA**

Allemand et al. [210] reported that it is possible to immobilise DNA on vinyl-silane surfaces. Specific binding by the DNA extremities is observed at pH = 5.5 in MES buffer (2-[N-Morpholino]-ethanesulphonic acid sodium salt). These results were confirmed, but an unusual discovery was also made: incubating  $\lambda$ -phage BSTE digest DNA (enzymatically fragmented DNA) at pH = 5.5 and then switching to pH = 8 resulted in the formation of very long DNA concatemers.

#### **Images of $\lambda$ -phage DNA**

Generally images of  $\lambda$ -phage DNA can be achieved with TO-PRO-3 in either the acidic MES buffer (pH = 5.5) or the physiological TE (Tris/EDTA) buffer (pH = 8). However, MES buffer is not the solution of choice for imaging, as the dye intercalated DNA strands are less bright than in the TE buffer. An explanation for this could be that at pH = 5.5 the DNA phosphate groups commence protonation, which may shield the DNA from cationic dye adhesion. Furthermore, imaging DNA with the dye PO-PRO-3 led to rapid bleaching of

the strands and brought no gain in contrast or brightness over TO-PRO-3. Therefore, the images are generally captured using DNA in the TO-PRO-3/TE buffer solution. In some cases preliminary DNA adhesion is first achieved by incubation in MES buffer, followed by imaging in TE buffer (cf. Appendix 5: DNA imaging protocols).

DNA is far less susceptible to condensation when prepared on silanised glass than on polylysine. In addition, the strands are loosely bound to the silane layer. Frequently only one end is attached to the surface, while the free end stretches upwards into the solution, i.e. out of the focal plane (cf. the long strand in Figure 91). By taking 40 cross-section images at 250nm intervals in the z-axis, a 3D fluorescence profile of the DNA is gained, which shows that the strand extends up from the surface by ca. 5 $\mu$ m. This can be seen more clearly in the solid 3D image in Figure 91 (Zeiss<sup>®</sup> LSM software), which shows the DNA strand as projected from the side. One explanation for this behaviour could be the preferred attachment of the  $\lambda$ -phage sticky-ends, which are the unhybridised end-groups on asymmetrically restricted DNA (cf. Figure 96). There is evidence that the hydrophobic nature of these regions accounts for their increased adhesiveness [111]. In fact, completely unhybridised single stranded ssDNA is very sticky and attaches non-specifically to most surfaces [112].

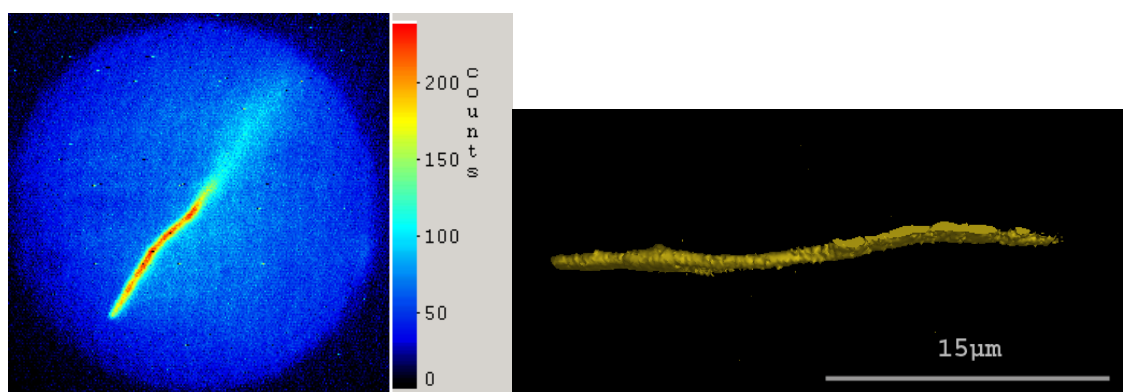


**Figure 91: Fluorescence image of a long  $\lambda$ -phage DNA concatemer (image size 30 $\mu$ m<sup>2</sup>). Right: 3D profile image of the same DNA as viewed from the side. The fluorescence discrimination level was set to 150 counts.**

## DNA mobility on silane surfaces

Longer DNA strands are generally less mobile, but terminally attached chains of ca. 2-3 $\mu\text{m}$  can move more or less freely about their end pivot. The image series in Figure 92 shows such a short DNA strand. The loose end rotates randomly, as indicated by the red arrows. The latter give the strand orientation relative to the first image, but do not signify the direction of the rotation. On some occasions the DNA is completely unattached to the silanised surface, in which case small DNA particles diffuse freely over the silanised surface.

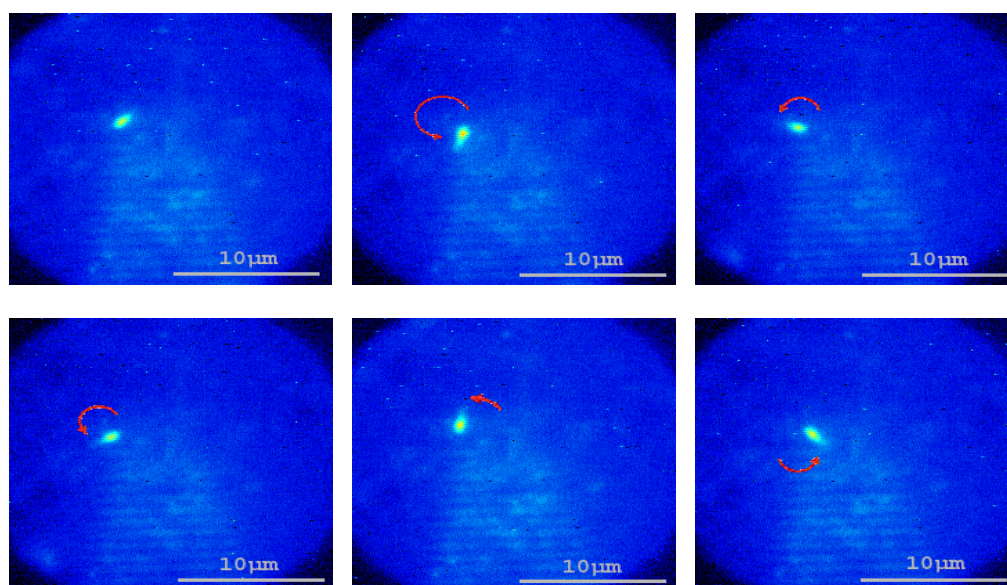


**Figure 92: Rotation of a terminally attached short DNA strand on a silanised coverslip. The images show six different randomly orientated positions of the strand.**

## Super-long $\lambda$ -phage DNA strands on silanised glass

Surprisingly, it is possible to generate super-long DNA chains from either the original  $\lambda$ -phage DNA or even the BSTE digest DNA, simply by exchanging the buffer solution during the preparation procedure. After overnight incubation of the DNA in MES buffer (pH = 5.5), the sample is washed and imaged in TE buffer (pH = 8). The super-long strands prepared in this way are often far longer than an individual 16 $\mu\text{m}$   $\lambda$ -phage DNA - in one documented case even >300 $\mu\text{m}$  long (cf. Figure 94).

The strands displayed homogenous fluorescence along the whole chain length with the occasional brighter node. Between different strands, the

fluorescence is also of uniform intensity, which indicates that these chains are single DNA double helices.

Images of a DNA mesh and a larger DNA knot with four loops are shown in Figure 93. Generally, tight bends are rare, suggesting a relatively high chain stiffness and persistence length.

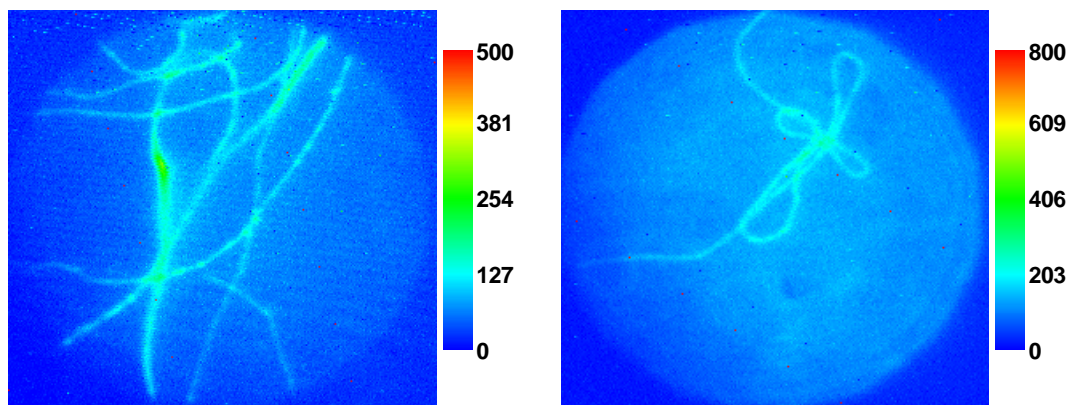


**Figure 93: Images ( $30\mu\text{m}^2$ ) of super-long  $\lambda$ -phage DNA strands on silanised glass.**

The longest detected complete DNA chain is shown in Figure 94. By gradually moving the sample through the illumination field, an image sequence of the whole chain could be generated. The length of the whole chain is ca.  $300\mu\text{m}$ ! This is nearly half a millimetre, which is far longer than the length of a  $\lambda$ -phage DNA unit of  $16\mu\text{m}$ , not to mention the longest BSTE digest fragment of  $3\mu\text{m}$ , from which this DNA was generated.

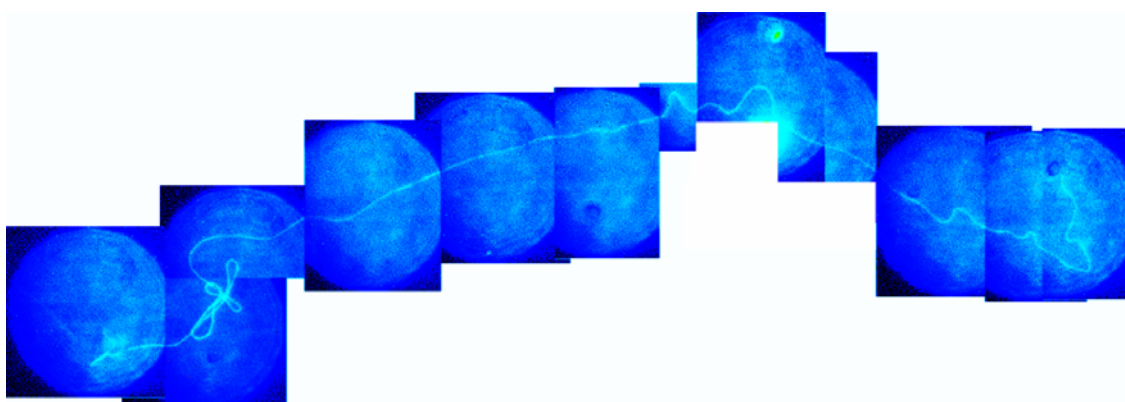


**Figure 94: Image collage ( $240\mu\text{m}\times 30\mu\text{m}$ ) of a  $>300\mu\text{m}$  super-long  $\lambda$ -phage DNA strand.**

How did the DNA get so long? Possible clues might be the small bright nodes noticed along the chains, which may be the result of junctions in the DNA. These junctions could fold back on the original DNA thus increasing the local fluorescence. A rather thick node can be seen in Figure 95.

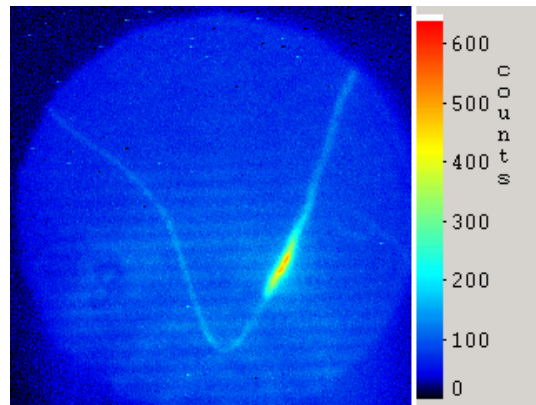


**Figure 95:** Image of a long strand with a bright node, generated from BSTE digest DNA (image size  $29\mu\text{m}^2$ ).

### DNA concatemers

The observed super-long strands are reminiscent of DNA concatemers [128]. These are connected sequences of e.g.  $\lambda$ -phage DNA units. They occur naturally when restriction enzymes in the phage virus fail to cut the original DNA strand into  $16\mu\text{m}$  long units, just prior to packaging into the virus capsule.

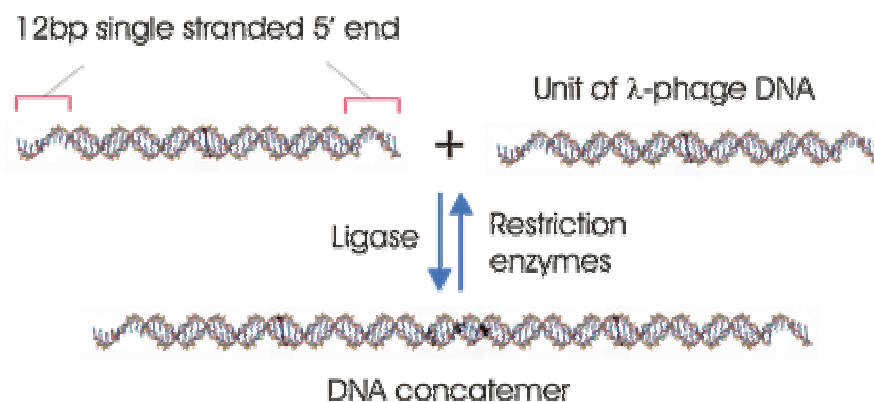


**Figure 96:**  $\lambda$ -Phage DNA concatemers

The canonical cut  $\lambda$ -phage units have a 12 base pair (bp) overhang, which have been described previously (cf. 2.3 Force spectroscopy of DNA on transparent surfaces) and are called “sticky ends” ends. These are probably hydrophobic, which may be the reason for the preferred terminal attachment of  $\lambda$ -phage DNA to hydrophobic surfaces such as silane covered glass. The unpaired ends also have the ability to re-hybridise by forming base pairs to the complementary end of another chain. This hydrogen bonding is sufficient to connect two chains, which can then be covalently bound by re-ligating the strands together with ligase enzymes, thus producing concatemers.

However, in the absence of ligating enzymes, explaining the formation of super-long DNA strands with hydrogen bonded concatemers seems unfeasible. The cohesion between the 12bp hydrogen bonded ends would not be strong enough. The force required to unzip DNA was measured by Bockelmann et al. to be between 10 - 15pN [211-214]. Higher forces of up to 50pN were measured by other groups [215-217], when the DNA was unzipped by pulling at the opposite 5' ends. However, forces of at least 65pN were exerted on the long DNA strands in the AFM manipulation experiments (cf. 5. Combined optical imaging and AFM).

Finally, no super-long DNA is generated when imaging in MES or TE buffer alone, which would still permit hybridisation of the sticky ends. Therefore another process must be responsible for the long DNA.

### **DNA polymerisation by interstrand hybridisation**

It is likely that the pH change plays an integral role in the formation of super-long DNA. Allemand et al. describe DNA protonation under acidic conditions [10]. At pH= 5.5 DNA protonation is already equal to a few percent.

Decreasing the pH induces partial melting of the double helix and frilling at the DNA ends [10]. By bringing the pH back to 8 it might be possible to re-hybridise the DNA in an alternative way, thus re-connecting the complementary strands of *different* DNA chains and generating very long polymeric DNA fibres. This is shown schematically in Figure 97.

Similar DNA junctions were described by Seaman et al. [218]. If the overlap is not perfect then DNA loops and folding could occur – an explanation for the bright nodes observed occasionally along the DNA chains? The process of interstrand hybridisation could also lead to the formation of Y-junctions or other DNA constructs [219, 220]. However, these were rarely observed (cf. Figure 98). To test for Y-junctions and confirm the interstrand hybridisation theory, high resolution AFM scanning images of the connection points would be useful [218, 221, 222].

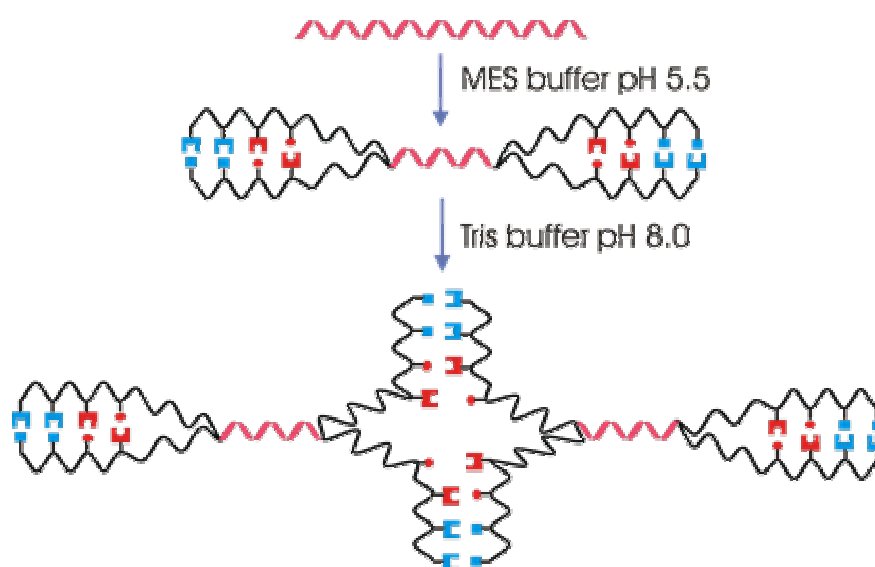


Figure 97: DNA junctions by interstrand re-hybridisation

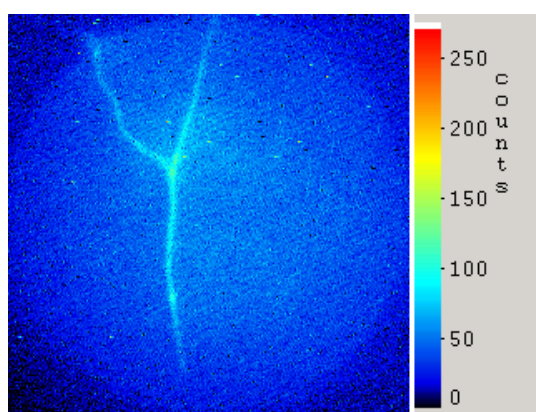


Figure 98: Fluorescence image of a possible DNA Y-junction; image size  $29\mu\text{m}^2$ .

Although the generation of super-long DNA strands is unlikely to become a new chemical method for polymerising DNA chains, it is an interesting discovery that may warrant further investigation.

### **Conclusion of the DNA imaging experiments**

Our results clearly show that there are fundamental differences in the DNA morphology on either polylysine coated or silanised surfaces.

On polylysine, single DNA strands can, in principle, be prepared and aligned using various fluid flow extension methods. However, the condensating effect of the electrostatically charged cationic PL surface leads to the formation of highly compacted DNA rods and balls. The whole DNA body is fixed to the surface.

On silanised surfaces the DNA regularly forms uncondensed single strands, which are often straightened to their full contour length. The general adhesion strength to the surface is weak and large parts of the DNA are observed to extend vertically up into the water phase. In addition, the DNA displays a high propensity for terminal attachment. Many cases were noted, in which the free end of a fixed DNA strand rotated or swivelled in the solution. Unattached DNA strands are also observed, as they rapidly diffuse through the solution or jitter randomly near the surface.

Furthermore, super-long DNA strands can be generated on silanised surfaces by an exchange of the buffer solution during the sample preparation procedure.

## 5. Combined optical imaging and AFM

So far, the experiments on DNA were done either by AFM force spectroscopy or by optical imaging methods. It could be shown, firstly, that it is possible to achieve characteristic single DNA force curves on transparent surfaces. Secondly, optical images of single DNA strands can be taken using TO-PRO-3 as an intercalating dye. In order to combine both experimental techniques a new setup is required which places the AFM head on top of the inverted optical microscope, thus guaranteeing optical access to the sample coverslip from below and simultaneous AFM cantilever access from above. Three series of combined experiments are described:

- Real-time DNA manipulation on polylysine and silane surfaces.
- Simultaneous AFM force spectroscopy and optical imaging.
- A new type of lateral force spectroscopy on long DNA strands.

### 5.1 The combined optics/AFM setup

A major difficulty encountered in the combined AFM/confocal optical setup is co-aligning the optical focus with the position of the AFM tip. This problem is circumvented by employing wide-field imaging. In this way the cantilever apex can be positioned laterally in the relatively large illumination field ( $\sim\varnothing 30\mu\text{m}$ ), while the sample is controlled by a high resolution piezo positioning system. Manipulation of the sample is achieved by moving the coverslip, while keeping the cantilever tip and optical focus in line.

#### The new microscope stage

A new home-built microscope stage (cf. Figure 99) was constructed so that the AFM head could be accommodated on top of the inverted microscope. The new stage is composed of three mechanical positioning systems in the X-Y plane:

- The largest brass stage element is screwed onto the microscope platform and enables the lateral movement of the whole AFM head and sample relative to the objective focus.
- Next, a piezo-stage (black) is required for the fine lateral displacement of the sample, with nm resolution. The piezo-stage position is



These three lateral displacing units are integrated into the sample stage in a compact fashion, because the AFM cantilever can only be lowered down to the sample by about a centimetre. At the same time the microscope objective needs to be pushed up through all the other mechanical elements to meet the sample coverslip from below.

Furthermore, due to the short working distance of the high  $N_A$  objectives, only 170 $\mu$ m thick coverslips can be used instead of objective slides. This has implications for the force spectroscopic measurements, which were found to be perturbed by rogue resonant vibrations of the freely swinging thin coverslips. The sample holder aperture was therefore reduced to 16mm $\varnothing$ . The interfering frequencies are greatly dampened by the oil objective, when brought into contact with the glass.

### **Fluorescence filters**

Unfortunately, the AFM diode IR light, which is used in the AFM head to generate the deflection signal, initially passed through the bandpass filters and overwhelmed the fluorescence signal. The main bandpass filter used in the detection setup is the 720  $\pm$ 75nm filter, which lets the fluorescence light pass from 645nm - 795nm. Importantly, light with a wavelength above 800nm is blocked, so the filter provides good protection against IR light. The only possible explanation for this leak is, therefore, that the diode light is actually bypassing the filters below 800nm.

A spectrum of the IR diode, which was taken using the detection spectrometer (cf. Figure 100), shows that the diode light is spectrally broad. A significant amount of light is detectable below 800nm, a region for which the filters are transparent. It is therefore impossible to suppress this light by conventional spectral filters. Unfortunately, the spectrally broad AFM diode is required to prevent interference signals in the AFM setup, so an exchange is not an immediate option.

The only other solution is to cut out the objectionable laser light below 800nm spectrally, before it reaches the sample. This involves incorporating a new bandpass filter 840  $\pm$ 35nm into the AFM head as a laser clean-up filter.

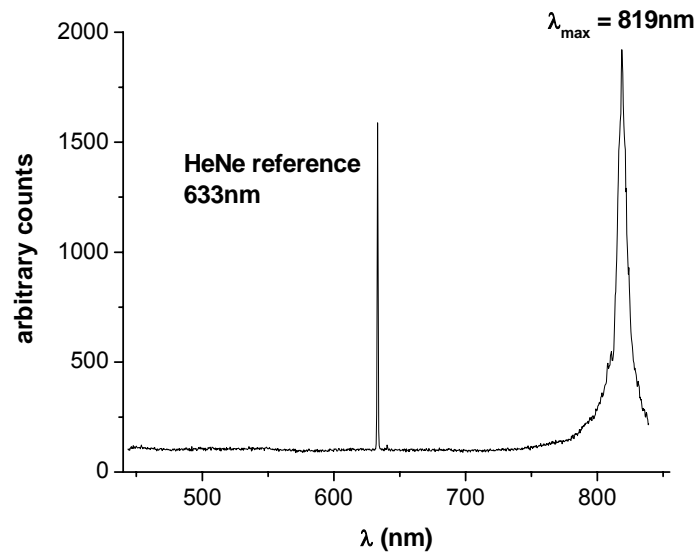


**Figure 100: AFM IR-diode spectrum**

The final solution is described in Figure 101. By mill-cutting an 8mm $\varnothing$  mould into the fluid cell holder, the filter (shown in green) can be positioned in the optical path of the IR laser beam (shown in red).

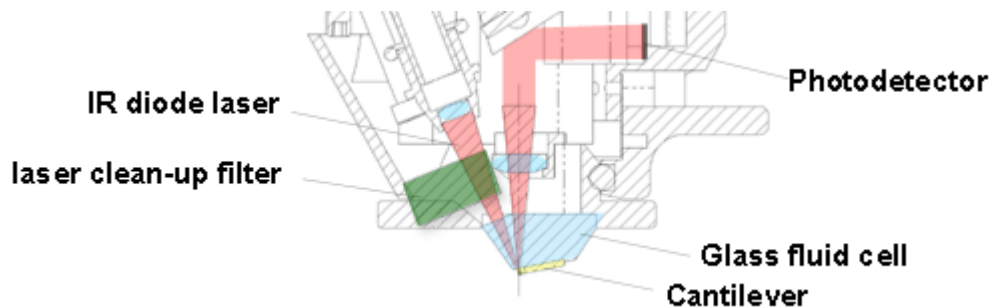


**Figure 101: AFM head and fluid cell with the new clean-up filter**

However, the beam is not completely parallel at this point and so a certain shift in the blocking filter spectrum has to be accounted for. The transmission spectrum of the new filter at various angles of incidence is shown in Figure 102. The angle of incidence for the IR laser beam is ca. 9°, which is still acceptable. With this filter, the diode laser light below 800nm can be blocked completely.

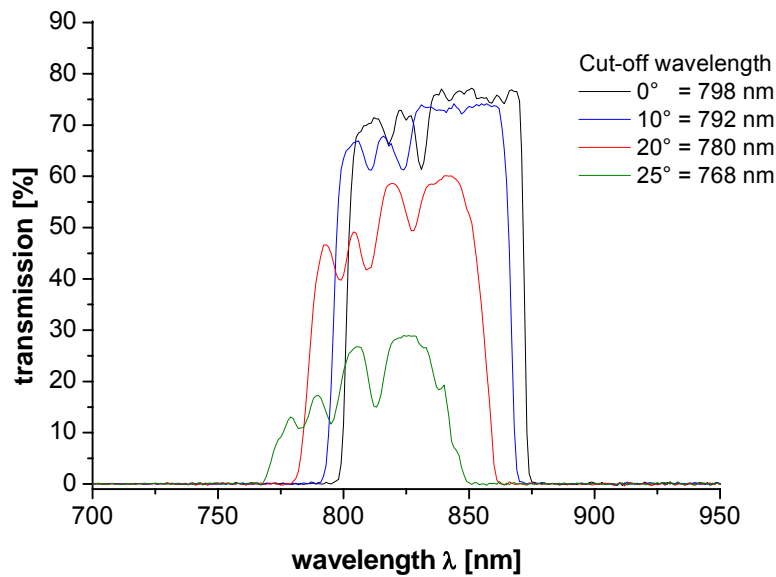


**Figure 102: Laser clean-up filter transmission spectrum at different angles of incidence**

### **Cantilever tip alignment procedure**

After mounting and calibrating the cantilever, the whole AFM head is transferred to the optical microscope stage. The head is then positioned laterally with the large stage screws so that the cantilever tip is in line with the optical axis of the microscope objective. Due to the relatively small tip dimensions and the limited field of view of the high  $N_A$  objectives (~ a few hundred  $\mu\text{m}$ ) a method is needed to find and zero in on the approximate tip position, which may initially be far out the viewing field. Fortunately, the intensity gradient of the scattered IR laser light serves this purpose, because scattered light from the cantilever could be detected even if the tip was far out of the lateral focus.

The first step in the alignment procedure is to bring the cantilever down into contact with the substrate and into the objective z-axis focus. By exploiting the IR light, scattered from the cantilever shank, the lateral position of the tip can be estimated (N.B. using neutral density filters rather than fluorescence blocking filters). By closing in on the highest signal intensity the shadow of the cantilever is brought into the field of view of the objective (cf. Figure 103). From then on, the tip can be identified through its intrinsic cantilever luminescence and directed to the centre of the illumination spot.

The tip remains in this lateral position, while the sample manipulation is achieved by moving the coverslip underneath.

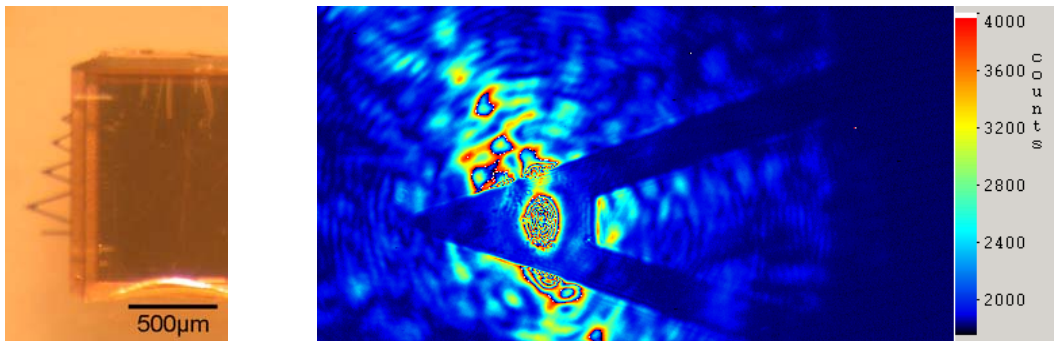


**Figure 103: (left) Conventional optical microscope image of the cantilever chip. (right) The IR diode reflected from the cantilever back surface (image: 283\*151µm).**

The tip alignment procedure is summarised in Figure 104. After positioning the tip in the illuminated area it lights up and can be identified by its intrinsic luminescence (cf. figure b, illumination of the tip). Focussing the objective up a few µm, the edges of the cantilever pyramid can be brought into view (cf. figure c). Figure d shows a tip fluorescence image without the AFM IR diode.

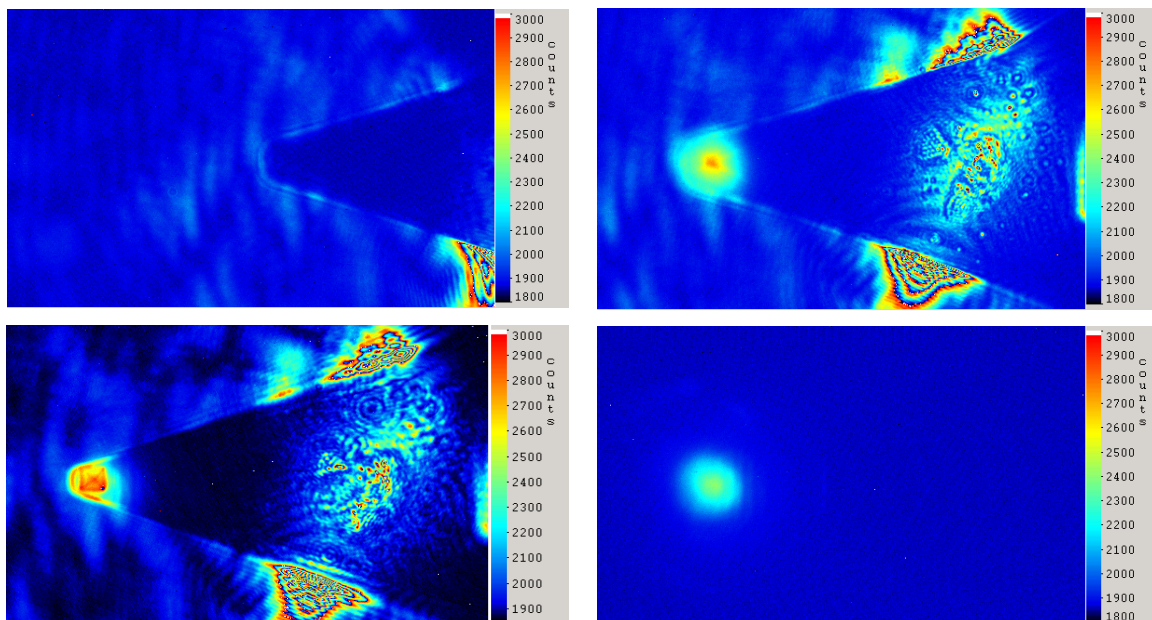


**Figure 104: Cantilever alignment procedure (image: 98µm\*65µm).**

**a) Positioning the cantilever**

**b) Tip luminescence and AFM laser**

**c) Tip edges in focus**

**d) Only tip luminescence**

## 5.2 Cantilever luminescence

All cantilevers examined emit a spectrally broad, red-shifted luminescence when subject to laser light of either 532nm or 632nm. Since the origin of the emitted light is unclear, it is termed luminescence to distinguish it from single molecule fluorescence. Surprisingly the luminescence of AFM cantilevers has hitherto not been described in detail in the literature. The only group to mention cantilever luminescence as a non-descript background signal was Wild et al. [223], although the group of Seidel et al. has also observed cantilever luminescence [224]. Images of the cantilever luminescence are shown in Figure 105. By focussing up a few micrometers, the cantilever pyramid edges can be identified.

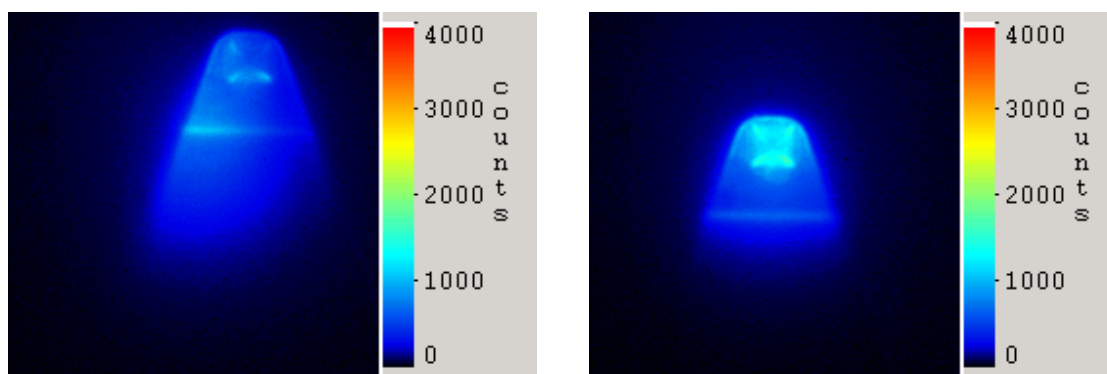


**Figure 105: Cantilever luminescence a) slightly off centre b) centered on the illumination spot.**

Although this luminescence is weak, it is of comparable magnitude to the fluorescence emitted by single molecule dyes. Generally, the luminescence depends on three factors:

- The illumination intensity
- The tip geometry
- The cantilever material

Tip cleaning does not make a difference and so the luminescence cannot be a contamination artefact. It is also not the result of Rayleigh scattering, as experiments with various filters show that it is shifted to longer wavelengths and an excitation wavelength blocking efficiency of  $\sim 10^{12}$  has no influence on the luminescence intensity.

## Tip geometry

The most striking influence on cantilever luminescence was witnessed for different tip lengths. Longer cantilevers do not reduce luminescence per se, but since only the tip apex is in focus ( $\sim 1\mu\text{m}$  depth) the luminescence background from the cantilever shank contributes less to the overall signal. Since the  $\text{Si}_3\text{N}_4$  Microlever™ cantilevers have a height of  $3.3\mu\text{m}$  the cantilever shank is generally visible. The Si Ultralevers™ were  $6\mu\text{m}$  long, which clearly reduces background luminescence. The best background signal is achieved with the Olympus® Biolevers™ (tip length  $11\mu\text{m}$ ). In this case only the very tip apex is in focus. The image in Figure 106 shows a  $\text{Si}_3\text{N}_4$  cantilever approach sequence. The tip is gradually brought down onto the coverslip surface and into focus with a speed of  $40\text{nm}/\text{sec}$ , while consecutive images of the fluorescence are taken.

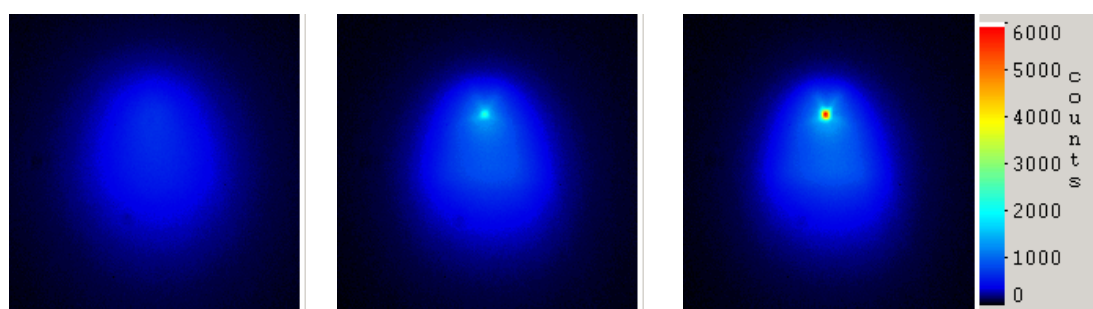


**Figure 106: Cantilever approach sequence; z-distance between the images  $\sim 1.5\mu\text{m}$ .**

If field enhancement effects are responsible for tip luminescence the actual shape of the tip may also play an important role [225].

## The cantilever substrate material

Various tip materials were tested: Si,  $\text{Si}_3\text{N}_4$  and gold. The following images were taken with a 20x air objective and illuminated with  $532\text{nm}$  light (detection:  $580\text{-}75\text{nm}$  bandpass filter). The images in Figure 107 show a Si cantilever (Veeco®, Ultralever™) at relatively high irradiation powers. The luminescence is weak.

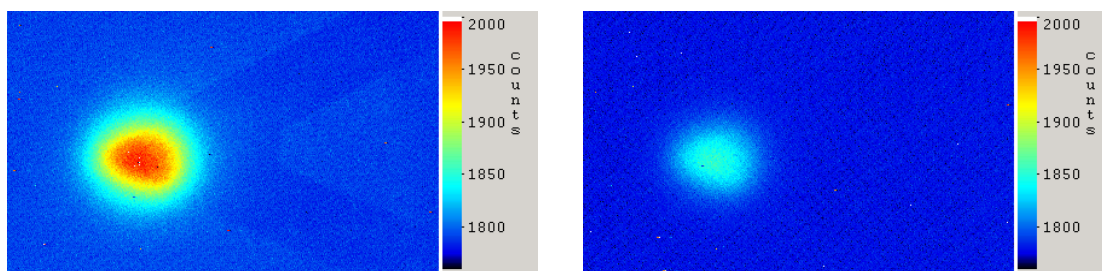


**Figure 107: Si cantilever (Veeco® Ultralever™ ULCT-AUHW); illuminated with a) 12mW and b) 1.2mW (~100W/cm<sup>2</sup>).**

Illuminating a Si<sub>3</sub>N<sub>4</sub> cantilever (Veeco® Microlever™) with the same laser power afforded the images in Figure 108. The Si<sub>3</sub>N<sub>4</sub> tips generally display brighter luminescence than the Si cantilevers, although the length of the cantilever must be taken into consideration (6μm for Si and 3.3μm for Si<sub>3</sub>N<sub>4</sub>).

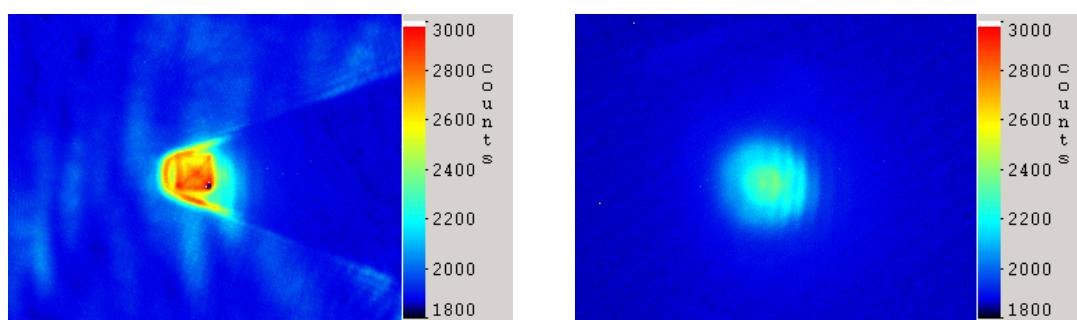


**Figure 108: SiN cantilever (Veeco® Microlever™ model : MLCT-AUHW) at 1.2mW. a) focussed on shank; b) focussed on the tip.**

Gold coated Si cantilevers ( $\mu$ -masch®, CSC12™, Anfatec®) were also tested. They display very low luminescence, but the tips are 15-20μm long, so only the apex is usually visible. Similar results are also achieved for the Olympus® Biolevers™, which are 11μm long and gold coated on both sides.

### **Methods to reduce cantilever luminescence**

A substantial reduction in background luminescence can be achieved by using TIR illumination, which limits the irradiation volume to a few hundred nm above the coverslip surface. The following images were taken of the same sample position. The left image shows a conventional wide-field image of a cantilever on a  $\lambda$ -phage DNA sample. The right image was taken in

objective-type TIR mode. The greater illumination depth of the wide-field arrangement, leads to a stronger signal, because more of the cantilever is irradiated. For the TIR image the luminescence is restricted to the tip peak.

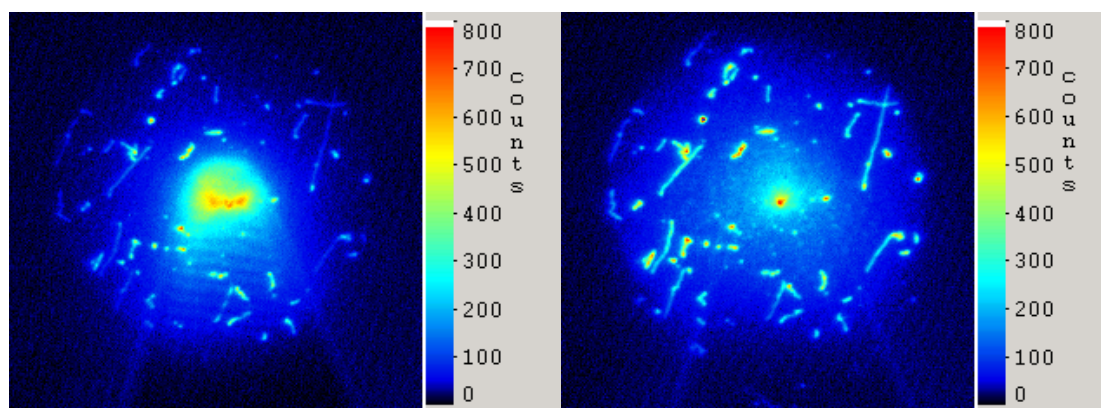


**Figure 109: Comparison of cantilever luminescence for wide-field and TIR imaging (image size  $48\mu\text{m}^2$ );  $\lambda$ -phage DNA sample with antifade on polylysine.**

Apart from using long cantilevers and imaging in TIR mode, the background tip luminescence can be reduced by decreasing the laser power. Generally the best approach is to use all three of these methods in combination. Applying TIR and long tips can avoid luminescence, but the tip apex is still illuminated, which is unfortunately the point of interest for most combined optical/AFM experiments. An alternative solution is to maintain constant illumination conditions throughout an experiment and subtract the “background” control image (including the tip luminescence) from each sample image then taken. This approach works well, especially for wide-field imaging conditions. If very low illumination intensities ( $\sim 1\text{W}/\text{cm}^2$ ) are sufficient to achieve high sample brightness, then the more complex TIR setup is not necessary. On the other hand, if higher laser powers are required, then TIR can greatly reduce the background fluorescence and tip luminescence. Finally cantilevers of different materials might be found, which lack inherent luminescence.

## **The origin of the cantilever luminescence**

The back-scattered light of an AFM tip was measured by Kolodny et al. [68]. Furthermore, other experiments describe the quenching of illuminated dyes in the proximity of metal tips [226-228]. Quenching occurs near metals over a distance of  $\sim 10\text{nm}$  and is therefore stronger for Au coated rather than Si cantilevers. However, neither of these methods revealed any wavelength shifted tip luminescence. Probably the illumination intensity in these experiments was too low.

Kramer and Trubesinger describe the fluorescence enhancement experienced by a single terrylene dye in the vicinity of a gold tip [223, 229]. The authors explain the enhanced fluorescence with localised resonant plasmon fields [230]. However, a strong cantilever luminescence is also observed for different tip materials including Si and  $\text{Si}_3\text{N}_4$ . Therefore, local plasmon resonance falls short of explaining tip luminescence.

Generally, the tip edges display an increased luminescence. Possibly, this is due to a non-resonant field enhancement or the lightning rod effect for pointed tip geometries [225]. Although such effects were described for very sharp tips with excitation field components along the tip axis, these conditions are not met for our imaging experiments [231].

Another explanation could be that scattered light from the tip acts as an illumination source and is afterwards converted into nondescript fluorescence by fluorescent impurities. Light scattering is stronger at the edges, as can be seen in the reflected laser light images with neutral density filters. Therefore light originating from these scattering hotspots would generate a stronger background fluorescence signal.

### 5.3 The manipulation of DNA on polylysine: writing with DNA

For the real-time manipulation experiments, the AFM cantilever is brought into surface contact and centred in the illumination field. A  $\lambda$ -phage DNA sample on polylysine is shown in Figure 110. Using the setup described in Figure 99, the glass substrate can be moved so that the DNA strands on the surface are pushed against the tip. This shows that the strands are firmly stuck to the surface by the whole length of the chain. Applying high forces leads to chain rupture. Usually the sliced ends retreat a few microns after scission [232], suggesting that the straightened chains were initially under tension.

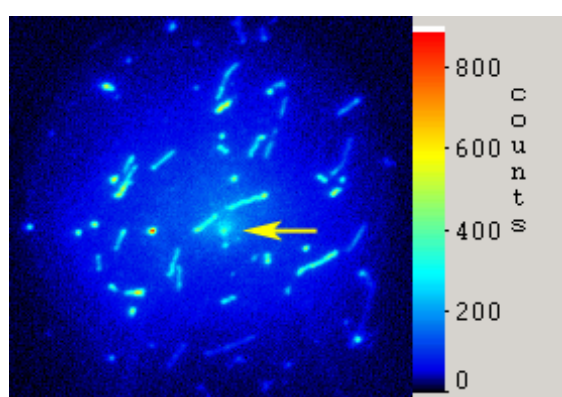


**Figure 110:** TIR image ( $38\mu\text{m}^2$ ) of  $\lambda$ -phage DNA prepared on polylysine. The AFM cantilever tip position is indicated by the yellow arrow. The sample has just been pushed upwards against the tip apex, which resulted in severance of the DNA strand and subsequent retraction of the cut ends.

However, on polylysine the DNA is more likely to form aggregated balls or condensed structures than single DNA chains. These agglomerated balls can be moved or picked up with the AFM tip. It is possible to push the compacted DNA bundles sideways. In some cases single DNA chains can be pulled out of the DNA balls, but usually the DNA reattaches immediately to the surface in the new position. An example of showing these processes is presented in the image series in Figure 111.

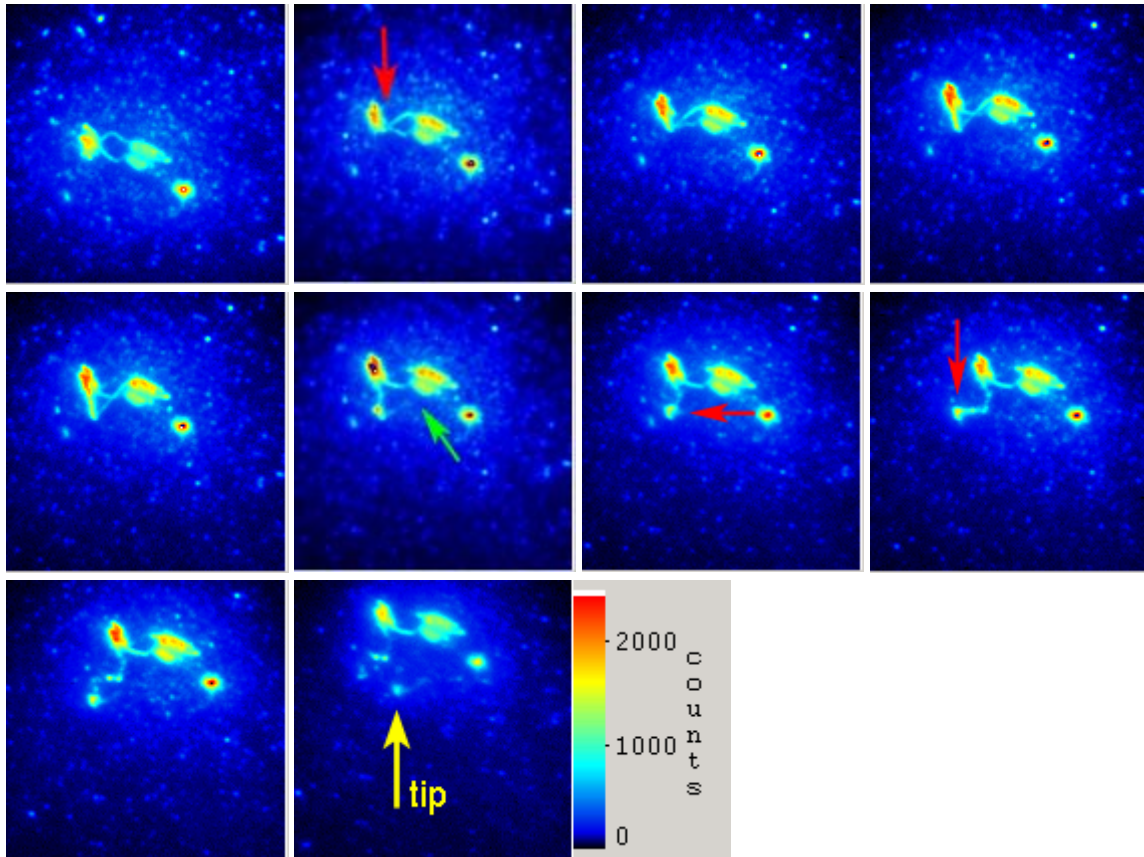


**Figure 111: Strand extraction from a DNA globule and deposition on a polylysine surface: The red arrow shows the relative movement direction of the tip with respect to the surface. The tip is pushed against the DNA strand connecting two globules. The DNA strand is extended and pulled out of the two neighboring globules.**

**Eventually, one end of the DNA-bridge between the globules ruptures (green arrow). After pulling upwards to measure a force curve, the second DNA strand end ruptures and much of the DNA remains on the tip (yellow arrow).**

**Sample of  $\lambda$ -phage DNA  $3.3 \cdot 10^{-10} \text{M}$  prepared with antifade on polylysine and imaged with  $69 \text{ W/cm}^2$  (image size  $28 \mu\text{m}^2$ ).**

Taking these results into account, it is no surprise that the AFM pulling experiments on polylysine rarely produced the characteristic single molecule force curves typical of DNA (cf. 2.3 Force spectroscopy of DNA on transparent surfaces). The chains were attached too strongly to the surface. Moreover, they were usually condensed or aggregated and thus necessarily afforded uncharacteristic force curves (e.g. without a clear B-S transition plateau).

## Writing with DNA on polylysine

By attaching a condensed DNA globule to the cantilever and stroking the tip over a polylysine coated surface, thin fluorescent fibres can be unravelled from the DNA ball onto the adhesive surface. In this way, defined fluorescent structures are written with the DNA “ink”, as is described in Figure 112.

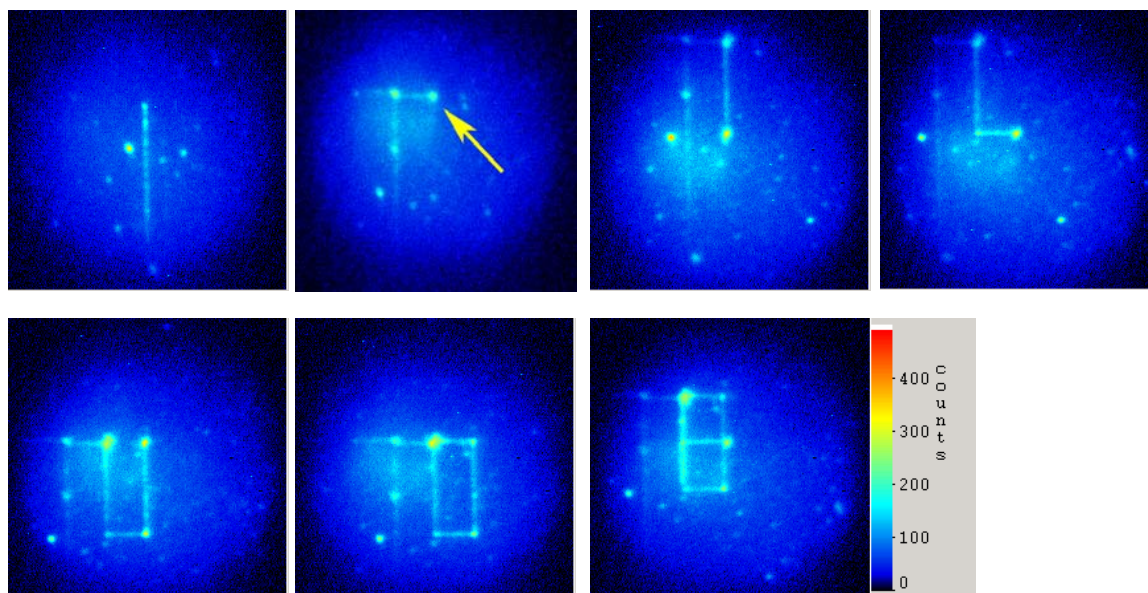
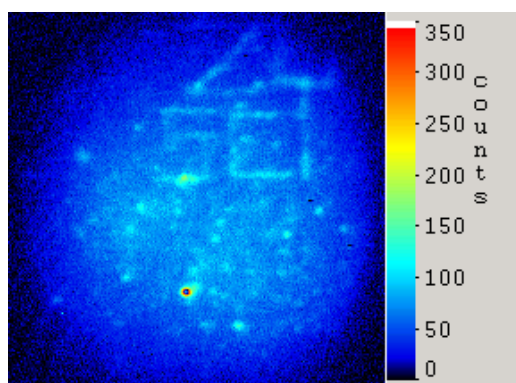


Figure 112: Fluorescence structures written by an AFM tip on polylysine with  $3.3 \times 10^{-12} \text{ mol/l}$   $\lambda$ -phage DNA in TE buffer (image size  $25 \mu\text{m}^2$ ). The tip position is indicated by the yellow arrow. The DNA is transferred to the surface at a constant rate. Positions at which the cantilever movement is halted are characterised by slightly brighter fluorescence spots.



Figure 113: left: Images ( $25 \mu\text{m}^2$ ) of DNA letters on a polylysine coated surface. The letter Z was completed to form the letters “ZUM”; right: fluorescence intensity profile image of the DNA letters.

The same method can be used to write DNA letters, such as the letter “Z”, which was then completed to “ZUM” (cf. Figure 113). Considering the total length of the written letters ( $>100\mu\text{m}$ ) these structures are certainly not composed of single DNA strands, but rather DNA bundles of condensed fibres, which are typical on polylysine samples. Eventually the ink begins to wane and so the letters “SCI” could not be completed.



**Figure 114: DNA writing “SCI”.**

### **The DNA “water-pen”**

*“A thousand letters can dance on the head of a pin.”*

By pushing a tip-attached ball of DNA over the polylysine surface, thin DNA fibres can be unravelled from the tip onto the surface, much like a pen deposits ink on a sheet of paper. By directing the tip over the sample, defined structures, such as alphabetical letters are “written” with this “DNA ink”.

The proposed principle of this method is described schematically in Figure 115. Thick condensed DNA fibres can be drawn from a ball of DNA on the tip, like a thread from a ball of wool. The written strands are deposited on the charged polylysine surface in the form of aggregated bundles. The deposition rate is more or less constant, but occasionally larger DNA balls are transferred when the tip is kept stationary for more than a few seconds.

The strands that are being cast onto the polylysine coated glass surface are probably composed of semi-aggregated DNA fibres, rather than single DNA strands. The condensating effect of polylysine on DNA was described previously (cf. 4.2.2 DNA condensation on polylysine surfaces).

Similar to a sticky spiders thread, these fibres can be spun off the tip and fixed onto the polylysine surface by a strong electrostatic interaction.

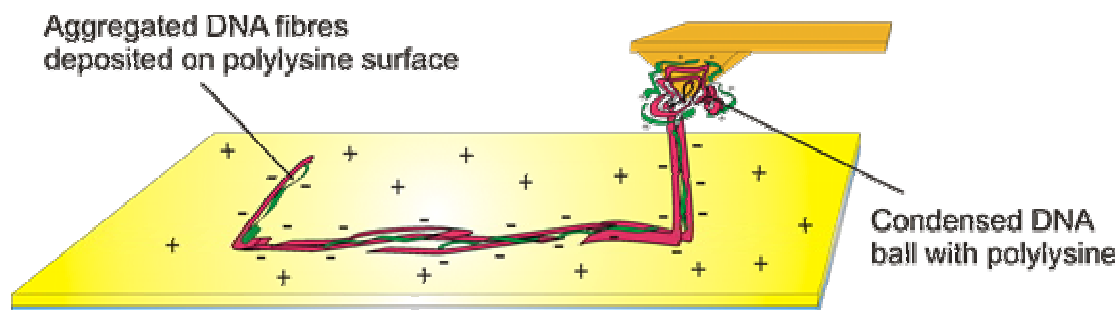


Figure 115: Deposition of the DNA thread with the water-pen.

### Comparison of the DNA “water-pen” with dip-pen technology

The DNA writing experiments on polylysine with the “water-pen” are similar to the “dip-pen” method devised by Mirkin et al. [233] Their group used an AFM tip to deposit small molecules on surfaces in a controlled fashion, thus generating nanometer sized patterns [234]. The key to this success is a thin water meniscus [235], which is used to regulate the “molecular ink” flow from the tip to the sample. The experiments are conducted in air and often involve grafting of thiol-functionalised molecules [236-239], or DNA oligomers to a gold surface [240, 241]. Recently, the dip-pen method has been used to fabricate fluorescent nanopatterns with rhodamine dyes [242] or modified DNA oligonucleotides on quartz glass [243].

Although the method employed for writing DNA letters on polylysine displays some similarities to the dip-pen technique, there are fundamental differences. In contrast to the Mirkin experiments, fluorescence from intercalated dyes is used to image the DNA in real-time during the deposition process. No subsequent labelling process is necessary.

In addition, the DNA ink-tip is completely submersed in the water phase. The driving force permitting this aqueous deposition is likely to be the highly attractive polylysine surface, which pulls the DNA off the tip, rather than the capillary forces in the dip-pen water meniscus.

## **DNA nanowires**

Further studies are required to investigate the exact nature of the deposited DNA fibres e.g. by AFM scanning experiments. However, the controlled deposition of thin DNA fibres may offer the possibility to generate nanometer sized patterns of DNA or even nanowires. These could be used in ultra high density biochips for fast screening assays or in the construction of nanoscale electric or optoelectric devices. Conventional semiconductor technology, which is based on lithographic processes, is expected to reach the theoretical limit of miniaturisation by 2012 [244]. After that, even smaller nanoelectric components are required, which cannot be constructed by conventional lithographic processes. Due to its extremely thin diameter of only 2nm, DNA could be employed as a conducting nanowire [245]. DNA has a high flexibility and can be functionalised at the ends. These are clear advantages over the stiff and hard-to-define carbon nanotubes [246, 247]. The low conductivity of DNA has been the main hindrance so far, but by metallising the DNA chains with Pd the conductivity could be increased [248-250]. In this way deposited DNA structures might be converted into conducting nanowires.

## **5.4 DNA manipulation on silane surfaces**

The scanning AFM microscope has previously been used to manipulate DNA on silanised mica surfaces with high spatial resolution [133]. However, no real-time manipulation was possible. Here the simultaneous fluorescence imaging of DNA is demonstrated during the manipulation.

In contrast to the experiments on polylysine, the DNA manipulation on silanised surfaces is not dominated by an overwhelming electrostatic adhesion to the surface. Instead, the DNA is usually loosely adsorbed to the silane layer. Furthermore, the nature of the DNA morphology is different, with far less aggregated and condensed structures. In most cases, the DNA adopted the form of thin uniform strands.

This has implications for the manipulation experiments. The DNA can be moved horizontally by the motion of the cantilever tip, without necessarily cutting the strands. An example is shown in Figure 116. The DNA strand is

manipulated with the tip as indicated by the red arrow. Three points of interest can be observed:

Firstly, the tip pushing experiments demonstrate the high rigidity of the DNA, which reacts to lateral forces like a “thin tube”, rather than a “fine string”. Instead of being forced into a sharp bend, the DNA would escape tension by an abrupt reorientation of the whole chain (cf. the loop in images 5 and 6).

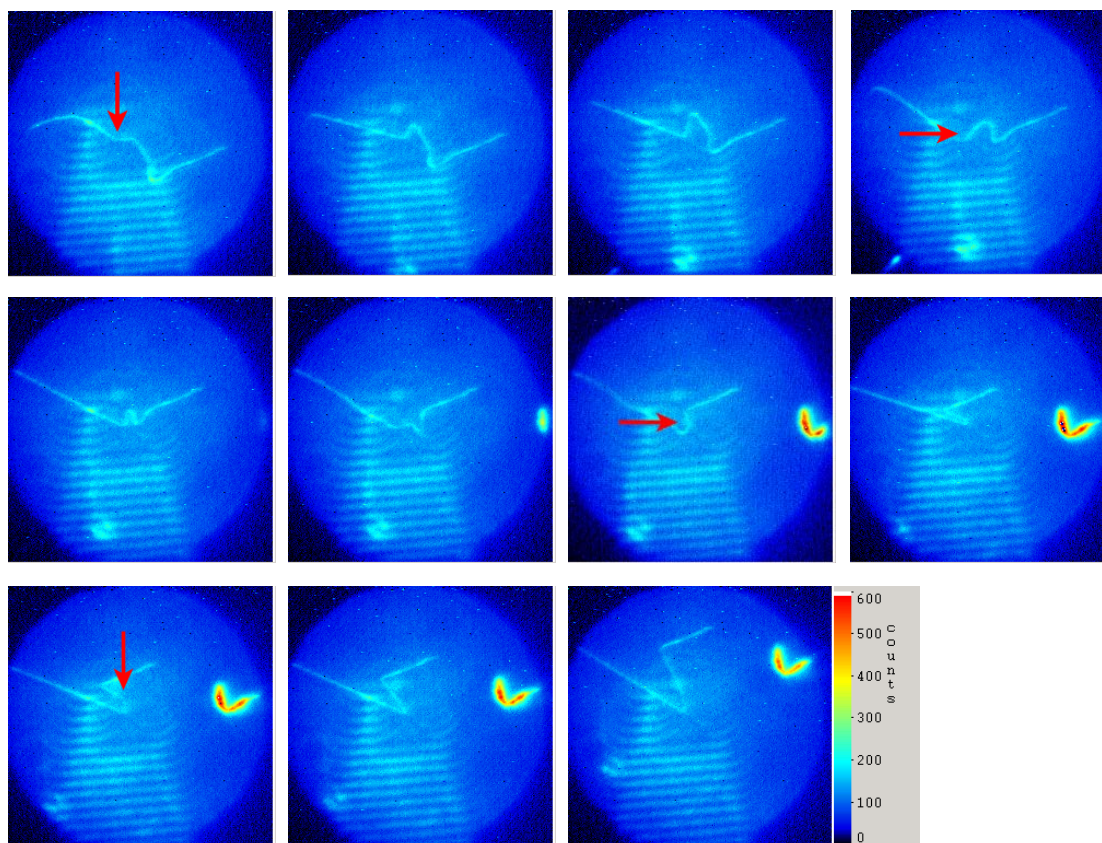


**Figure 116: Zip-like motion of pushed super-long DNA;  $\lambda$ -phage BSTE digest DNA on silanised glass; imaged at  $1.4W/cm^2$  (image size  $29\mu m^2$ ); red arrow = relative tip motion.**

Secondly, the DNA adhesion, although generally much weaker than on polylysine, was characterised by local attachment points, especially the ends. This led to a zip-like motion as the DNA was torn off the surface bit by bit when these anchor points ruptured. In fact, the forces required to sever these fixed points were relatively high, at least in the range of a few tens of piconewtons (cf. 5.6 Single molecule lateral force spectroscopy of DNA).

Frequently the DNA itself ruptured, before one of the attached termini was pulled off.

The reason for this behaviour could be local sticky segments along the DNA. Unhybridised regions of the double helix are purportedly hydrophobic [10, 111, 112] and completely unhybridised ssDNA is very sticky, attaching non-specifically to surfaces [39]. Partially unwound segments of the DNA could either be generated by nicks in the helix due to irradiation or be a direct consequence of the process involved in forming super-long DNA. The junctions thus generated between individual segments of the long DNA would provide ample possibilities for unpaired and thus hydrophobic DNA extremities. These regions may be adhering to the hydrophobic silane layer, causing the zipper-like tearing motion of the DNA. It would be interesting to simultaneously measure the forces required for these rip-off events by AFM force spectroscopy.

In retrospect, these results also help to clarify the processes involved in the AFM force pulling experiments of DNA on silanised surfaces (cf. 2.3 Force spectroscopy of DNA on transparent surfaces). Through terminal or local attraction of the sticky regions in an otherwise unattached chain, the DNA is far more easily picked up and stretched on a silanised than on a polylysine substrate. Furthermore, the strands are less likely to condense and form aggregated bundles or globules. Consequently, frequent and characteristic single molecule force curves are observed.

Finally, the images show that DNA is highly elastic, as has also been demonstrated previously by single molecule force spectroscopy experiments. Under high tension, the DNA chains can be snapped. Rupture occurs at the tip, thus cutting the DNA strand into two parts. More examples of DNA manipulation on silane layers are provided in the lateral force spectroscopy section.

## 5.5 Combined force spectroscopy/optical imaging

The combined setup is capable of measuring the force spectroscopic properties of attached single molecules in the conventional way by stretching these molecules upwards off the surface. By correlating the fluorescence signal available through simultaneous optical imaging, additional information can be gained e.g. on the dynamics of the intercalated dyes under strand tension.

### 5.5.1 Combined experiments on polylysine

The image series in Figure 118 shows a DNA sample on polylysine with the DNA coiled up into large globules, as described in the imaging section. In principle, it is possible to attach these DNA balls to the cantilever and pull at them. However, the DNA usually sticks strongly to the surface and cannot be moved without strand rupture. Occasionally, the whole DNA ball is transferred to the tip.

In Figure 118, a condensed DNA ball is fished up onto the tip by one end, while remaining fixed to the surface through the rest of the globule. The motion of the cantilever during a typical force curve pulling cycle is explained in Figure 117. Since the tip touches the surface at an angle, it is pushed into the sample at the end of an approach curve. Likewise, at the start of the retraction curve, the tip initially scrapes over the surface before lifting off.

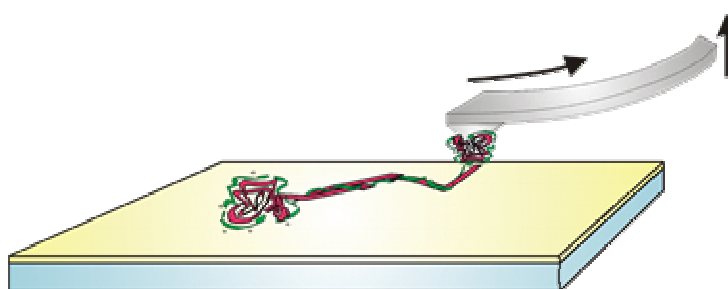


**Figure 117: The cantilever is scraped over the surface during a force spectroscopy pulling cycle.**

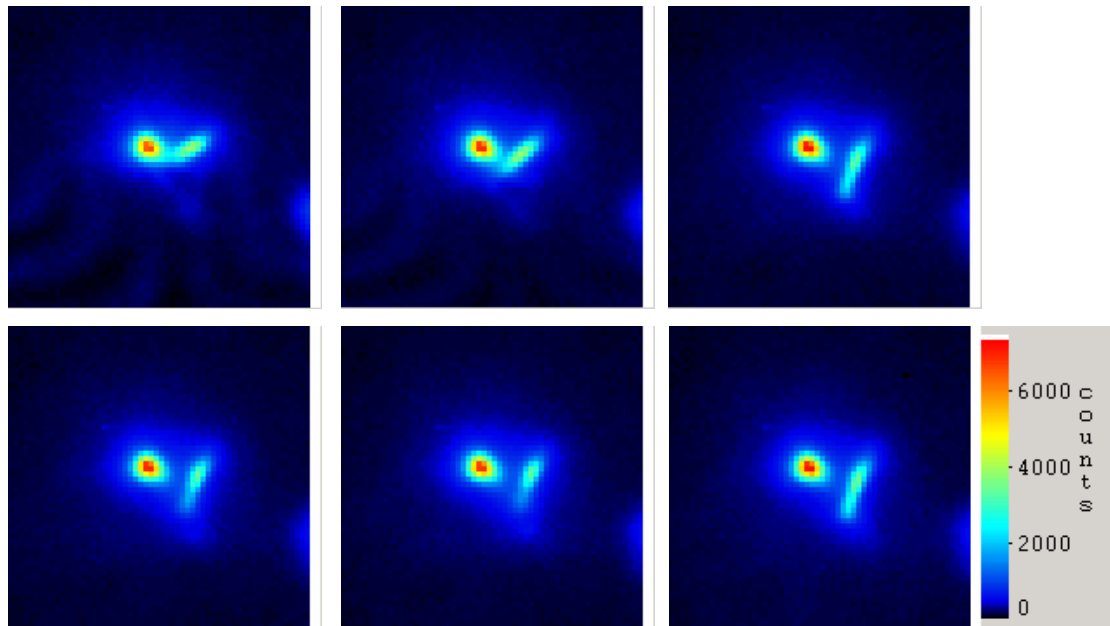


**Figure 118: Image series of DNA on polylysine with simultaneous force spectroscopy (image size  $12\mu\text{m}^2$ );  $\lambda$ -phage DNA  $3 \cdot 10^{-10}\text{M}$  ( $1.2\text{W}/\text{cm}^2$ ).**

This effect can be seen in Figure 118. After pushing the DNA southwards (cf. images 1-3) the tip lifts off the surface stretching the DNA upwards (cf. images 4-6). Although a drop in fluorescence can be observed during the stretching motion, this is due to the DNA bundle moving up out of focus. In the last image the connection to the tip is ruptured and the DNA abruptly drops back onto the surface (cf. image 6), immediately bringing back the full fluorescence signal.

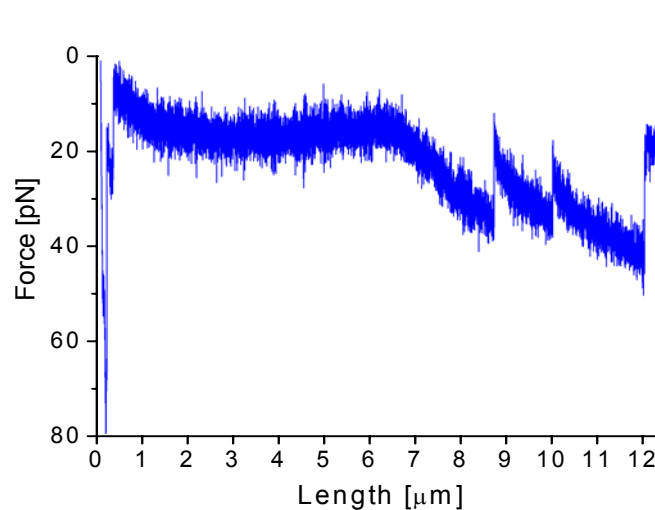


**Figure 119: Simultaneous DNA force curve with multiple rupture events.**

The simultaneously measured force curve corresponding to the image series in Figure 118 clearly shows that there were multiple attachment points of the DNA bundle to the tip, which successively ruptured at  $8.5\mu\text{m}$ ,  $9\mu\text{m}$  and  $12\mu\text{m}$ . The last rupture event occurs after image no.5 in Figure 118, after which the DNA bundle falls back onto the surface, thereby immediately restoring the full fluorescence signal. The forces reached in this experiment of up to  $40\text{pN}$  are too low to show the characteristic B-S plateau ( $65\text{pN}$ ) typical of single molecule DNA pulling curves.

These results fit in with the DNA condensation theory put forward to explain DNA aggregation on polylysine surfaces. According to this theory, DNA can take on the form of an interconnected multi-strand bundle with polylysine, so force pulls with consecutive rupture events are to be expected. Furthermore, the long rupture lengths measured for these fibres of ca.  $10\mu\text{m}$  are typical of DNA on polylysine. A bundle of interwoven DNA strands could be longer than the individual DNA chains composing the fibre.

This experiment showed that in principle it is possible to conduct simultaneous AFM and optical imaging experiments. However, the difficulty in preparing single strand DNA samples on polylysine and the resulting uncharacteristic force curves led to the investigation of different substrate surfaces, such as silanised glass coverslips for combined optical/AFM experiments.

### 5.5.2 Combined experiments on silanised surfaces

In the following image series on silanised glass (cf. Figure 120) one end of a single DNA strand is attached to the cantilever and pulled, while the other end on the right remains fixed to the surface. The position and relative movement of the cantilever is indicated by the red arrow.

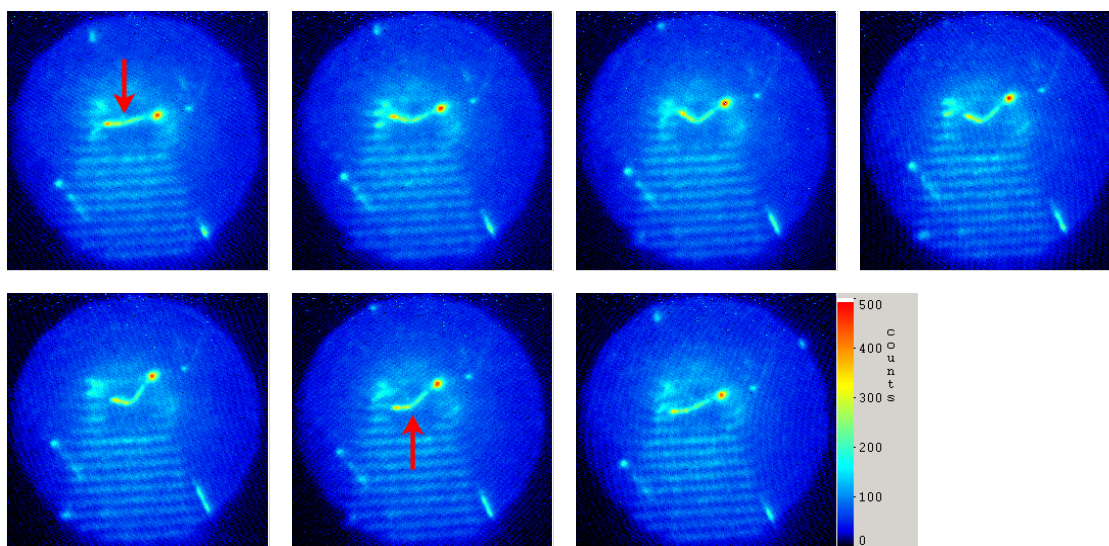


**Figure 120:** The reversible manipulation of a single DNA strand on silanised glass (image  $30\mu\text{m}^2$ );  $\lambda$ -phage digest DNA imaged at  $1.4\text{W}/\text{cm}^2$ ; red arrow = tip movement

The molecule could be stretched through a reversible 1Hz pulling cycle (pulling speed  $\sim 2\mu\text{m}/\text{sec}$ ). This stretching cycle was repeated about 20 times, before the attachment finally ruptured. The images in Figure 120 show the position of the DNA at various stages in the pulling sequence, although they were not taken from one single cycle. After pushing the cantilever southwards and up from the surface (first 4 images) the direction is reversed and the DNA is pushed back into its original position (last 3 images).

The corresponding force curves to the images in Figure 120 from this same series of consecutive pulling cycles are presented in Figure 121. There is only a slight hysteresis between the retraction and the approach curves (blue and red respectively). Furthermore, the characteristic second DNA plateau can be identified as a shoulder at ca. 800nm. It also displays a slight hysteresis. However, the B-S transition plateau at 65pN is converted into a gradual increase in force, due to the effect of the intercalating dye TO-PRO-3 (cf. 2.3 Force spectroscopy of DNA on transparent surfaces). There is still

room for speculation as to the severity of the change in the B-S transition in this specific experiment, but the high dye concentration may have played a role.

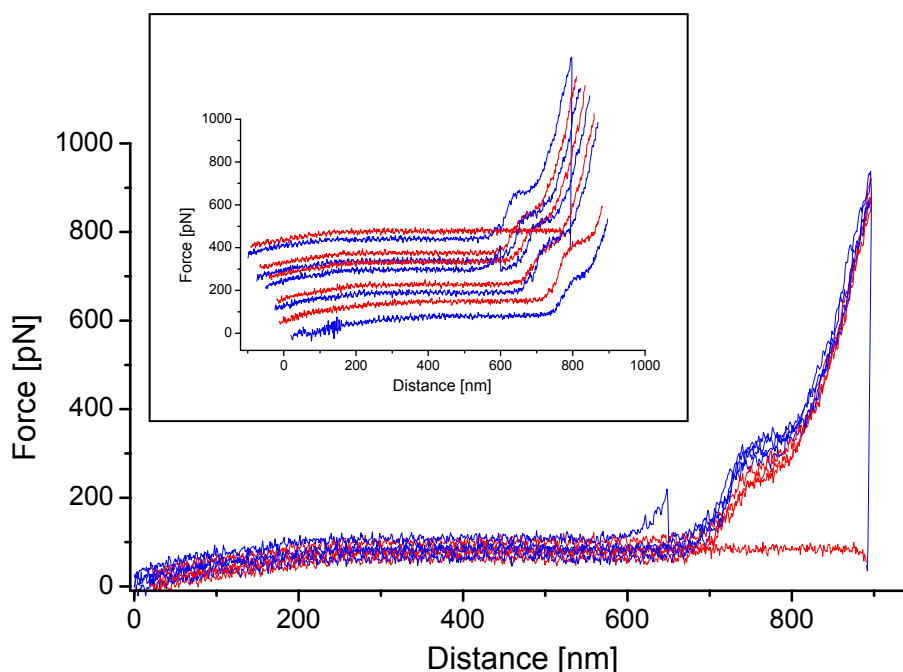


**Figure 121: Reversible force curves of DNA on silane corresponding to the images in the last figure. For clarity, the inset graph shows the subsequent pulling cycles with an offset in the x and y axis.**

By gradually increasing the pulling length, the force was increased with each cycle until the DNA-tip connection finally ruptured, as seen in the sharp vertical drop at 850pN in the last blue curve. Unfortunately, the slow frame rate of the camera only permitted image snapshots with 1 sec intervals and by the time the AFM pulling speed could be reduced, the DNA had already fallen off the tip. Therefore, no precise correlation between the image sequence and the positions in the pulling cycle could be established. A drastic drop in signal intensity was not observed, but then the images display the average fluorescence signal taken over the whole camera exposure time, so no correlated fluorescence/force information could be gained from this experiment.

### 5.5.3 Conclusion of the combined experiments

The silanised coverslips afford samples with isolated DNA molecules that show reversible force curves. On rare occasions, these molecules can be directed to the cantilever tip and pulled upwards, thereby stretching the DNA. The goal is to measure the fluorescence of the DNA strand, at different chain tensions during a pulling cycle. However, five major experimental obstacles were encountered which complicate the simultaneous imaging and pulling experiments.

Firstly, good samples are required with single, uncondensed and straightened DNA chains that can be stretched reversibly. This is possible on silanised coverslips.

Secondly, cantilever fluorescence quenching, although probably significant for single dye molecules, is not an obstacle for DNA imaging with many intercalated dyes. A clear conclusive answer to the question of quenching by cantilever tips has yet to be given [223, 229].

The third problem occurs when long DNA strands are pulled upwards, out of the focal plane of the objective. Neither TIR nor wide-field imaging or confocal microscopy can be employed to circumvent this difficulty. Pulling molecules that are longer than ca. 1-2  $\mu\text{m}$  will extend these beyond the laser focus, thus automatically decreasing the detection efficiency of the fluorescence signal. Under these circumstances it is not possible to determine the effect of DNA tension on dye fluorescence alone. An apparent solution is to use shorter DNA molecules. For this purpose  $\phi\text{X-174}$  DNA was synthesised by standard biochemical linearisation techniques using the unique cutting XHO-I restriction enzyme. The  $\phi\text{X-174}$  DNA is 5386 bp long, which corresponded to a chain length of merely 1.8 $\mu\text{m}$  – about the length of the optical z-focus. Although this approach is promising and future experiments should follow along this line, the shorter DNA strands turned out to be harder to pick up with the cantilever tip and so the attempts so far were fruitless.

Fourthly, slow force pulling experiments with cycle periods in the range of minutes are necessary to gain enough imaging data for each stretching position. However, in this case cantilever drift becomes significant. Drift usually originates from thermal fluctuations, which lead to tip bending when tip

materials are combined with different thermal extension coefficients, as is the case for gold and  $\text{Si}_3\text{N}_4$  tips [134]. Heating by both laser sources can become a problem on a long time scale. Slow force curves are therefore often skewed by cantilever drift. A solution would be to speed up the frame rate to ca. 10Hz, while pulling with reasonably slow cycles of 0.1Hz. This should provide 50 images for the approach and retraction cycle – enough to determine any variation in the fluorescence signal at different forces. Incidentally, photon pressure, which can exert a force of  $\sim 3.3\text{pN}$  from a 1mW laser source through conservation of momentum [251], was constant with time and therefore not a problem.

Finally, the toughest nut to crack is that a single molecule is hard to find and pick up with the cantilever tip. The synergistic effect of knowing the rough position of both the molecule and the tip is a help, but turned out to be insufficient to guarantee efficient and specific attachment. Like finding a needle in a haystack, picking up a molecule of  $\sim 1\text{nm}$  dimensions with a tip of  $\sim 50\text{nm}\varnothing$  is arduous, when the position accuracy of both is determined by diffraction limited optics to ca. 300nm. Attaching DNA therefore remained an elusive and random event. Merely bringing the cantilever into the vicinity of the strand was not enough. The processes governing tip attachment, namely hydrophobic interactions, required specific conditions to be met, such as sticky ends or unhybridised regions, before a strong tip fixation could occur.

Therefore, the next step would be to obtain high resolution AFM scanning images of the DNA. This may provide details of DNA junctions or termini, which could be addressed directly with the tip, thereby increasing the probability of attachment. A further promising way to improve the probability of attachment would be to silanise the tip surface or even use a layer of polylysine to increase the cantilever adhesiveness towards DNA. This was attempted, but the polylysine coated tips quickly attracted free floating DNA from the solution, rendering them contaminated with a brightly fluorescing DNA layer. Carefully washing of the sample surface to remove any free DNA from the sample prior to tip immersion could provide a remedy. In general, a more specific binding method, possibly even by means of covalent bonds (e.g. peptide linkers), would be helpful.

## 5.6 Single molecule lateral force spectroscopy of DNA

The difficulty of specific tip attachment illustrates the general disjunction in intermarrying optical microscopy with conventional AFM force spectroscopy. Although reversible force curves of DNA are possible on silane surfaces, they are not easy to come by on samples with extremely low DNA coverage. On the other hand, for single molecule fluorescence detection, the DNA strands must be in low concentration, so as to be discernable against a non-fluorescing background. Our intention was to overcome this dilemma by exploiting the fact that tip attachment should be far more probable, when individual strands can be observed optically so that the tip can be directed exactly to the DNA position. Unfortunately, this initial assumption was thwarted by the fact that the tip radius (25nm) and the DNA diameter (2nm) were far smaller than the optical resolution of the detection apparatus (300nm). Tip adhesion therefore remained an unpredictable event, with an inherently low probability of attachment. On the other hand, picking up targeted DNA strands with the help of optical detection did not necessarily lead to satisfactory reversible force curves. Until a clear solution could be found, additional ways to stretch DNA were sought.

A prospective solution to the problems discussed in the previous chapter is the use of a new method to stretch single DNA chains – termed *single molecule lateral force spectroscopy*. In the past, the lateral forces exerted on a cantilever have been used in scanning AFM microscopy to determine surface friction. By measuring the lateral twist of the cantilever shank during scanning, additional tribological information about the surface is provided, whereas the classical vertical cantilever bending gives the height profile. Furthermore, in the same way that the stretching force is calculated in conventional force spectroscopy from the vertical deflection signal and the cantilever spring constant, the lateral force can be determined by establishing the lateral spring constant of the cantilever [134]. Rudimentary measurements of the lateral tip twist during horizontal cutting of a DNA strand on mica have been used to estimate the DNA rupture force to ~500pN [134], albeit with very low force resolution. A similar experiment is envisaged, which measures the

tension in single molecules during horizontal stretching parallel the substrate surface – *single molecule lateral force spectroscopy*.

The advantages of this approach for the combined optical imaging setup are manifold:

- Pulling the molecules sideways keeps them in the focal plane of the objective at all times.
- Vertical drift of the cantilever is minimised, because the tip remains on the surface.
- The applied force is controlled through the length extension of the strand, and thus the experiment has no limiting pulling speed.
- Horizontal tip stretching does not rely on random tip attachment. Like plucking a tripwire or a violin string, long polymer chains can be addressed by pushing the tip against the midsection of a strand that is fixed to the surface by at least two points.

These advantages make lateral force spectroscopy the method of choice for combined optical experiments. By measuring the lateral deflection signal a direct measure of the force exerted by the tip on the DNA during lateral stretching can be gained.

Furthermore, since the graph of force vs. distance is known for a standard DNA chain, a given DNA extension length can always be mapped to a specific force. Therefore, the tension in the DNA strand can be determined indirectly from the stretching length, which is known from the optical images. In this way the measurement of the lateral deflection signal is not required and the complex lateral mode calibration process is avoided.

### **Quantitative evaluation of the DNA fluorescence during lateral stretching**

With this new method it is possible to analyse the fluorescence from a DNA chain during stretching. Super-long single DNA strands are prepared from  $\lambda$ -phage BSTE digest DNA on silanised glass coverslips and manipulated with the AFM tip, so that they are fixed to the surface by at least two points. This is

described schematically in Figure 122. The two fixed points are symbolically fastened to the surface with pinheads. In reality unhybridised regions or sticky ends are probably responsible for these local adhesion points. In order to stretch the DNA, the tip is kept in position, while the sample coverslip is moved underneath. In this way the strands can be pushed against the stationary tip and thus stretched.

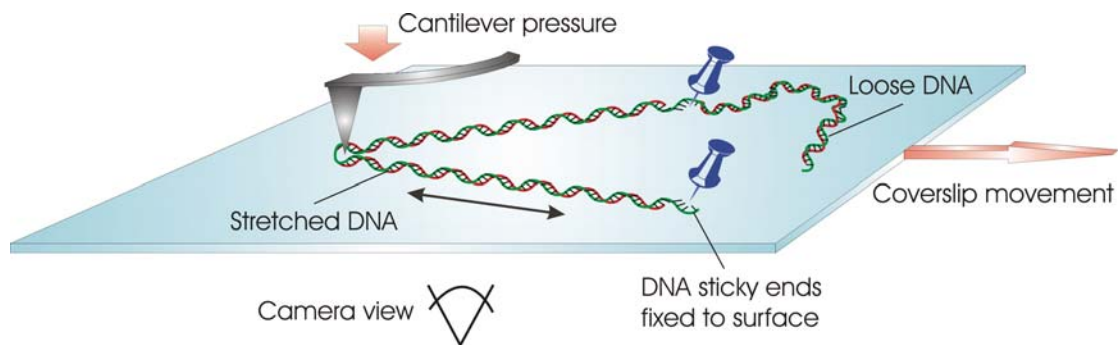


**Figure 122: Schematic description of the lateral stretching experiment**

The camera views the sample from below the glass coverslip, so the cantilever is always facing upwards in the following images. The tip is kept in the centre of the illumination field.

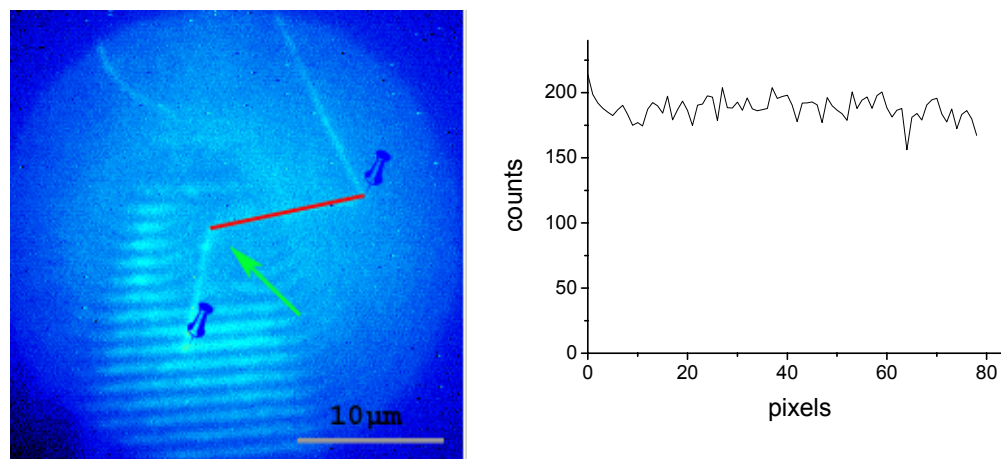


**Figure 123 left: Image of a fixed (blue pins) and stretched DNA strand (cantilever tip indicated by green arrow).**

**right: Line profile fluorescence cross-section of a DNA strand (red line).**

To establish a representative fluorescence intensity value for the DNA in each of the images the average fluorescence is determined for a line profile of 50 pixels length, taken along the extended DNA strand and starting at the tip position (cf. Figure 123). Since the illumination intensity profile decreases slightly outwards from the centre, the tip is positioned in the centre of the illumination spot. This guarantees that the DNA strands always experience the same irradiation intensity gradient, irrespective of the orientation of the chains. Thus, the DNA manipulation images provide both the average fluorescence intensity and the length of the corresponding stretched DNA. The extension factor is the end-to-end distance of the stretched DNA divided by the original length (the contour length under zero force). Finally, a graph can be plotted of the average strand fluorescence along the chain for each chain extension. This has been done for several of the manipulation image series.

### **Elastic extension of a single DNA chain**

The image series in Figure 124 was taken in total internal reflection (TIR) mode. The cantilever is positioned in the centre of the image. A super-long DNA strand can be seen to the left of a large DNA ball that has attached itself loosely to the cantilever shank and now jitters about in solution. By pushing the sample against the tip the strand can be stretched sideways (the direction of the sample movement is given by the black arrow). After the third image the movement is paused, which fixes the strand at the tip position. The mechanism of this attachment process is unclear, but may involve local nicks generated by tip friction along the DNA chain. These partially denatured sections are particularly adhesive towards the hydrophobic silane surface. The strand is then subsequently stretched vertically by moving the sample southwards. In the final image the DNA slips away under the tip and snaps back into a relaxed conformation.

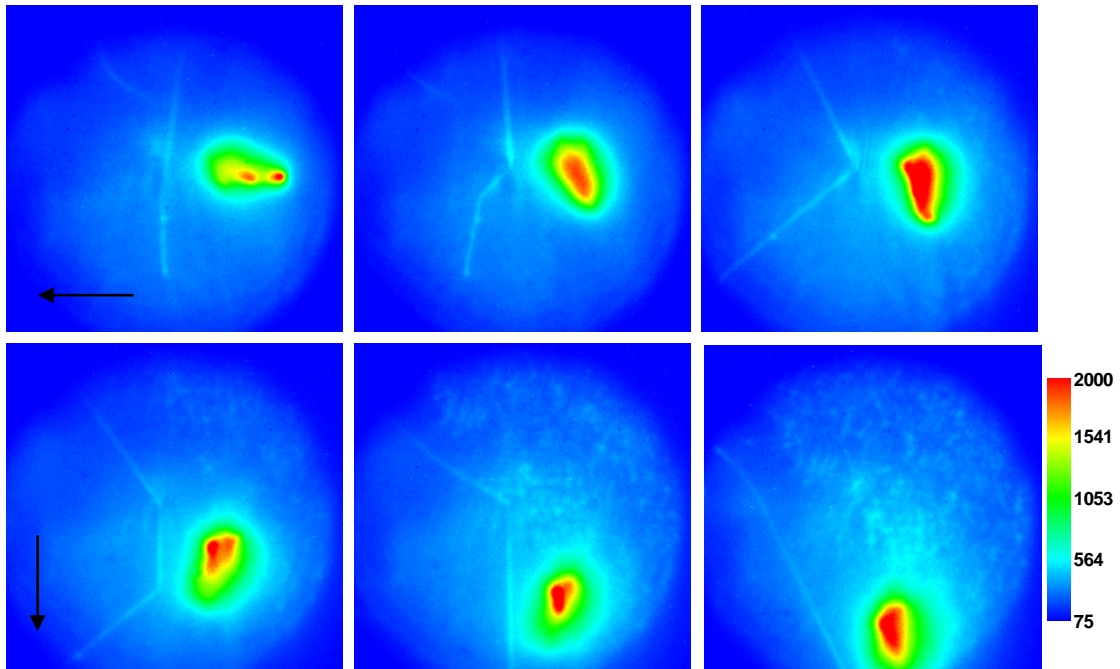


Figure 124: TIR image ( $28 \mu\text{m}^2$ ) series of a super-long DNA strand on a silanised surface. By pushing the sample to the left, against the stationary cantilever tip (image centre), the strand can be stretched sideways (images 1, 2 & 3). After fixing the DNA, the sample is then moved downwards (image 4 and 5). Finally the DNA slips away under the cantilever and snaps back into a relaxed conformation (image 6).

In order to analyse the lengths and fluorescence of the DNA in this series a small bright node on the DNA chain (cf. green arrow, Figure 125) is used as a marker. The node itself may be a DNA knot or some form of DNA junction – a remnant of the generation process of super-long DNA.

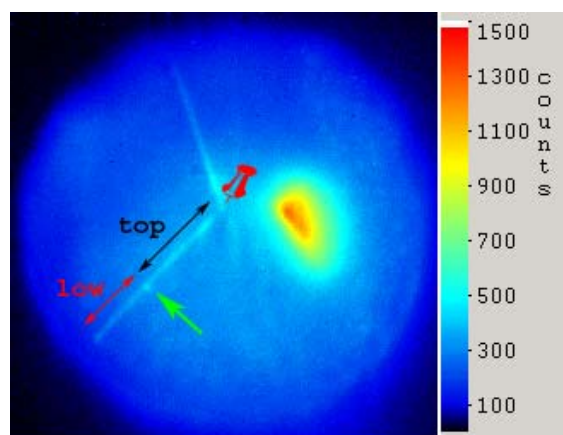


Figure 125: Length determination of a DNA strand. The **red pin** indicates the tip; the **green arrow** gives the position of the DNA node.

The respective lengths of the DNA strand can be measured for the sections from the tip to the node (top section) and from the node to the lower DNA anchor point (lower section). In this way, the extension coefficients during stretching for different sections of the DNA can be studied. If the extension is uniform along the whole strand, then both top and lower sections should display the same extension coefficient.

The results of these length measurements are summarised in table 13. The total length of the strand increased from 76 pixels (9.1 $\mu$ m) to 125 pixels (15.0 $\mu$ m) during the stretching process. This corresponds to an extension factor of 1.64 or an increase of 64%. However, the original DNA chain was probably not fully elongated before stretching. Due to microscopic loops and bends, the full contour length was not reached until image no. 41, when the last attachment point to the surface was ruptured. From image 41 onwards the strand extension increases at a constant pace, as can be seen in Figure 126.

Total length (pix)	Lower section (pix)	top section (pix)	Length % of lower section	Length % of top section	Extension factor 76=1.0
76	39	37	51.3	48.7	1.00
86	40	46	46.5	53.5	1.13
93	40	53	43.0	57.0	1.22
97	41	56	42.3	57.7	1.28
100	41	59	41.0	59.0	1.32
106	45	61	42.5	57.5	1.39
108	45	63	41.7	58.3	1.42
112	44	68	39.3	60.7	1.47
119	45	72	37.8	60.5	1.57
120	47	73	39.2	60.8	1.58
125	50	75	40.0	60.0	1.64

**table 13: Length of the DNA at different chain extensions**

Furthermore, a detailed analysis of the two DNA sections shows that the upper section expanded faster than the part below the node (cf. table 13). This can be deduced from the relative length percentages. Prior to stretching, both sections are about the same length. By the last image the lower part is only 40% of the total length.

The elastic module of both DNA sections should be the same. However, this phenomenon can be explained by the strand gliding along the tip during the stretching process, like a rope pulled around a pole. In this case the stretched strand is “borrowing” DNA from the remaining chain above the tip. Therefore a total extension factor of 1.26, as calculated for the lower section of the DNA, is more accurate.

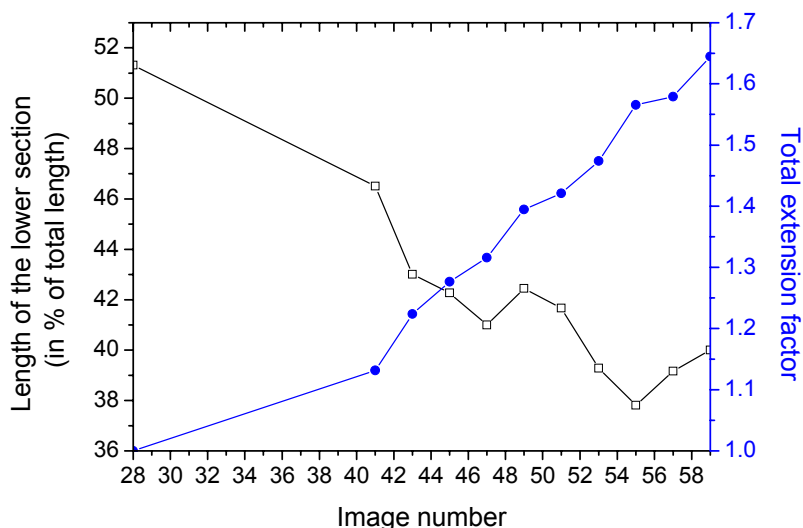


**Figure 126: The percentage length of the lower section and the extension factor of the whole chain at different chain lengths.**

Finally, due to the large DNA ball in close vicinity to the strand, a representative analysis of the fluorescence intensity is not possible for this series.

### Reversible stretching of a fixed strand

The wide-field imaging series in Figure 127 shows the super-long DNA strand from the above experiment (cf. Figure 124), which has been pre-aligned and fixed at two positions: the lower chain end and at the corner point. The extension factor of the strand was previously calculated to be 1.26, so similar to a tightened violin string, the DNA between these two points is already under significant tension. The black arrow indicates the sample movement direction. Now, in analogy to plucking the violin string, the stationary tip is used to stretch the strand northwards (image no1-3). If the tension is large enough,

the DNA escapes the strain, by slipping away underneath the cantilever apex and snapping back to its previous position (image no.5 and no.8). In this image series, the DNA could be stretched repeatedly by moving the sample against the tip. The last three of these cycles are presented in Figure 127. Finally the strand ruptured, as shown in the final image (no. 12).

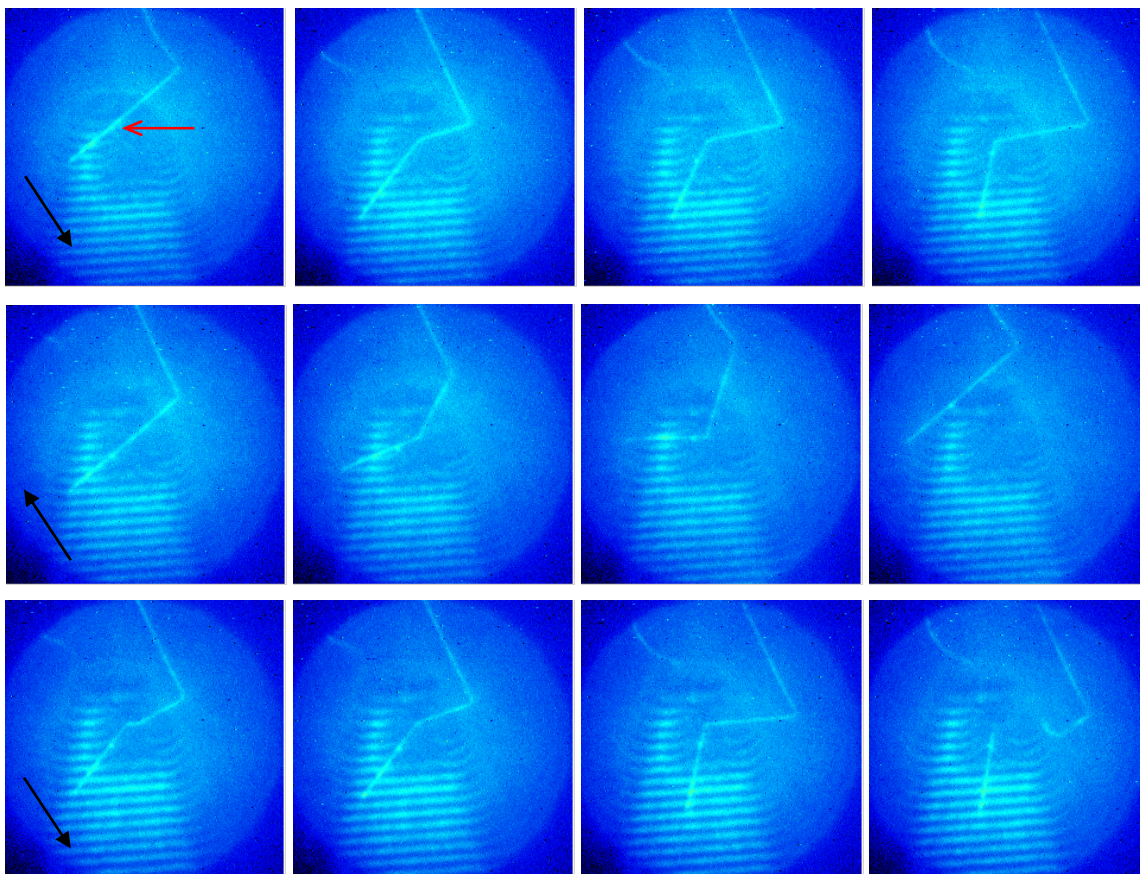


**Figure 127: Manipulation wide-field image series of super-long DNA ( $28\mu\text{m}^2$ ); the red arrow indicates the tip position; the black arrow shows the sample movement direction.**

Although the DNA glides along the tip during stretching, as has been demonstrated in the previous imaging series (cf. Figure 126), it was now firmly fixed to the corner position. These points of attachment to the surface are indicated by the blue pins in Figure 128. In order to prove that the strand is in fact immobilised and firmly stuck at these points, the relative extension factors for the top and lower sections of the DNA are calculated during an extension cycle. If both sections expand at the same rate, thus maintaining the same

relative length, then the DNA must be fixed at the corner position. However, if gliding is possible around this corner, then more and more DNA from above the corner pin will be pulled down as tension in the stretched strand rises and the relative length of the top section will increase compared to the lower section.

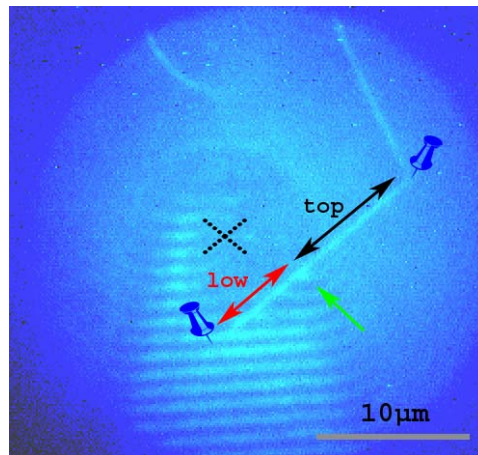


Figure 128: The DNA was fixed firmly to the sample at the positions indicated by the blue pins. The cross shows the tip position and the green arrow points to the DNA node. The length increase for the top and lower sections of the DNA is compared during stretching.

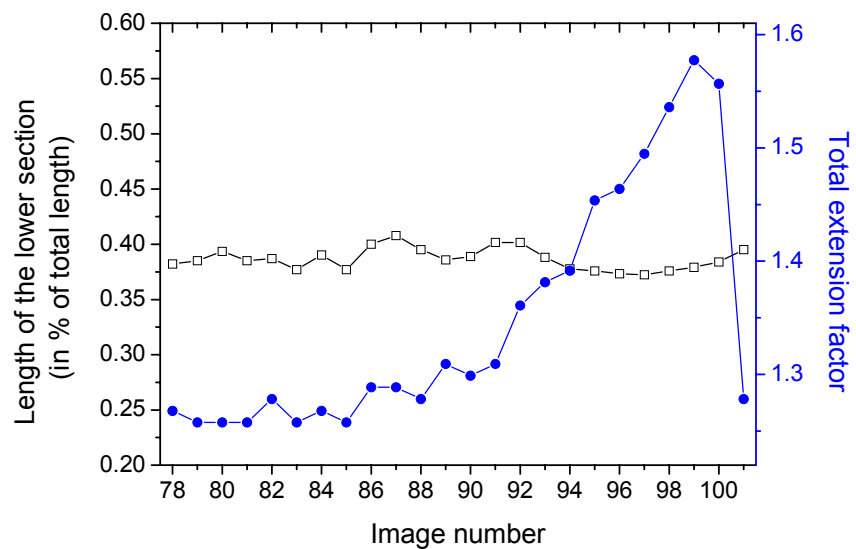


Figure 129: Relative length of the lower DNA section compared to the total extension factor.

The results of this measurement are shown in Figure 129. Stretching the DNA gradually increased the total extension of the chain between the pins. However, in contrast to the image series described previously in Figure 126, the DNA is now fixed at the corner point and the relative length of both sections remains constant. Thus, the whole chain is stretched in a uniform manner, with all parts of the strand contributing equally to the increase in length.

Since the relationship between DNA extension and force is known for a single strand and has been described by conventional DNA force curves (cf. Figure 26), it is possible to assign a value for the tension in the chain by measuring the length of the DNA during the stretching process. However, it should be noted that the high dye concentration generally influences the characteristic shape of the DNA force curves to the extent that the uniform B-S transition is no longer a plateau, but is rather replaced by a gradual increase in force (cf. Figure 35). The DNA was frequently stretched to about 1.6 times the contour length, which is well into the range of the B-S transition, but interestingly, not enough to reach the end of the B-S plateau at  $\sim 1.7$  extension, after which the chain elastic modulus changes and the tension in the strand increases sharply. With or without dye, the force on the strand will have reached about 65pN at an extension factor of  $\sim 1.6$ , a level, which was repeatedly reached during the stretching cycles.

Now that the extension factor of the DNA is known for each image in the series, the average fluorescence along the strand can also be measured by taking line profiles as described in Figure 123. The graph in Figure 130 corresponds to the manipulation experiment depicted in the first two image rows of Figure 127 and shows an analysis of the fluorescence intensity vs. the extension length.

Both plots of the pulling cycles for the first row (cf. red circles) and middle row (cf. black squares) in Figure 127 show a clear inverse linear relationship between chain stretching and average fluorescence. Starting at a value of about 200, the average fluorescence decreases with strand extension. The fluorescence is then regained immediately after the strand snaps back to its original position. However, the slope of this decrease changes between each of the pulling cycles. The reason for this is not completely clear, but it

may be an artefact due to the background luminescence of the cantilever, which is often visible in wide-field imaging. In this series the shadow of the cantilever can be seen as a striped interference pattern below the tip apex. By either pulling towards or away from the cantilever shank, more or less of this background signal contributes to the measured fluorescence line profile, thus, influencing the slope of the graph. Nevertheless, all of the ~10 fluorescence curves measured showed a linear decrease in the fluorescence, albeit with variable slopes.

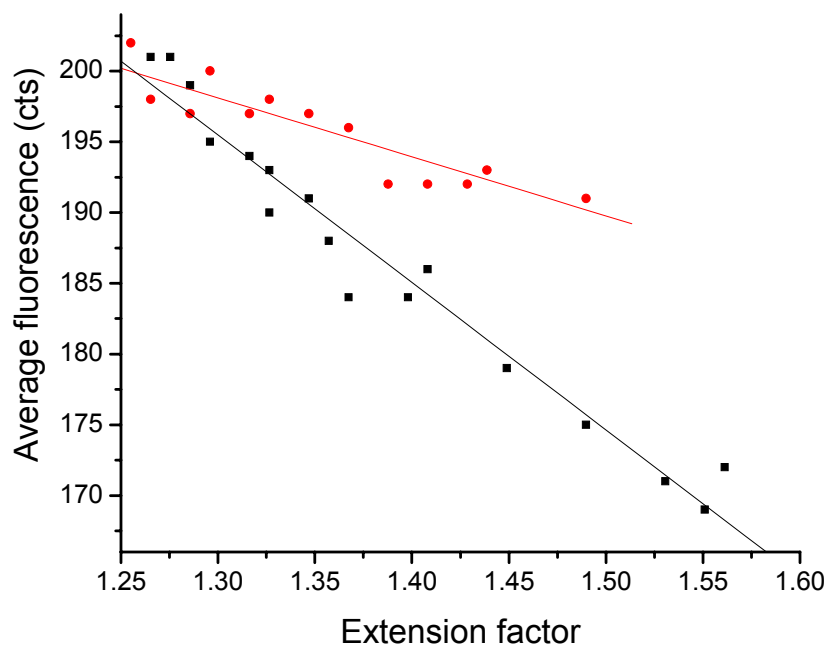


**Figure 130: Average chain fluorescence vs. extension factor for the top row (red) and middle row (black) in Figure 127.**

## Local attachment points

Another image series is shown in Figure 131. As in the previous examples, the DNA tends to adhere to the surface at certain positions, indicated by the green arrows. These have been explained by nicks or local unhybridised regions along the chain, which stick to the surface through hydrophobic interaction. One by one, all of these links are broken and the DNA is zipped off the surface. In the last image the DNA has escaped from underneath the tip and snapped back into its original conformation.

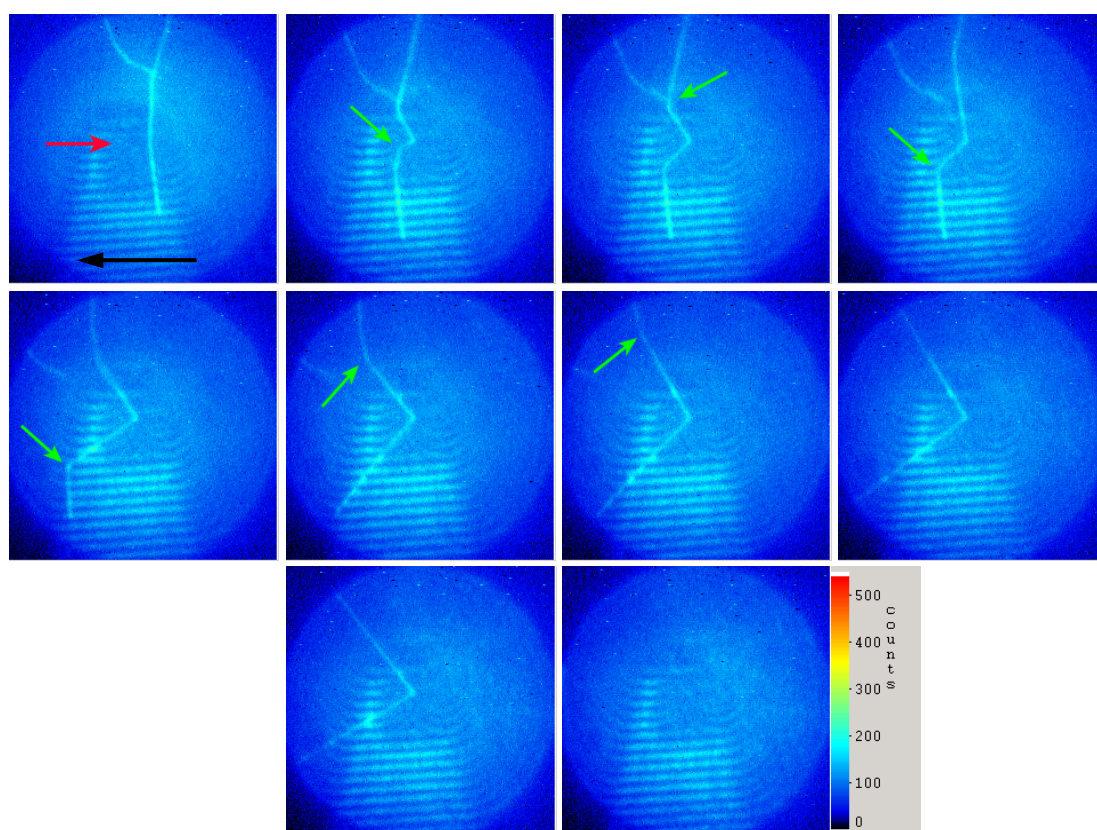


**Figure 131: Zipping a super-long DNA strand off a silanised surface (image size  $28\mu\text{m}^2$ ). The red arrow indicates the tip position and the sample movement is given by the black arrow. The green arrows show the points of attachment to the surface.**

The results of the fluorescence analysis for this series are shown in Figure 132. Both parts of the stretched DNA strand (above and below the tip) display a linear decrease in average fluorescence counts with strand extension. The chain can be stretched to nearly 1.6 times the original length, which is close to the extension factor at the end of the B-S transition (1.7). Beyond this value

the stretch modulus of the DNA is known to change. The strand stiffens and further stretching leads to a rapid build up of chain tension. None of the DNA strands in the measured stretching series were observed to extend beyond a factor of about 1.65. At this point, the strands either ruptured or slipped under the tip. It is interesting to note that the maximum extension observed is about the length of the B-S plateau. However, it is not completely clear whether greater lengths were ever reached, because the acquisition time for one camera image was one second, during which slightly higher extension factors could have been achieved. By speeding up the camera frame rate, more detailed information could be gained on this crucial stretching region.

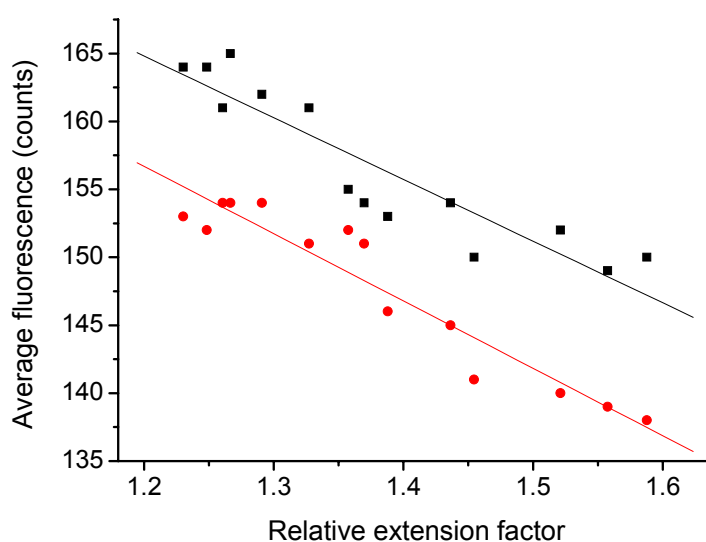


**Figure 132: Fluorescence of the upper (above the tip, black squares) and lower (below the tip, red circles) DNA strand section vs. extension.**

## DNA Rupture

Shoelaces usually tear at the knot, because at this position the strand experiences the highest lateral strains. The same should hold true for DNA. From Figure 122, it is clear that during stretching, the tip will locally bend the strand beyond the natural curvature expected for a tube-like molecule such as DNA (persistence length  $\sim 50\text{nm}$ ). Therefore, the greatest strain will occur immediately at the tip and this will be the position with the highest rupture probability. In addition, the possibility of roughening the DNA and creating

local nicks has been proposed in conjunction with the DNA gliding along the cantilever (cf. DNA fixation in Figure 124). This would create predetermined breaking points along the DNA chain. In fact, rupture events did often occur immediately at the tip position. An example is shown in Figure 133. After rupture, the left end of the strand is fixed to the surface, possibly by a newly formed sticky end. The other severed end snaps back up into the solution (image no.2), before gradually returning to the surface (image no.3).

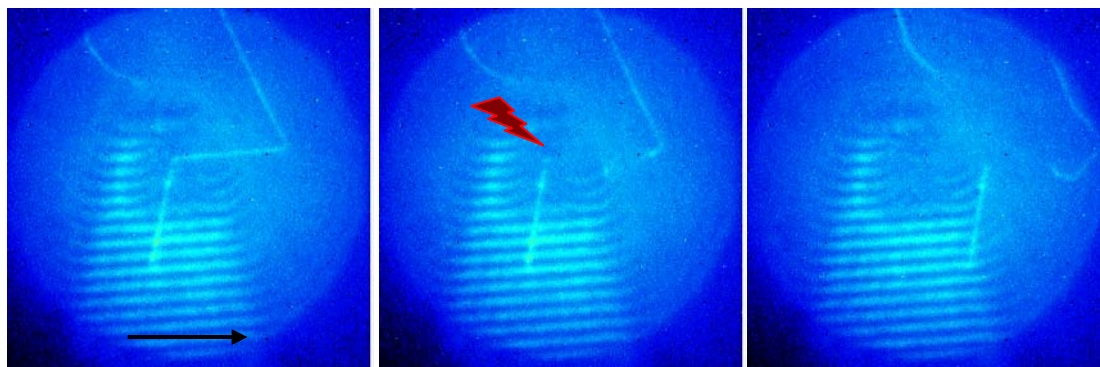


**Figure 133:** Consecutive image frames (size  $27\mu\text{m}^2$ ) from a series showing a typical DNA rupture event at the tip (red lightning bolt); the sample movement direction is indicated by the black arrow.

However, rupture does not always occur at the tip. The example in Figure 134 shows a highly stretched strand that snapped at a position along the DNA about  $3\mu\text{m}$  from the tip. The rupture position is indicated by the red lightning bolt. The two loose ends are then pulled apart as indicated by the red arrows.

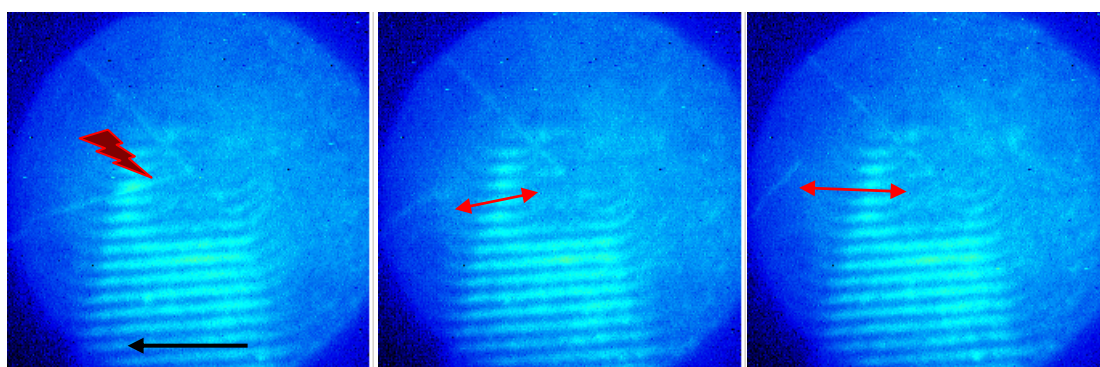


**Figure 134:** DNA rupture event in the middle of the strand (red lightning bolt); the sample movement direction is indicated by the black arrow. (image size  $27\mu\text{m}^2$ )

## **Summary of the lateral stretching experiments**

DNA strands, which have been fixed to a silanised coverslip by at least two points, can be repeatedly stretched parallel to the sample surface, thus confirming the high elasticity of single DNA chains, which was predicted by single molecule force spectroscopy [17]. The strands are generally extended in a uniform fashion, with each section of the chain contributing equally to the length increase. Occasionally the DNA chain slides along the tip during stretching. Furthermore, the strands stick to the surface at specific points, resulting in a non-uniform zipping motion during rupture of these links. Strand rupture frequently occurs at the tip position, but the DNA chain has also been observed to snap in the middle during stretching.

An analysis of the fluorescence intensity in the images provides a means to compare the fluorescence signal of dyes associated or intercalated into a DNA strand for different stretching lengths. As shown previously by force spectroscopy, the length of a strand is directly related to a specific chain tension. Thus, by simultaneously monitoring the length and fluorescence of a single DNA strand in the optical images, the relationship between dye fluorescence and force can be evaluated.

The results of these measurements indicate that there is a fully reversible inverse relationship between average strand fluorescence and stretching length. The exact slope of this relationship appears to vary for each of the stretching experiments, but this may be due to background signal from the cantilever tip. Furthermore, the strands can be stretched to ca. 1.65 times the original contour length, before either rupturing or slipping away underneath the cantilever tip. Earlier findings by Smith et al. [17] have shown that DNA can be overstretched to approximately 1.7 times the contour length with a force of 65pN. At larger extensions the stretching force increases rapidly. Evidently the forces reached by lateral force extension are therefore at least ca. 65pN, corresponding to the B-S plateau region in DNA force curves.

## 5.7 Discussion of the combined AFM/optical experiments on DNA

### The nature of DNA adhesion to different surfaces

The image sequences showing the lateral manipulation and stretching of super-long DNA strands provide the profoundest insight into the surface adhesion mechanisms of DNA. On polylysine, DNA is rarely mobile enough to be displaced and generally adheres strongly to the surface by the whole chain body. This can be attributed to the electrostatic interaction between the negatively charged DNA phosphate backbone and the positively charged lysine moieties on the surface.

On silane, DNA interacts with the substrate at specific points. By exerting an increasing force these can be torn off one by one in a zip-like fashion. Strong ionic bonds are lacking on silanised surfaces, but possibly local unhybridised regions along the DNA are responsible for the site specific surface adhesion. Since these regions are purportedly hydrophobic [115], they can interact with the water-repelling silane layer, in contrast to the main chain body, which is charged and hydrophilic. The strength of these hydrophobic attachment points is variable. Most are broken before the DNA reaches the end of the B-S plateau length i.e. at 65pN, but some withstand higher forces, even surviving severance of the DNA chain itself.

Furthermore, the adhesion mechanisms involved in AFM force spectroscopy, governing DNA attachment to gold-coated substrates or to the  $\text{Si}_3\text{N}_4$  cantilever tip, may be of a similar hydrophobic nature. In this context, it is not surprising that force spectroscopic data on silane coated surfaces strongly resemble the results achieved on gold in terms of rupture force and rupture length, whereas DNA on polylysine afforded different pulling curve statistics (cf. table 5).

This conclusion contradicts earlier findings by Bensimon et al., suggesting that a covalent bond is responsible for DNA binding to silanes, which is formed by the electrophilic addition of the free terminal DNA phosphate group to the vinyl end-group of the alkene-silanised surfaces [252].

Similar hydrophobic interactions may be the dominant adhesion mechanism involved in a greater spectrum of other AFM force pulling experiments with different molecules, such as organic polymers or sugar chains. Essentially these interactions are based on *Van der Waals* bonding between oleophilic materials and their repulsion to enter into the water phase.

### **The nature of TO-PRO-3 adhesion to DNA**

The fluorescence bleaching experiments show that there are at least two bleaching rates, corresponding to two dye species, for TO-PRO-3 associated to DNA. The slow rate is attributed to intercalated dye, for which the chromophore is more protected from free radicals. The fast rate could be due to electrostatically attached or groove-binding dyes, which are more exposed to radicals or singlet oxygen and thus bleach faster.

The best imaging results are achieved using relatively high dye concentrations, for which all intercalation slots are likely to be filled and a high degree of external DNA binding has been proposed [190]. To study the DNA binding mechanisms and dye dynamics of TO-PRO-3 under tension, the fluorescence is compared for different DNA extension forces. Five possible results were envisaged:

Firstly, a higher average fluorescence is detected with increasing strand length. However, this solution bears no feasible model and is therefore highly unlikely. Secondly, the fluorescence intensity stays constant with increasing length. This would mean that the number of dye sites is related to the DNA extension length, i.e. more sites are generated as the DNA is stretched. For intercalated dyes this is not possible and even externally bound dyes are associated to the charge on the DNA surface, which is constant for a given number of base pairs. Therefore, this result is not expected. Thirdly, the dye fluorescence decreases linearly with length. This dilution scenario assumes a fixed number of dye positions, which are merely distributed over an increasing length during stretching. Fourthly, dyes could be expunged from the DNA with increasing strand tension. If the rate of dye dissociation is proportional to the length i.e. the force, then a quadratic decrease in average chain fluorescence with length would be observed. Finally, a sharp drop in dye

association to the DNA at a certain length/force value would be the consequence if processes such as DNA double strand melting or dehybridisation were induced during the stretching process.

The results of the lateral stretching experiments show that there is a reversible linear relationship between chain length and fluorescence intensity. When the strands are stretched the average fluorescence decreases with increasing length. This shows that the number of dyes along the DNA is maintained throughout the experiment. Stretching merely leads to a dilution of the fluorescence. The fluorescence signal is fully restored, when the DNA snaps back into its original conformation.

Evidently no new dyes are incorporated into the DNA during stretching. The association rate for TO-PRO-3 is high and so the limiting factor is the number of free dye positions available for association, which is consequently not increased during stretching. At the same time the dyes are not expelled from the DNA either.

In summary, although intercalating dyes are known to significantly affect the shape of DNA force curves [131, 132], at least up to the B-S transition force region, no change in dye dynamics, to and from the DNA, can be registered under strand tension.

This is not necessarily expected, as DNA overstretching might well have expunged the intercalated dyes. However, externally bound TO-PRO-3 could be less sensitive to chain extension than the intercalated dyes. Above a concentration ratio of 5:1 bp/dye, cyanine dyes can bind externally to the DNA [186]. Thus inhomogeneous binding modes could make an interpretation of the results difficult. A possible solution would be to reduce the dye concentration below the limit of 5:1 bp/dye, although this would be at the price of a reduced image contrast.

To test the nature of dye adhesion to DNA, the polarisation angle of the dye fluorescence was examined. Previous experiments have used optical tweezers to stretch tethered DNA strands and measure the polarisation angle of the fluorescence for intercalating dyes such as YOYO-1. Their results indicate a transmission dipole moment of  $69^\circ$  relative to the strand axis [139]. This value could be an average of the two binding modes: intercalation ( $90^\circ$ ) and groove binding ( $60^\circ$ ).

A similar experiment on pre-aligned single DNA strands on a glass surface was therefore conducted. The results of these measurements show that the fluorescence signal from the aligned and stretched DNA strands is randomly polarised. Irrespective of the alignment angle of the strands, no clear polarisation of the emitted fluorescence could be detected. The most obvious explanation for this finding is that the majority of the dyes are not intercalated, but rather loosely adsorbed to the DNA surface.

Therefore, to establish the behaviour of intercalated TO-PRO-3 alone, the dye concentration would have to be reduced, assuming this binding mode exists, as suggested by Beisker et al. [107].

### **The B-S transition in DNA force spectroscopy**

P. Cluzel [16] and S. Smith [17] were able to show that at a longitudinal stress of 65pN, dsDNA B-DNA undergoes a reversible transition to a stretched “S-form”, which is 1.7 times longer. The transition is highly co-operative, occurring within a narrow force regime of 2pN and increasing the rise per base pair from 3.4 to 5.8Å [135]. Gaub et al. have used AFM force spectroscopy to pull single DNA molecules to even higher forces and observe a second “melting” plateau in the force-extension curves, which is attributed to the dissociation of the double helix [130]. By measuring the plateau force height in acidic and basic conditions, Williams and Bloomfield have alternatively argued that the B-S transition is itself due to melting and dissociation of the double helix, rather than a stretched DNA conformational change [174].

With the combined optical/AFM setup it is possible to monitor the DNA fluorescence, while imposing a specific force on the strand. Using this new approach, the theories of B-S and melting transition can be put to the test. The fluorescence signal gives a measure of the degree of dye intercalation into DNA. It seems reasonable that the dyes, which are stuck between the base pairs, would separate from the DNA double helix during a strain induced melting process. Even if the dyes stay with the two single strands as they dissociate from another, some kind of local accumulation is expected, which could be identified as brighter and darker regions along the remaining fibre.

Thus stretching the DNA strand into the 65pN plateau force region should show whether the B-S plateau in the force curve can in fact be associated with strand separation or is the result of a conformational transition.

However, no dramatic change in the fluorescence is observed up to an extension factor of  $\sim 1.65$ , which is nearly the complete B-S transition length. Under tension the fluorescence decreases linearly with the extension length, but remains uniform along the whole chain and returns completely when the DNA recoils to its original length. The immediate conclusion is that no strand dehybridisation is involved in the B-S transition.

Although this is probably true, there could also be other reasons for the lack of dye dissociation during DNA stretching. Firstly, the intercalating dye itself, which intercalates into DNA and wraps around the helix with the free arm, could be preventing strand dissociation. YOYO-1 prevents folding of giant duplex DNA [182]. Possibly these dyes can act as clamps, thereby fastening both strands together through electrostatic adhesion.

Secondly, it was shown that a high degree of external binding is probably involved for the TO-PRO-3 concentrations used. The dye might therefore stay with the DNA fibre even if local melting occurred. Other similar cyanine dyes also bind to RNA, but with significantly lower binding constants and very much decreased fluorescence enhancements [106, 253]. This should be noticed in the fluorescence images.

Finally, it would be interesting to stretch DNA beyond the B-S plateau range. At extensions of more than 1.7 times the contour length, the DNA undergoes a second enthalpic transition. This second shoulder in the force curve at ca. 250pN has been attributed to double helix denaturation [38, 39]. Possibly dye dissociation would set in at these higher forces.

## 6. Conclusion and Outlook

### 6.1 Summary and conclusion

The motivation for this work was to combine the single molecule techniques of *AFM force spectroscopy* and *fluorescence microscopy*. Through the AFM cantilever, a mechanical influence can be exerted on single fluorescent dyes. At the same time, the emission spectra of other polymers or dye stained DNA strands can be investigated under strain, allowing new insights into the physical properties of single molecules. To this end, a combined AFM/optical imaging setup was constructed, which enables the real-time manipulation of a sample with an AFM tip and the simultaneous optical TIR imaging of the fluorescence.

Early experiments focussed on the fluorescence detection and force spectroscopy of polymer tethered molecules such as Cy5 or a range of hemi-cyanines. In principle, it is possible to image these fluorophores either by confocal, wide-field or TIR methods and single dye spectra were available. However, the low fluorescence quantum yield, photostability and difficulties in the chemical attachment rendered these dyes unsuitable for the combined experiments. Alternatives were sought, although a renaissance of these systems is envisioned should the chemical challenges be overcome.

On the other hand, the preliminary force spectroscopic work led to the investigation of various polysaccharides and the influence of complexing palladium on the mechanical properties of these polymers. A new type of force curve with horizontal plateaus was discovered for these systems and investigated in depth. Furthermore, a solvation model was devised, which describes the plateau-type force curves based on the hydration energy of a single polymer chain.

By intercalating TO-PRO-3 into DNA, a more promising fluorescent polymer system was established for the combined optical/AFM experiments. The following detailed analysis of the photophysics showed that it is feasible to image single DNA strands with these dyes. Furthermore, optically transparent polylysine-coated or silanised glass surfaces were adapted, which permitted characteristic single molecule DNA force spectroscopy.

However, the DNA was strongly fixed to the positively charged polylysine layer and displayed a clear propensity towards condensation. The morphological stages of condensation, from single chains, over dense rods, to aggregated DNA globules, were described extensively. An influence on the DNA force curves was also observed, manifesting itself in very long uncharacteristic pulling events of DNA on polylysine surfaces.

On silanised glass, the DNA is not nearly as liable to condensation. Moreover, the single strands attached to the hydrophobic surface at specific points, especially the termini. In addition, a chemical preparation protocol, involving a pH change, led to the discovery of super-long DNA strands. This is attributed to the polymerisation of short DNA fragments by junction formation.

Using the combined setup, it is possible to manipulate single DNA strands. On polylysine, DNA can be displaced and cut. Furthermore, by transferring a condensed ball to the tip, patterns or letters of DNA-ink were written onto the surface. In contrast, on silanised glass surfaces, long DNA strands can be stretched and extended elastically to 1.65 times the contour length, leading to successive rupturing of the attachment points.

Unfortunately, it turned out that AFM force spectroscopy and simultaneous optical imaging experiments are compromised by inherent practical limitations. These include the imaging frame rate, cantilever drift for slow pulling speeds, restrictions imposed by the optical focus and, most importantly, the selective addressing and attachment of a single dye or polymer to the cantilever tip. The latter is particularly significant, because single molecule microscopy requires dilute samples in order to image an individual dye against a non-fluorescent background. On the other hand, conventional single molecule force spectroscopy employs the shot-gun approach. The improbable event of tip attachment is achieved by repeatedly dipping the cantilever tip down into a densely covered sample surface. In addition, this incongruity between the two methods could not be resolved by utilising the fluorescence images to gain a rough knowledge of the molecule position, thereby increasing the attachment probability.

The solution was found in a new technique, which was termed *lateral single molecule force spectroscopy*. This method circumvents the aforementioned difficulties by stretching the polymers parallel to the coverslip

surface instead of vertically away from it. Specific cantilever attachment is no longer required. The tip is applied by pulling at the midsection of a strand, which is fixed to the surface by at least two points.

In this way, the overstretching elasticity of DNA can be observed optically and in real-time. Similar to a violin string being pulled taught, the DNA snaps back into its original conformation when escaping from underneath the tip apex. The images also revealed an inverse linear relationship between the average strand fluorescence and the stretching extension. At least for the B-S plateau force region of up to 65pN, no dramatic drop in dye fluorescence is observed. These results refute speculation that the B-S transition is the result of double helix dehybridisation.

## **6.2 Outlook**

Future experiments and improvements are envisaged for the various single molecule fields related to this work.

### **Force spectroscopy on sugars**

The force spectroscopy experiments on sugars could be extended to study the in situ reactions with complexing agents such as Pd metal derivatives or other reagents. By reversibly measuring the force curves of a stretched polymer before, during and after addition of the reactants, the direct influence on the mechanics of a single polysaccharide chain may be determined. Possibly, new reaction intermediates or pathways could be stabilised by the use of chain tension or, alternatively, conformational changes such as the chair-boat transition prevented by the action of metal complexes. The reaction mechanisms and kinetics of single polymer molecules would be a lucrative field to investigate.

More research is needed to fully understand the plateau force curves observed. Especially a change of sample conditions such as solvent polarity, temperature or pH should have an influence on the hydration energies experienced by these molecules when pulled from a densely covered sample surface into a relatively poor solvent. A quantitative analysis of these factors

would corroborate the hydration energy theory put forward to explain plateau force pulling events.

### **Other polymer systems for AFM force spectroscopy**

The application of force spectroscopy to different systems could provide macromolecular chemistry with a new tool for the analysis of the mechanical properties of macroscopic polymers. Parameters such as enthalpic conformational transitions under strain, rupture strengths, desorption or chain-pull-out forces may be relevant for tear-propagation or the specific surface adhesiveness of polymer materials. Furthermore, dynamic force spectroscopy enables an in-depth study of the frictional and visco-elastic behaviour of single chains under mechanical strain [217, 254-256]. A multitude of organic polymers [37, 99, 257-261] or siloxanes [36, 262-267] have already been investigated.

### **Chemical attachment**

A crucial question for nearly all cantilever manipulation experiments that do not rely solely on pushing and pulling is the physical fixation of a single molecule to the tip. A strong chemical attachment would be an enormous step forward for the whole field. True covalent bonding would enable an accurate measurement of the bond rupture forces and greatly facilitate reversible pulling, thereby enabling single molecule chemistry on a polymer that never falls off the tip. Attempts in this direction have been made [42, 268, 269], but a universal solution has yet to be found.

### **Manipulation of single TDI molecules**

The influence of a cantilever tip brought into the proximity of a single molecule has been studied previously and quenching [228, 229, 270] or field enhancement [223] effects were proposed. However, a clear improvement would be to use the best dye available for these experiments - terrylenediimide (TDI). This would provide unequivocal evidence for or against quenching. In addition, applying mechanical pressure to the environment of a

single fluorophore might lead to spectral shifts in dye fluorescence or other new phenomena.

### **DNA patterning and conducting wires**

The need for new smaller conducting nanowires [244, 245, 271, 272] and the potential use of DNA chains [248-250] has been discussed. The new method developed, involving a cantilever tip as a DNA water-pen for writing thin polynucleotide structures on positively charged surfaces, may have some potential in this context, if the practicability can be ameliorated.

### **The combined optical/AFM force experiment**

The shortcomings of the combined AFM force spectroscopy and optical imaging experiment have been discussed. Nevertheless, a range of important improvements could still be made. These include:

- The use of sharp, long cantilever tips.
- Chemical treatment of the tip surface to improve adhesion.
- A faster imaging frame rate.
- Different DNA dyes [106, 176, 183], in particular YOYO-1 [190, 273].
- A reduced intercalator dye concentration.
- AFM scanning of the sample to determine the exact position of the DNA chain, before attempting a pulling experiment.
- The use of short DNA strands such as  $\phi$ X-174.
- Prior attachment of the DNA to the tip, rather than the surface, before surface contact. This would guarantee a number of dangling molecules and possibly improve the probability of a successful pulling experiment. Tip contamination could be minimised.

### **Single molecule lateral force spectroscopy**

The DNA strand tension can be calculated from the chain extension length, by comparison with a standard DNA force curve. However, it could actually be determined directly from the cantilever twisting deflection signal. This would require the use of a quadrant photodetector for the AFM deflection signal and the calibration of the cantilever lateral spring constant.

## Electronic switching of a single luminescent polymer

Finally, a completely new type of experiment is proposed, which combines fluorescence detection, AFM force spectroscopy and also single molecule electrical conduction.

An electroluminescent polymer (and fluorescent) could be picked up and spanned between the cantilever and a transparent conducting indium tin oxide (ITO) surface. Applying a current would drive the molecular luminescence, which could be turned on or off at will (artificial blinking).

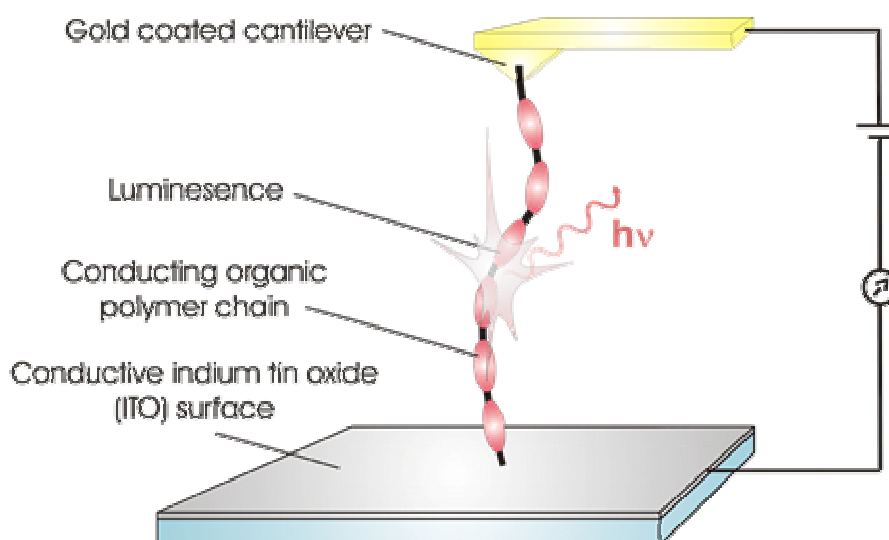


**Figure 135: A single electroluminescent polymer spanned between the tip and a conducting surface.**

The single molecule fluorescence of conducting polymers has been examined previously, most notably of the conjugated polymer MEH-PPV [274-277]. These dyes have great industrial significance as light emitting diodes.

Preliminary experiments show that it is possible to stretch MEH-PPV with an AFM tip, the force curves being similar to those of other organic polymers [258]. The main challenge will be to establish a good electrical contact between the surfaces and the polymer chain so that current can flow without having to apply high voltages, which might short the system [278]. Double bond breaks along the chain and a potentially low photo-oxidative stability must also be taken into account, but if the experiment succeeds it will undoubtedly be the smallest light bulb in the world.

## Appendix 1: Coverslip surface preparation procedures

### Coverslip cleaning procedures

Glass coverslips (24mm\*60mm) are cleaned by immersion for >1 day in a Hellmanex™ solution (Hellma®), which is diluted with ultrapure HPLC water. The coverslips are then washed and submersed for another day in HPLC water, where they can be stored prior to use. After extraction they are washed copiously with HPLC-pure water, dried under vacuum and used expeditiously to reduce the density of fluorescent impurities.

### Gold coated coverslips

To prepare gold coated coverslips, first, a 5nm Cr/Ni-layer has to be generated on the clean glass surface by vacuum deposition, which is then followed by a 35nm thick Au layer. The intermediate Cr/Ni layer increases the adhesion of the gold on the glass.

### Polylysine coated coverslips

The thin film coatings of polylysine (Fluka®, poly-L-lysine-hydrobromide; mol wt. 30000-70000; 1 PL strand contains ca. 220 lysine groups [112, 120] ) on the cleaned coverslips are achieved by compressing a 5µl drop of a 5µg/ml aqueous PL solution between two coverslips and then separating the surfaces after overnight drying in a evacuated desiccator.

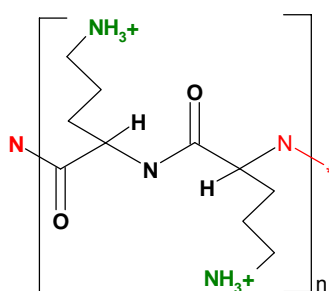


Figure 136: Polylysine

The amino moieties of the polylysine result in a net positive charge on the surface, to which the negatively charged DNA can adhere. Assuming complete adsorption of the polylysine and a homogeneous distribution on the surface, a 5µl polylysine drop corresponds to  $\sim 1.1 \cdot 10^{-10}$  mol of lysine

groups ( $M=227\text{g/mol}$ ). Evenly distributed over the surface of two coverslips ( $2*24*60\text{mm}=2.88*10^9\mu\text{m}^2$ ), this results in a lysine moiety density of 23000 charged groups per  $\mu\text{m}^2$ , which is ca.  $\sim 105$  polylysine strands/ $\mu\text{m}^2$ .

### Alkylsilanised coverslips

Cleaned and vacuum dried coverslips are silanised by gas-phase adsorption. A 1ml drop of 7-octenyl-trichlorosilane (Sigma<sup>®</sup>) is allowed to evaporate in a previously evacuated desiccator containing the coverslips. After  $>1$  day of adsorption in the silane-saturated atmosphere, the originally hydrophilic coverslips acquire a strongly hydrophobic surface. The surface contact angle of the aqueous solutions increases (c.f.  $15^\circ$  for  $\text{SiO}_2$  [279]), due to the formation of a water-repelling silane monolayer on the glass. Coverslips are used immediately after silanisation.

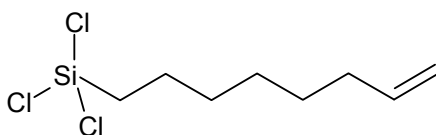


Figure 137: 7-Octenyl-trichlorosilane

### The silanisation process

The choice of silanisation conditions depends on the substrate. Glass, oxidised silicon or silica have amorphous surfaces with a variable number of Si-O-Si and Si-OH groups exposed on the surface [280, 281]. The silanol groups of these substrates are sufficiently reactive to allow substitution reactions with alkoxy silanes, such as APTES (aminopropyl-triethoxysilane) [282]. Generation of the silane film can occur in solution, in which case 5% silane solutions in toluene are used [283], or by gas phase adsorption [279, 284]. Gas phase adsorption leads to the well ordered monolayers on the surface.

However, the reaction of the surface silanol groups with monomethoxysilanes produces poorly stable films [252, 264] and it is not clear whether the silane layer is merely physisorbed through hydrogen bonds or actually forms covalent bonds to the surface. The stability can be improved by

using multiple reactive groups, such as trichloro- [265, 285, 286] or trimethoxysilanes [287], which can form cross-links when baked at 100°C.

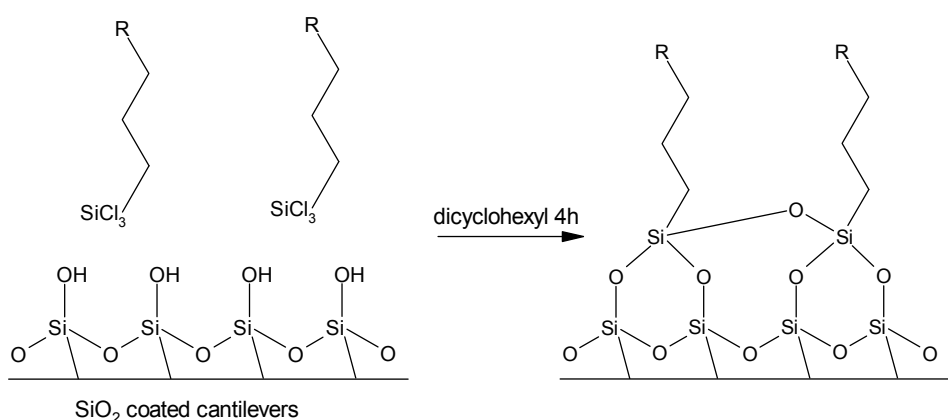


**Figure 138: Cross-linking with trichlorosilanes**

It has been suggested that water is the decisive agent in this process. Water hydrolyses the chlorosilanes to form silanol groups. These then condensate, thereby generating a cross-linked layer of silane on the substrate surface [287].

## Appendix 2: Sample preparation: polysaccharides

### Buffer solutions (MES, PBS)

The MES (2-[N-Morpholino]-ethanesulphonic acid sodium salt) buffer is generated, according to Sigma<sup>®</sup>, by neutralising 50mmol of the aqueous acid with 0.9mmol of a 0.1M NaOH solution to obtain the buffer solution with a pH of 5.5. The pH was verified using a pH-meter. Phosphate buffered saline (PBS, pH 7.4) ensures a stable physiological pH value of 7.4. It consists of a 10mM phosphate solution with 150mM aqueous NaCl (saline).

### CM-Cellulose (CMC) and CM-Amylose (CMA) solutions

The sodium salts of carboxymethyl-cellulose (Sigma<sup>®</sup>, C5013) and carboxymethyl-amyllose (Sigma<sup>®</sup>, C4947) are each dissolved in HPLC-pure water or PBS to a concentration of 0.5 or 0.1% wt/vol. For plateau measurements the solutions are diluted with HPLC-pure water to 0.01% wt/vol.

### **CM-Cellulose-Pd-en solutions [132]**

The sodium salt of carboxymethyl-cellulose is made by dissolving CMC (0.15mM) in an aqueous palladium-ethylenediamine (Pd-en) solution (0.15mM). After 30 min the solution becomes transparent, slightly yellow and very viscous. It is stored in the fridge at 4°C to stabilise the complex. Prior to use, it is diluted to 0.01% wt/vol.

### **AFM pulling experiments**

Generally, ~30  $\mu$ l of the 0.1% or 0.5% CMC or CMA solutions are added to a glass coverslip with a pipette. The sample is then incubated overnight in a humid atmosphere. The following day the moist samples are rinsed copiously with HPLC-pure water before use. For the plateau curve measurements ~30 $\mu$ l of the 0.01% solution is allowed to dry on the coverslip overnight. The next day, the samples are re-wetted with a few drops of water and rinsed again after a few hours. Typically, a 2kHz sampling rate for the deflection signal and a pulling velocity of between 0.5 $\mu$ m/s to 16 $\mu$ m/s is used (digital filter bandwidth 1kHz).

### **Appendix 3: DNA force spectroscopy**

A 50 $\mu$ l drop of the 20 $\mu$ g/ml  $\lambda$ -phage BSTE digest II (Sigma<sup>®</sup>) stock solution is applied to the corresponding glass, gold or polylysine coated coverslips and left to absorb overnight. The following day, unattached DNA fragments and precipitated salt are purged from the surface by washing with TE buffer. By measuring the UV adsorption spectra of the rinsing buffer it was shown previously that approximately 10% of the DNA remained attached to the gold surface after washing [258], resulting in a DNA surface density of ca. 0,4  $\mu$ g/cm<sup>2</sup>. Finally, a 100 $\mu$ l drop of TE buffer is applied to the DNA sample and the force curves are measured [121].

Force curves on silane are measured by first diluting the original  $\lambda$ -phage digest DNA by a factor of 1000 in MES buffer to afford a 1 $\mu$ g/ml DNA stock solution. A 50 $\mu$ l drop of the DNA solution is then applied to a freshly silanised coverslip and left to incubate on the surface overnight without drying. Following rinsing the next day with MES buffer, the force curves are taken

analogously to the samples on gold or polylysine. To achieve reversible pulls it is important not to press too hard into the glass surface when picking up a molecule and to gradually increase the pulling length of the tip, to prevent early rupture of the attachment.

To determine the effect of TO-PRO-3 on the force curves, the DNA covered silanised surfaces are prepared as described above. A 100µl drop of the stock dye solutions with  $5 \cdot 10^{-6} \text{M}$  TO-PRO-3 is then added as the measurement medium.

## Appendix 4: LabView<sup>®</sup> programs

The first LabView<sup>®</sup> program enables real-time manual control of the piezo-driven sample position in the combined AFM/optical imaging experiments. This is achieved by reading out the keyboard arrow keys and converting this signal into a voltage for the piezo i.e. sample movement.

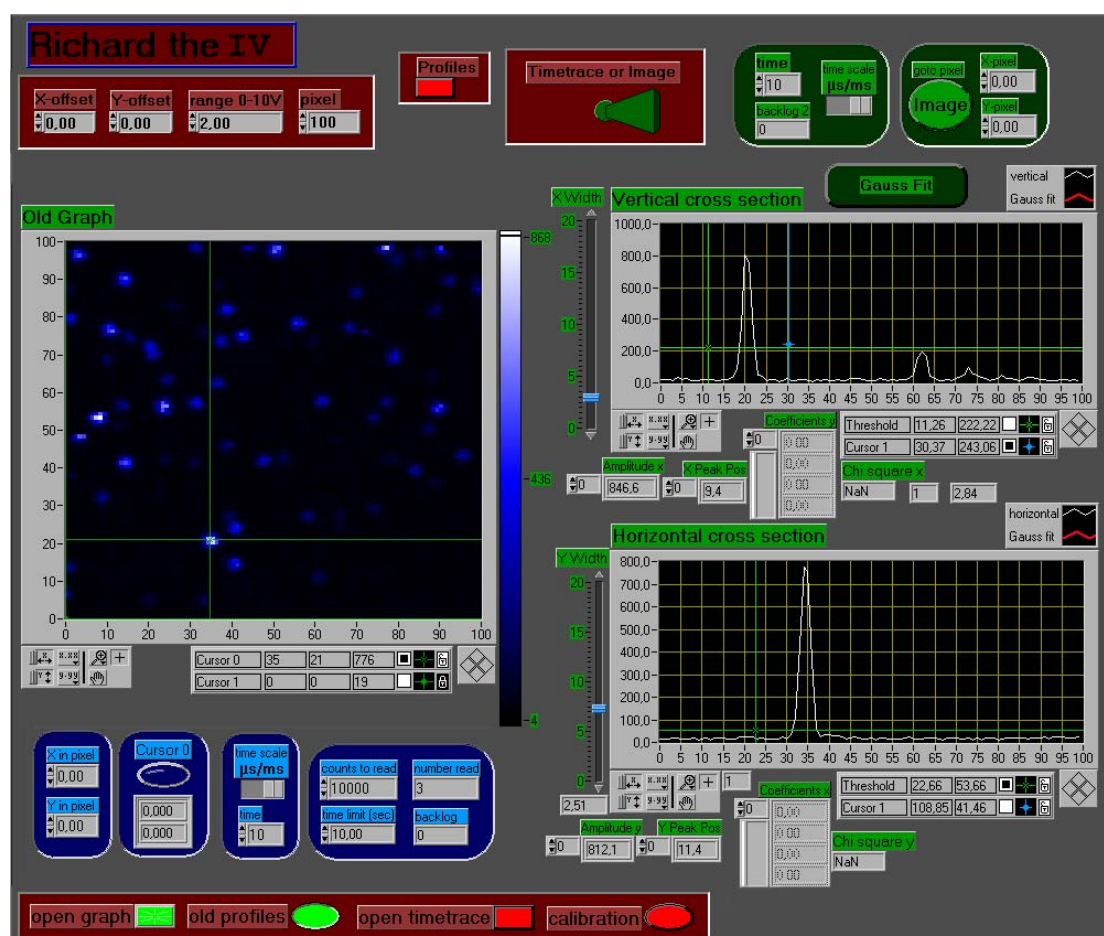


Figure 139: LabView program for confocal scanning images of fluorescent dyes.

The second program is used in confocal microscopy to simultaneously monitor the APD fluorescence signal, while controlling the scanning piezo position (cf. Figure 139). This allows high speed data acquisition of the fluorescence signal with up to 20 $\mu$ s time resolution. Four modes are possible. In the calibration mode the APD signal is plotted continuously. This is used for maximising signal intensity e.g. for pinhole adjustment. The second mode enables time traces of single sample positions e.g. to monitor single molecule fluorescence. The third mode generates confocal scanning images with variable size and integration time per pixel. The sample may then be directed to a user-defined position in the previously scanned image to take a time trace. Finally images may be loaded and analysed by plotting the x and y cross sections. It is also possible to fit these line profiles, e.g. of a single molecule dye, with a Gaussian curve to determine the FWHM of a peak cross-section, thus giving a quick estimate of the setup resolution and objective z-focus.

## **Appendix 5: DNA imaging protocols**

### **DNA solutions**

$\lambda$ -Phage DNA (250 $\mu$ g,  $7.94 \times 10^{-12}$  mol) with a length of 48502bp is obtained from Sigma<sup>®</sup>. After 1:20 and 1:200 dilution with TE buffer (TRIS/EDTA = 150mM NaCl, 10mM Tris, 1mM EDTA; pH = 8) Fluka<sup>®</sup> the final stock solutions with  $3.18 \times 10^{-10}$ mol/l DNA (10 $\mu$ g/ml; c(bp) $1.6 \times 10^{-5}$ mol/l) and  $3.18 \times 10^{-11}$ mol/l (1 $\mu$ g/ml; c(bp) $1.6 \times 10^{-6}$ mol/l) DNA are prepared.

$\lambda$ -Phage digest BSTE II, with a length distribution of 117-8454bp (Sigma<sup>®</sup>) is diluted with TE buffer (Tris/EDTA), resulting in a stock solution of 20 $\mu$ g/ml; c(base pairs) =  $3.1 \times 10^{-5}$ mol/l.

TO-PRO-3<sup>®</sup> (Molecular Probes<sup>®</sup>; MW = 671g/mol) stock solutions are prepared by diluting the original 1mM DMSO dye solutions in a 7:3 Glycerol/Water mixture to afford a  $1 \times 10^{-4}$  M dye concentration. By further dilution in TE buffer, working solutions with a final dye concentration of  $5 \times 10^{-6}$ M and  $1 \times 10^{-7}$ M were generated.

## DNA imaging

DNA images are prepared on silanised or polylysine coated glass surfaces by overnight incubation of a 50 $\mu$ l drop of the  $\lambda$ -phage or  $\lambda$ -phage BSTE II digest DNA solution, in humid atmosphere. After copious washing with the corresponding buffer a 100 $\mu$ l drop of aqueous 5\*10<sup>-6</sup>M TO-PRO-3<sup>®</sup> in TE buffer + 1% slowfade<sup>®</sup> (Molecular Probes<sup>®</sup>) is added and the sample mounted on the inverted microscope stage. Images with 1 sec exposure time are taken with an illumination intensity of 1.2 W/cm<sup>2</sup>. Using this solution, photobleaching is avoided and an image series of the DNA can be taken over a period of minutes to hours without significant loss of fluorescence.

The final DNA concentration on the sample depended on the adsorption and washing process, so an exact comparison of base pair to dye ratio could only be estimated. However, taking the value found for gold surfaces of 10% DNA remaining on the surface, the DNA concentration in a 100 $\mu$ l drop would be  $c(\text{bp}) = 1.6 \cdot 10^{-6} \text{ mol/l}$ . This corresponds to a bp/dye ratio of ca. 1:4.

Silanised and polylysine coated glass surfaces are sufficiently transparent for high contrast imaging of DNA. However, gold surfaces were rejected, because fluorescence absorption and/or quenching greatly reduced the signal detectable through the gold.

## Super-long DNA

To generate super-long DNA, the original  $\lambda$ -phage BSTE digest DNA is diluted in MES buffer (pH = 5.5) by a factor of 1000 to yield a 1 $\mu$ g/ml DNA working solution. A 50 $\mu$ l drop of this solution is applied to a freshly silanised surface and left to incubate overnight. The following day the sample is washed a few times with TE buffer (pH = 8) and mounted for imaging in the corresponding dye solution.

## Appendix 6: DNA straightening procedures

To align the DNA a dried polylysine coated coverslip ( $5\mu\text{g}/\text{ml}$ ) is mounted on a spin coating machine and rotated at 3000-5000 rpm . Following washing with a few droplets of ultrapure HPLC water, two to five  $10\mu\text{l}$  drops of  $3 \times 10^{-11}\text{M}$   $\lambda$ -phage DNA are dispensed on the spinning surface. Finally, the surface is rinsed with TE buffer ( $\sim 300\mu\text{l}$ ).

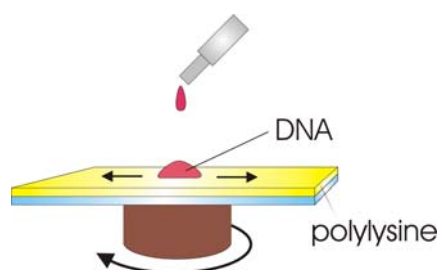


Figure 140: Spin straightening of a DNA sample

For pressure straightening a  $5\mu\text{l}$  -  $50\mu\text{l}$  drop of the DNA solution is placed on a coated coverslip. By quickly placing a second coverslip over the first and applying a force, the solution is spread out evenly between the two glass surfaces. After pressing, the second coverslip is carefully lifted off again.

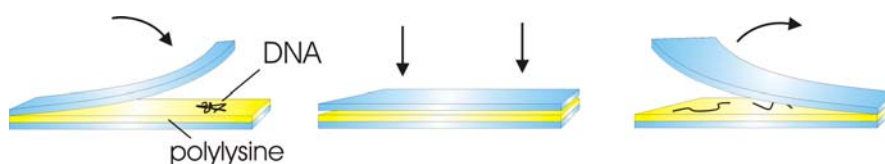


Figure 141: Pressure straightening

## Curriculum vitae

### Personal Data

Name	Andrew Hards
Address	Terofalstrasse 75, 80689 Munich
Born	06.02.1974 in London
Nationality	GB
Marital status	single

### Higher Education

05/1999 - 03/2004	LMU Munich, PhD thesis, Prof. Bräuchle. Subject: The combined AFM manipulation and fluorescence imaging of single DNA molecules.
09/1998 - 04/1999	Hokkaido University, Japan, Diploma thesis, Prof. Shimomura, Institute for Electronic Science. Subject: Monolayers of thiophene amphiphiles with nucleobase head groups.
07/1998	Diploma exam chemistry
11/1993	LMU Munich, chemistry
10/1992-10/1993	TU Munich, electrical engineering

### School

1982 – 07/1992	European School, European Baccalaureate
1980/81	German and American primary school Munich

## **Publications**

*Andrew Hards, Chunqing Zhou, Markus Seitz, Andreas Zumbusch,  
Christoph Bräuchle.*

Simultaneous AFM manipulation and optical imaging of single DNA strands  
(submitted Nano Letters 2004)

*Chunqing Zhou, Andrew Hards, Alexandra Scherer, Andreas Zumbusch and  
Christoph Bräuchle.*

Anomalous force spectroscopic curves of single carboxymethyl-cellulose chains with  
multiple quantised plateaus.

(to be submitted 2004)

*Andrew Hards, Matthias Arnsdorf*

The correlation between reaction time and intelligence

(Young Scientist 07/1990)

1. Binning, G., et al., *Surface Studies by Scanning Tunneling Microscopy*. Physical Review Letters, 1982. **49**: p. 57-61.
2. Binnig, G., C.F. Quate, and C. Gerber, *Atomic force microscope*. Physical Review Letters, 1986. **56**: p. 930-933.
3. Giessibl, F.J., *Atomic resolution of the silicon (111)-(7 \* 7) surface by atomic force microscopy*. Science, 1995. **267**(5194): p. 68-71.
4. Barth, C. and M. Reichling, *Imaging the atomic arrangements on the high-temperature reconstructed  $\alpha$ -Al<sub>2</sub>O<sub>3</sub>(0001) surface*. Nature, 2001. **414**(6859): p. 54-57.
5. Lyubchenko, Y., et al., *Atomic force microscopy of long DNA: Imaging in air and under water*. Proceedings of the National Academy of Sciences of the United States of America, 1993. **90**(6): p. 2137-40.
6. Hansma, H.G., et al., *Atomic force microscopy of DNA in aqueous solutions*. Nucleic Acids Research, 1993. **21**(3): p. 505-12.
7. Rivetti, C. and S. Codeluppi, *Accurate length determination of DNA molecules visualized by atomic force microscopy: evidence for a partial B- to A-form transition on mica*. Ultramicroscopy, 2001. **87**(1/2): p. 55-66.
8. Hegner, M. and W. Grange, *Mechanics and imaging of single DNA molecules*. Journal of Muscle Research and Cell Motility, 2002. **23**(5-6): p. 367-375.
9. Perkins, T.T., et al., *Relaxation of a single DNA molecule observed by optical microscopy*. Science, 1994. **264**(5160): p. 822-6.
10. Allemand, J.F., et al., *pH-dependent specific binding and combing of DNA*. Biophysical Journal, 1997. **73**(4): p. 2064-2070.
11. Smith, D.E., H.P. Babcock, and S. Chu, *Single-polymer dynamics in steady shear flow*. Science, 1999. **283**(5408): p. 1724-1727.
12. Smith, S.B., L. Finzi, and C. Bustamante, *Direct mechanical measurements of the elasticity of single DNA molecules by using magnetic beads*. Science, 1992. **258**(5085): p. 1122-6.
13. Bustamante, C., et al., *Single-molecule studies of DNA mechanics*. Current Opinion in Structural Biology, 2000. **10**(3): p. 279-285.
14. Gosse, C. and V. Croquette, *Magnetic tweezers: micromanipulation and force measurement at the molecular level*. Biophysical Journal, 2002. **82**(6): p. 3314-3329.
15. Lavery, R., et al., *Structure and mechanics of single biomolecules: Experiment and simulation*. Journal of Physics: Condensed Matter, 2002. **14**(14): p. R383-R414.
16. Cluzel, P., et al., *DNA: an extensible molecule*. Science, 1996. **271**(5250): p. 792-4.
17. Smith, S.B., Y. Cui, and C. Bustamante, *Overstretching B-DNA: The Elastic Response of Individual Double-Stranded and Single-Stranded DNA Molecules*. Science, 1996. **271**(5250): p. 795-799.
18. Ashkin, A., *Optical trapping and manipulation of neutral particles using lasers*. Proceedings of the National Academy of Sciences of the United States of America, 1997. **94**(10): p. 4853-4860.
19. Leger, J.F., et al., *Structural Transitions of a Twisted and Stretched DNA Molecule*. Physical Review Letters, 1999. **83**(5): p. 1066-1069.
20. Arai, Y., et al., *Tying a molecular knot with optical tweezers*. Nature, 1999. **399**(6735): p. 446-8.
21. Lee, G.U., D.A. Kidwell, and R.J. Colton, *Sensing Discrete Streptavidin-Biotin Interactions with Atomic Force Microscopy*. Langmuir, 1994. **10**(2): p. 354-7.
22. Florin, E.L., V.T. Moy, and H.E. Gaub, *Adhesion forces between individual ligand-receptor pairs*. Science, 1994. **264**(5157): p. 415-17.
23. Hugel, T. and M. Seitz, *The study of molecular interactions by AFM force spectroscopy*. Macromolecular Rapid Communications, 2001. **22**(13): p. 989-1016.
24. Janshoff, A., et al., *Force spectroscopy of molecular systems - single molecule spectroscopy of polymers and biomolecules*. Angewandte Chemie, International Edition, 2000. **39**(18): p. 3212-3237.
25. Zlatanova, J., S.M. Lindsay, and S.H. Leuba, *Single molecule force spectroscopy in biology using the atomic force microscope*. Prog Biophys Mol Biol, 2000. **74**(1-2): p. 37-61.
26. Yuan, C., et al., *Energy landscape of streptavidin-biotin complexes measured by atomic force microscopy*. Biochemistry, 2000. **39**(33): p. 10219-23.
27. Lo, Y.-S., Y.-J. Zhu, and T.P. Beebe, Jr., *Loading-Rate Dependence of Individual Ligand-Receptor Bond-Rupture Forces Studied by Atomic Force Microscopy*. Langmuir, 2001. **17**(12): p. 3741-3748.
28. Conti, M., G. Falini, and B. Samori, *How strong is the coordination bond between a histidine tag and Ni-nitrilotriacetate? An experiment of mechanochemistry on single molecules*. Angewandte Chemie, International Edition, 2000. **39**(1): p. 215-218.
29. Rief, M., et al., *Single molecule force spectroscopy on polysaccharides by atomic force microscopy*. Science, 1997. **275**(5304): p. 1295-1297.
30. Marszalek, P., H. Li, and J.M. Fernandez, *Fingerprinting polysaccharides with single-molecule atomic force microscopy*. Nature Biotechnology, 2001. **19**(3): p. 258-262.
31. Rief, M., et al., *Reversible unfolding of individual titin immunoglobulin domains by AFM*. Science, 1997. **276**(5315): p. 1109-1112.

32. Weisel, J.W., H. Shuman, and R.I. Litvinov, *Protein-protein unbinding induced by force: single-molecule studies*. Current Opinion in Structural Biology, 2003. **13**(2): p. 227-235.
33. Carrion-Vazquez, M., et al., *Mechanical design of proteins studied by single-molecule force spectroscopy and protein engineering*. Progress in Biophysics and Molecular Biology, 2000. **74**(1-2): p. 63-91.
34. Best, R.B. and J. Clarke, *What can atomic force microscopy tell us about protein folding?* Chemical Communications (Cambridge, United Kingdom), 2002(3): p. 183-192.
35. Fowler, S.B., et al., *Mechanical Unfolding of a Titin Ig Domain: Structure of Unfolding Intermediate Revealed by Combining AFM, Molecular Dynamics Simulations, NMR and Protein Engineering*. Journal of Molecular Biology, 2002. **322**(4): p. 841-849.
36. Al-Maawali, S., et al., *Study of the Polydispersity of Grafted Poly(dimethylsiloxane) Surfaces Using Single-Molecule Atomic Force Microscopy*. Journal of Physical Chemistry B, 2001. **105**(18): p. 3965-3971.
37. Hugel, T., et al., *Elasticity of Single Polyelectrolyte Chains and Their Desorption from Solid Supports Studied by AFM Based Single Molecule Force Spectroscopy*. Macromolecules, 2001. **34**(4): p. 1039-1047.
38. Rief, M., H. Clausen-Schaumann, and H.E. Gaub, *Sequence-dependent mechanics of single DNA molecules*. Nature Structural Biology, 1999. **6**(4): p. 346-349.
39. Clausen-Schaumann, H., et al., *Mechanical stability of single DNA molecules*. Biophysical Journal, 2000. **78**(4): p. 1997-2007.
40. Bustamante, C., Z. Bryant, and S.B. Smith, *Ten years of tension: single-molecule DNA mechanics*. Nature, 2003. **421**(6921): p. 423-427.
41. Bao, G., *Mechanics of biomolecules*. Journal of the Mechanics and Physics of Solids, 2002. **50**(11): p. 2237-2274.
42. Grandbois, M., et al., *How strong is a covalent bond?* Science, 1999. **283**(5408): p. 1727-1730.
43. Tamarat, P., et al., *Ten Years of Single-Molecule Spectroscopy*. Journal of Physical Chemistry A, 2000. **104**(1): p. 1-16.
44. Orrit, M. and J. Bernard, *Single pentacene molecules detected by fluorescence excitation in a p-terphenyl crystal*. Physical Review Letters, 1990. **65**(21): p. 2716-19.
45. Moerner, W.E. and L. Kador, *Optical detection and spectroscopy of single molecules in a solid*. Physical Review Letters, 1989. **62**(21): p. 2535-8.
46. Moerner, W.E., *A Dozen Years of Single-Molecule Spectroscopy in Physics, Chemistry, and Biophysics*. Journal of Physical Chemistry B, 2002. **106**(5): p. 910-927.
47. Kulzer, F., et al., *Single-molecule optical switching of terrylene in p-terphenyl*. Nature, 1997. **387**(6634): p. 688-691.
48. Basche, T., S. Kummer, and C. Braeuchle, *Direct spectroscopic observation of quantum jumps of a single molecule*. Nature, 1995. **373**(6510): p. 132-4.
49. Weiss, S., *Fluorescence spectroscopy of single biomolecules*. Science, 1999. **283**(5408): p. 1676-1683.
50. Ishii, Y. and T. Yanagida, *Single molecule detection in life science*. Single Molecules, 2000. **1**(1): p. 5-16.
51. Zumbusch, A. and G. Jung, *Single molecule spectroscopy of the green fluorescent protein: a critical assessment*. Single Molecules, 2000. **1**(4): p. 261-270.
52. Seisenberger, G., et al., *Real-time single-molecule imaging of the infection pathway of an adeno-associated virus*. Science, 2001. **294**(5548): p. 1929-1932.
53. Nie, S., D.T. Chiu, and R.N. Zare, *Probing individual molecules with confocal fluorescence microscopy*. Science, 1994. **266**(5187): p. 1018-21.
54. Funatsu, T., et al., *Imaging of single fluorescent molecules and individual ATP turnovers by single myosin molecules in aqueous solution*. Nature, 1995. **374**(6522): p. 555-9.
55. Dickson, R.M., et al., *On/off blinking and switching behavior of single molecules of green fluorescent protein*. Nature, 1997. **388**(6640): p. 355-358.
56. Schmidt, T., et al., *Characterization of Photophysics and Mobility of Single Molecules in a Fluid Lipid Membrane*. Journal of Physical Chemistry, 1995. **99**(49): p. 17662-8.
57. Betzig, E. and R.J. Chichester, *Single molecules observed by near-field scanning optical microscopy*. Science, 1993. **262**(5138): p. 1422-5.
58. Axelrod, D., *Total internal reflection fluorescence microscopy*. Methods in Cell Biology, 1989. **30**: p. 245-70.
59. Tokunaga, M., et al., *Single molecule imaging of fluorophores and enzymic reactions achieved by objective-type total internal reflection fluorescence microscopy*. Biochemical and Biophysical Research Communications, 1997. **235**(1): p. 47-53.
60. Axelrod, D., *Total internal reflection fluorescence microscopy in cell biology*. Methods in Enzymology, 2003. **361**(Biophotonics, Part B): p. 1-33.
61. Conibear, P.B. and C.R. Bagshaw, *A comparison of optical geometries for combined flash photolysis and total internal reflection fluorescence microscopy*. Journal of Microscopy, 2000. **200**(3): p. 218-229.

62. Ambrose, W.P., P.M. Goodwin, and J.P. Nolan, *Single-molecule detection with total internal reflection excitation: comparing signal-to-background and total signals in different geometries*. Cytometry, 1999. **36**(3): p. 224-231.
63. Pohl, D.W., W. Denk, and M. Lanz, *Optical stethoscopy: image recording with a resolution of  $\lambda/20$* . Appl. Phys. Lett., 1984. **4**: p. 651-653.
64. Trautman, J.K. and J.J. Macklin, *Time-resolved spectroscopy of single molecules using near-field and far-field optics*. Chemical Physics, 1996. **205**(1,2): p. 221-9.
65. Kim, J.M., et al., *Simultaneous topographic and fluorescence imaging of single DNA molecules for DNA analysis with a scanning near-field optical/atomic force microscope*. Analytical Chemistry, 2001. **73**(24): p. 5984-5991.
66. Lal, R. and P. Roger, *Multimodal Atomic Force Microscopy: Biological Imaging Using AFM combined with Light Fluorescence and Confocal Microscopies*. Int. Journal Imaging Syst Technology, 1997. **8**: p. 293-300.
67. Foubert, P., et al., *Mechanical and optical manipulation of porphyrin rings at the submicrometer scale*. Nanotechnology, 2000. **11**(1): p. 16-23.
68. Kolodny, L.A., et al., *Spatially correlated fluorescence/AFM of individual nanosized particles and biomolecules*. Analytical Chemistry, 2001. **73**(9): p. 1959-1966.
69. Putman, C.A.J., et al., *Atomic force microscope with integrated optical microscope for biological applications*. Review of Scientific Instruments, 1992. **63**(3): p. 1914-17.
70. Vickery, S.A. and R.C. Dunn, *Combining AFM and FRET for high resolution fluorescence microscopy*. Journal of Microscopy, 2001. **202**(2): p. 408-412.
71. Hugel, T., et al., *Single-molecule optomechanical cycle*. Science, 2002. **296**(5570): p. 1103-1106.
72. Rohrig, U.F., U. Troppmann, and I. Frank, *Organic chromophores under tensile stress*. Chemical Physics, 2003. **289**(2-3): p. 381-388.
73. Rohrig, U.F. and I. Frank, *First-principles molecular dynamics study of a polymer under tensile stress*. Journal of Chemical Physics, 2001. **115**(18): p. 8670-8674.
74. Morikawa, K. and M. Yanagida, *Visualization of individual DNA molecules in solution by light microscopy: DAPI staining method*. J Biochem, 1981. **89**(2): p. 693-6.
75. Gurrieri, S., et al., *Direct visualization of individual DNA molecules by fluorescence microscopy: characterization of the factors affecting signal/background and optimization of imaging conditions using YOYO*. Analytical Biochemistry, 1997. **249**(1): p. 44-53.
76. Maier, B. and J.O. Raedler, *Shape of Self-Avoiding Walks in Two Dimensions*. Macromolecules, 2001. **34**(16): p. 5723-5724.
77. Bink, K., et al., *TO-PRO-3 is an optimal fluorescent dye for nuclear counterstaining in dual-color FISH on paraffin sections*. Histochemistry and Cell Biology, 2001. **115**(4): p. 293-299.
78. Lo, Y.-S., et al., *Specific Interactions between Biotin and Avidin Studied by Atomic Force Microscopy Using the Poisson Statistical Analysis Method*. Langmuir, 1999. **15**(4): p. 1373-1382.
79. Oesterhelt, F., M. Rief, and H.E. Gaub, *Single molecule force spectroscopy by AFM indicates helical structure of poly(ethylene-glycol) in water*. New Journal of Physics [Electronic Publication], 1999. **1**: p. Article 6.1-6.11.
80. Flory, P.J., *Statistical Mechanics of Chain Molecules*. 1969: Interscience Publishers. 432 pp.
81. Cantor, C.R. and P.R. Schimmel, *Biophysical Chemistry Part III: The Behavior of Biological Macromolecules*. 1980, New York: W.H. Freeman and Company.
82. Rief, M., *Kraftspektroskopie an einzelnen Molekülen*. 1997, LMU University: Munich. p. 16.
83. Fisher, T.E., et al., *The micro-mechanics of single molecules studied with atomic force microscopy*. Journal of Physiology, 1999. **520 Pt 1**: p. 5-14.
84. Kratky, O. and G. Porod, *X-ray investigation of dissolved chain molecules*. Recueil des Travaux Chimiques des Pays-Bas et de la Belgique, 1949. **68**: p. 1106-22.
85. Marko, J.F. and E.D. Siggia, *Stretching DNA*. Macromolecules, 1995. **28**(26): p. 8759-70.
86. Odijk, T., *Stiff Chains and Filaments under Tension*. Macromolecules, 1995. **28**(20): p. 7016-18.
87. Bouchiat, C., et al., *Estimating the persistence length of a worm-like chain molecule from force-extension measurements*. Biophysical Journal, 1999. **76**(1, Pt. 1): p. 409-413.
88. Micic, M., et al., *Scanning electron microscopy studies of protein-functionalized atomic force microscopy cantilever tips*. Scanning, 1999. **21**(6): p. 394-7.
89. Florin, E.L., et al., *Sensing specific molecular interactions with the atomic force microscope*. Biosensors & Bioelectronics, 1995. **10**(9/10): p. 895-901.
90. Butt, H.-J. and M. Jaschke, *Calculation of thermal noise in atomic force microscopy*. Nanotechnology, 1995. **6**(1): p. 1.
91. Viani, M.B., et al., *Small cantilevers for force spectroscopy of single molecules*. Journal of Applied Physics, 1999. **86**(4): p. 2258-2262.
92. Ahlrichs, R., et al., *Polyol metal complexes. Part 30. Aqueous ethylenediamine dihydroxo palladium(II): A coordinating agent for low- and high-molecular weight carbohydrates*. Chemistry-A European Journal, 1998. **4**(5): p. 835-844.
93. Zou, S., et al., *Study on Polymer Micelles of Hydrophobically Modified Ethyl Hydroxyethyl Cellulose Using Single-Molecule Force Spectroscopy*. Langmuir, 2001. **17**(16): p. 4799-4808.

94. Li, H., et al., *Single-molecule force spectroscopy on polysaccharides by AFM-nanomechanical fingerprint of  $\alpha$ -(1,4)-linked polysaccharides*. Chemical Physics Letters, 1999. **305**(3,4): p. 197-201.
95. Marszalek, P.E., et al., *Atomic levers control pyranose ring conformations*. Proceedings of the National Academy of Sciences of the United States of America, 1999. **96**(14): p. 7894-7898.
96. Marszalek, P.E., et al., *Polysaccharide elasticity governed by chair-boat transitions of the glucopyranose ring*. Nature, 1998. **396**(6712): p. 661-664.
97. Haupt, B.J., T.J. Senden, and E.M. Sevick, *AFM Evidence of Rayleigh Instability in Single Polymer Chains*. Langmuir, 2002. **18**(6): p. 2174-2182.
98. Zhang, W., et al., *Desorption Force of Poly(4-vinylpyridine) Layer Assemblies from Amino Groups Modified Substrates*. Journal of Physical Chemistry B, 2002. **106**(49): p. 12705-12708.
99. Conti, M., et al., *The desorption process of macromolecules adsorbed on interfaces: the force spectroscopy approach*. ChemPhysChem, 2001. **2**(10): p. 610-613.
100. Haupt, B.J., J. Ennis, and E.M. Sevick, *The Detachment of a Polymer Chain from a Weakly Adsorbing Surface Using an AFM Tip*. Langmuir, 1999. **15**(11): p. 3886-3892.
101. Cui, S., C. Liu, and X. Zhang, *Simple Method to Isolate Single Polymer Chains for the Direct Measurement of the Desorption Force*. Nano Letters, 2003. **3**(2): p. 245-248.
102. Maeda, N., T.J. Senden, and J.-M. di Meglio, *Micromanipulation of phospholipid bilayers by atomic force microscopy*. Biochimica et Biophysica Acta, 2002. **1564**(1): p. 165-172.
103. Miller, A.F. and A.M. Donald, *Surface and Interfacial Tension of Cellulose Suspensions*. Langmuir, 2002. **18**(26): p. 10155-10162.
104. Muller, N., *Is there a region of highly structured water around a nonpolar solute molecule?* J. Solution Chem., 1988. **17**: p. 661-672.
105. Matsumoto, S., K. Morikawa, and M. Yanagida, *Light microscopic structure of DNA in solution studied by the 4',6-diamidino-2-phenylindole staining method*. Journal of Molecular Biology, 1981. **152**(2): p. 501-16.
106. Haugland, *Handbook of Fluorescent Probes and Research Chemicals, 9th Ed.* Molecular Probes, 2003.
107. Beisker, W., E.M. Weller-Mewe, and M. Nusse, *Fluorescence enhancement of DNA-bound TO-PRO-3 by incorporation of bromodeoxyuridine to monitor cell cycle kinetics*. Cytometry, 1999. **37**(3): p. 221-229.
108. Rampal, S., M.-S. Liu, and F.-T. A. Chen, *Characterization of TO-PRO-3 as an intercalator for double-stranded DNA analysis with red diode laser-induced fluorescence detection*. Journal of Chromatography, A, 1997. **781**(1 + 2): p. 357-365.
109. Milanovich, N., et al., *Binding of TO-PRO-3 and TOTO-3 to DNA: Fluorescence and Hole-Burning Studies*. Journal of Physical Chemistry, 1996. **100**(21): p. 9181-6.
110. Kwak, K.J., H. Kudo, and M. Fujihira, *Imaging stretched single DNA molecules by pulsed-force-mode atomic force microscopy*. Ultramicroscopy, 2003. **97**(1-4): p. 249-255.
111. Kang, S.H., M.R. Shortreed, and E.S. Yeung, *Real-Time dynamics of single-DNA molecules undergoing adsorption and desorption at liquid-solid interfaces*. Analytical Chemistry, 2001. **73**(6): p. 1091-1099.
112. Michalet, X., *Stretching single-stranded DNA on a surface*. Nano Letters, 2001. **1**(7): p. 341-343.
113. Schneegans, M. and E. Menzel, *Gold crystals solidified in air are hydrophilic*. Journal of Colloid and Interface Science, 1982. **88**(1): p. 97-9.
114. Michalet, X., et al., *Dynamic molecular combing: stretching the whole human genome for high-resolution studies*. Science, 1997. **277**(5331): p. 1518-23.
115. Bensimon, A., et al., *Alignment and sensitive detection of DNA by a moving interface*. Science, 1994. **265**(5181): p. 2096-8.
116. Bensimon, D., et al., *Stretching DNA with a receding meniscus: experiments and models*. Physical Review Letters, 1995. **74**(23): p. 4754-7.
117. Herrick, J. and A. Bensimon, *Imaging of single DNA molecule: applications to high-resolution genomic studies*. Chromosome research, 1999. **7**(6): p. 409-23.
118. Cai, W., et al., *Ordered restriction endonuclease maps of yeast artificial chromosomes created by optical mapping on surfaces*. PNAS, 1995. **92**(11): p. 5164-8.
119. Maier, B. and J.O. Raedler, *Conformation and Self-Diffusion of Single DNA Molecules Confined to Two Dimensions*. Physical Review Letters, 1999. **82**(9): p. 1911-1914.
120. Woolley, A.T. and R.T. Kelly, *Deposition and characterization of extended single-stranded DNA molecules on surfaces*. Nano Letters, 2001. **1**(7): p. 345-348.
121. Yokota, H., et al., *Spin-stretching of DNA and protein molecules for detection by fluorescence and atomic force microscopy*. Analytical Chemistry, 1999. **71**(19): p. 4418-22.
122. Wang, W., J. Lin, and D.C. Schwartz, *Scanning force microscopy of DNA molecules elongated by convective fluid flow in an evaporating droplet*. Biophysical Journal, 1998. **75**(1): p. 513-520.
123. Cai, X.-E. and J. Yang, *Molecular forces for the binding and condensation of DNA molecules*. Biophysical Journal, 2002. **82**(1, Pt. 1): p. 357-365.

124. Matulis, D., I. Rouzina, and V.A. Bloomfield, *Thermodynamics of Cationic Lipid Binding to DNA and DNA Condensation: Roles of Electrostatics and Hydrophobicity*. Journal of the American Chemical Society, 2002. **124**(25): p. 7331-7342.
125. Fang, Y. and J.H. Hoh, *Surface-directed DNA condensation in the absence of soluble multivalent cations*. Nucleic acids research, 1998. **26**(2): p. 588-93.
126. Kartalov, E.P., M.A. Unger, and S.R. Quake, *Polyelectrolyte surface interface for single-molecule fluorescence studies of DNA polymerase*. BioTechniques, 2003. **34**(3): p. 505-508,510.
127. Lyon, W.A., et al., *A Dual-Beam Optical Microscope for Observation and Cleavage of Single DNA Molecules*. Analytical Chemistry, 1998. **70**(9): p. 1743-1748.
128. Taylor, J.R., M.M. Fang, and S. Nie, *Probing specific sequences on single DNA molecules with bioconjugated fluorescent nanoparticles*. Analytical Chemistry, 2000. **72**(9): p. 1979-86.
129. Williams, M.C. and I. Rouzina, *Force spectroscopy of single DNA and RNA molecules*. Current Opinion in Structural Biology, 2002. **12**(3): p. 330-336.
130. Clausen-Schaumann, H., M. Rief, and M. Seitz, *Artificial noses sniff DNA*. ChemPhysChem, 2000. **1**(2): p. 89-90.
131. Krautbauer, R., et al., *Discriminating small molecule DNA binding modes by single molecule force spectroscopy*. FEBS Letters, 2002. **510**(3): p. 154-158.
132. Krautbauer, R., et al., *Mechanical fingerprints of DNA drug complexes*. Single Molecules, 2002. **3**(2-3): p. 97-103.
133. Hu, J., et al., *Artificial DNA patterns by mechanical nanomanipulation*. Nano Letters, 2002. **2**(1): p. 55-57.
134. Guthold, M., et al., *Quantitative manipulation of DNA and viruses with the nanomanipulator scanning force microscope*. Surface and Interface Analysis, 1999. **27**(5-6): p. 437-443.
135. Lai, P.-Y. and Z.-C. Zhou, *Stretching a double-stranded DNA: Nature of the B-form to the S-form transition*. Journal of Chemical Physics, 2003. **118**(24): p. 11189-11199.
136. Schotanus, M.P., K.S. Aumann, and K. Sinniah, *Using Force Spectroscopy To Investigate the Binding of Complementary DNA in the Presence of Intercalating Agents*. Langmuir, 2002. **18**(14): p. 5333-5336.
137. Krautbauer, R., H. Clausen-Schaumann, and H.E. Gaub, *Cisplatin changes the mechanics of single DNA molecules*. Angewandte Chemie, International Edition, 2000. **39**(21): p. 3912-3915.
138. Husale, S., W. Grange, and M. Hegner, *DNA mechanics affected by small DNA interacting ligands*. Single Molecules, 2002. **3**(2-3): p. 91-96.
139. Bennink, M.L., et al., *Single-molecule manipulation of double-stranded DNA using optical tweezers: interaction studies of DNA with RecA and YOYO-1*. Cytometry, 1999. **36**(3): p. 200-8.
140. Yeung, E.S., S.H. Kang, and M.R. Shortreed, *Real-time dynamics of single-DNA molecules undergoing adsorption and desorption at liquid-solid interfaces*. Abstracts of Papers, 222nd ACS National Meeting, Chicago, IL, United States, August 26-30, 2001, 2001: p. COLL-302.
141. Wolfgang Rettig, B.S., Sigurd Schrader, Holger Seifert, *Photostability of fluorescent dyes for single molecule spectroscopy*. Applied Fluorescence in Chemistry, Biology and Medicine. 1998: Springer Verlag. 193ff.
142. Soper, S.A., et al., *The photophysical constants of several fluorescent dyes pertaining to ultrasensitive fluorescence spectroscopy*. Photochemistry and Photobiology, 1993. **57**(6): p. 972-7.
143. Eggeling, C., et al., *Photobleaching of fluorescent dyes under conditions used for single-molecule detection: evidence of two-step photolysis*. Analytical Chemistry, 1998. **70**(13): p. 2651-2659.
144. Agronskaia, A., et al., *Two-Color Fluorescence in Flow Cytometry DNA Sizing: Identification of Single-Molecule Fluorescent Probes*. Analytical Chemistry, 1999. **71**(20): p. 4684-4689.
145. Widengren, J. and P. Schwille, *Characterization of photoinduced isomerization and back-isomerization of the cyanine dye Cy5 by fluorescence correlation spectroscopy*. Journal of Physical Chemistry A, 2000. **104**(27): p. 6416-6428.
146. Mais, S., et al., *Terrylene diimide: A Novel Fluorophore for Single-Molecule Spectroscopy and Microscopy from 1.4 K to Room Temperature*. Journal of Physical Chemistry A, 1997. **101**(45): p. 8435-8440.
147. Ambrose, W.P., et al., *Single molecule detection and photochemistry on a surface using near-field optical excitation*. Physical Review Letters, 1994. **72**(1): p. 160-3.
148. Jung, G., et al., *The Role of Dark States in the Photodynamics of the Green Fluorescent Protein Examined with Two-Color Fluorescence Excitation Spectroscopy*. Journal of Physical Chemistry A, 2000. **104**(5): p. 873-877.
149. Basche, T., et al., *Photon antibunching in the fluorescence of a single dye molecule trapped in a solid*. Physical Review Letters, 1992. **69**(10): p. 1516-19.
150. Ha, T., et al., *Hindered rotational diffusion and rotational jumps of single molecules*. Physical Review Letters, 1998. **80**(10): p. 2093-2096.
151. Lu, H.P. and X.S. Xie, *Single-molecule spectral fluctuations at room temperature*. Nature, 1997. **385**(6612): p. 143-146.

152. Weber, M.A., F. Stracke, and A.J. Meixner, *Dynamics of single dye molecules observed by confocal imaging and spectroscopy*. Cytometry, 1999. **36**(3): p. 217-223.
153. Blum, C., et al., *Discrimination and interpretation of spectral phenomena by room-temperature single-molecule spectroscopy*. Journal of Physical Chemistry A, 2001. **105**(29): p. 6983-6990.
154. Nie, S. and R.N. Zare, *Optical detection of single molecules*. Annual Review of Biophysics and Biomolecular Structure, 1997. **26**: p. 567-596.
155. Seebacher, C., *Einzelmolekülspektroskopie von organischen Farbstoffmolekülen in porösen Festkörpern*, in *PhD thesis*. 2002, LMU.
156. Macklin, J.J., et al., *Imaging and time-resolved spectroscopy of single molecules at an interface*. Science, 1996. **272**(5259): p. 255-8.
157. Guettler, F., et al., *Fluorescence microscopy of single molecules*. Chemical Physics Letters, 1994. **217**(4): p. 393-7.
158. Georgiou, G.N., I.E. Morrison, and R.J. Cherry, *Digital fluorescence imaging of fusion of influenza virus with erythrocytes*. FEBS Letters, 1989. **250**(2): p. 487-92.
159. Steyer, J.A. and W. Almers, *A real-time view of life within 100 nm of the plasma membrane*. Nat Rev Mol Cell Biol, 2001. **2**(4): p. 268-75.
160. Tinnefeld, P., D.-P. Hertel, and M. Sauer, *Photophysical Dynamics of Single Molecules Studied by Spectrally-Resolved Fluorescence Lifetime Imaging Microscopy (SFLIM)*. Journal of Physical Chemistry A, 2001. **105**(34): p. 7989-8003.
161. Abdel-Mottaleb, M.S., et al., *Photophysics of Molecular Rotors of Functionalized Surface-active Styrylcyanine Dyes*. J. Chem. Soc. Faraday Trans. 2, 1989. **85**(11): p. 1779-1788.
162. Eaton, D.F., *Reference materials for fluorescence measurement*. Pure and Applied Chemistry, 1988. **60**(7): p. 1107-14.
163. Kubin, R.F. and A.N. Fletcher, *Fluorescence quantum yields of some rhodamine dyes*. Journal of Luminescence, 1983. **27**(4): p. 455-62.
164. Soper, S.A., L.M. Davis, and E.B. Shera, *Detection and identification of single molecules in solution*. Journal of the Optical Society of America B: Optical Physics, 1992. **9**(10): p. 1761-9.
165. Axelrod, D., *Total internal reflection fluorescence microscopy*. Methods in Cellular Imaging, 2001: p. 362-380.
166. Suzuki, Y., et al., *Imaging of the fluorescence spectrum of a single fluorescent molecule by prism-based spectroscopy*. FEBS Letters, 2002. **512**(1-3): p. 235-239.
167. Kawano, Y., et al., *High-numerical-aperture objective lenses and optical system improved objective type total internal reflection fluorescence microscopy*. Proceedings of SPIE-The International Society for Optical Engineering, 2000. **4098**(Optical Devices and Diagnostics in Materials Science): p. 142-151.
168. Jung, G., *Zweifarbigen-Fluoreszenz-korrelationspektroskopie am Grün Fluoreszierenden Protein und seine Mutanten*. 2001, LMU Munich: Munich.
169. Vilfan, M., I. Musevic, and M. Copic, *AFM observation of force on a dielectric sphere in the evanescent field of totally reflected light*. Europhysics Letters, 1998. **43**(1): p. 41-46.
170. Laddada, R., et al., *Detection of an evanescent field scattered by silicon tips in an apertureless scanning near-field optical microscope*. European Physical Journal: Applied Physics, 1999. **6**(2): p. 171-178.
171. Waring, M.J., *Complex formation between ethidium bromide and nucleic acids*. J Mol Biol, 1965. **13**(1): p. 269-82.
172. Coury, J.E., et al., *A novel assay for drug-DNA binding mode, affinity, and exclusion number: Scanning force microscopy*. Proceedings of the National Academy of Sciences of the United States of America, 1996(93): p. 12283-12286.
173. LePecq, J.B. and C. Paoletti, *A fluorescent complex between ethidium bromide and nucleic acids. Physical-chemical characterization*. J Mol Biol, 1967. **27**(1): p. 87-106.
174. Williams, M.C., et al., *Effect of pH on the overstretching transition of double-stranded DNA: evidence of force-induced DNA melting*. Biophysical Journal, 2001. **80**(2): p. 874-881.
175. Guo, X.H., E.J. Huff, and D.C. Schwartz, *Sizing single DNA molecules*. Nature, 1992. **359**(6398): p. 783-4.
176. Glazer, A.N. and H.S. Rye, *Stable dye-DNA intercalation complexes as reagents for high-sensitivity fluorescence detection*. Nature, 1992. **359**(6398): p. 859-61.
177. Rye, H.S., et al., *Stable fluorescent complexes of double-stranded DNA with bis-intercalating asymmetric cyanine dyes: properties and applications*. Nucleic acids research, 1992. **20**(11): p. 2803-12.
178. Ma, Y., M.R. Shortreed, and E.S. Yeung, *High-throughput single-molecule spectroscopy in free solution*. Anal Chem, 2000. **72**(19): p. 4640-5.
179. Schafer, B., et al., *Single molecule DNA restriction analysis in the light microscope*. Single Molecules, 2000. **1**(1): p. 33-40.
180. Matsuura, S., et al., *Real-time observation of a single DNA digestion by lambda exonuclease under a fluorescence microscope field*. Nucleic Acids Res, 2001. **29**(16): p. E79.
181. Filippova, E.M., et al., *Quantifying Double-Strand Breaks and Clustered Damages in DNA by Single-Molecule Laser Fluorescence Sizing*. Biophys. J., 2003. **84**(2): p. 1281-1290.

182. Yoshinaga, N., T. Akitaya, and K. Yoshikawa, *Intercalating fluorescence dye YOYO-1 prevents the folding transition in giant duplex DNA*. *Biochem Biophys Res Commun*, 2001. **286**(2): p. 264-7.
183. Netzel, T.L., et al., *Base-Content Dependence of Emission Enhancements, Quantum Yields, and Lifetimes for Cyanine Dyes Bound to Double-Strand DNA: Photophysical Properties of Monomeric and Bichromophoric DNA Stains*. *Journal of Physical Chemistry*, 1995. **99**(51): p. 17936-47.
184. Petty, J.T., J.A. Bordelon, and M.E. Robertson, *Thermodynamic Characterization of the Association of Cyanine Dyes with DNA*. *Journal of Physical Chemistry B*, 2000. **104**(30): p. 7221-7227.
185. *Molecular Probes Handbook*. 2002.
186. Kanony, C., B. Akerman, and E. Tuite, *Photobleaching of asymmetric cyanines used for fluorescence imaging of single DNA molecules*. *J. Am. Chem. Soc.*, 2001. **123**(33): p. 7985-95.
187. Aakerman, B. and E. Tuite, *Single- and double-strand photocleavage of DNA by YO, YOYO and TOTO*. *Nucleic Acids Research*, 1996. **24**(6): p. 1080-90.
188. Wennmalm, S. and R. Rigler, *On Death Numbers and Survival Times of Single Dye Molecules*. *Journal of Physical Chemistry B*, 1999. **103**(13): p. 2516-2519.
189. Haugland, *Handbook of Fluorescent Probes and Research Chemicals, 5th Ed.* Molecular Probes, 1992(5th).
190. Larsson, A., et al., *Characterization of the Binding of the Fluorescent Dyes YO and YOYO to DNA by Polarized Light Spectroscopy*. *Journal of the American Chemical Society*, 1994. **116**(19): p. 8459-65.
191. Baumann, C.G., et al., *Ionic effects on the elasticity of single DNA molecules*. *PNAS*, 1997. **94**(12): p. 6185-90.
192. Burak, Y., G. Ariel, and D. Andelman, *Onset of DNA aggregation in presence of mono- and multivalent counterions*. Los Alamos National Laboratory, Preprint Archive, Condensed Matter, 2003: p. 1-12, arXiv:cond-mat/0304002.
193. Dahlgren, P.R. and Y.L. Lyubchenko, *Atomic Force Microscopy Study of the Effects of Mg<sup>2+</sup> and Other Divalent Cations on the End-to-End DNA Interactions*. *Biochemistry*, 2002. **41**(38): p. 11372-11378.
194. Cherny, D.I., et al., *Analysis of various sequence-specific triplexes by electron and atomic force microscopies*. *Biophysical Journal*, 1998. **74**(2, Pt. 1): p. 1015-1023.
195. Pope, L.H., et al., *Atomic force microscopy studies of intercalation-induced changes in plasmid DNA tertiary structure*. *Journal of Microscopy*, 2000. **199**(1): p. 68-78.
196. Seong, G.H., et al., *Single-Molecular AFM Probing of Specific DNA Sequencing Using RecA-Promoted Homologous Pairing and Strand Exchange*. *Analytical Chemistry*, 2000. **72**(6): p. 1288-1293.
197. Hegner, M., P. Wagner, and G. Semenza, *Immobilizing DNA on gold via thiol modification for atomic force microscopy imaging in buffer solutions*. *FEBS Letters*, 1993. **336**(3): p. 452-6.
198. Medalia, O., et al., *AFM imaging in solution of protein-DNA complexes formed on DNA anchored to a gold surface*. *Ultramicroscopy*, 2002. **90**(2/3): p. 103-112.
199. Hansma, H.G., *Varieties of imaging with scanning probe microscopes*. *Proceedings of the National Academy of Sciences of the United States of America*, 1999. **96**(26): p. 14678-14680.
200. Schwartz, D.C., et al., *Ordered restriction maps of Saccharomyces cerevisiae chromosomes constructed by optical mapping*. *Science*, 1993. **262**(5130): p. 110-14.
201. Netz, R., *Electrostatics of genetic substances simple physical principles determine macromolecular structures of DNA*. *Physik Journal*, 2002. **1**(9): p. 51-56.
202. Fang, Y. and J. Yang, *Effect of Cationic Strength and Species on 2-D Condensation of DNA*. *Journal of Physical Chemistry B*, 1997. **101**(18): p. 3453-3456.
203. Fang, Y. and J. Yang, *Two-Dimensional Condensation of DNA Molecules on Cationic Lipid Membranes*. *Journal of Physical Chemistry B*, 1997. **101**(3): p. 441-449.
204. Baumann, C.G., et al., *Stretching of single collapsed DNA molecules*. *Biophysical Journal*, 2000. **78**(4): p. 1965-1978.
205. Yoshikawa, K., et al., *Large discrete transition in a single DNA molecule appears continuous in the ensemble*. *Physical Review Letters*, 1996. **76**(16): p. 3029-31.
206. Golan, R., et al., *DNA Toroids: Stages in Condensation*. *Biochemistry*, 1999. **38**(42): p. 14069-14076.
207. Hansma, H.G., et al., *DNA condensation for gene therapy as monitored by atomic force microscopy*. *Nucleic Acids Research*, 1998. **26**(10): p. 2481-2487.
208. Endlich, N. and K.O. Greulich, *Observation and manipulation of different structural variants of individual cation-DNA complexes in the light microscope*. *Journal of Biotechnology*, 1995. **41**(2-3): p. 149-53.
209. Trubetskoy, V.S., et al., *Quantitative Assessment of DNA Condensation*. *Analytical Biochemistry*, 1999. **267**(2): p. 309-313.
210. Allemand, J.F., D. Bensimon, and V. Croquette, *The elasticity of a single supercoiled DNA molecule*. *Science*, 1996. **272**(5263): p. 797.

211. Bockelmann, U., et al., *Unzipping DNA with optical tweezers: high sequence sensitivity and force flips*. Biophysical Journal, 2002. **82**(3): p. 1537-1553.
212. Cocco, S., R. Monasson, and J.F. Marko, *Force and kinetic barriers to unzipping of the DNA double helix*. Proc Natl Acad Sci U S A, 2001. **98**(15): p. 8608-13.
213. Bockelmann, U., B. Essevaz-Roulet, and F. Heslot, *DNA strand separation studied by single molecule force measurements*. Physical Review E: Statistical Physics, Plasmas, Fluids, and Related Interdisciplinary Topics, 1998. **58**(2-B): p. 2386-2394.
214. Bockelmann, U., B. Essevaz-Roulet, and F. Heslot, *Molecular Stick-Slip Motion Revealed by Opening DNA with Piconewton Forces*. Physical Review Letters, 1997. **79**(22): p. 4489-4492.
215. Strunz, T., et al., *Dynamic force spectroscopy of single DNA molecules*. Proceedings of the National Academy of Sciences of the United States of America, 1999. **96**(20): p. 11277-11282.
216. Schumakovitch, I., et al., *Temperature dependence of unbinding forces between complementary DNA strands*. Biophys J, 2002. **82**(1 Pt 1): p. 517-21.
217. Grange, W., et al., *Molecular recognition and adhesion of individual DNA strands studied by dynamic force microscopy*. Single Molecules, 2001. **2**(2): p. 75-78.
218. Sha, R., F. Liu, and N.C. Seeman, *Atomic Force Microscopic Measurement of the Interdomain Angle in Symmetric Holliday Junctions*. Biochemistry, 2002. **41**(19): p. 5950-5955.
219. Yang, X., et al., *Ligation of DNA triangles containing double crossover molecules*. Journal of the American Chemical Society, 1998. **120**(38): p. 9779-9786.
220. Li, X., et al., *Antiparallel DNA Double Crossover Molecules As Components for Nanoconstruction*. Journal of the American Chemical Society, 1996. **118**(26): p. 6131-6140.
221. Sha, R., et al., *Atomic force microscopy of parallel DNA branched junction arrays*. Chemistry and Biology, 2000. **7**(9): p. 743-51.
222. Mao, C., W. Sun, and N.C. Seeman, *Designed Two-Dimensional DNA Holliday Junction Arrays Visualized by Atomic Force Microscopy*. Journal of the American Chemical Society, 1999. **121**(23): p. 5437-5443.
223. Kramer, A., et al., *Optical near-field enhancement at a metal tip probed by a single fluorophore*. Applied Physics Letters, 2002. **80**(9): p. 1652-1654.
224. Gaiduk, A., et al., *Fluorescence Properties of Cantilevers for Simultaneous Atomic Force and Optical Spectroscopy*. Poster CENS summerschool, 2002.
225. Kottmann, J.P., et al., *Non-regularly shaped plasmon resonant nanoparticle as localized light source for near-field microscopy*. Journal of Microscopy, 2001. **202**(1): p. 60-65.
226. Novotny, L., *Single molecule fluorescence in inhomogeneous environments*. Applied Physics Letters, 1996. **69**(25): p. 3806-3808.
227. Bian, R.X., et al., *Single molecule emission characteristics in near-field microscopy*. Physical Review Letters, 1995. **75**(26): p. 4772-5.
228. Yang, T.J., G.A. Lessard, and S.R. Quake, *An apertureless near-field microscope for fluorescence imaging*. Applied Physics Letters, 2000. **76**(3): p. 378-380.
229. Trabesinger, W., et al., *Single-molecule near-field optical energy transfer microscopy*. Applied Physics Letters, 2002. **81**(11): p. 2118-2120.
230. Ashino, M. and M. Ohtsu, *Fabrication and evaluation of a localized plasmon resonance probe for near-field optical microscopy/spectroscopy*. Applied Physics Letters, 1998. **72**(11): p. 1299-1301.
231. Novotny, L., E.J. Sanchez, and X.S. Xie, *Near-field optical imaging using metal tips illuminated by higher-order Hermite-Gaussian beams*. Ultramicroscopy, 1998. **71**(1-4): p. 21-29.
232. Crut, A., et al., *Transverse fluctuations of single DNA molecules attached at both extremities to a surface*. Physical Review E: Statistical, Nonlinear, and Soft Matter Physics, 2003. **67**(5-1): p. 051910/1-051910/6.
233. Piner, R.D., et al., *"Dip-pen" nanolithography*. Science, 1999. **283**(5402): p. 661-663.
234. Zhang, M., et al., *A MEMS nanoplotted with high-density parallel dip-pen nanolithography probe arrays*. Nanotechnology, 2002. **13**(2): p. 212-217.
235. Weeks, B.L., et al., *Effect of dissolution kinetics on feature size in dip-pen nanolithography*. Physical Review Letters, 2002. **88**(25, Pt. 1): p. 255505/1-255505/4.
236. Lee, K.-B., et al., *Protein nanoarrays generated by dip-pen nanolithography*. Science, 2002. **295**(5560): p. 1702-1705.
237. Liu, X., et al., *Arrays of magnetic nanoparticles patterned via "dip-pen" nanolithography*. Advanced Materials, 2002. **14**(3): p. 231-234.
238. Demers, L.M., et al., *Orthogonal assembly of nanoparticles building blocks on dip-pen nanolithographically generated templates of DNA*. Angewandte Chemie, International Edition, 2001. **40**(16): p. 3071-3073.
239. McKendry, R., et al., *Creating Nanoscale Patterns of Dendrimers on Silicon Surfaces with Dip-Pen Nanolithography*. Nano Letters, 2002. **2**(7): p. 713-716.
240. Schwartz, P.V., *Meniscus Force Nanografting: Nanoscopic Patterning of DNA*. Langmuir, 2001. **17**(19): p. 5971-5977.
241. Liu, M., et al., *Production of Nanostructures of DNA on Surfaces*. Nano Letters, 2002. **2**(8): p. 863-867.

242. Noy, A., et al., *Fabrication of Luminescent Nanostructures and Polymer Nanowires Using Dip-Pen Nanolithography*. Nano Letters, 2002. **2**(2): p. 109-112.
243. Demers, L.M., et al., *Direct patterning of modified oligonucleotides on metals and insulators by dip-pen nanolithography*. Science, 2002. **296**(5574): p. 1836-1838.
244. Niemeyer, C.M., *Tools for the biomolecular engineer*. Science, 2002. **297**(5578): p. 62-63.
245. Ball, P., *Circuit Training*. Nature Science Update, 2001.
246. Falvo, M.R., et al., *Nanometer-scale rolling and sliding of carbon nanotubes*. Nature, 1999. **397**(6716): p. 236-238.
247. Dwyer, C., et al., *DNA-functionalized single-walled carbon nanotubes*. Nanotechnology, 2002. **13**(5): p. 601-604.
248. Richter, J., et al., *Nanoscale palladium metallization of DNA*. Advanced Materials, 2000. **12**(7): p. 507-510.
249. Richter, J., et al., *Construction of highly conductive nanowires on a DNA template*. Applied Physics Letters, 2001. **78**(4): p. 536-538.
250. Ford, W.E., et al., *Platinated DNA as precursors to templated chains of metal nanoparticles*. Advanced Materials, 2001. **13**(23): p. 1793-1797.
251. Merkel, R., *Force spectroscopy on single passive biomolecules and single biomolecular bonds*. Physics Reports, 2001. **346**(5): p. 343-385.
252. Lin, W., et al., *New nonlinear optical materials: expedient topotactic self-assembly of acentric chromophoric superlattices*. Angewandte Chemie, International Edition in English, 1995. **34**(13/14): p. 1497-9.
253. Nygren, J., N. Svanvik, and M. Kubista, *The interactions between the fluorescent dye thiazole orange and DNA*. Biopolymers, 1998. **46**(1): p. 39-51.
254. Liu, Y.Z., S.H. Leuba, and S.M. Lindsay, *Relationship between stiffness and force in single molecule pulling experiments*. Langmuir, 1999. **15**(24): p. 8547-8548.
255. Leuba, S.H., et al., *The mechanical properties of single chromatin fibers under tension*. Single Molecules, 2000. **1**(2): p. 185-192.
256. Pickering, J.P., et al., *Viscoelastic energy dissipation and time-dependent adhesion hysteresis on the nanometer scale with atomic force microscopy*. Polymer Preprints, 2000. **41**(2): p. 1478-1479.
257. Hinterdorfer, P., et al., *Poly(ethylene glycol): an ideal spacer for molecular recognition force microscopy/spectroscopy*. Single Molecules, 2000. **1**(2): p. 99-103.
258. Oesterhelt, F., M. Rief, and H.E. Gaub, *Single molecule force spectroscopy by AFM indicates helical structure of poly(ethylene-glycol) in water*. New Journal of Physics, 1999. **1**: p. No pp. Given, Article 6.
259. Li, H., et al., *Hydrogen Bonding Governs the Elastic Properties of Poly(vinyl alcohol) in Water: Single-Molecule Force Spectroscopic Studies of PVA by AFM*. Macromolecules, 2000. **33**(2): p. 465-469.
260. Yamamoto, S., Y. Tsujii, and T. Fukuda, *Atomic Force Microscopic Study of Stretching a Single Polymer Chain in a Polymer Brush*. Macromolecules, 2000. **33**(16): p. 5995-5998.
261. Butt, H.-J., et al., *Steric Forces Measured with the Atomic Force Microscope at Various Temperatures*. Langmuir, 1999. **15**(7): p. 2559-2565.
262. Senden, T.J., J.M. Di Meglio, and P. Auroy, *Anomalous adhesion in adsorbed polymer layers*. European Physical Journal B: Condensed Matter Physics, 1998. **3**(2): p. 211-216.
263. Johnston, E., et al., *Networks from a,w-Dihydroxypoly(dimethylsiloxane) and (Tridecafluoro-1,1,2,2-tetrahydrooctyl)triethoxysilane: Surface Microstructures and Surface Characterization*. Macromolecules, 1999. **32**(24): p. 8173-8182.
264. Wenzler, L.A., et al., *Measurements of Single-Molecule Bond-Rupture Forces between Self-Assembled Monolayers of Organosilanes with the Atomic Force Microscope*. Langmuir, 1997. **13**(14): p. 3761-3768.
265. Wenzler, L.A., et al., *Single-Molecule Bond-Rupture Force Analysis of Interactions between AFM Tips and Substrates Modified with Organosilanes*. Analytical Chemistry, 1997. **69**(14): p. 2855-2861.
266. Hilal, N., et al., *(Bio)fouling of polymeric membranes: atomic force microscope study*. Engineering in Life Sciences, 2002. **2**(5): p. 131-135.
267. Williams, J.M., T. Han, and T.P. Beebe, Jr., *Determination of Single-Bond Forces from Contact Force Variances in Atomic Force Microscopy*. Langmuir, 1996. **12**(5): p. 1291-5.
268. Grandbois, M., et al., *Covalent attachment of a single dextran polymer between the tip of an atomic force microscope and a gold surface*. Materials Research Society Symposium Proceedings, 1999. **576**(Organic/Inorganic Hybrid Materials II): p. 171-175.
269. Garnier, L., et al., *Covalent bond force profile and cleavage in a single polymer chain*. Journal of Chemical Physics, 2000. **113**(6): p. 2497-2503.
270. Segura, J.M., et al., *Tip-induced spectral dynamics of single molecules*. Chemical Physics Letters, 2001. **340**(1,2): p. 77-82.
271. International Technology Roadmap for Semiconductors, 2000.

272. Maynor, B.W., et al., *Direct-Writing of Polymer Nanostructures: Poly(thiophene) Nanowires on Semiconducting and Insulating Surfaces*. Journal of the American Chemical Society, 2002. **124**(4): p. 522-523.
273. Carlsson, C., et al., *Optical and Photophysical Properties of the Oxazole Yellow DNA Probes YO and YOYO*. Journal of Physical Chemistry, 1994. **98**(40): p. 10313-21.
274. Hu, D., J. Yu, and P.F. Barbara, *Single-Molecule Spectroscopy of the Conjugated Polymer MEH-PPV*. Journal of the American Chemical Society, 1999. **121**(29): p. 6936-6937.
275. Huser, T., M. Yan, and L.J. Rothberg, *Single chain spectroscopy of conformational dependence of conjugated polymer photophysics*. Proceedings of the National Academy of Sciences of the United States of America, 2000. **97**(21): p. 11187-11191.
276. McNeill, J.D., et al., *Field-Induced Photoluminescence Modulation of MEH-PPV under Near-Field Optical Excitation*. Journal of Physical Chemistry B, 2001. **105**(1): p. 76-82.
277. Bowden, N.B., et al., *Synthesis of Fluorescently Labeled Polymers and Their Use in Single-Molecule Imaging*. Macromolecules, 2002. **35**(21): p. 8122-8125.
278. Uji-i, H., et al., *Nanospark at the interface between organic solvents and tin-doped indium oxide*. Applied Physics Letters, 2001. **79**(16): p. 2660-2662.
279. Strother, T., et al., *Synthesis and Characterization of DNA-Modified Silicon (111) Surfaces*. Journal of the American Chemical Society, 2000. **122**(6): p. 1205-1209.
280. Benters, R., et al., *DNA microarrays with PAMAM dendritic linker systems*. Nucleic Acids Research, 2002. **30**(2): p. e10/1-e10/7.
281. Burtman, V., A. Zelichenok, and S. Yitzchaik, *Organic quantum-confined structures through molecular layer epitaxy*. Angewandte Chemie, International Edition, 1999. **38**(13/14): p. 2041-2045.
282. Christoffels, L.A.J., A. Adronov, and J.M.J. Frechet, *Surface-confined light harvesting, energy transfer, and amplification to fluorescence emission in chromophore-labeled self-assembled monolayers*. Angewandte Chemie, International Edition, 2000. **39**(12): p. 2163-2167.
283. Kiss, E. and C.G. Goelander, *Chemical derivatization of muscovite mica surfaces*. Colloids and Surfaces, 1990. **49**(3-4): p. 335-42.
284. Dancil, K.-P.S., D.P. Greiner, and M.J. Sailor, *A Porous Silicon Optical Biosensor: Detection of Reversible Binding of IgG to a Protein A-Modified Surface*. Journal of the American Chemical Society, 1999. **121**(34): p. 7925-7930.
285. Osborne, M.A., et al., *Probing DNA Surface Attachment and Local Environment Using Single Molecule Spectroscopy*. Journal of Physical Chemistry B, 2001. **105**(15): p. 3120-3126.
286. Luzinov, I., et al., *Epoxy-Terminated Self-Assembled Monolayers: Molecular Glues for Polymer Layers*. Langmuir, 2000. **16**(2): p. 504-516.
287. Zhao, X. and R. Kopelman, *Mechanism of Organosilane Self-Assembled Monolayer Formation on Silica Studied by Electric Field Induced Second-Harmonic Generation*. Journal of Physical Chemistry, 1996. **100**(26): p. 11014-11018.